All-Optical Production of a Degenerate Gas of ^{6}Li: Characterization of Degeneracy

by

Stephen Riley Granade

Department of Physics
Duke University

Date:_____
Approved:

_____
Dr. John E. Thomas, Supervisor

_____
Dr. Daniel J. Gauthier

_____
Dr. Konstantin Matveev

_____
Dr. Horst Meyer

_____
Dr. Calvin Howell

Dissertation submitted in partial fulfillment of the
requirements for the degree of Doctor of Philosophy
in the Department of Physics
in the Graduate School of
Duke University

2002

ABSTRACT

(Physics)

All-Optical Production of a Degenerate Gas of ^{6}Li: Characterization of Degeneracy

by

Stephen Riley Granade

Department of Physics
Duke University

Date:_____
Approved:

_____
Dr. John E. Thomas, Supervisor

_____
Dr. Daniel J. Gauthier

_____
Dr. Konstantin Matveev

_____
Dr. Horst Meyer

_____
Dr. Calvin Howell

An abstract of a dissertation submitted in partial fulfillment of
the requirements for the degree of Doctor of Philosophy
in the Department of Physics
in the Graduate School of
Duke University

2002

Abstract

In this dissertation, I describe the first production of a degenerate Fermi gas of ^{6}Li by all-optical means and the characterization of that gas in the quantum degenerate regime. An optical trap formed by an ultrastable CO_2 laser confines 3.5×10^6 lithium atoms. The atoms are then evaporatively cooled to the quantum degenerate regime, at which point 1×10^5 atoms remain at a temperature of $\sim 4\,\mu$K, around half the system's Fermi temperature. I describe how the trapped atoms' number and temperature are determined by absorption imaging via a CCD camera with a resolution of $3.3\,\mu$m, and how that determination must be modified to account for fermionic effects. Furthermore, I explain how the degenerate gas's interaction strength can be characterized by measuring the gas's density profile. To that end, I present a theory for calculating the zero-temperature density distribution of a two-state fermionic gas by balancing the forces on that gas. The work described in this dissertation offers many future avenues of study, as degenerate Fermi gases are rich with interesting physical behavior.

Single-state Fermi gases do not interact; two states must be trapped if one wishes to cool these atoms through evaporation or create a fermionic superfluid. Unlike magnetic traps, optical traps can confine any and all atomic hyperfine states, allowing the trapping of any two-state combinations and thus increasing the types of interactions that can be studied. While many groups have begun using optical traps in the final stage of their degeneracy experiments, this dissertation's experiments are

the first to employ an optical trap for all stages of trapping and cooling fermions to degeneracy, dramatically simplifying the procedure to reach the quantum degenerate regime.

Properties of our ^{6}Li gas, such as its temperature and interaction strength, are readily adjusted, making it ideal for a number of applications, including quantum computing and the creation of high-precision frequency standards, where the exclusion principle suppresses dephasing collisions. Perhaps most exciting is the possibility of observing a fermionic superfluid. The states of ^{6}Li that we trap are predicted to have some of the highest critical temperatures (in units of the Fermi temperature) ever seen in superfluids, and are thus analogs of high-temperature superconductors.

Acknowledgments

No work of scholarship is created in a vacuum. While footnotes and references acknowledge the people who contributed direct ideas, there are many who have a vital yet indirect role, people who may not ever show up in the bibliography.

My parents, Ray and Ronnie, did much to foster my love of reading and learning. Though I did not realize it at the time, in hindsight their tolerance of my many projects and interests was nothing short of miraculous. They gave me books and told me that whatever path I pursued in life, they would support me. Even when it appeared that I might become an actor or director they never batted an eye, and they helped me realize that I could go to graduate school in physics and that once there I could do well.

I have been blessed with a brother who is both family and friend, though at times we fought ferociously. Andrew has been my confidant many times, and I count myself lucky for it. His wife Joy, though a later addition to our family, is also among my closest friends. Some day we will live close enough to have weekly game nights.

Ouachita Baptist University is a small college, yet somehow it manages to attract a disproportionate number of excellent faculty. In my next-to-last year there a new faculty member named Bob Hamilton joined the physics department. He agreed to be my advisor, and gave me my first true glimpse of what physics research was like. He helped guide me in my journey to graduate school, and was willing to tell me

the truth about what it would be like while never doubting I would persevere.

Capturing my advisor John Thomas in words is akin to trapping the wind with a net. He is funny, engaging, manic, and possesses one of the sharpest minds I have ever encountered. His grasp of the theories of physics is sure, and yet he never lets theory overwhelm his keen experimental sense. Many times I would be wrestling with some problem in the lab, only to have him come in and find a solution within ten minutes. John's love of physics is infectious, and he did a fine job of steering both me and the experiment. He also radiates quotes in the same way uranium radiates alpha particles. Some of my favorites include:

- "All our techniques are completely universal, except they only work on one thing."
- "$\pi/2$ is 1. And I don't care about 2. 2 is 1 also."
- "I only think ahead in hindsight."
- "A constant's a gaussian. It's just kind of big."
- "It's a long shot, but it has a good chance."
- "For my money, infinite need not be all that infinite."
- "This is wrong, but suppose..."

I have worked with a number of excellent people in John's research group. When I first arrived, Tom Savard, Adam Wax, Chris Baird, Zehuang Lu, Ken O'Hara, and Hongzhi Zhao helped acclimate me to research and the group as a whole. I spent much of my first three years working closely with Tom Savard. He taught me how

to align an A/O and how to deal with a recalcitrant dye laser. Despite how close he was to being graduated and how anxious he must have been, he was still willing to take the time to teach me. I helped with his data analysis while he was writing his dissertation, and the insight he gave me during that process has helped me with my dissertation. Our post-doc Dr. Samir Bali was invaluable. He offered a different perspective on many aspects of our experiment, and his paper-writing skills were unmatched in our group. These days Samir has his own cooling and trapping group at Miami University; our loss is MU's gain.

Working with Ken O'Hara has been a pleasure. Much of the foundation of this dissertation is due to Ken. He is methodical and careful, two qualities which made an unruly and gargantuan experiment manageable. He is tireless, working long after my inclination was to throw in the towel, and generous in sharing his wide-ranging knowledge of physics. I owe a debt to him that I will never be able to repay.

My closest co-worker has been Michael Gehm. Mike and I joined John's group at the same time, and worked on the experiment together. He is a font of ideas, and quick to see what needs to be done and the best way to do it. His physical insight, his knowledge of what our formulas and theories mean in the real world, is a source of inspiration. Without him this experiment would have foundered long ago. In addition, his friendship has made graduate school a much more pleasant place.

I have also enjoyed working with the newer students in our group, Frank Reil, Kim Fook Lee, Staci Hemmer, and D. J. Cecil. I wish them the best of luck, and hope their graduate school experience is as good as mine.

There have been several Michaels who have affected the course of my graduate career. Mike Gehm was one; Michael Stenner is another. Michael has been both

a friend and colleague, and has been willing to loan us just one more AOM driver or lens holder. Without his help I would have been hard-pressed to complete the precision timing system.

My committee, which included Dr. Daniel J. Gauthier, Dr. Konstantin Matveev, Dr. Horst Meyer, and Dr. Calvin Howell, has helped make this dissertation better than it would have been without their input. For that I thank them.

Two groups of people, my Sunday School class and the denizens of ifMUD, offered their support and fellowship during my writing. They listened sympathetically to my grumbling, made witty comments about the process, and in general helped keep my spirits up. (At one point I was asked why I was wasting my time on a dissertation when I could be writing a romance novel. Somehow I doubt Harlequin would be interested in a novel with lines such as, "'My, that's a very large laser,' she whispered coherently.")

The person to whom I am the most indebted, though, is my wife Misty. She persevered through the first year of graduate school, when she would see me for only a few hours every week. She never complained, though the stress of that time was difficult. She has supported me during the long stretches when nothing seemed to be working on the experiment. When I was unsure whether or not I would finish graduate school she was there to assure me that I could and would. To top it off, she has given me a second family. Her mom Kate, Don and Linda Clark, Uncle Stoney and Aunt Mel, her grandparents, cousins—all have welcomed me and been a source of strength throughout. And all of it is because of Misty. Without her, my life would be far less.

For Misty

Contents

Abstract **vii**

Acknowledgments **ix**

List of Figures **xxi**

List of Tables **xxv**

1 Introduction **1**

1.1 1999–2001: To Degeneracy 3

1.2 Dilute and Degenerate 5

1.3 Historical Perspective of Trapping 8

1.3.1 Magneto-Optical Traps Start Things Off 8

1.3.2 Magnetic Traps Reach Degeneracy 11

1.3.3 Optical Traps Push for Superfluidity 15

1.4 Significance of Current Work 17

1.4.1 Stable Optical Trap Using a Commercially-Available Laser . 17

1.4.2 The All-Optical Route to Fermi Degeneracy 19

1.4.3 Low-Temperature Physics 20

1.5 Dissertation Organization 21

2 ^{6}Li Interactions **25**

2.1 Elastic Scattering at Cold Temperatures 26
2.2 S-Wave Scattering Length 29
2.3 Magnetic Tuning of the Scattering Length 32
2.4 Feshbach Resonances 34
2.5 Fermi Superfluidity 36
2.5.1 Cooper Pairing 36
2.5.2 Resonance Superfluidity 40
2.6 States of ^{6}Li Used in the Experiment 41

3 Optical Trapping **45**

3.1 The Physics of Optical Trapping 46
3.2 Noise and Optical Traps 54
3.2.1 Intensity Noise 55
3.2.2 Position Noise 57
3.3 A Quiet Commercial CO_2 Laser 58
3.3.1 Measuring the Noise Spectra 60
3.3.2 Intensity Noise 61
3.3.3 Position Noise 65
3.4 First-Stage Trapping Apparatus 66
3.4.1 Vacuum System 67
3.4.2 ^{6}Li Oven 72
3.4.3 Zeeman Slower 73
3.4.4 Magneto-Optical Trap 74
3.4.5 Lasers, Acousto-Optical Modulators, and Optical Layout . . 75
3.4.6 MOT Loading Procedure 82

3.5 CO_2 Laser Trapping 83
3.5.1 Optical Setup 83
3.5.2 Optical Alignment 86
Standard Alignment Procedure 87
Alignment Using a Split Image Technique 89

4 Characterizing the Optical Trap 93

4.1 Fluorescence Measurement 94
4.2 Absorption Imaging 97
4.3 Timing System 101
4.3.1 Computer Control 101
4.3.2 Multiplexer System 104
4.4 CCD Camera System 105
4.4.1 CCD Camera 105
4.4.2 Optical Probe Setup 106
Fluorescence Measurement Setup 107
Absorption Imaging Setup 107
4.4.3 Camera Magnification 110
4.4.4 Determining Atomic Number and Temperature 111
4.4.5 Time of Flight Measurements 113
4.4.6 Effect of Fermi Statistics on Temperature Measurement . . . 115
4.5 Measuring Trap Parameters 118
4.5.1 Modification of the CO_2 Laser Acousto-Optic Modulator Driver 118
4.5.2 Shaking the Trap 120
4.5.3 Parametric Resonance 122

5 Evaporative Cooling to Degeneracy **125**

5.1 Boltzmann Equation Approach to Evaporation 129

5.1.1 Density of States in the Optical Trap 129

5.1.2 The Boltzmann Equation and the Ergodic Assumption . . . 131

5.1.3 Scaling Laws 134

5.2 The $|2\rangle - |1\rangle$ Mixture 138

5.3 Additions to the Optical Setup 140

5.3.1 Acousto-Optic Modulator 140

5.3.2 The "Chopper" 144

5.4 Correcting First-Order Beam Misalignment 148

5.4.1 The Imaging Approach 148

5.4.2 AOM Frequency Correction 150

5.5 Evaporation to Degeneracy 153

5.6 Summary 159

6 Density of a Two-Component Interacting Fermi Gas at Zero Temperature **161**

6.1 Force Balance 162

6.1.1 Homogeneous ^{6}Li Gas 163

6.1.2 Two-State ^{6}Li Gas 167

6.2 Stability of the Gas 168

6.3 Density Calculation 175

6.4 Summary 179

7 Conclusion **181**

7.1 Chapter Summary 182
7.2 Improvements to the Experiment 186
7.3 Future Outlook 187

A Split-Image Calculation **191**

B The Computer-Controlled Timing System **197**

B.1 Physical Components 198
B.2 The Basic Timing File 200
B.3 The Perl Preprocessor 203
B.4 LabView and C Code 206
B.5 Example of Creating a Timing File 207
B.5.1 Sequence of Events 207
B.5.2 Mapping Events to Variables 208
B.5.3 Mapping Event Variables to Channels 215

C Fermionic Density Calculation **223**

Bibliography **229**

Biography **237**

List of Figures

1.1 Optical Molasses 9

1.2 Magneto-Optical Trap 11

1.3 Magnetic Trap 12

1.4 Evaporative Cooling 13

1.5 Optical Trap 16

1.6 Scale of Evaporation 20

2.1 Triplet and Singlet Molecular Potentials 31

2.2 Shape and Feshbach Resonances 34

2.3 Scattering Length Near a Feshbach Resonance 35

2.4 Formation of a Cooper pair 37

2.5 Hyperfine States of ^{6}Li 41

2.6 Magnetic Field Dependence of a_{12} 43

3.1 Dipoles Induced by an Electric Field 47

3.2 Intensity Noise 56

3.3 Position Noise 58

3.4 Experimental Setup for Measuring Noise 60

3.5 Low Resolution Intensity Noise Spectrum for the DEOS Laser . . . 62

3.6 High Resolution Intensity Noise Spectrum for the DEOS Laser . . . 63

3.7 Exponential Heating Time due to Intensity Noise 64

3.8 Voltage Fluctuations With and Without Razor Blade 66
3.9 Oven and Zeeman Region of the Vacuum System 69
3.10 Trapping Region of the Vacuum System 70
3.11 Recirculating Oven 72
3.12 Locking Region Oven 76
3.13 Acousto-Optic Modulator in Double-Passed Configuration 77
3.14 Creating the Slower and MOT Beams 80
3.15 Optical Setup of the MOT Beams 81
3.16 Optical Setup of CO_2 Laser Trap 85
3.17 Split-Image Alignment of the Aspheric Lens 90

4.1 Fluorescence Measurement System 96
4.2 Calculating the Absorption Image 99
4.3 Binning of an Image 101
4.4 Schottky Diode Termination of Timing System Outputs 103
4.5 Optical Setup for the Probe Beams 106
4.6 Absorption Imaging System 108
4.7 Image Rotation due to Angled Beam 109
4.8 Measurement of the Camera Magnification 110
4.9 Clebsch-Gordan Coefficients for Camera Beam Transition 112
4.10 CO_2 Laser AOM Driver Modification 119
4.11 PMT Signal Following Trap Shaking 121
4.12 PMT Signal Following Parametric Resonance 123

5.1 The Evaporative Process 126

5.2 Low-Field Values of a_{12} 139
5.3 Location of Cooling Plates on the CO_2 Laser AOM 141
5.4 AOM Voltage versus CO_2 Laser Power 143
5.5 Blocking the Rooftop Mirror 144
5.6 CO_2 Laser Beam Profile After Occlusion 145
5.7 Occluded CO_2 Laser Beam at the Trap 146
5.8 The "Chopper" 147
5.9 $4f$ Imaging Setup 149
5.10 Interference in the First-Order Beam 150
5.11 Frequency Correction 151
5.12 Temperature During Evaporation 154
5.13 T Versus T_F During Evaporation 155
5.14 Velocity Distribution After 10 Seconds 156
5.15 Velocity Distribution After 40 Seconds 157
5.16 Velocity Distribution After 60 Seconds 158

6.1 Gas Displacement by a Sound Wave 169
6.2 Radial Density Distribution of Fermi Gases 177
6.3 Axial Density Distribution of Fermi Gases 178

A.1 Focal Lengths and Principal Points 192
A.2 Setup for Split Image Detection 193

B.1 Block Diagram of the Timing System Physical Components 198
B.2 Schottky Diode Termination of Timing System Outputs 199
B.3 Block Diagram of the Timing System Software Components 203

B.4 Block Diagram of the MOT Optical Setup 210
B.5 Block Diagram of Probe Beam Optical Setup 212
B.6 MOT AOM Timing Diagram 216

List of Tables

3.1 Typical Oven Temperatures 73

4.1 PMT Voltages and Gain 95

4.2 Multiplexer Logic States 104

A.1 Lens Characteristics 194

B.1 Timing System Channel Assignments 215

B.2 MOT/Repumper AOM States 216

Chapter 1

Introduction

On October 9th, 2001, the Royal Swedish Academy of Sciences announced the recipients of the 2001 Nobel Prize for Physics. Eric A. Cornell, Wolfgang Ketterle, and Carl E. Wieman were awarded the prize "for the achievement of Bose-Einstein condensation in dilute gases of alkali atoms, and for early fundamental studies of the properties of the condensates." In just six years, Bose-Einstein condensation (BEC) in a dilute atomic vapor had gone from a dream of experimentalists to a sub-field of physics worthy of a Nobel prize.

The creation of BEC in a dilute gas by three groups in 1995 [1, 2, 3] opened the door to a myriad of experiments. BEC was not a new idea: Einstein had first predicted its existence in 1925 [4]. The first BEC experiments involved superfluid ^{4}He, a liquid. But liquids are strongly interacting, and Einstein's original concept of BEC involved an ideal gas. The dilute nature of the alkali gases used in recent BEC experiments leads to interactions which are both weak, especially when compared to interactions in a liquid, and well-understood. Thus comparisons between theory and actual experimental results are more easily made. The interactions can even be widely adjusted by application of a magnetic field [5, 6, 7]. In addition, a BEC can be a source of coherent matter waves [8, 9, 10] for use in atom lithography and the exploration of matter-wave optical effects.

Given the success of BEC experiments, the next natural question was, "What about making a degenerate gas of fermions instead?" Prior to the relatively recent work involving alkali gases, the only dilute system of degenerate fermions studied was that of ^{3}He dissolved in superfluid ^{4}He.[1] A degenerate gas of fermions would possess many of the same benefits as a similar gas of bosons: weak and well-understood interactions, control of those interactions via a magnetic field, and the chance to explore many-body interactions [12, 13].

Most exciting, though, is the possibility of producing a fermionic superfluid gas. To do so requires both attractive s-wave interactions between atoms and a gas which is dense enough, so that atoms may pair up and form composite bosons. By magnetically tuning these s-wave interactions it may be possible to create a superfluid, either through formation of Cooper pairs, as in the Bardeen-Cooper-Schrieffer (BCS) theory of superconductivity [14, 15], or by having very strong interactions and creating a resonance superfluid [16, 17]. The two stable fermionic alkali atoms, ^{40}K and ^{6}Li, both have two-state mixtures which exhibit large and attractive interactions, allowing observation of superfluidity at the highest critical temperatures T_c of any Fermi superfluids [18, 16], in units of the Fermi temperature.

There is a problem hidden in the above. Superfluidity requires that *two* hyperfine states of the atom in question be trapped, as they play the same role as spin states in canonical BCS theory. But the problem is worse yet: evaporative cooling, the most direct and experimentally tested method of cooling a dilute alkali gas, also requires that two hyperfine states be trapped. Evaporative cooling depends on collisions to rethermalize the gas. At the very low temperatures required for degeneracy, only s-wave scattering collisions occur, and such collisions between two fermions in the

[1] For an overview of such experiments, see Ref. [11].

same state are not allowed by the Pauli exclusion principle.

Magnetic traps are a standard tool for atomic trapping experiments. While optical traps were employed in the early years of atomic trapping, their usefulness was limited due to then-unexplained heating and trap-loss rates [19, 20, 21]. By far the majority of BEC work has been done using magnetic traps—only one group has produced a BEC using an optical trap [22], and that only recently. However, magnetically-trapped mixtures of ^{6}Li, the atom I worked with, are nearly unusable due to large spin-exchange and dipolar decay rates [23]. Unlike magnetic traps, optical traps are able to trap atoms regardless of their state, allowing experimentalists to use two-state mixtures of ^{6}Li which do not suffer from excessive spin-exchange or dipolar decay rates. I have thus helped develop a stable optical trap [24] and used it to evaporatively cool a two-state mixture of ^{6}Li to degeneracy [25]. Slight changes in the experiment should allow exploration of resonant interactions of the two-state mixture and potentially observe Cooper pairing and superfluidity. In addition, it will be possible to study suppression of three-body collisions in a two-state Fermi gas and the mechanical stability of strongly attractive or repulsive mixtures.

1.1 1999–2001: To Degeneracy

Before discussing the general motivation for my work on degenerate Fermi gases, I must put the contents of this dissertation in perspective. My work builds strongly on Ken O'Hara's dissertation work [26]. By 1999 he, along with Mike Gehm and myself, and under the supervision of Dr. John Thomas, had developed a custom-built 65 W CO_2 laser and used it to trap and cool ^{6}Li. The optical trap lifetime was 300 s, two orders of magnitude greater than prior optical trap lifetimes. Temperatures of $T = 2.4\,\mu$K were reached, but the phase space density was only $\rho \simeq 1.6\times10^{-3}$, well

short of the quantum degenerate regime.

At the start of Mike Gehm's and my dissertation work in 1999, it was unclear whether it was even possible to reach quantum degeneracy in a single-beam optical trap. Many thought a crossed-beam optical trap was necessary in order to have tight confinement in all directions. The first all-optical Bose-Einstein condensate was produced in just such a trap [22].

Mike and I were stubborn, convinced that a single-beam optical trap could be used to produce a quantum degenerate gas. We reworked the experiment, starting nearly from scratch. We needed more laser power in our optical trap in order to confine more atoms and thus increase the amount of evaporative cooling we could perform. We needed a way to measure the number and temperature of our atomic cloud in one shot. We needed an easier and more flexible way of controlling our equipment.

In order to increase the laser power in our optical trap, we bought and installed a 140 W commercial CO_2 laser more than doubling the power in our optical trap. We also retroreflected the trapping beam, nearly doubling the power in the trap again. In order to measure the number and temperature of our gas, we installed a CCD camera and developed an absorption measurement technique. In order to control the camera and other equipment with split-second accuracy over 100s of seconds, we created a computer-controlled timing system.

The experiments described in this dissertation are the result of an extraordinary group effort. The tasks on the road to degeneracy were divided among us as necessary. I developed the timing system while Mike worked on the theory of absorption imaging. I worked on how to analyze our gas's temperature and phase space density while Mike designed a Monte-Carlo simulation of our optical trap's

loading and cooling. Together, along with Ken O'Hara as our post-doc, we cooled ^{6}Li to the quantum degenerate regime in 2001, and in doing so created the world's first degenerate fermionic gas by all-optical means.

This dissertation describes how we trapped and cooled ^{6}Li to the quantum degenerate regime. I will focus on the characterization of these gases: How do we determine the atoms' temperature and number when Fermi effects are large? When the atoms are degenerate, how do we measure their interaction strength? Mike Gehm's dissertation is a companion to this one. While describing the same experiments, he discusses the physics that we investigated in the process of reaching degeneracy, such as the dynamics of trapped gases and signal-to-noise associated with imaging.

1.2 Dilute and Degenerate

Why is there such interest in quantum degenerate gases of neutral alkali atoms? The gases have two major features that make them of great interest to experimentalists and theorists alike: they are dilute, and they are degenerate.

"Dilute" is relatively easy to define. A gas is considered dilute if the average distance between gas particles is much greater than the range of their interparticle interactions, so that interactions between particles are weak. If the range of the interparticle potential is given by r_0, then we can consider a characteristic interaction volume r_0^3. The number of particles in a given volume is the number density n. Thus a gas is dilute if the number of particles in the interaction volume, nr_0^3, is much less than one.

"Degenerate" is a more complex term, as might be expected given the rich behaviors exhibited by degenerate systems. Roughly speaking, a gas of identical,

non-interacting particles becomes degenerate when they are packed tightly enough that their wave functions overlap, causing them to exhibit macroscopic quantum behavior.

More rigorously, a particle of mass m and temperature T has an associated quantum wavepacket. The wavelength of this wavepacket is given by the thermal deBroglie wavelength,

$$\lambda_{dB} = \frac{h}{\sqrt{2\pi m k_B T}}. \tag{1.1}$$

In the same way that one determines what makes a gas dilute, one can consider a characteristic wavelength volume, given by λ_{dB}^3. This volume can be thought of as the wavepacket volume. Then the number of particles in this volume is given by $n\lambda_{dB}^3$, a quantity known as the phase-space density. When $n\lambda_{dB}^3 > 1$, on average particles' wavepackets overlap and the gas is degenerate. As noted by Hagley *et al.* [27], this is far from a normal happenstance. Air has a number density of $\sim 0.03\,\mathrm{nm}^{-3}$ and $\lambda_{dB} \sim 0.02\,\mathrm{nm}$, giving a phase-space density of $\sim 2\times10^{-7}$.

What happens when a gas becomes degenerate depends on whether it is a boson or a fermion. The two are distinguished by how the multi-particle wave function of the gas behaves if one swaps the label of any two particles in that gas. If the particles are bosons and thus have integer spin, their wave functions are symmetric and do not change sign when labels are swapped. If the particles are fermions and thus have half-integer spin, their wave functions are antisymmetric. The two types of particles behave very differently at low temperatures. The behavior of bosons is dictated by Bose-Einstein statistics; fermions, by Fermi-Dirac statistics.

Bosons are gregarious and, as they are cooled further and further, begin to congregate in the system's ground state. When the temperature and density of a homogeneous bosonic gas are such that $n\lambda_{dB}^3 = 2.612$, the gas undergoes a phase

transition in which a significant fraction of the gas particles drop into the ground state, forming a Bose-Einstein condensate. Fermions, on the other hand, are loners. Due to the Pauli exclusion principle, particles in a cooled fermionic gas do not drop into the ground state. Instead they pile up, one to an energy state, like people on the rungs of a ladder. There is no Fermi phase transition analogous to that of Bose-Einstein condensation.

It is the weak interparticle interactions that help make dilute alkali gases a good experimental system, as the problem of creating an applicable theory becomes much more tractable. Any introductory textbook on statistical mechanics will discuss Bose-Einstein and Fermi-Dirac statistics. It is when strong interactions must be taken into consideration that things become far less tractable. Liquid helium, one of the earliest examples of a quantum degenerate system, has interactions so strong that they cannot be treated by perturbation theory [28].

The low temperatures present in experiments involving degenerate alkali gases also help simplify the theory of interparticle interactions. Three-body collisions are rare because the gas is dilute, and at these temperatures, two-particle head-on collisions that impart no change in angular momentum, known as s-wave collisions, dominate. Further, in the low-energy limit, the s-wave collision cross section is characterized by one number, the scattering length a. In this limit the effective potential between two atoms whose positions are separated by $\mathbf{x}$ is given by

$$V(\mathbf{x}) = \frac{4\pi\hbar^2 a}{m}\,\delta(\mathbf{x}), \tag{1.2}$$

where m is the mass of the particles and δ indicates a delta-function potential.

From the above equation we see that the effective potential will be attractive if $a < 0$. This is important, as the formation of Cooper pairs and thus a fermionic

superfluid requires that interaction between atoms be attractive. The easiest way to satisfy this condition is for a to be negative; and the larger a is, the stronger the attractive potential and the higher the temperature at which fermionic superfluids form.

1.3 Historical Perspective of Trapping

While the dilute nature of alkali gases makes for simpler theoretical description, it also increases the difficulty of reaching the quantum degenerate regime. Because n is so small, correspondingly low temperatures must be reached in order for $n\lambda_{dB}^3 > 1$. The phase-space density of trapped gases must be increased by many orders of magnitude in order to reach degeneracy. The story of atomic cooling and trapping is thus one of ever-improving technology and experimental techniques. For nearly a decade, physicists worked to make alkali gases colder and more dense, with progress coming in fits and starts.

1.3.1 Magneto-Optical Traps Start Things Off

Although magneto-optical traps (MOTs) have been extensively covered in the literature[2], it is worth discussing them briefly, as they are the workhorse of atomic trapping experiments.

MOTs cool a gas by utilizing the momentum transferred when photons scatter from an atom. Imagine two laser beams counter-propagating left and right, both detuned to the red side of the atomic resonance for the atom to be trapped, as in Figure 1.1. Now place an atom in the beams. Should the atom begin moving right,

[2]See, for example, Ref. [29] for an astoundingly long list of references.

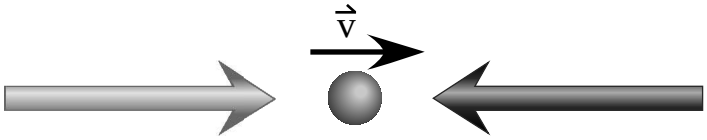

Figure 1.1: An atom between two red-detuned, counter-propagating laser beams. As the atom moves to the right, it preferentially scatters photons from the beam travelling from right to left due to the Doppler shift. This arrangement gives rise to a viscous damping force, which in turn led to the arrangement being called "optical molasses."

the beam propagating from left to right will be Doppler-shifted towards the blue, shifting it closer to resonance. Meanwhile, the beam propagating from right to left is red-shifted *further* from resonance. The net effect is that the atom will begin preferentially scattering photons from the beam that is propagating opposite to its direction of motion. The resulting momentum transfer will serve to slow the atom. Should the atom instead move left, it will begin preferentially scattering photons from the right-propagating beam, and once again will be slowed. The result is a viscous damping force, which slows the atom regardless of the direction in which it moves. The force on the atom as a function of its velocity v is a combination of the force due to each beam separately. If both beams have the same intensity I, that force is

$$\begin{aligned} F &= \hbar k \frac{\Gamma}{2} \left[\frac{I/I_{sat}}{4(\Delta - kv)^2/\Gamma^2 + (1 + 2I/I_{sat})} \right] \\ &- \hbar k \frac{\Gamma}{2} \left[\frac{I/I_{sat}}{4(\Delta + kv)^2/\Gamma^2 + (1 + 2I/I_{sat})} \right]. \end{aligned} \tag{1.3}$$

I_{sat} is the saturation intensity of the atom, Γ is the linewidth of the transition, and Δ is the detuning of the beams from resonance. Near $v = 0$, the force can be expanded in powers of v, giving a linear form of the force, $F = -\alpha v$, where the

friction coefficient α is

$$\alpha = -4\hbar k^2 \frac{I}{I_{sat}} \frac{2\Delta/\Gamma}{[4\Delta^2/\Gamma^2 + (1 + 2I/I_{sat})]^2}. \tag{1.4}$$

This one-dimensional setup can be generalized to three dimensions by placing counter-propagating beams along three orthogonal axes. The result is a three-dimensional field in which atoms experience a viscous damping force. Due to the friction-like qualities of this damping force, such a setup was given the name "optical molasses."

Despite its damping ability, optical molasses is not a true trap. There is no restoring force to drag atoms back to a central location. Atoms entering optical molasses are slowed, but they are continually absorbing and re-emitting photons from all directions and thus can leave the region where the six laser beams overlap by a random-walk process. The atoms are confined in velocity space but not in position.

The addition of a magnetic field and the use of circularly-polarized light in the optical molasses provide the necessary restoring force. Figure 1.2 demonstrates the idea in one dimension using an atom with a transition from $J = 0$ to $J' = 1$. A linear magnetic field is applied, thus splitting the magnetic sublevels of the $J' = 1$ level. Where the magnetic field is zero, there is no splitting; away from that point, the m sublevels split in opposite directions. The red-detuned counter-propagating beams are $\sigma^{\pm}$ polarized, and thus drive the $\Delta m = \pm 1$ transitions, respectively. As an atom moves right, the $m = -1$ transition is magnetically shifted closer to resonance, causing the atom to scatter photons preferentially from the left-propagating σ^- beam. The resulting force moves the atom back towards the magnetic zero point. Should the atom move left, it begins absorbing more photons

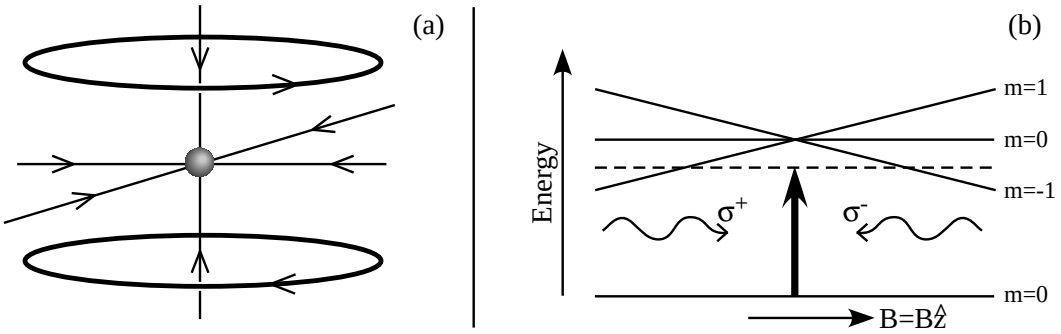

Figure 1.2: The magneto-optical trap. (a) The physical layout of the trap, showing the beams along orthogonal axes and the position of the magnetic coils. (b) The level structure of an example atom undergoing a transition from $J = 0$ to $J' = 1$ in a MOT. A linear magnetic field $\mathbf{B} = B\hat{\mathbf{z}}$ is applied to split the upper levels.

from the right-propagating σ^+ beam. Thus to the viscous damping force of optical molasses is added a spring-like restoring force $F = -\kappa z$. The three-dimensional version has counter-propagating $\sigma^\pm$ beams along all three orthogonal axes and a set of anti-Helmholtz coils to provide a spherical quadrupole magnetic field, which is linear in all directions near the zero point of the field.

MOTs are very effective at trapping and cooling a large number of atoms, with final temperatures ranging from $10\,\mu\text{K} - 1\,\text{mK}$ and densities on the order of $10^{11}\,\text{atoms/cm}^3$. This only gives a phase space density of $\sim 10^{-6}$, though. Much more work is required to produce a degenerate alkali gas.

1.3.2 Magnetic Traps Reach Degeneracy

In BEC experiments, neutral atoms are loaded into a magnetic trap and cooled via evaporation. A magnetic trap utilizes the physics behind the Stern-Gerlach effect: a magnetic field gradient produces a force on a magnetic dipole. A non-uniform magnetic field $\mathbf{B}$ with a non-zero local minimum is sufficient to form a magnetic trap. The force on the atom due to the field is given by $F = -\boldsymbol{\mu} \cdot \nabla\mathbf{B}$, where $\boldsymbol{\mu}$ is

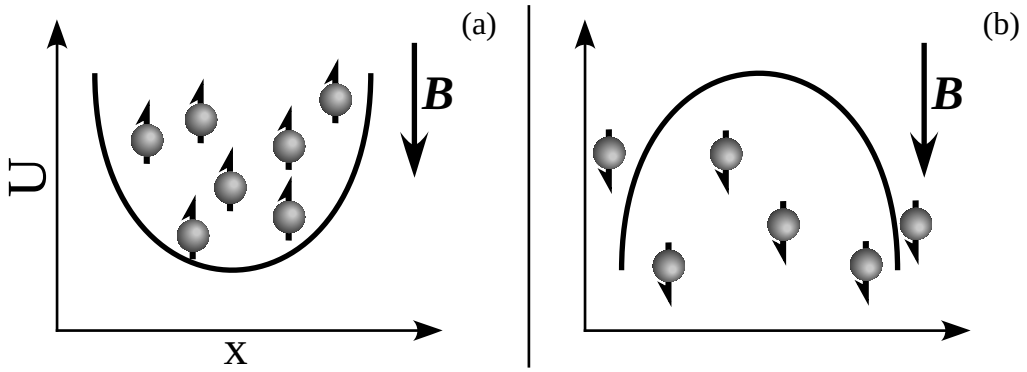

Figure 1.3: The magnetic potential energy of a one-dimensional magnetic trap due to a field **B**. In (a) the atoms, represented with arrows to show the direction of their magnetic moments, are weak-field seeking and thus are trapped. In (b) the atoms are strong-field seeking; for them, the energy curve is inverted and the atoms are not trapped.

the magnetic dipole of the atom. Alkali atoms are readily trapped by this method, since they have large permanent magnetic dipole moments.

As can be seen by the equation for the magnetic gradient force on the atom, only certain atomic states, those for which $\boldsymbol{\mu}$ is anti-parallel to $\mathbf{B}$, can be trapped. If $\boldsymbol{\mu}$ is anti-parallel to $\mathbf{B}$, then the overall force is positive and the point of lowest energy occurs when $|\mathbf{B}| = 0$. Atomic states for which this is true are known as weak-field-seeking states. If $\boldsymbol{\mu}$ and $\mathbf{B}$ are aligned, then the overall force is positive, and the atom is repelled from the region where $|\mathbf{B}| = 0$. These are known as strong-field-seeking states. It is possible for weak-field-seeking atoms to become strong-field-seeking through a spin-flip interaction. When this occurs randomly through two-body collisions it serves to remove atoms from the trap.

Evaporative cooling is nothing more than the selective removal of hot atoms from a sample, allowing the remaining atoms to rethermalize at a lower temperature than before. The oft-cited everyday example of evaporative cooling is that of a cup of coffee left on a table to cool. Through collisions, some water molecules gain enough

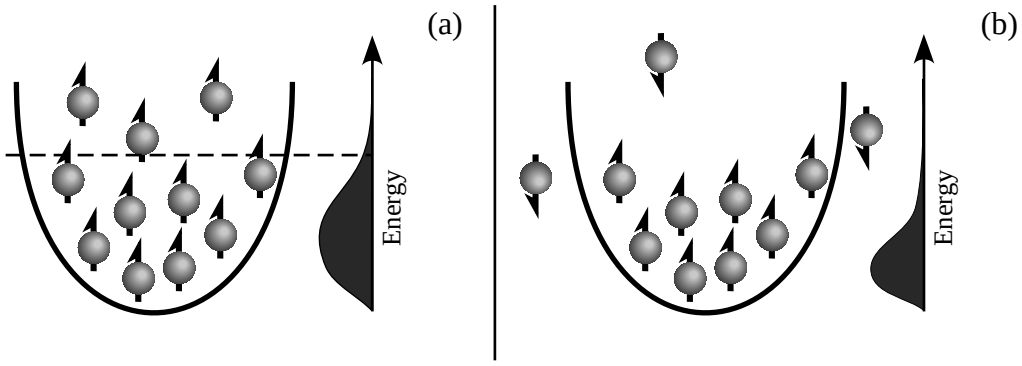

Figure 1.4: Atoms in a trap. The most energetic ones from (a) are selectively removed in (b), leaving the energy distribution of the sample (shown to the side of the trap) with a lower temperature.

energy to leave the coffee as water vapor, carrying away energy and leaving the rest of the liquid coffee cooler.

The two keys to evaporative cooling are energy selectivity and rethermalization. Without energy selection, any atom may be pulled from the sample, resulting only in a net decrease in the number of atoms trapped and not a decrease in temperature. Without rethermalization, which occurs through elastic collisions, the gas's overall temperature cannot decrease after the hot atoms are removed, leaving phase space density unchanged. "Evaporation" would be nothing more than velocity selection.

Selectively removing the most energetic atoms from a magnetic trap can be done through radio frequency (rf) transitions. An rf field is applied to the magnetic trap, its amplitude and frequency chosen so as to flip the spin of atoms which have relatively high energy yet are still bound. This is possible because the energy levels of the atoms are shifted by the Zeeman effect of the magnetic field. Atoms at different heights in the magnetic potential therefore have different transition frequencies. By using an rf field of the appropriate frequency, only atoms highest in the potential will experience a spin flip and escape from the trap. This rf knife thus scrapes away the high-energy atoms. The frequency of the knife can be altered over

time so as to remove progressively lower-energy atoms, making the sample colder and colder, driving it towards the degenerate regime.

This technique, which worked so well in the BEC experiments, is more problematic when applied to fermions. Evaporative cooling can be successful only if collisions occur. As mentioned earlier, at low temperatures, *s*-wave collisions dominate the interactions between two atoms. But the Pauli exclusion principle forbids *s*-wave collisions between fermions in the same state. To cool fermions evaporatively, one must trap a two-state mixture.

Magnetic traps pose two further requirements: the magnetic dipoles of the two states must have the same sign, and the two states must not suffer from excessive spin-flip collisions. There are states of ^{40}K which satisfy both conditions, and a degenerate gas of fermions has been produced by dual-knife evaporation of a two-state mixture of ^{40}K [30]. However, all of the two-state ^{6}Li mixtures which can be magnetically trapped have very large spin-exchange collision rates.

One way around this difficulty is to use sympathetic cooling. In sympathetic cooling, two isotopes of the same atom, a bosonic and a fermionic one, are trapped. Low-temperature collisions between bosons and fermions are allowed, providing the rethermalization necessary for evaporative cooling. By cooling the bosonic isotope using standard rf techniques, the fermionic isotope can be simultaneously cooled. Two groups have used a mixture of ^{6}Li and ^{7}Li in a magnetic trap for this purpose [31,32] and in doing so produced both a ^{7}Li BEC and a degenerate gas of ^{6}Li. One group has used ^{23}Na to cool ^{6}Li to degeneracy [33]. There are notable experimental drawbacks to this approach, the largest of which is the equipment required to trap two isotopes rather than one.

Moreover, if the goal is to explore superfluidity, a magnetic trap cannot be the

final tool used. The two states of ^{6}Li and ^{40}K that are predicted to exhibit Cooper pairing at experimentally accessible temperatures are strong-field seeking [14, 34]. To explore superfluidity, a different trap must be employed.

1.3.3 Optical Traps Push for Superfluidity

An optical trap confines atoms via the optical dipole force. In an electric field $\mathbf{E}$, a neutral atom becomes polarized as its electrons are pulled in one direction and its protons in the other, according to its polarizability α_P. The atom's induced dipole moment is then $\mathbf{d} = \alpha_P \mathbf{E}$, and the interaction potential between this dipole and the electric field is

$$U = -\frac{1}{2}\overline{\mathbf{d} \cdot \mathbf{E}} = -\frac{1}{4}\alpha_P |\boldsymbol{\mathcal{E}}|^2, \tag{1.5}$$

where the bar over the dot product indicates that it is averaged over several optical cycles and $\boldsymbol{\mathcal{E}}$ is the slowly-varying amplitude of $\mathbf{E}$. If an atom has a polarizability greater than zero, then in an electric field gradient the atom will be attracted to regions of high intensity. One method of using this to trap atoms is to take a Gaussian laser beam and focus it tightly. $|\boldsymbol{\mathcal{E}}|$ is greatest at this focus, causing atoms with a positive polarizability to be attracted to that point.

The polarizability of an atom in the ground state is positive if the laser is detuned to the red of resonance. Further, the trapping potential is independent of spin state if the laser light is linearly polarized and the detuning is much greater than the hyperfine splitting of the states in question. A sufficiently detuned laser is capable of trapping any and all spin states of an atom—or, indeed, almost anything, including micron-sized particles [35]! In this manner the two lowest energy states of a fermion can be trapped, thus avoiding exothermic collisions in which one atom falls into a lower energy state. Even more promising, the states of ^{6}Li and ^{40}K which

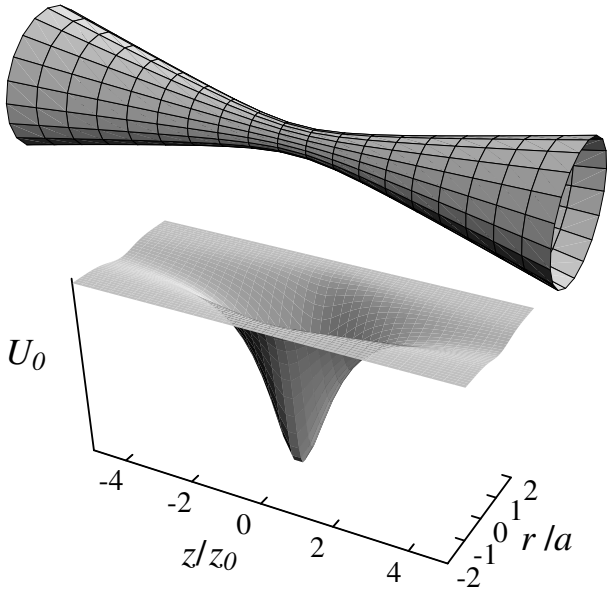

Figure 1.5: An optical trap formed by tightly focusing a Gaussian beam. The potential energy in the x-z plane is shown below the beam.

are best suited for superfluidity experiments can be confined in an optical trap.

Forced evaporation is possible in an optical trap by reducing the strength of the laser beam that forms the trap. Doing so lowers the depth of the trapping potential, allowing the most energetic atoms to leave. As the laser power continues to decrease, the atomic gas cools further. This technique is equally applicable to bosons [22] and fermions [25].

1.4 Significance of Current Work

1.4.1 Stable Optical Trap Using a Commercially-Available Laser

When our group first began work on an optical trap for neutral atoms, the longest 1/e lifetimes observed for an optical dipole force trap were just under 10 s [19, 36]. The authors of one 1997 review article [37] stated:

> In the limit of far detuning, one expects the light to create an almost *conservative potential*, such that in practice the lifetime of the trap is only limited by the background pressure.... As expected the lifetime [of one representative far-off-resonance optical trap] varies linearly with the pressure, except at very low pressures ($\simeq 10^{-11}$ Torr) where it tends to saturate at a few seconds due to other possible heating mechanisms (e.g. beam vibration).

"Other possible heating mechanisms" were indeed the major factor limiting optical trap lifetimes, specifically the noise caused by beam intensity fluctuations and vibration [38, 39]. To limit these sources of noise as much as possible, as part of Ken O'Hara's dissertation work our group built a custom ultrastable CO_2 laser and in doing so achieved trap lifetimes of 300 s [24].

This laser had a number of troubling drawbacks, however. The most crucial was its dependence on rare or hand-made parts. The laser tube was made of specially-blown Pyrex. The diffraction grating which served as an output coupler was custom-built by Hyperfine Inc. The power supplies employed vacuum tubes, and were on loan from Lincoln Laboratory. All of these components would be difficult to replace were something to happen to them.

Less crucial but more annoying on a day-to-day basis was how the CO_2 laser power drifted. No stabilization system was used in order to limit potential sources of noise, so it was not uncommon to begin taking data only to find that the laser had drifted and its power fallen significantly—though ultrastable on short time scales, the laser would drift over minutes.

Finally, at the beginning of my dissertation work, we were unable to cool atoms down into the quantum degenerate regime using our home-built laser. One solution was to trap more atoms, as more atoms allow lower temperatures to be reached through evaporative cooling. The number of atoms trapped depends on the laser's intensity, so an increase in laser power was necessary.

We had not used a commercial CO_2 laser because we had been unable to find one with noise characteristics which suited our needs. But in the course of my dissertation work, we discovered an RF-excited CO_2 laser from Coherent/DEOS, the LC100-NV, which not only had noise characteristics which were potentially sufficient for our needs but also produced 140 W of power, more than double that produced by our custom-built CO_2 laser. In addition, RF-excited CO_2 lasers exhibit far less power drift than does our custom-built CO_2 laser. Using this commercial laser, Mike Gehm and I were able to create an optical trap with a lifetime of 400 s [25], and with it cool ^{6}Li to the quantum degenerate regime.

Our use of this laser has a number of benefits. For one, it lowers the barrier for other experimental groups to create a similar trap. Rather than having to build a special CO_2 laser, experimenters can buy a laser which is readily available from Coherent/DEOS. For another, the LC100-NV is easier to operate than our custom-built CO_2 laser. It employs a sealed-tube design rather than the flowing gas design we used in our laser, and turning it on is a matter of flipping three switches rather

than opening gas cylinders, adjusting gas flow, and then jump-starting the laser using a Tesla coil. And, as previously mentioned, the LC100-NV is RF-excited and thus its power is more stable over long periods of time than was our custom-built laser.

1.4.2 The All-Optical Route to Fermi Degeneracy

As explained above, there are benefits to using an optical trap for trapping and cooling neutral fermions. The states of ^{6}Li and ^{40}K for which Cooper pairing is predicted to occur cannot be trapped magnetically. To explore superfluidity and the BCS transition one needs an optical trap. In that case, why not solely utilize an optical trap? Doing so obviates the need to transfer cooled atoms from a magnetic trap into an optical one and then select the appropriate atomic states, which would lengthen the time required to perform experiments and increase the complexity of the experimental setup.

Mike Gehm and I have shown that it is possible to evaporatively cool a gas of fermions to degeneracy directly in an optical trap. (Figure 1.6 shows the range of temperatures involved in cooling ^{6}Li in our experiments.) This was done using the two lowest ground states of ^{6}Li, states which are also predicted to form Cooper pairs at experimentally-achievable temperatures. Prior to the experiments described in this dissertation, all cooling of fermions to degeneracy was done in magnetic traps, either by trapping two hyperfine states and performing direct evaporative cooling [30] or by sympathetically cooling fermions using a bosonic isotope of the same atom [31, 32, 33].

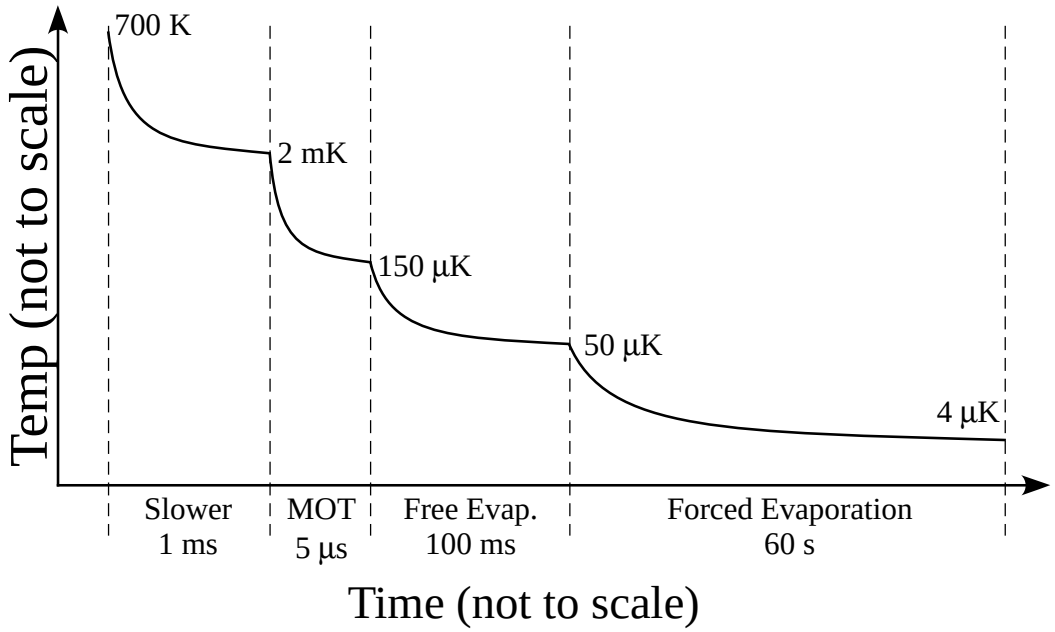

Figure 1.6: A plot of our gas's temperature as a function of time (not to scale). The plot shows the steps taken in our cooling process, how long each step takes, and the resulting temperature.

1.4.3 Low-Temperature Physics

The creation of a dilute, degenerate gas of fermions allows the exploration of a number of interesting physical phenomena. As such a gas is cooled, Fermi statistics become more and more pronounced. For instance, the size of the atomic cloud initially shrinks as it is cooled, but eventually the Pauli exclusion principle prevents that from happening. Collective oscillations, in which a two-component Fermi gas is allowed to oscillate in a harmonic trap, is an interesting field of study. The behavior of a Fermi gas when excited in this manner depends on the relative strength of interactions between the two components. Thus these oscillations provide a method of exploring the quantum statistics of a degenerate gas. While collective oscillations of BECs have been explored by many groups [40, 41, 42], to date only two experiments involving collective oscillations of fermions have occurred [43, 44].

Furthermore, if cooled sufficiently, a gas of ^{6}Li in the appropriate two states should exhibit Cooper pairing according to BCS theory and then form a superfluid of those pairs, in a manner analogous to how electrons become superconducting.

The mixture of the two hyperfine states of ^{6}Li that we trap and cool is predicted to exhibit a Feshbach resonance when a magnetic field of $\sim 850\,\mathrm{G}$ is applied. A Feshbach resonance occurs when the energy of a bound molecular state is degenerate with that of a two-body continuum state. While producing this magnetic field is beyond the capability of the experimental setup described in this dissertation, new magnets now installed in the system should allow study of this Feshbach resonance.

One of the most important features of a Feshbach resonance is that the *s*-wave interactions can be altered from strongly attractive to strongly repulsive by varying the magnetic field. By taking advantage of this fact, it should be possible to explore resonance superfluidity, in which a fermionic superfluid is created via strong interactions instead of the weak ones that occur in traditional BCS theory. Resonance superfluids should occur at relatively high temperatures compared to the Fermi temperature of the gas; they also may provide the opportunity to explore the regime between the weak pairing of a BCS superfluid and the tightly-bound bosons of BEC, as they lie somewhere between the two in terms of interaction strength.

1.5 Dissertation Organization

The organization of this dissertation is as follows. Chapter 2 discusses the various types of interactions between ultracold ^{6}Li that are of interest in my experiments. The origin of the scattering length as it applies to *s*-wave scattering is covered in more depth, including its magnetic field dependence and the existence of a Feshbach resonance in our chosen mixture of spin states. In addition, the chapter touches

briefly on how superfluidity comes about through the creation of Cooper pairs and how a resonant superfluid, which involves strong interactions and thus involves a different mechanism than Cooper pairing, may be possible.

Chapter 3 then turns from the theory of interactions to the practicalities of trapping ^{6}Li. The physics of optical trapping is covered, along with discussion of the types of noise which plagued previous optical traps by causing excessive atom loss. The hardware required to realize a stable optical trap is complex, but not forbiddingly so.

This in turn leads to how to characterize both the optical trap and the trapped atoms, since it is natural to wonder both what such a trap is like and how many atoms are trapped in it; this is discussed in Chapter 4. The most direct way of measuring those atoms is by imaging the trapped cloud onto a CCD camera. Using such a camera requires timing accurate to within tens of microseconds over hundreds of seconds, and necessitated development of a precision timing system. After a discussion of the camera and timing system and their integration into the experiment, I then discuss measuring the parameters of the trap and how it is possible to measure the temperature of the atomic gas without sticking a thermometer through the vacuum system and into the gas.

Given these methods of characterization, we are prepared to cool atoms to the quantum degenerate regime. Chapter 5 touches on a Boltzmann-equation theory of evaporative cooling and how such a theory gives rise to scaling laws relating the collision rate, phase-space density, and number of atoms to the trap depth during evaporation. Evaporative cooling was not as experimentally easy as hoped due to a misalignment of the CO_2 laser beam as we lowered its power. Despite this difficulty I was able to reach temperatures of $T/T_F < 0.5$; since then we have developed a

scheme which should allow us to correct the misalignment.

In Chapter 6, the density of a two-state fermionic gas as a function of scattering length is derived. Since the density will vary as the scattering length changes, it will provide a measure of the fermions' interactions, further characterizing our degenerate gas. Finally, Chapter 7 summarizes my major results and points towards future experiments which should be possible given slight changes in the experimental setup.

Chapter 2

^{6}Li Interactions

How cold atoms scatter elastically off of one other is at the heart of our experiments. Without scattering, there would be no rethermalization and thus no evaporative cooling. The formation of a Fermi superfluid through Cooper pairing is mediated by scattering interactions. Given the importance of elastic scattering, it is worth reviewing some of the relevant physics.

This chapter will provide a brief overview of elastic scattering, specialized to the case of two ultracold ^{6}Li atoms. Such scattering can be described by one parameter, the s-wave scattering length a_s. ^{6}Li can have an unusually large and negative scattering length due to near-zero-energy and Feshbach resonances in the ^{6}Li-^{6}Li triplet molecular potential, leading to very strong interactions. The hyperfine structure of ^{6}Li complicates matters, as it couples the triplet and singlet molecular potentials. The result is a scattering length which varies with magnetic field.

The s-wave scattering length varies little, though, except near a scattering resonance. What causes these resonances, and how the scattering length behaves near them, will be discussed. Following that, this chapter will explore fermionic superfluidity by formation of Cooper pairs, the same mechanism which produces superconductivity of electrons in a metal. The traditional BCS theory of Cooper pairing becomes invalid when the scattering length is large and the interactions

between atoms strong; the theory of resonance superfluidity, which describes how fermionic superfluids form in the limit of strong interactions due to a resonance, will be discussed. According to resonance superfluidity theories, ^{6}Li should form a system analogous to superconductivity, but with the highest transition temperature with respect to its Fermi temperature T_c/T_F ever produced. Finally, the choice of which magnetic hyperfine states of ^{6}Li to use in our experiments will be explained.

2.1 Elastic Scattering at Cold Temperatures

The scattering of two particles of mass m that interact through a central potential[1] $V(r)$ can be viewed as the scattering of one particle of reduced mass $\mu = m/2$ by the potential $V(r)$ in the center of mass coordinate system. The interaction between two neutral alkali atoms is dominated by an electrostatic molecular potential that is central in nature, allowing us to treat neutral alkali scattering in this manner. Furthermore, at cold temperatures the interaction between atoms is dominated by s-wave interactions, which, according to the Wigner-Eckhart theorem, interact through a scalar potential: because the interaction depends only on the relative distance $\mathbf{r}$ between the two atoms, the interaction must be scalar.

There is a fundamental connection between how scattering events are measured in the lab and the quantum mechanical description of those events. Scattering experiments involve measuring the differential cross section $d\sigma/d\Omega$, while quantum mechanics describes particles in terms of wave functions ψ. The bridge between the two is the scattering amplitude $f(\Omega)$. The scattering amplitude is directly related

[1] A central potential is one with no angular dependence, *i.e.* it is only a function of the relative distance r between the two atoms.

to the differential cross section by the formula

$$\frac{d\sigma}{d\Omega} = |f(\Omega)|^2. \tag{2.1}$$

It also related to the stationary scattering wave function, in which a free particle is scattered by a central potential. The wave function for a free particle is a plane wave, given by $\exp(i\mathbf{k}\cdot\mathbf{r})$. In the asymptotic limit, the wave function of a scattered particle contains both the original plane wave term and a spherical wave term due to scattering:

$$\psi(k,\mathbf{r}) \underset{\mathbf{r}\to\infty}{=} A\left(e^{i\mathbf{k}\cdot\mathbf{r}} + f(\Omega)\frac{e^{ikr}}{r}\right). \tag{2.2}$$

The scattering amplitude connects the measurable differential cross section with the quantum mechanical wave function.

When dealing with elastic scattering between very cold atoms, one of the most useful tools is partial wave analysis. As the name implies, partial wave analysis involves treating the scattered wave function as being composed of individual waves which, when superposed, form the final wave function. Since a central potential conserves angular momentum, partial waves of quantized angular momentum are commonly used in partial wave analysis. The eigenfunctions of angular momentum are the spherical harmonics $Y_{lm}(\theta,\phi)$, where l and m are the orbital angular momentum and magnetic quantum numbers, respectively. Expanding a wave function in terms of these eigenfunctions gives

$$\psi(k,\mathbf{r}) = \sum_{l=0}^{\infty}\sum_{m=-l}^{+l} c_{lm}(k)R_{lm}(k,r)Y_{lm}(\theta,\phi), \tag{2.3}$$

where R_{lm} are the radial portions of the partial wave functions and c_{lm} are the

expansion coefficients. Each partial wave is an eigenstate $|l, m\rangle$.

The wave function of a free particle can be taken to be a plane wave propagating in the **z** direction. Such a wave is independent of the azimuthal angle ϕ. In that case $m = 0$. Since $Y_{l,0}(\theta) \propto P_l(\cos\theta)$, where $P_l(\cos\theta)$ are the Legendre polynomials, the partial wave expansion for a free particle can be shown to be

$$\psi(k, \mathbf{r})_{free} = e^{i\mathbf{k}\cdot\mathbf{r}} = \sum_{l=0}^{\infty}(2l+1)i^l j_l(kr)P_l(\cos\theta), \tag{2.4}$$

where j_l are the spherical Bessel functions and $P_l(\cos\theta)$ are the Legendre polynomials.

A central potential necessarily has spherical symmetry, and thus the scattering amplitude can only depend on θ and $m = 0$ in the partial wave expansion. Given this, the scattering amplitude can be shown to be [45]

$$f(k, \theta) = \sum_{l=0}^{\infty}(2l+1)\frac{e^{2i\delta_l(k)} - 1}{2ik}P_l(\cos\theta), \tag{2.5}$$

where δ_l are the phase shifts—a measure of how much the interaction has affected the outgoing wave function. Were the phase shifts all equal to zero, $f(k, \theta)$ would be zero and the scattered wave function would then be the same as the incoming one.

The benefit of this formalism is that it greatly simplifies the theory of scattering between two cold atoms. Each term in the expansion given in Eq. (2.5) is an angular momentum eigenstate $|l\rangle$. At low temperatures only a few angular momentum partial waves are energetically allowed. At *very* low temperatures, *s*-wave ($l = 0$) collisions dominate, making the description of scattering simple enough that it can be described by one parameter, the scattering length.

2.2 S-Wave Scattering Length

For s-wave scattering, $l = 0$ and a number of the above equations can be simplified. For example, Eq. (2.5) simplifies to

$$\begin{aligned} f(k) &= \frac{e^{2i\delta_0(k)} - 1}{2ik} \\ &= e^{i\delta_0(k)} \frac{\sin(\delta_0(k))}{k} \end{aligned} \tag{2.6}$$

and the differential cross section (2.1) becomes

$$\frac{d\sigma}{d\Omega} = \left| \frac{\sin \delta_0}{k} \right|^2 . \tag{2.7}$$

The total cross section, found by integrating the differential cross section over all solid angles, is

$$\sigma = \int d\Omega \frac{d\sigma}{d\Omega} = \left| \frac{\sin \delta_0}{k} \right|^2 \int d\Omega = 4\pi \frac{\sin^2 \delta_0}{k^2}. \tag{2.8}$$

Note that, according to this equation, the maximum cross section for a collision with relative momentum $\hbar k$ is $4\pi/k^2$. This is known as the unitarity limit to the cross section, and arises from the optical theorem.

It turns out that, at these low energies, $\tan \delta_0(k) \propto k$ for many potentials [45]. The scattering length a [46] is defined as

$$a \equiv - \lim_{k \to 0} \frac{\tan \delta_0(k)}{k}. \tag{2.9}$$

Once this definition is made, the scattering amplitude at low energies becomes

$$\lim_{k\to 0} f(k) = \lim_{k\to 0} \frac{\sin\delta_0(k)}{k} = \lim_{k\to 0} \frac{\tan\delta_0(k)}{k} = -a. \tag{2.10}$$

The cross section in this limit can be found by using (2.9) and some trigonometric identities:

$$\begin{aligned}
\sin^2\delta_0(k) &= 1 - \cos^2\delta_0(k) \\
&= 1 - \frac{1}{\sec^2\delta_0(k)} \\
&= 1 - \frac{1}{1+\tan^2\delta_0(k)} \\
&= \frac{\tan^2\delta_0(k)}{1+\tan^2\delta_0(k)} \\
&= \frac{k^2a^2}{1+k^2a^2}.
\end{aligned} \tag{2.11}$$

Substituting this into (2.8) gives the total cross section as

$$\begin{aligned}
\sigma &= \frac{4\pi a^2}{1+k^2a^2} \\
&\underset{\mathbf{k}\to 0}{=} 4\pi a^2.
\end{aligned} \tag{2.12}$$

The scattering length thus parameterizes collisions at low energy.

There is one more salient fact about the scattering length which bears noting: in general, its sign indicates whether the associated effective potential is attractive or repulsive. Neutral atoms colliding at low temperatures experience an effective delta-function contact potential [26] of

$$V_{eff}(\mathbf{r}) = \frac{4\pi\hbar^2 a}{M}\delta(\mathbf{r}). \tag{2.13}$$

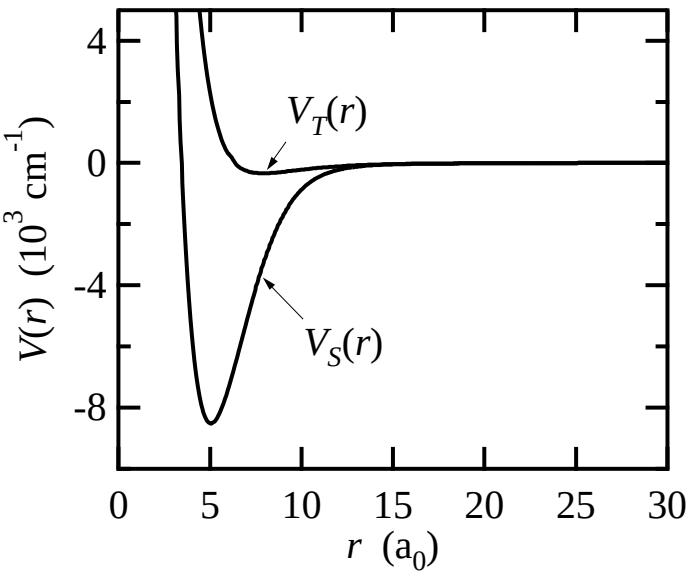

Figure 2.1: The triplet and singlet molecular potentials for two ^{6}Li atoms undergoing an s-wave collision.

From this we see that $a > 0$ for a repulsive potential, while for an attractive potential $a < 0$.

There are two ^{6}Li scattering lengths, one for each of the possible s-wave collision potentials. Two ^{6}Li atoms undergoing an s-wave collision can approach each other along a singlet potential $V_s(r)$ if their valence electron spins combine to form a singlet spin state; otherwise, the two atoms will experience a triplet potential $V_T(r)$. Figure 2.1 shows the two molecular potentials.[2]

The scattering lengths can be found by numerically determining the phase shift δ_0 of the asymptotic wave function in the potentials' presence, as is done in [26], and then applying that phase shift to (2.9). The ^{6}Li scattering length for the singlet potential is $a_s = 38.75a_0$, where a_0 is the Bohr radius. For the triplet potential, the

[2]The potentials were constructed from several different sources [47, 48, 49, 50, 51, 52, 53, 54] by Ken O'Hara [26].

scattering length is $a_t = -2240a_0$.

2.3 Magnetic Tuning of the Scattering Length

Elastic collisions are governed by the interaction between the two colliding atoms. These interactions can be altered by application of a magnetic field, which modifies the energy levels of each atom via the Zeeman effect. Doing so alters the collisional properties of the atoms and thus the scattering length. In effect magnetic fields provide a way of tuning the value of the scattering length.

For an ultracold alkali atom in the ground state, the internal Hamiltonian of an atom in a magnetic field $\mathbf{B}$ is a combination of the hyperfine interaction and the Zeeman interaction:

$$\mathcal{H}_{int} = \frac{a_{hf}}{\hbar^2}\mathbf{s}_e \cdot \mathbf{i}_n + \left(\frac{2\mu_e}{\hbar}\mathbf{s}_e - \frac{\mu_n}{\hbar}\mathbf{i}_n\right) \cdot \mathbf{B}, \tag{2.14}$$

where a_{hf} is the hyperfine constant for the atom, μ_e and μ_n are respectively the electron and nuclear magnetic moments, $\mathbf{s}_e$ is the electron spin and $\mathbf{i}_n$ the nuclear spin. As $\mathbf{B}$ is varied, the last term in the Hamiltonian will change, leading to changes in the scattering length. Section 2.6 lists the eigenstates of (2.14) for ^{6}Li.

Physically this change arises due to the hyperfine interaction varying the admixture of molecular singlet and triplet potentials two ^{6}Li atoms experience during an *s*-wave collision. The particular combination of the potentials will determine the scattering length, and this combination will vary as the magnetic field varies.

Calculating the changes in the scattering length is computationally non-trivial. The rigorous approach is to use a coupled-channel formalism [55]. Roughly speaking, a channel is one possible pair of states for the two colliding atoms, either before

or after the collision. Channel eigenstates are often written as $|\{\alpha,\beta\}_{\pm}\rangle$[3], where this state asymptotically becomes the states $|\alpha\rangle$ and $|\beta\rangle$ (the eigenstates of (2.14)) for the two atoms when separated by very large distances. The scattering wave function Ψ for fermions can then be expanded in this channel-state basis as

$$\Psi = \sum_{\{\alpha,\beta\}} \psi_{\{\alpha,\beta\}}(\mathbf{r})\,|\{\alpha,\beta\}_{-}\rangle\,. \tag{2.15}$$

Substituting this state into the Schrödinger equation leads to a set of coupled differential equations. Physically the coupled equations correspond to only a given subset of post-collision channels (called exit channels) being accessible from a given pre-collision (or entrance) channel. A channel is accessible, or open, if the relative kinetic energy between the two atoms in that channel is positive at a given total energy; otherwise, the channel is closed. A coupled-channel calculation gives the coupling between entrance and exit channels and the strength of those couplings, and as an added bonus gives the magnetic-field-dependent form of the scattering length. In some cases a full-blown coupled-channel calculation is not necessary, as approximations such as the Asymptotic Boundary Condition approximation [56,26] can be used.

Knowing how the scattering length varies with magnetic field is important. Many experiments with degenerate fermionic gases are predicated on the ability to control interactions by magnetically tuning the scattering length. For the purpose of the experiments described in this dissertation, the scattering length tuning given in Ref. [56] is sufficient.

[3]The $\pm$ indicates the symmetry of the two colliding atoms. Symmetric combinations are indicated by $+$; antisymmetric, by $-$. For fermions, the wave functions must be antisymmetric.

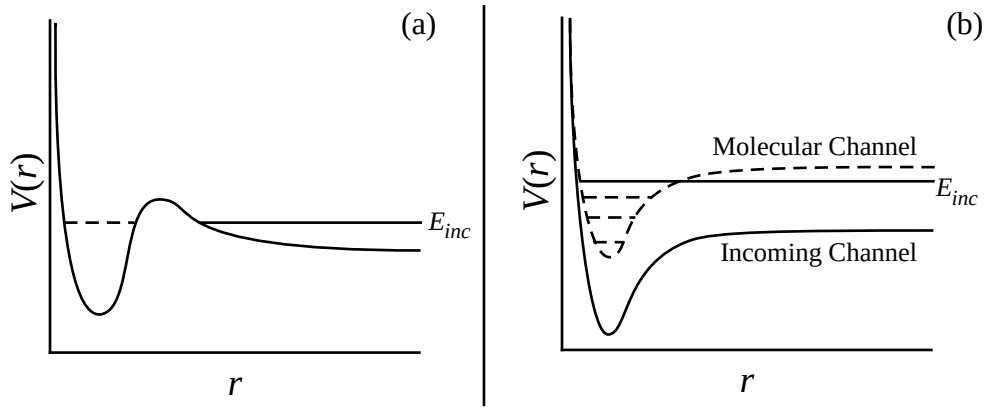

Figure 2.2: An example of (a) a shape resonance and (b) a Feshbach resonance. In the shape resonance the quasibound state (whose energy is represented by a dashed straight line) is due to the potential barrier, and is of the same internal state as that of the incoming particle. In the Feshbach resonance the bound state is that of a molecule (dashed curve), making it a different internal state than the incoming channel (solid curve). The incident particle energy E_{inc} in (b) is the same as that of one of the molecular bound states.

2.4 Feshbach Resonances

Changes to the scattering length through magnetic fields are limited, for the most part. The *s*-wave scattering length depends only weakly on magnetic field strength—except near a resonance.

There are two types of collision resonances: shape (or potential) resonances and Feshbach resonances. Both resonances occur when an incoming open channel has the same energy as a bound or quasibound state. In shape resonances the closed quasibound state is formed by a potential barrier and involves the same internal state of the system as the incoming channel. In Feshbach resonances the closed bound state is a molecular one, and therefore involves a different internal state than that of the incoming channel.

Physically, Feshbach resonances occur at specific values of the magnetic field B because the free state of the incoming channel and the molecular state of the

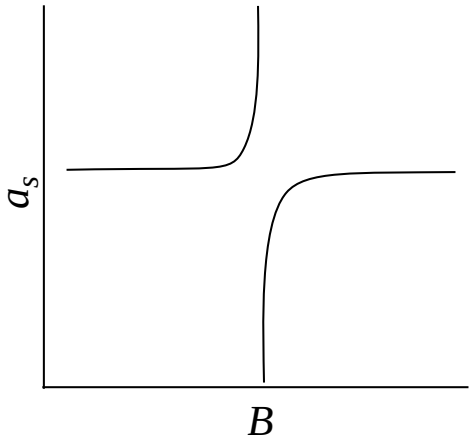

Figure 2.3: The dispersive behavior of the s-wave scattering length a_s near a Feshbach resonance.

closed channel have different magnetic moments, causing their energies to shift at different rates as B is changed. Near a Feshbach resonance, the s-wave scattering length varies dispersively [57]:

$$a = a_i \left(1 - \frac{\Delta}{B - B_0}\right), \tag{2.16}$$

where a_i is the scattering length away from the resonance, B_0 is the value of the magnetic field at which the resonance occurs, and Δ is the width of the resonance. In theory, the scattering length near a resonance varies over the range $\pm\infty$. In practice this full range cannot be achieved, as the cross section is unitarity limited to $4\pi/k^2$.

While our experiments do not yet employ a Feshbach resonance, the existence of such a resonance was an important consideration when Mike Gehm and I chose our two-state mixture of ^{6}Li. As will be explained in Section 2.6, we chose a mixture which exhibits a Feshbach resonance at $\sim 850\,\mathrm{G}$. Similarly, one of the most exciting future experiments involving our degenerate gas of ^{6}Li is the observation of Fermi

superfluidity, which may require use of a Feshbach resonance. Though superfluidity is not directly a part of my dissertation work, it informed many of our experimental choices and is thus worth exploring briefly.

2.5 Fermi Superfluidity

The ability to tune atomic interactions using magnetic fields, coupled with the large range of scattering lengths available through Feshbach resonances, make many experiments possible. One such possible experiment is the creation of a fermionic superfluid. Two possible mechanisms for fermionic superfluidity exist. One is the formation of Cooper pairs mediated by a weak interaction, as described by the theory of Bardeen, Cooper, and Schrieffer. The other is creation of a resonance superfluid through strong interactions between fermions. To date no experimental group has achieved superfluidity in a dilute neutral gas of fermions.

2.5.1 Cooper Pairing

Bosons and fermions behave very differently in the quantum degenerate regime. Bosons undergo a phase transition, becoming a superfluid. Fermions have no such phase transition. However, any given bosonic atom is comprised of electrons, protons, and neutrons—all of which have a spin of $1/2$ and are thus fermions. Given that bosons are fundamentally comprised of fermions, it is not unreasonable to imagine combining two degenerate fermions through strong interactions to create a composite boson which would then Bose-condense.

Many attempts were made to explain superconductivity using this theory [58], since superconductivity consists of electrons, which are fermions, behaving as if

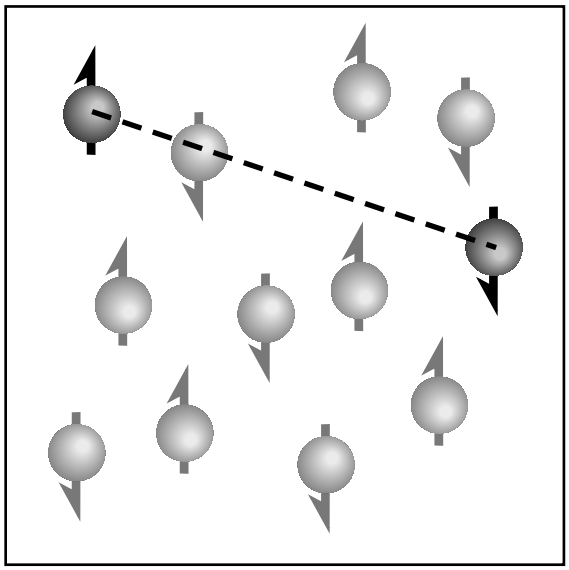

Figure 2.4: Formation of a Cooper pair between two atoms of opposite spin and momentum. The distance between the two atoms in the pair is greater than the interatomic spacing. The arrows on the atoms indicate direction of their spin.

they are part of a superfluid. Bardeen, Cooper, and Schrieffer were able to show that superconductivity instead resulted from a different mechanism. The fermions do not become tightly-bound composite bosons which then form a BEC, in which bosons are strongly coupled. Instead, two fermions which are widely separated in space form pairs via a weak attractive interaction; those pairs then condense into a single quantum state. These pairs are created near the Fermi surface. In the case of electrons, the necessary attractive interaction takes the form of electron-phonon interactions, causing two states of opposite momentum and spin to form pairs [59].

It seems counterintuitive that Cooper pairs would form at all, given how weak the attractive forces involved are.[4] Were one to isolate two particles from the rest of the sample, the probability of them binding via the given attractive forces is nearly

[4]In dilute alkali gases it is possible to utilize a Feshbach resonance and thus increase the interaction strength until the attractive forces are no longer weak. In this case the gas begins to take on the characteristics of a BEC, and BCS theory no longer applies. This will be discussed in Section 2.5.2.

zero. It is other fermions in the system that make Cooper pairing not only possible but probable [60]. The interaction of two particles near the Fermi surface is radically altered by the presence of the other fermions through the Pauli exclusion principle. The net result is that bound states can exist no matter how weak the attractive interaction. In addition, the presence of the other fermions causes the Cooper pairs to form near the Fermi surface: below the surface, there are few unoccupied states for two fermions to scatter into in the process of forming a Cooper pair.

Though similar to diatomic molecules, Cooper pairs have striking differences. Any two fermions can form a Cooper pair, as long as they have approximately the same Fermi momentum [60]. The particles do not have to be identical, or even need to have the same mass. The distance between atoms in a Cooper pair is much larger than the mean distance between two adjacent particles.

Since a Cooper pair is made of two fermions, its wave function must be anti-symmetric under the exchange of particles, so that $\psi_{1,2} = -\psi_{2,1}$. This must be satisfied by the appropriate choice of the particles' relative angular momentum and spin states. For a one-state gas of fermions, s-wave interactions are not allowed and Cooper pairs must form via p-wave interactions. If two spin states of a fermionic gas are trapped, then s-wave interactions will dominate the pairing (since d-wave interactions are rare at such cold temperatures).

The critical temperature T_c at which the superfluid phase transition occurs differs depending on the number of fermionic states involved. For a single-component spin-polarized gas, which contains only one fermionic state, the critical temperature in terms of the Fermi temperature is [15]

$$\frac{T_c}{T_F} \simeq \exp\left\{-\frac{\pi}{2(k_F|a_p|)^3}\right\}, \tag{2.17}$$

where T_F is the Fermi temperature, k_F is the Fermi wavenumber, and a_p is the p-wave analogue of the s-wave scattering length. Unfortunately, this value of T_c for ^{6}Li is ridiculously low, as for ^{6}Li at densities of $n = 10^{12}\,\mathrm{cm}^{-3}$, $T_F \simeq 600\,\mathrm{nK}$ and $k_F|a_p| \simeq 7\times10^{-3}$. The resulting critical temperature of $T_c \simeq 10^{-1988887}T_F$ is unachievable by experimental techniques.

The critical temperature can be increased by trapping two states. If the two states have a positive s-wave scattering length a_s, their interaction is repulsive; however, Cooper pairs can still form. Two atoms in the same hyperfine state can interact via phonons in the density of atoms in the other hyperfine state, causing an attractive triplet p pairing [61]. In this case the critical temperature is

$$\frac{T_c}{T_F} \simeq \exp\left\{-13\left(\frac{\pi}{2k_F|a_s|}\right)^2\right\}. \tag{2.18}$$

This value for the critical temperature is higher than that given by Eq. (2.17), but still experimentally infeasible. For $n = 10^{12}\,\mathrm{cm}^{-3}$ in each spin state, $k_F|a_s| \simeq 0.43$, leading to a critical temperature of $T_c \simeq 10^{-76}T_F$.

Should the s-wave scattering length be negative and the interaction thus attractive, the critical temperature is higher still [60]:

$$\frac{T_c}{T_F} \simeq \exp\left\{-\frac{\pi}{2k_F|a_s|}\right\}. \tag{2.19}$$

The critical temperatures for a two-state Fermi gas with an attractive s-wave interaction is much higher than in the previous two cases, especially given the large and negative s-wave scattering length of ^{6}Li. Critical temperatures that are equal to a few percent of T_F can be achieved. For $n = 10^{12}\,\mathrm{cm}^{-3}$ in each spin state, $k_F|a_s| \simeq 0.43$, giving a critical temperature of $T_c \simeq .025T_F$.

2.5.2 Resonance Superfluidity

A glance at Eq. (2.19) suggests that one way of increasing the critical temperature is to increase a_s. Doing so could potentially bring the critical temperature much closer to the Fermi temperature. One method of increasing a_s is to utilize Feshbach resonances, as discussed in Section 2.4. If a_s becomes large, the system moves out of the regime in which BCS theory, which requires weak coupling, is valid.

BCS superfluids and Bose-Einstein condensates are to a certain extent at opposite ends of a continuous spectrum. BCS superfluids form in systems with weak attractive interactions between composite Fermi pairs, while BECs form from bosons whose composite fermions are tightly bound. Early work by Leggett [60] showed that a fermionic superfluid should move smoothly from a BCS superfluid to a BEC of diatomic molecules as a_s is varied. In further extensions to Leggett's early work, Randeira [62] also found that a BCS superfluid should become a BEC of strongly-bound fermions with no phase transition from one to the other. Randeira concluded his paper by saying,

> [T]he problem of the crossover from BCS theory to Bose-Einstein condensation is a very rich one, and there are possibly new surprises in the intermediate coupling regime that we have yet to uncover.

Degenerate alkali gases are a promising system for studying this transition, as their interactions can be tuned over a wide range. Holland *et al.* [16] have recently developed a theory for fermionic superfluids in the strong-coupling regime where BCS theory no longer holds, a state which they call "resonance superfluidity." They have applied this theory to the two lowest ground states of ^{6}Li and have found that $T_c \simeq 0.5T_F$ near the Feshbach resonance at $\sim 850\,\mathrm{G}$ [63], a temperature which is well

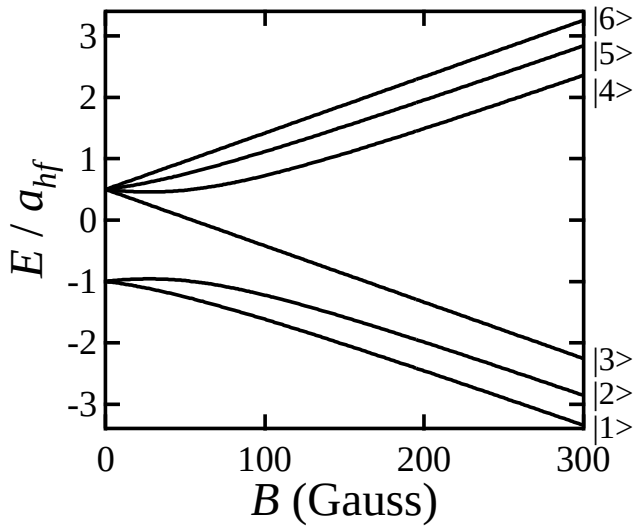

Figure 2.5: The six hyperfine ground states of ^{6}Li and how their energy changes in a magnetic field.

within our experimental reach. If this prediction holds, such a resonant superfluid would have the highest value of T_c/T_F ever seen in a fermionic superfluid.

2.6 States of ^{6}Li Used in the Experiment

^{6}Li has one single valence electron with spin $s_e = 1/2$ and a nuclear spin of $i_n = 1$. The two spins are coupled through the hyperfine interaction (a magnetic dipole interaction), resulting in six internal ground states. In an external magnetic field **B**, both spins couple to the field. The resulting internal Hamiltonian is given in (2.14). In the absence of a magnetic field, the Hamiltonian is diagonal in the $|f, m_f\rangle$ basis, where $\mathbf{f} = \mathbf{s}_e + \mathbf{i}_n$ and m_f is the projection of **f** along the $\hat{\mathbf{z}}$ axis. The two eigenstates are $|f = 3/2, m_f = \pm 3/2, \pm 1/2\rangle$ and $|f = 1/2, m_f = \pm 1/2\rangle$. The energies of these two states are $E_{3/2} = a_{hf}/2$ and $E_{1/2} = -a_{hf}$, respectively, leading to a zero-field ground-state splitting of $E_{hf} = 3a_{hf}/2$, where $E_{hf}/h = 228.2\,\mathrm{MHz}$.

In the presence of a magnetic field the six eigenstates, labeled $|1\rangle - |6\rangle$ in order of increasing energy, are superpositions of the product states $|m_s, m_i\rangle$, where m_s and m_i are the $\hat{\mathbf{z}}$-axis projections of $\mathbf{s}_e$ and $\mathbf{i}_n$, respectively. The eigenstates are [56]

$$\begin{aligned}
|1\rangle &= \sin\theta_+ \,|1/2, 0\rangle - \cos\theta_+ \,|-1/2, 1\rangle \\
|2\rangle &= \sin\theta_- \,|1/2, -1\rangle - \cos\theta_- \,|-1/2, 0\rangle \\
|3\rangle &= |-1/2, -1\rangle \\
|4\rangle &= \cos\theta_- \,|1/2, -1\rangle + \sin\theta_- \,|-1/2, 0\rangle \\
|5\rangle &= \cos\theta_+ \,|1/2, 0\rangle + \sin\theta_+ \,|-1/2, 1\rangle \\
|6\rangle &= |1/2, 1\rangle \,,
\end{aligned} \tag{2.20}$$

where

$$\begin{aligned}
\sin\theta_\pm &= \frac{1}{\sqrt{1 + 1/2(Z^\pm + R^\pm)^2}}, \\
Z^\pm &= \frac{\mu_n + 2\mu_e}{a_{hf}} B \pm \frac{1}{2}, \\
R^\pm &= \sqrt{(Z^\pm)^2 + 2},
\end{aligned} \tag{2.21}$$

and $\cos\theta_\pm$ is related to $\sin\theta_\pm$ through the usual trigonometric identities. Each superposition of $|m_s, m_i\rangle$ states involved in a given eigenstate has the same value for $m_f = m_i + m_s$. Figure 2.5 shows how the energies of these six eigenstates vary with magnetic field.

To prevent exothermic inelastic collisions, we trap and cool a mixture of the $|1\rangle$ and $|2\rangle$ states. Those states are the ones with the least energy, and spin-exchange s-wave collisions resulting in both atoms in the $|1\rangle$ state are forbidden by the exclusion principle. Spin-exchange collisions resulting in atoms being transferred to any of the

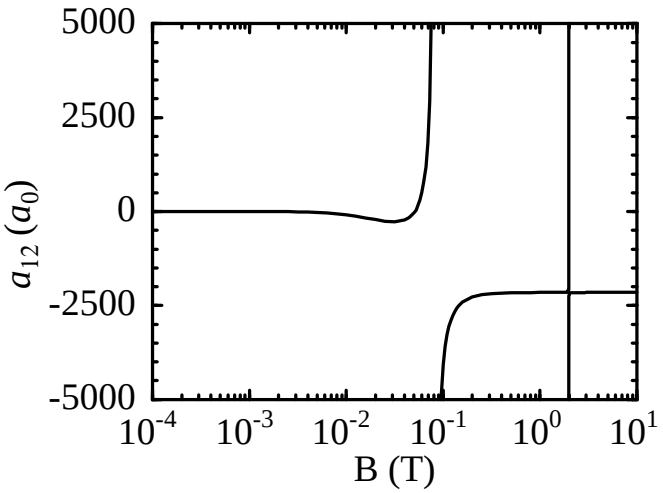

Figure 2.6: How the scattering length a_{12} for the states $|1\rangle$ and $|2\rangle$ varies with magnetic field, from Ref. [56]. The divergences in the scattering length at $\sim 850\,\mathrm{G}$ and at $\sim 20000\,\mathrm{G}$.

other eigenstates require at least 10 mK of energy, more than is available at our low experimental temperatures. Figure 2.6 shows the scattering length a_{12} for these two states as a function of magnetic field, taken from Ref. [56]. At $B = 0$ the scattering length is zero,[5] indicating that we must apply a magnetic field when evaporatively cooling atoms in these two states. This is a useful feature, as interactions, and thus evaporative cooling, can effectively be turned off by removal of the magnetic field. At $B = 0.085\,\mathrm{T}$ and again at $B = 2\,\mathrm{T}$ there are Feshbach resonances, providing the tantalizing possibility of observing resonance superfluidity in a $|1\rangle - |2\rangle$ mixture.

In summary, we have briefly reviewed the theory behind elastic scattering at cold temperatures and shown how such scattering can potentially lead to the formation of both a traditional BCS superfluid and a resonant superfluid. The two states of ^{6}Li best suited for our experiments have also been chosen. Having laid this groundwork, I will now turn to our optical trap, with which we trap a two-state mixture of ^{6}Li

[5]This is, as far as we can determine, due solely to accidental interferences.

and cool it to degeneracy.

Chapter 3

Optical Trapping

One motif in the cooling of fermions to degeneracy is the usefulness of doing so using a two-state mixture rather than a gas in which all of the fermions are in a single hyperfine state, as the latter is non-interacting at low temperatures. While a single-state gas of fermions may be cooled evaporatively through sympathetic cooling, evaporative cooling of a two-state mixture is easier. Sympathetic cooling requires that both bosonic and fermionic isotopes be confined together, which in turn requires a more complex experimental setup. Many experiments involving degenerate fermions, such as studies of the damping of collective oscillations and exploration of superfluidity, require a two-state mixture. One difficulty with trapping two states is that the states may have inelastic collisions, in which one or both atoms undergo a change of internal state and, in doing so, release enough energy to escape the trap. Such collisions in ^{6}Li can be avoided by trapping the two hyperfine states with the lowest energy; in that case, since the dominant collisions will be *s*-wave ones, the Pauli exclusion principle will prevent the atoms from decaying into the single lowest-energy state. The only possible changes in atomic internal state will then be to a higher-energy state, and require more energy than the atoms have at low temperature. The two lowest-energy hyperfine states are strong-magnetic-field-seeking states, and cannot be trapped magnetically. They can be confined by

an optical trap, however, as an optical trap provides a nearly state-independent trapping potential. It is for these reasons that we have developed an ultrastable optical trap using a commercial CO_2 laser.

Before explaining our specific implementation of an optical trap, I will discuss the physics behind optical trapping, beginning with a simple derivation of the optical dipole potential. Noise in the lasers used to create optical traps severely limited early optical trap lifetimes, as fluctuations in the laser intensity and variations in the direction of the laser transferred energy to the trapped atoms and heated them until they escaped the trap in just a few seconds. I will discuss both of these forms of noise and how our optical trap has a lifetime of hundreds of seconds, thanks to careful control of laser intensity and direction. While we custom-built a CO_2 laser specifically to minimize potential noise sources and performed a number of early experiments using it [24, 64], in 2001 we found a commercial CO_2 laser with noise characteristics that made it sufficiently quiet for our needs. The details of this commercial laser will be explained. Following that, I will explain the setup used in our experiments, from the vacuum system and the MOT which serves as our precooling trap to the arrangement of lenses and mirrors used with our CO_2 laser.

3.1 The Physics of Optical Trapping

A tightly-focused Gaussian beam tuned well below resonance was one of the first proposed atomic traps [65]. Such a beam would induce an electric dipole in atoms, then confine the atoms via interactions between the induced dipole and the laser beam field. Conceptually, the physics is simple: the beam's electric field induces a dipole, as the protons and the electrons which surround them are pulled in opposite directions. The scalar polarizability of an atom α_P is a measure of how large a dipole

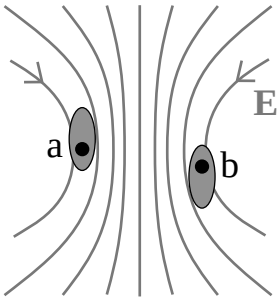

Figure 3.1: An electric field **E** induces a dipole in two atoms. Atom **a** has a positive polarizability, and will be attracted to regions of strong intensity, while atom **b** has a negative polarizability and will be repelled from the same region.

d will be induced for a given electric field, as given by $\mathbf{d} = \alpha_P \mathbf{E}$. The induced dipole will then interact with the atom's electric field, giving rise to a potential

$$U = -\frac{1}{2}\overline{\mathbf{d} \cdot \mathbf{E}} = -\frac{1}{2}\alpha_P \overline{\mathbf{E} \cdot \mathbf{E}}. \tag{3.1}$$

The factor of 1/2 arises from the dipole being induced rather than permanent, and the bar over the dot product indicates that it is to be averaged over several optical cycles. Taking the time average of the dot product gives

$$U = -\frac{1}{4}\alpha_P |\boldsymbol{\mathcal{E}}|^2 = -\frac{2\pi}{c}\alpha_P I, \tag{3.2}$$

where $\boldsymbol{\mathcal{E}}$ is the slowly-varying amplitude of **E**, c is the speed of light, and I is the intensity of the electric field, given by $\boldsymbol{\mathcal{E}}^2 = 8\pi I/c$. From this we see that the electric dipole potential will be attractive or repulsive depending on the sign of α_P. Atoms with a positive polarizability will be attracted to regions of high intensity, while atoms with a negative polarizability will be repelled from the same regions.

The polarizability will be positive if the driving electric field's frequency is less than that of the atomic transition to an excited state, as can be demonstrated with

a simple physical picture of atomic polarizability. Consider the atom as having two energy levels, and its electron of mass m_e as being harmonically bound with an eigenfrequency of ω_0, the transition frequency between the ground and excited states. This electron is then driven by a sinusoidally-varying electric field. The electron will obey the equation of motion for a driven harmonic oscillator,

$$\ddot{\mathbf{x}} + \omega_0^2 \mathbf{x} = \frac{e\mathbf{E}(t)}{m_e}. \tag{3.3}$$

The particular solution to this differential equation is

$$\mathbf{x}(t) = \frac{e}{m_e} \frac{1}{\omega_0^2 - \omega^2} \mathbf{E}(t). \tag{3.4}$$

The dipole induced by this motion is $\mathbf{d} = e\mathbf{x}$. However, the induced dipole is also by definition equal to $\alpha_P \mathbf{E}$, so that the polarizability is

$$\alpha_p = e\frac{\mathbf{x}}{\mathbf{E}} = \frac{e^2}{m_e} \frac{1}{\omega_0^2 - \omega^2}. \tag{3.5}$$

If the laser field's frequency is less than ω_0, then α_P is positive and the dipole oscillates in phase with the electric field, making the atom attracted to regions of high intensity. If $\omega > \omega_0$ then $\alpha_P < 0$, the dipole oscillates 180° out of phase with the electric field and the atom is repelled from regions of high intensity. Thus laser beams which are red-detuned from an atom's optical transition will serve to attract that atom.

A focused Gaussian beam can provide the necessary spatial variation in the potential U to confine atoms. The intensity of a focused Gaussian beam in cylindrical

coordinates is

$$I(r,z,\phi) = \frac{I_0}{1+(z/z_0)^2}\exp(-2r^2/r_0^2), \tag{3.6}$$

where z is taken to be the direction of the beam's propagation. I_0 is the beam's peak intensity, $z_0 = \pi a^2/\lambda$ is its Rayleigh length, r_0 is the $1/e^2$ intensity radius, and λ is the wavelength of light. This intensity results in an electric dipole potential of

$$U(r,z,\phi) = -\frac{U_0}{1+(z/z_0)^2}\exp(-2r^2/r_0^2), \tag{3.7}$$

where U_0, the well depth of the potential, is equal to $(2\pi\alpha_P/c)I_0$. This potential in turn gives rise to a force

$$\mathbf{F}(r,z,\phi) = -\frac{U_0}{1+(z/z_0)^2}\left(\frac{2z/z_0}{1+(z/z_0)^2}\hat{\mathbf{z}} + \frac{4r}{r_0^2}\hat{\mathbf{r}}\right)\exp(-2r^2/r_0^2). \tag{3.8}$$

As with many potentials, the one from Eq. (3.7) is approximately harmonic near its center, which corresponds to the beam's focus. Expanding this potential for small values of z/z_0 and r/a results in

$$U(r,z,\phi) \underset{r\ll r_0, z\ll z_0}{=} -U_0 + \frac{U_0}{z_0^2}z^2 + \frac{2U_0}{r_0^2}r^2. \tag{3.9}$$

Ultracold atoms will be confined near the focus and thus experience this anisotropic harmonic potential. We can define oscillation frequencies for this potential, such that Eq. (3.9) becomes

$$U(r,z,\phi) = -U_0 + \frac{1}{2}M\omega_z^2 z^2 + \frac{1}{2}M\omega_r^2 r^2, \tag{3.10}$$

where M is the mass of the atoms. Comparing the two equations shows that the

oscillation frequencies for atoms at the focus of a Gaussian beam will be

$$\omega_z = \sqrt{\frac{2U_0}{Mz_0^2}} \qquad \omega_r = \sqrt{\frac{4U_0}{Mr_0^2}}. \tag{3.11}$$

The actual value of the polarizability α_P can be found using a semiclassical two-level approach in which the atom is coupled to a classical electric field by the electric dipole interaction $\boldsymbol{\mu} \cdot \mathbf{E}$ [26]. This approach yields the expectation value of the dipole operator $\langle \boldsymbol{\mu} \rangle = \alpha_P \mathbf{E}$ and thus the polarization:

$$\begin{aligned} \alpha_P &= \frac{\mu_{eg}^2}{\hbar}\left(\frac{1}{\omega_0 - \omega} + \frac{1}{\omega_0 + \omega}\right) \\ &= \frac{2\omega_0 \mu_{eg}^2}{\hbar(\omega_0^2 - \omega^2)}, \end{aligned} \tag{3.12}$$

where $\mu_{eg} = \langle e|\mu|g\rangle$ is the dipole matrix element for the ground and excited state. Note that (3.12) has the same form as (3.5).

Near resonance, these results should reproduce the standard Rabi oscillation results [66], as I will show. Equation (3.12) can be simplified in the case that the laser field detuning $\Delta = \omega_0 - \omega$ is small enough that $|\Delta| \ll \omega_0$. In this limit we can make the rotating-wave approximation and neglect the counter-rotating term $1/(\omega_0 + \omega)$, which is by far the smaller of the two terms. The polarization is then simply

$$\alpha_P = \frac{\mu_{eg}^2}{\hbar}\frac{1}{\omega_0 - \omega} = \frac{\mu_{eg}^2}{\hbar\Delta}. \tag{3.13}$$

The dipole potential from (3.2) is then

$$U = -\frac{\mu_{eg}^2 \mathcal{E}^2}{4\hbar\Delta} = -\frac{\hbar\Omega^2}{4\Delta}, \tag{3.14}$$

where $\Omega = \mu_{eg}\mathcal{E}/\hbar$ is the Rabi oscillation frequency. These results also simplify in the opposite limit of large detuning, as will be later shown.

One problem that limits the temperature of atoms confined in a MOT is heating due to the scattering of photons from the atoms. Given the cold temperatures we wish to achieve in an optical trap, it is important to minimize the scattering rate. The scattering rate is linked to the rate at which the oscillating dipole of the atom radiates energy, which is given by the Larmor power formula

$$P = \frac{2}{3}\frac{\overline{\ddot{\mathbf{d}}^2}}{c^3} = \frac{1}{3c^3}\omega^4\alpha_P^2\mathcal{E}^2. \tag{3.15}$$

The rate at which photons are scattered is then

$$\Gamma_{sc} = \frac{P}{\hbar\omega} = \frac{\sigma_s I_0}{\hbar c k}, \tag{3.16}$$

where σ_s is the scattering cross section

$$\sigma_s = \frac{8\pi}{3}\alpha_P^2 k^4. \tag{3.17}$$

The scattering rate gives rise to a recoil heating rate $\dot{Q}_r$ that is given by the rate at which photons are scattered times twice the energy of each photon,

$$\dot{Q}_r = \Gamma_{sc}\frac{(\hbar k)^2}{M} \tag{3.18}$$

In the limit of small detuning, (3.13) and (3.14) can be substituted into the above two equations, giving

$$\Gamma_{sc} = \frac{\mu_{eg}^4 k^3}{3\hbar^3\Delta^2}\mathcal{E}^2 = \frac{4\omega_0^3\mu_{eg}^2}{3\hbar c^3}\left(\frac{\omega}{\omega_0}\right)^3\frac{\Omega^2}{4\Delta^2} \simeq \frac{\Gamma\Omega^2}{4\Delta^2}, \tag{3.19}$$

where I have used $\omega = ck$ and the approximation that, in this limit, $\omega/\omega_0 \simeq 1$.

$$\Gamma \equiv \frac{1}{\tau_{spont}} = \frac{4\omega_0^3 \mu_{eg}^2}{3\hbar c^3} \tag{3.20}$$

is the Einstein A coefficient, which determines the rate of spontaneous emission; τ_{spont} is the spontaneous lifetime. In terms of the well depth U_0, the scattering rate is

$$\Gamma_{sc} = \frac{\Gamma}{\hbar\Delta} U_0. \tag{3.21}$$

Since $\Omega^2 \propto I_0$, (3.14) and (3.19) show that it is possible to decrease the scattering rate without losing well depth. From those two equations, the well depth is proportional to I_0/Δ and the scattering rate is proportional to I_0/Δ^2. Detuning the trap laser further from resonance and proportionately increasing the intensity of that laser serves to decrease the scattering rate without reducing the well depth.

If the detuning is increased dramatically in an effort to limit optical heating by photon scattering, as is done in far-off-resonance traps (FORTs) [21, 67, 68],[1] the above equations no longer hold, as the rotating wave approximation is invalid [69]. However, the polarizability in the limit limit of large detuning and low frequency ($\omega \ll \omega_0$) becomes

$$\alpha_P = \alpha_s \frac{1}{1 - \omega^2/\omega_0^2} \simeq \alpha_s \tag{3.22}$$

where

$$\alpha_s = 2\mu_{eg}^2/\hbar\omega_0 = \frac{3c^3}{2\omega_0^4 \tau_{spont}} \tag{3.23}$$

is the static polarizability of the two-level atom [69, 21]. (For the ground state of ^{6}Li, $\alpha_s = 24.3 \times 10^{-24}\,\mathrm{cm}^3$ [70].) This means that the dipole interaction with the

[1] In some references, such as [69], these traps are called QUESTs—quasi-electrostatic traps.

oscillating field of the laser can be taken to be that of a dipole interacting with a *static* field of strength $\mathcal{E}$. The dipole potential then becomes

$$U = -\frac{1}{4}\alpha_s \mathcal{E}^2 = -\frac{2\pi}{c}\alpha_s I, \tag{3.24}$$

which is the same as (3.2) with α_P replaced by α_s. The maximum depth of this potential is $U_0 = 2\pi\alpha_s I_0/c$.

Similarly, the scattering cross section in this limit is the same as in (3.17) with the replacement of α_p by α_s:

$$\sigma_s = \frac{8\pi}{3}\alpha_s^2 k^4. \tag{3.25}$$

We can then substitute this value of σ_s, $\alpha_s = 2\mu_{eg}^2/\hbar\omega_0$, and U_0 into (3.16), giving the scattering rate in this limit as

$$\Gamma_{sc} = \frac{2\Gamma}{\hbar\omega_0}\left(\frac{\omega}{\omega_0}\right)^3 U_0. \tag{3.26}$$

The photon scattering rate is less than that predicted in (3.21) by a factor of $2(\omega/\omega_0)^3\Delta/\omega_0$.

To give some representative numbers, our optical trap is formed by a 65 W CO_2 laser beam with a wavelength of 10.6 μm which is focused to a spot with a $1/e^2$ intensity radius of $r_0 = 47\,\mu$m. The resulting peak intensity is $I_0 = 2P/\pi a^2 = 1.9\,\mathrm{MW/cm^2}$, yielding a well depth of $U_0 = 690\,\mu$K and an optical scattering rate from (3.26) of two photons per hour. The associated recoil heating rate is only $\Gamma_{sc}(\hbar k)^2/M = 16\,\mathrm{pK/sec}$. The ω^3 scaling of Γ_{sc} lowers the scattering rate of CO_2 laser traps by three orders of magnitude, and the heating rate by five orders of magnitude, as compared to those of lasers whose frequencies are closer to the visible spectrum.

3.2 Noise and Optical Traps

Optical traps may produce very small optical-scattering heating rates when they are far-detuned from resonance, but in early experiments they suffered from unexpected and unexplained heating rates. For example, Adams *et al.* [20] found that their optical trap's lifetime *decreased* as they increased their laser's intensity. They measured a 1/e trap lifetime of 2.7 s; at low intensities, the trap lifetime was expected to be dominated by collisions between the trapped atoms and background gas atoms, giving an extrapolated trap lifetime of 14 s. However,

> The lifetime data...were found to vary inversely with the trapping intensity and to be independent of the initial atomic number and density. At present we have no consistent explanation for the observed intensity and density dependence of the trap loss.

To avoid this problem, some groups used lasers detuned to the blue of resonance, which repel atoms. Atoms can be confined by using several sheets of blue-detuned light to form walls; since this light repels atoms, they should spend less time in regions of high intensity and thus hopefully experience less heating. However, as Lee *et al.* found [19], even these blue-detuned traps produced unexplained heating rates. In their experiments, trap lifetime was independent of background pressure from 7×10^{-11} Torr to 2×10^{-11} Torr, and in this region appeared to be limited by a heating rate nearly thirty times greater than that produced by optical scattering.

Two years later, in 1997, these heating rates were still unexplained. In their article reviewing laser cooling and trapping [37], C. S. Adams and E. Riis stated that the lifetime of optical traps tended to "saturate at a few seconds due to other possible heating mechanisms." One of these possible heating mechanisms is noise

caused by fluctuations of the trapping laser. Changes in the laser intensity and position can give rise to nontrivial heating rates, as shown by Tom Savard *et al.* [38].

3.2.1 Intensity Noise

Near the bottom of a trap formed by a Gaussian beam, atoms experience a harmonic potential, as shown in Section 3.1. If the intensity of this Gaussian beam fluctuates, atoms in that harmonic potential will be heated exponentially. To see why, consider one of the trap frequencies from Eq. (3.11), which I will call ω_{tr}. The model Hamiltonian for an atom of mass M in the harmonic potential will be

$$\mathcal{H} = \frac{p^2}{2M} + \frac{1}{2}M\omega_{tr}^2 x^2. \tag{3.27}$$

However, $\omega_{tr}^2 \propto U_0 \propto I_0$, where I_0 is the time-averaged intensity of the laser beam. If the laser intensity fluctuates, it will change the value of ω_{tr}^2. This modifies the Hamiltonian:

$$\mathcal{H} = \frac{p^2}{2M} + \frac{1}{2}M\omega_{tr}^2[1+\epsilon(t)]x^2, \tag{3.28}$$

where $\epsilon(t)$ is the fractional fluctuation of the laser intensity in terms of I_0:

$$\epsilon(t) = \frac{I(t) - I_0}{I_0}. \tag{3.29}$$

The correlation function for the intensity fluctuations is then

$$\langle \epsilon(t)\epsilon(t+\tau)\rangle = \frac{1}{T}\int_0^T dt\, \epsilon(t)\epsilon(t+\tau). \tag{3.30}$$

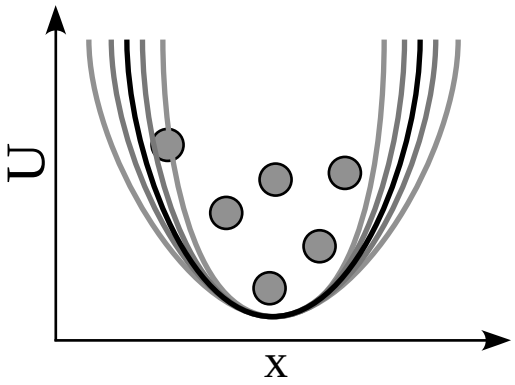

Figure 3.2: Noise in the intensity of the laser causes fluctuations in the trap spring constant. This leads to parametric heating of the trapped atoms.

Given this correlation function, the one-sided power spectrum for the fractional intensity noise will be

$$S_\epsilon(\omega) = \frac{2}{\pi}\int_0^\infty d\tau\, \cos\omega\tau\, \langle \epsilon(t)\epsilon(t+\tau)\rangle\,. \tag{3.31}$$

The heating rate due to intensity fluctuations can be found via first-order time-dependent perturbation theory [38], and is

$$\frac{d\langle E\rangle}{dt} = \Gamma_{int}\langle E\rangle\,, \tag{3.32}$$

indicating that exponential heating occurs. $\langle E\rangle$ is the average energy of the trapped atoms, and the rate constant Γ_{int} in terms of the trap oscillation frequency in Hz $\nu_{tr} = \omega_{tr}/2\pi$ is

$$\Gamma_{int} = \pi^2\nu_{tr}^2 S_\epsilon(2\nu_{tr}). \tag{3.33}$$

Since the rate constant depends on ν_{tr}^2, it is dependent on the intensity of the trapping beam. The dependence of Γ_{int} on the noise power spectrum at twice the trap oscillation frequency indicates that it is a parametric process.

Physically, fluctuations in intensity serve to change the trap's depth. From (3.11) we see that oscillation frequencies, and thus the spring constants of the harmonic trap, depend on U_0. Fluctuations in U_0 change the trap spring constant; fluctuations in the spring constant produce heating. The parametric nature of the heating arises because atoms interact with the sides of the potential twice per cycle. The fluctuations in force that the atoms experience will be ϵkx, where k is the trap's spring constant and x the atom's distance from the trap center. As atoms heat and move up in the potential, they stray farther and farther from the center. The resulting increase in x leads to ever-larger force fluctuations and, since heating is proportional to the mean square force fluctuation $(\epsilon kx)^2$ and $x^2 \propto E$, exponential heating.

3.2.2 Position Noise

Fluctuations in the laser beam's position alter the value of x from (3.27). If we now take $\epsilon(t)$ to be equal to $\epsilon_x(t)$, the fluctuation in the position of the trap's center, then the Hamiltonian of the system is

$$\mathcal{H} = \frac{p^2}{2M} + \frac{1}{2}M\omega_{tr}^2[x - \epsilon_x(t)]^2. \tag{3.34}$$

The one-sided power spectrum of position noise $S_x(\omega_{tr})$ can be defined analogously to (3.31). Applying first-order time-dependent perturbation theory gives the heating rate as [38]

$$\langle \dot{E} \rangle = \frac{\pi}{2}M\omega_{tr}^4 S_x(\omega_{tr}). \tag{3.35}$$

The heating due to position noise is independent of energy, unlike that due to intensity noise, and depends on the position noise spectrum at a given frequency

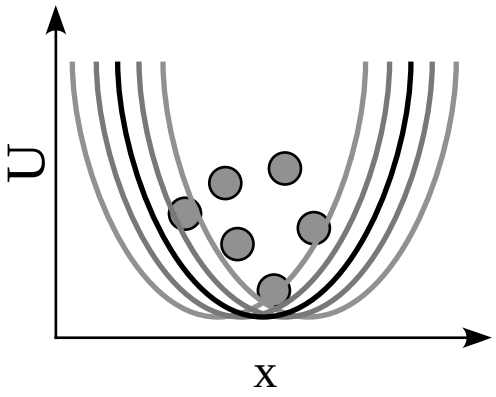

Figure 3.3: Position noise moves the trap from side to side, shaking the atoms and heating them.

ω_{tr}.

The change in position moves the trap from side to side, shaking the atoms like marbles in a bowl. This pushes the center of mass of the trapped atoms; anharmonicities in the trap convert this center-of-mass motion into motion relative to the center of mass, transferring energy to the atoms and heating them until they are able to escape the trap.

3.3 A Quiet Commercial CO_2 Laser

To address the twin requirements of large detuning and high stability, our group decided to use a CO_2 laser. CO_2 lasers operate at a wavelength of 10.6 μm, while the resonant transition for ^{6}Li occurs at 671 nm. The resulting red detuning of $\omega/\omega_0 = 1/15.8$ is well into the regime where the electrostatic limit holds and the induced dipoles can be viewed as interacting with a static field. CO_2 lasers are also very stable when well designed, and can produce the high intensities required to offset the large detuning.

Our initial experiments employed a custom-built CO_2 laser, as we were unable

to find a commercial one which would meet our stringent noise requirements. This laser's construction was detailed in [26]. With that laser, we were able to achieve trap lifetimes of 360 s and cool 15,000 atoms per state to a temperature of 2.4 μK and a phase-space density of around 1.6×10^{-3}. In 2001, we discovered a commercial laser from Coherent-DEOS that potentially had noise specifications that rendered it usable in a long-lifetime optical trap. We purchased one and determined that it indeed met our noise requirements.[2]

The laser is an LC-100NV CO_2 laser from Coherent-DEOS, and is rated to produce 100 W of 10.6 μm light, though the one we purchased provides 140 W of power. The LC-100NV uses a sealed-tube rather than a flowing-gas design. The sealed-tube design allows the CO_2's absorption line to be pressure-broadened, preventing the power drifts we experienced with our home-built laser. The laser tube is excited by an rf power supply. In the standard commercial configuration, the LC-100NV includes an integrated DC power supply to power its rf supply; however, we had Coherent-DEOS remove the integrated power supply. Instead we use a separate Agilent 6573A DC power supply to produce the 50 A of stable current that the rf supply requires, in order to reduce potential noise in the laser. The LC-100NV rf power supply can be pulse modulated, varying the laser's power from a few watts to its maximum 140 W. Though the laser cannot be used for trapping while in pulse modulation mode, the lower-powered beam can be used to align the experiment's optical setup more safely.

The laser head and rf power supply are cooled by a Thermo NESLAB Merlin M-75 recirculating chiller. The M-75 is capable of removing 2410 W at a temperature of 20 °C. We operate the M-75 at a temperature of 15 °C, where it can remove

[2]The details of the noise measurements will be presented later in the chapter.

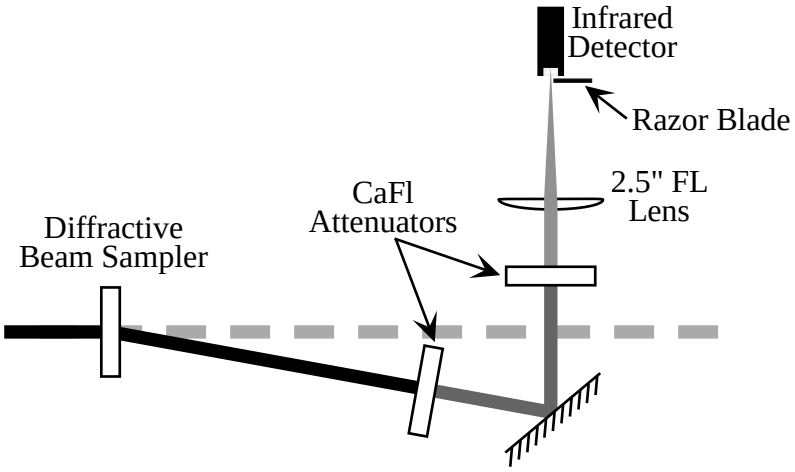

Figure 3.4: The experimental setup used to measure both intensity and position noise of the CO_2 laser. The razor blade can be slid into the beam to make measurements of the position noise of the laser.

$\sim$2250 W of power. The cooling liquid used is a mixture comprised of 75% distilled water and 25% DOWFROST by volume. DOWFROST is a low-toxicity propylene glycol fluid that includes corrosion inhibitors, a necessity in a closed-loop cooling system such as that formed by the M-75 chiller and the LC-100NV laser. The DOWFROST also serves to lower the mixture's freezing point below 0 °C, though we do not cool the mixture this much due to problems with water condensing from the air onto the cooled equipment.

3.3.1 Measuring the Noise Spectra

To measure our laser's intensity and position noise, we use a low-noise infrared detector. Since the detector is incapable of absorbing the laser's full 140 W, only a portion of the beam is directed into the detector. A diffractive beam sampler deflects 0.25% of the laser power into a beam travelling at a 10.2° angle from the primary beam. This deflected beam passes through two CaF_2 attenuators, reducing its power to $\sim$ 100 mW, and is then focused by a 2.5 in. focal-length plano-convex

ZnSe lens onto the infrared detector. When measuring position noise, a razor blade is placed so as to cover half of the detector; in this manner fluctuations in the beam position become fluctuations in intensity.

The detector is a Boston Electronics PD-10.6-3 infrared detector. Its output is fed into a Perry Electronics 481-1 low-noise preamplifier, and then into a Tektronix TDS644B digital oscilloscope. The oscilloscope records $V(t)$, the detector voltage as a function of time; that function is then read by a computer program written in LabView by Tom Savard. Using this data, the computer program calculates $S_V(\nu)$, the one-sided power spectrum of the voltage, as given by (3.31). Many such spectra are recorded and averaged together to give the final power spectrum.

3.3.2 Intensity Noise

The CO_2 laser's intensity noise is measured without the razor blade (shown in Figure 3.4) in place. The voltage power spectrum from the infrared detector is recorded both with the laser beam incident on the detector and with the laser beam blocked. The latter results in a voltage power spectrum that corresponds to the electronic noise power spectrum of the detector, pre-amplifier, and oscilloscope. Subtracting this from the spectrum obtained when the laser beam is not blocked gives a voltage power spectrum $S_V(\nu)$ which directly corresponds to the intensity noise spectrum $S_\epsilon(\nu)$.

Two intensity noise power spectra are measured, one at low resolution over a large frequency range, the other at high resolution over a smaller frequency range. Figure 3.5 shows the low-resolution spectrum, while Figure 3.6 shows the high-resolution one. For the low-resolution spectrum, data was recorded at 500,000 samples per second, giving a Nyquist frequency of 250 kHz. To prevent noise at

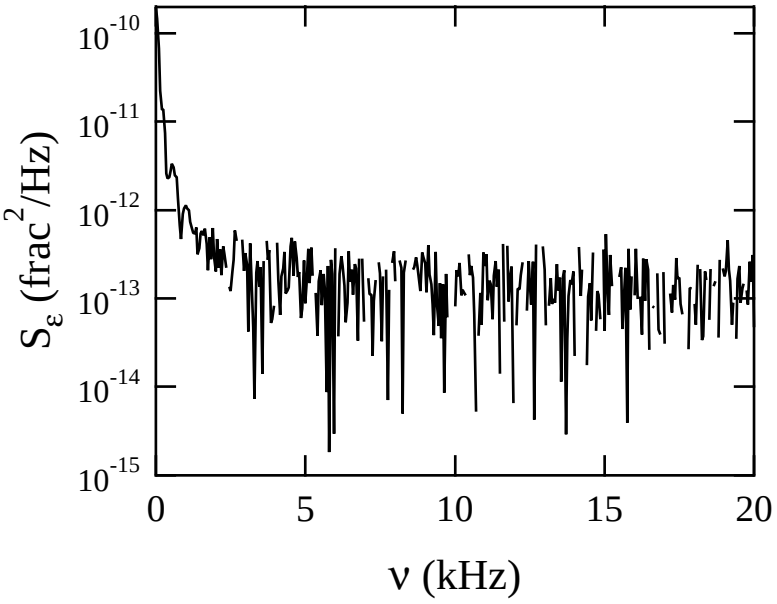

Figure 3.5: The low-resolution intensity noise power spectrum for the DEOS LC-100NV CO_2 laser. The electronic noise power spectrum has been subtracted off to arrive at this spectrum. At high frequencies, the noise due to the laser falls below the electronic noise of the detector and thus detector sensitivity.

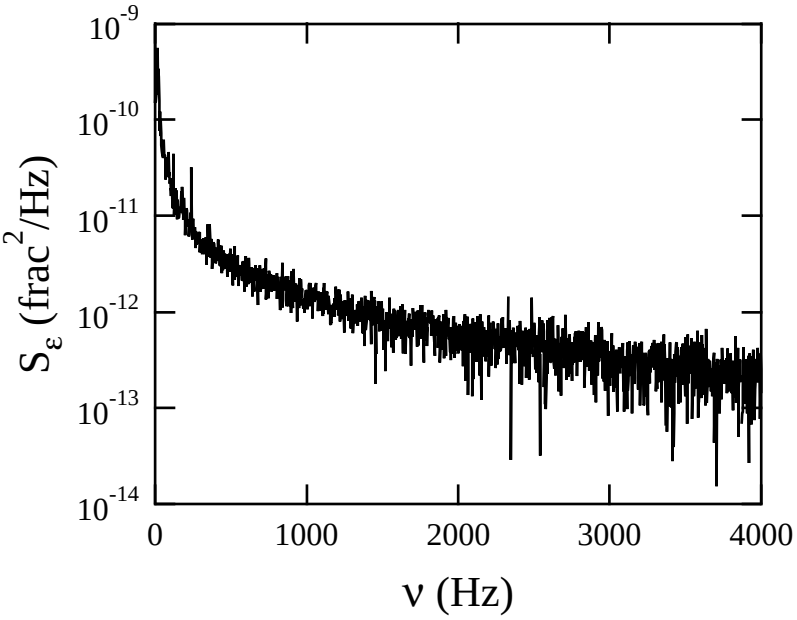

Figure 3.6: The high-resolution intensity noise power spectrum for the DEOS LC-100NV CO_2 laser. The electronic noise power spectrum has been subtracted from the recorded data to obtain this spectrum.

higher frequencies from being aliased into the recorded data, the signal from the low-noise amplifier was passed through a 50 kHz (3-dB point) low-pass filter. Above 7 kHz, the laser intensity noise spectrum is comparable to the infrared detector's electronic noise.

The high-resolution spectrum was recorded at 25,000 samples per second, giving a Nyquist frequency of 12.5 kHz. To prevent noise at higher frequencies from being aliased into the recorded data, the signal from the low-noise amplifier was passed through a 5 kHz (3-dB point) low-pass filter.

From these spectra, the exponential heating rate experienced by atoms near the bottom of the trap can be calculated. As shown in Section 3.2.1, the average energy of those atoms will increase according to $\langle \dot{E} \rangle = \Gamma_{int} \langle E \rangle$, where the rate constant is given by (3.33). Figure 3.7 shows Γ_{int}^{-1} as a function of trap frequency ν. The

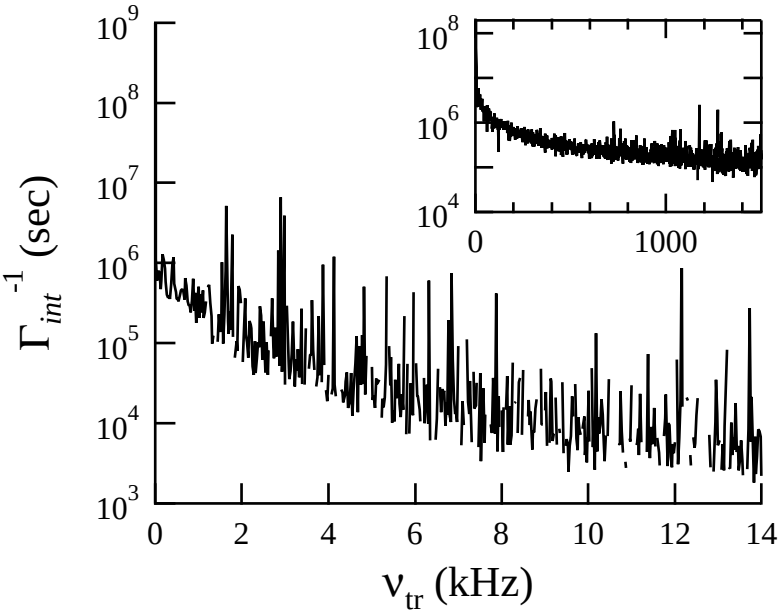

Figure 3.7: The predicted exponential heating time Γ_{int}^{-1} due to intensity noise in the CO_2 laser. The missing sections of the graph indicate points where the measured intensity noise was comparable to or less than the background electronic noise. The main graph is the heating time based on the low-resolution data, while the inset shows the heating time based on the high-resolution data.

missing sections of the graph are where the intensity noise is comparable to the electronic noise, so that when the electronic noise is subtracted from the measured intensity noise, the result is negative, leading to a nonsensical value for Γ_{int}^{-1}. At our trap radial frequency of 6.6 kHz, $\Gamma_{int}^{-1} \simeq 23,000$ sec, which is large compared to our trap lifetime of $\simeq 350$ sec.

3.3.3 Position Noise

In measuring the position noise of the CO_2 laser, the razor blade from Figure 3.4 is placed so that it covers half of the detector. This converts $\epsilon_x(t)$, the position noise in the horizontal direction, to intensity noise: as the beam moves horizontally, the total power reaching the detector will change as more or less of the beam is blocked by the razor blade. (Power fluctuations are given by $\Delta P = \sqrt{2}P_0\epsilon_x(t)/(r_0\sqrt{\pi})$. r_0 is the $1/e^2$ intensity radius of the Gaussian laser beam and P_0 is the total power of the unblocked beam.) In doing so, the intensity noise power spectrum then contains contributions both from true position noise and from intensity noise. Subtracting the intensity noise voltage power spectrum found in Section 3.3.2 from the power spectrum measured with the razor blade in place gives $S'_V(\nu)$, the portion of the voltage power spectrum due solely to fluctuations in the position of the beam. The one sided power spectrum of the position fluctuations $S_x(\nu)$ is then given by

$$S_x(\nu) = \frac{\pi}{2} r_0^2 \, S'_\epsilon(\nu), \tag{3.36}$$

where

$$S'_\epsilon(\nu) = \frac{1}{4} S'_V(\nu). \tag{3.37}$$

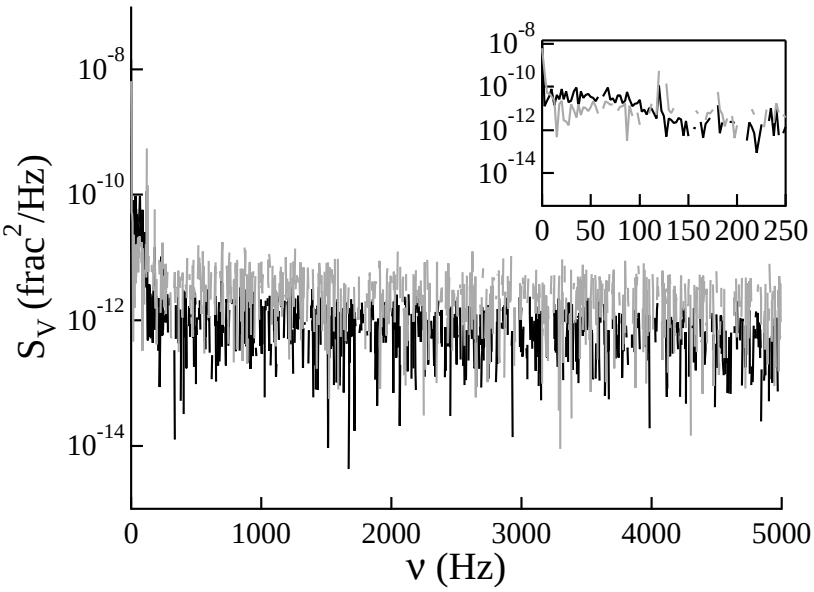

Figure 3.8: Fractional voltage fluctuations with and without the razor blade. The lighter grey trace is with the razor blade; the darker, without. The inset shows the same two traces from 0 Hz to 250 Hz.

The factor of 1/4 arises from the incident intensity being equal to $I_0/2$ due to half of the beam being obstructed by the razor blade.

Figure 3.8 compares intensity noise measured with the razor blade removed to that measured with the razor blade blocking half of the detector. The lighter grey trace is the intensity noise as measured with the razor blade in place. As can be seen, the two are virtually identical, indicating that the position noise is less than can be measured with the equipment.

3.4 First-Stage Trapping Apparatus

If one's goal is to study a degenerate gas of fermions, an ultrastable laser is of little use by itself. A source of atoms is required before trapping and cooling experiments can be carried out. The use of an optical trap requires a source of *cold* atoms, as

optical traps are not very deep. The trap depth of our CO_2 laser trap is $690\,\mu$K, equivalent to a ^{6}Li thermal speed of 1.4 m/s, while the atoms emerging from our atomic slower are travelling at 40 m/s [71]. Moreover, optical traps form a conservative potential, so that any atom which enters the trap will have enough energy to escape again. Optical traps must be loaded by a trap which is not conservative, such as a magneto-optical trap (MOT).

This section presents the apparatus used to prepare atoms for loading into our CO_2 laser trap. Our ultra high vacuum (UHV) system is capable of producing a vacuum of $< 10^{-11}$ Torr, a necessity for long trap lifetimes. The requisite ^{6}Li gas is produced by an oven whose construction will be discussed. The hot beam of atoms from the oven is then slowed from a peak velocity of 1100 m/s to a final one of 40 m/s by a Zeeman slower. A MOT confines the atoms from the slower and cools them, preparing them for loading into the CO_2 laser trap. A brief explanation of both the slower and the MOT will be given, as they are crucial elements in the steps leading to evaporative cooling of ^{6}Li in a CO_2 laser trap.

3.4.1 Vacuum System

Creation of an ultra high vacuum environment necessitates the use of multiple vacuum pumps. Our experimental setup includes two main types of pumps: ion pumps and titanium sublimation (Ti sub) pumps. Ion pumps combine a number of different technologies in one pump, including the use of so-called "getter" materials which bind chemically-active gases. Typical ion pumps have two flat rectangular cathodes with an anode between them made of many open-ended boxes or tubes. The cathodes and anode are enclosed by a permanent magnet and are charged to create a high electric potential. The cathodes are made of a getter material such

as titanium, so that gases which react with titanium will be bound to the cathode, removing them from the surrounding environment. More inert gases are ionized by the electron flow between cathode and anode, and are then attracted to and buried in the cathode. In the process, the ions sputter titanium from the cathodes onto unshielded surfaces in the ion pump, increasing the surface area of titanium available for bonding with unwanted gases. Ion pumps produce no acoustic noise or vibrations, and require little to no maintenance. Their main disadvantage is that they are inefficient at pressures greater than 10^{-5} Torr, and must be pre-pumped by a mechanical pump such as a turbomolecular one.

As the name implies, titanium sublimation pumps use the getter properties of titanium. A Ti sub pump consists of a filament of titanium. This filament heats when an electric current is passed through it, causing titanium to evaporate. The evaporated titanium then coats the inside of the vacuum system, in effect turning the walls of the vacuum system into a pump. The rate of pumping depends on the amount of surface area covered by the titanium. Eventually most of the deposited titanium forms stable bonds and no longer traps gas. At this point the Ti sub pump filament must be heated again to deposit a fresh layer of titanium, increasing the pumping speed once again. Ti sub pumps have no effect on unreactive gases like helium, which is why they must be used in conjunction with other pumps like ion pumps.

Our vacuum system comes in three sections: the oven region, the Zeeman slower region, and the trapping region. A detailed description of all three regions can be found in Tom Savard's thesis [72].

Unsurprisingly, the oven region holds the ^{6}Li oven, which will be described in Section 3.4.2. This region consists of the oven itself, which looks like a corncob

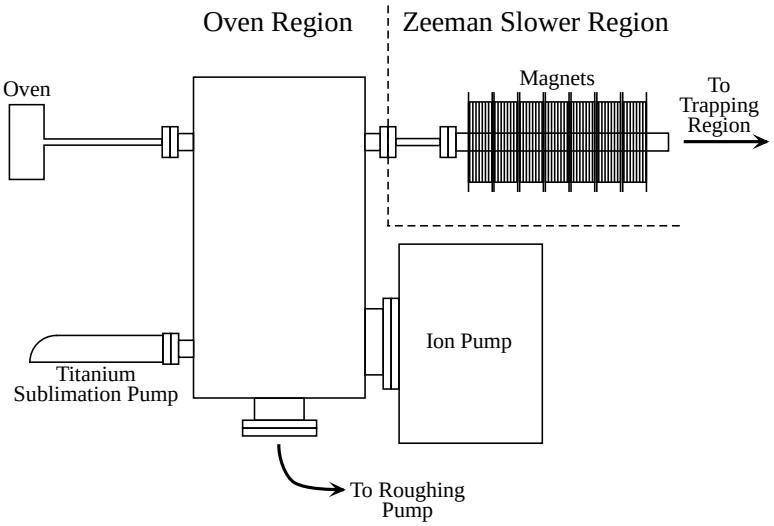

Figure 3.9: Side view of the oven and Zeeman slower region of the vacuum system.

pipe; a 4 in. diameter tube between the oven to the Zeeman slower region; and both ion and Ti sub pumps, which are attached to the 4 in. diameter tube. The oven produces a gas of lithium, most of which is directed in a stream which passes through the Zeeman slower region and into the vacuum system's trapping region. Enough stray ^{6}Li gas is produced to increase the pressure in the entire oven region. To keep this region's pressure around 10^{-9} Torr, we use a 300 liter/sec. ion pump from Physical Electronics and a Ti sub pump from Varian Vacuum Inc, as shown in Figure 3.9. The large 4 in. diameter tube to which the oven and two pumps are attached includes a port at the bottom which can be closed by a valve; when first pumping the system down to low vacuum, a small 20 liter/sec turbomolecular pump is attached to this port until the pressure is low enough that the ion pump can operate reliably, at which point the valve is closed and the turbomolecular pump removed. During regular operation, the Ti sub pump must be run every two weeks to maintain low pressures. A run consists of flowing 47 amps of current through the Ti sub pump filaments for seven minutes.

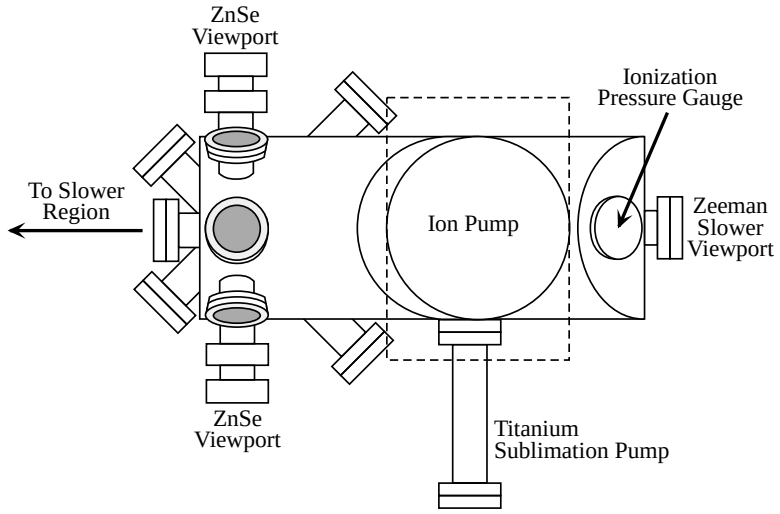

Figure 3.10: A top view of the trapping region of the vacuum system.

The Zeeman slower region is a 22 in. long tube around which the Zeeman slower's magnets are placed. The tube's inner diameter is only 1.5 in. The slower region's long tube is connected to the oven region by a 6 in. long nipple with an inner diameter of 3 mm. The benefit of using a connecting tube with such a small inner diameter is that it limits the conductance between the oven and trapping regions, allowing the trapping region to have a pressure that is two orders of magnitude better than that in the oven region when the oven is producing ^{6}Li gas. The oven region, nipple, and slower region are all connected by 2 3/4 in. conflat flanges.

The trapping region consists of two large 6 in. diameter stainless steel tubes connected at right angles to form something approximating an L. The horizontal tube has thirteen viewports which give optical access to the region; they are used for trapping beams and camera access. All but two of the viewports are made of anti-reflection-coated glass mounted in a 2 3/4 in. flange. Glass absorbs 10.6 μm light, so cannot be used to make the viewport windows through which the CO_2 laser beam is to pass. Instead, crystalline ZnSe is used. It is impossible to make

vacuum seals involving ZnSe which have a leak rate low enough to support ultra high vacuum. Instead, we use viewports which are double-sealed and differentially pumped by an ion pump, as described in Ken O'Hara's thesis [26]. The region between the viewport's two seals is kept at a pressure of $< 10^{-9}$ Torr.

The center of the horizontal 6 in. tube is offset from that of the slower and oven regions, so that the ^{6}Li atomic beam does not pass through the MOT and FORT region and knock atoms from these traps through elastic collisions. One viewport, the Zeeman slower port, is set such that its center is aligned with that of the slower region and oven nozzle. The laser beam used in the Zeeman slower passes through this viewport. Unfortunately, atoms from the oven which are not slowed coat the inside of this viewport, making it opaque and reducing the transmission of the Zeeman slowing beam. The deposited film of ^{6}Li must be periodically removed by heating the viewport to 250 °C for twenty-four hours.

The vertical tube holds the pumps for this region, a 240 liter/sec ion pump from Varian Vacuum Inc. and a titanium sublimation pump. The large connecting tube ensures that the ion pump's speed will not be conduction-limited. In addition, its large surface area is ideal for coating with titanium from the Ti sub pump. The Ti sub pump is located so that there is no direct line of sight from the pump to any of the viewports, preventing the deposition of titanium onto the viewports. To deposit a monolayer of Ti, 47 amps of current are sent through the Ti sub pump for seven minutes. The result is a pressure of $< 10^{-11}$ Torr, smaller than can be read by our ion vacuum gauge.

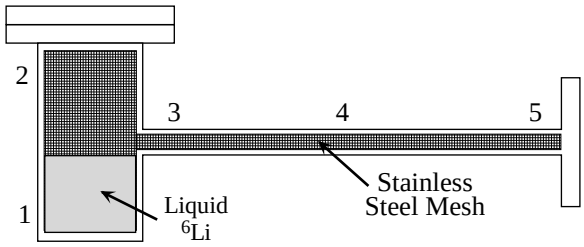

Figure 3.11: The ^{6}Li recirculating oven. The numbers correspond to points at which thermocouples are attached.

3.4.2 ^{6}Li Oven

The oven consists of a small reservoir cylinder, 2.5 in. tall and 3/4 in. in diameter, and a 6 1/4 in. long nozzle located halfway up the cylinder, both made of 316 stainless steel. The oven is wrapped with five different sequential sections of nichrome wire (corresponding to the numbered sections in Figure 3.11), then coated with high-temperature cement from OMEGA. Current is passed through the lengths of wire to heat the oven. The cylinder is filled with 2 g of ^{6}Li and then heated to $\sim 430\,^\circ$C, producing liquid ^{6}Li with a vapor pressure of $\sim 10^{-4}$ Torr. The nozzle, which has an inner diameter of 1/8 in. along most of its length,[3] collimates the escaping ^{6}Li vapor with an angle of 21 mrad.

To increase the length of time for which it can be used without being refilled, the oven is designed to recirculate unused ^{6}Li. A fine mesh made of 316 stainless steel is threaded through the nozzle and connected to a similar mesh lining the inside of the reservoir. During operation, the currents in the five sections of nichrome wire are varied to produce a temperature gradient along the nozzle. Typical temperatures are given in Table 3.1. This temperature gradient and the steel mesh serve to wick condensed liquid ^{6}Li back into the reservoir.

[3]The nozzle end is drilled out to an inner diameter of 3/16 in. to help prevent ^{6}Li from clogging the end and to thin the wall, lowering the end's thermal conductivity and limiting the amount of heat transferred to the oven region from the oven.

	1	**2**	**3**	**4**	**5**
Temp (°C)	380	375	430	360	250

Table 3.1: Typical Oven Temperatures

3.4.3 Zeeman Slower

Atoms emerge from the oven with an average speed of $\sim 1500\,\mathrm{m/s}$, far faster than can be trapped by any neutral atom trap. The atomic beam must be slowed before it can be trapped.

Atomic beam slowers employ the radiation pressure force, the same force which gives rise to optical molasses, as was mentioned in Section 1.3.1. When an atom absorbs a photon from a laser beam, its momentum is changed by $\hbar k$ in the direction of the beam. Should the atom then re-emit that photon through spontaneous emission, it again receives a momentum "kick" of $\hbar k$. In the case of spontaneous emission, though, the kick is in a random direction. Averaged over many absorption-emission cycles, the change in momentum due to spontaneous emission will average to zero. The net change in momentum, then, is in the direction of the laser beam. Applying an on-resonant counter-propagating laser beam to an atomic beam will slow the atoms in the beam.

There is one difficulty with this approach. The frequency of laser light the atoms experience will change as the atoms slow due to the Doppler effect, so that the effective laser frequency is no longer resonant with the atom's transition frequency. The two ways around this difficulty are to modify the laser's frequency or modify the atom's transition frequency. Some early experiments [73] took the former approach by scanning the laser beam frequency frequency to keep it resonant with a group of slowing atoms. This resulted in pulses of atoms, as slow atoms were only produced at the end of the frequency scan, at which point the process began again.

Zeeman slowers take the latter approach by tuning the atomic transition frequency with a magnetic field. Given the appropriate choice of a spatially-varying magnetic field, all atoms with a velocity below maximum will be slowed. Our Zeeman slower uses ten independent magnetic coils to produce the appropriate spatially-varying magnetic field to slow all ^{6}Li atoms with a velocity of 1100 m/s or less to a final velocity of 40 m/s. The full details of the slower construction are covered in Chris Baird's dissertation [71].

3.4.4 Magneto-Optical Trap

As was covered in Section 1.3.1, MOTs combine the viscous damping force of optical molasses with a restoring force arising from the spatially-varying Zeeman shift of an atom's hyperfine levels. Electromagnets are placed on the vacuum system's top and bottom viewports to provide the magnetic field gradient necessary for the restoring force. The temperature of atoms trapped in a MOT is limited by the stochastic nature of photon absorption and re-emission inherent in optical molasses, which causes the atoms to experience a random walk in momentum space. The temperature limit due to the scattering of photons is known as the Doppler limit, and for a three-dimensional optical molasses is given by [74]

$$T_{Doppler} = \frac{\hbar \Gamma_{spont}}{2k_B}, \tag{3.38}$$

where Γ_{spont} is the linewidth of the atomic transition[4]. The value of this temperature limit for ^{6}Li is $T_{Doppler} = 140\,\mu$K.

[4]Cooling below the Doppler limit is possible in some alkali atoms. The derivation of the Doppler limit uses the two-level atom approximation. Other cooling mechanisms, which depend on multiple ground- and excited-state hyperfine levels, occur but are not accounted for in the two-level derivation. Unfortunately these sub-Doppler cooling mechanisms do not occur in ^{6}Li [26].

^{6}Li has two ground states, the $|F = 3/2\rangle$ and $|F = 1/2\rangle$ states. The frequency of light used in the MOT is that of the transition frequency from the $|F = 3/2\rangle$ ground state to the $|F' = 5/2\rangle$ excited state. Should an atom decay from the excited state into the lower $|F = 1/2\rangle$ ground state, it would no longer be strongly affected by the laser beams of the MOT and would be able to escape the trap. To prevent this from happening, the MOT beams include light that is resonant with the $|F = 1/2\rangle$ atoms. This "repumper" light serves to excite atoms in the $|F = 1/2\rangle$ state until they eventually decay from the excited state back into the $|F = 3/2\rangle$ state.

3.4.5 Lasers, Acousto-Optical Modulators, and Optical Layout

The laser and optical setup used for the Zeeman slower and MOT are nearly identical to that described in [26]. The 671 nm light required to drive the first excited-state transition in ^{6}Li is produced by a Coherent Model 699-21 Ring Dye Laser. The dye used is 1.17 g of LD688 dissolved in 1.1 L of 2-phenoxyethanol. A Coherent Innova Model 310 Argon Ion Laser pumps the dye laser. The argon ion laser produces 6 W of power; the dye laser, 750 mW of power when the dye is new. As is typical with fluorescent laser dyes, the output power from the LD688 dye drops with use, falling to 400 mW after several weeks of continuous use.

The dye laser's frequency is referenced to the ^{6}Li resonance frequency using the fluorescence from a collimated beam of lithium. This beam is created in a separate vacuum system, known as the locking region, and from an oven other than that used for the trapping experiments. The oven and vacuum system design are described in [75], though some changes have been made to the oven which produces the ^{6}Li beam.

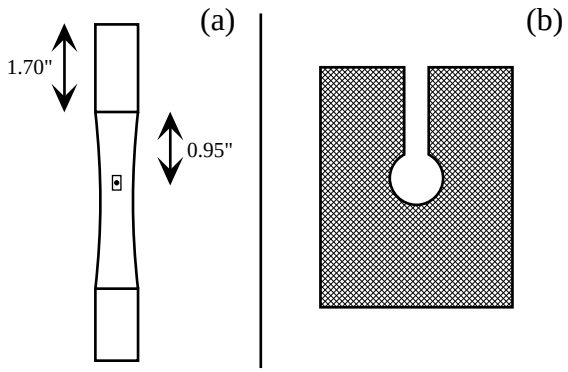

Figure 3.12: (a) The oven design used in the locking region vacuum system. A 0.5 in. diameter stainless steel tube is used. (b) The mesh added to the tube to prevent condensation of ^{6}Li at the top of the oven. The hole in the mesh is lined up with the oven's exit hole.

The new ovens are made from a 0.5 in. diameter tube of 316 stainless steel, rather than tantalum, and their design is shown in Figure 3.12. One end of the oven is crimped, and a flat spot that is 0.005 in. deep is made 0.95 in. from the end of the crimped part by a milling machine. In the middle of the flat spot a 250 μm hole is drilled to allow ^{6}Li vapor to escape during operation. In early versions of the stainless steel oven, gaseous ^{6}Li would recondense near the top, where the oven is cooled. The recondensed ^{6}Li would lower oven resistivity at that point, further cooling the oven top and resulting in more condensation and the formation of a plug of solid lithium which would block the exit hole. Once that occurred, the oven became useless. To prevent this, a wicking mesh similar to the one described in Section 3.4.2 was added to the oven, and the crimp in the oven top is placed closer to the exit hole than in prior designs. The hole in the mesh is lined up with the oven's exit hole. Once the mesh is in place, the oven is filled with around 1.3 g of ^{6}Li. The second end of the oven is then crimped and the entire oven installed in the locking region vacuum system as described in [75].

A beam from the dye laser is sent into the locking region. Its direction is per-

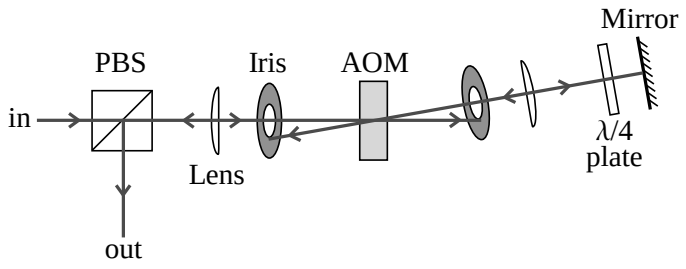

Figure 3.13: An acousto-optic modulator (AOM) in a double-passed configuration. The laser light passes through the AOM, changing its frequency by an amount δ. It then passes through a quarter-wave plate, hits a mirror, and passes through the same quarter-wave plate again, changing the polarization of the light by 90°. The light passes through the AOM once more, adding another shift of δ to its frequency, and is deflected by the polarizing beam splitter (PBS) cube due to the light's changed polarization. The irises block light scattered into other orders by the AOM.

pendicular to the collimated atomic beam to minimize deviations in the resonance frequency due to the Doppler shift. The atomic beam is not perfectly collimated, resulting in a Doppler-broadened fluorescence signal 40 MHz in width. The fluorescence signal is measured by a photo-multiplier tube (PMT), which converts the amount of light into a voltage.

To lock the laser to this signal, the laser beam sent to the locking region is frequency modulated at 11 kHz by an acousto-optic modulator (AOM). This also modulates the fluorescence signal and hence the voltage from the PMT. Lock-in detection of the modulation produces a voltage which is proportional to the derivative of the fluorescence line shape. This voltage will be zero at the transition's peak since the derivative of the line shape is zero at the line shape center. The voltage from the lock-in amplifier is fed into a servo loop [76], which produces an error voltage to adjust the laser frequency appropriately.

We use AOMs extensively in the experiment. An AOM is a crystal with a piezoelectric transducer at one end. Radio frequency (rf) power drives the transducer, creating a sound wave in the crystal. The sound wave produces a density grating

across the crystal, which results in an index of refraction grating. Light passing through the crystal is Bragg scattered off of this grating, producing light in several different orders. By rotating the crystal relative to the incoming laser beam, most of the laser power can be scattered into the first Bragg order. One of the first orders corresponds to an upshift in laser frequency; the other, a downshift.

Before passing through an AOM, a beam is focused using a plano-convex lens, with the AOM being placed at the focal point of the lens. The lens focal length is such that the focused optical beam is smaller than the vertical dimension of the sound wave. For our AOMs, which typically introduce frequency shifts of $\delta \simeq 110\,\mathrm{MHz}$, we use lenses with a 30 cm focal length. First-order deflection efficiencies of 84% of the total incoming power are readily achieved.

AOMs have two features which make them of general use in the experiment. The first is that they alter the frequency of light passing through them. The exact frequency shift δ depends on the crystal and the frequency of the rf power fed to the transducer. By varying the frequency of the rf power, the frequency shift can also be varied, giving control over the frequency of light used; this is how the frequency of the locking region beam is modulated. Changing δ changes the Bragg angle through which the beam is scattered, which can cause optical alignment problems. To circumvent this problem we employ a "double-pass" setup, as shown in Figure 3.13. Angle changes due to changes in δ are minimized by this retroreflecting setup.

The second feature is that the first-order beam vanishes when rf power is removed. By blocking or diverting the unshifted beam, usually by placing an iris or other aperture around the first-order beam, one creates an optical shutter. The turn-on and turn-off speed of an AOM is approximately that of the time the sound

waves take to traverse the crystal, making AOMs well suited for use as a fast optical shutter.

The drawback to AOMs is that the angle at which the first-order beam leaves the AOM changes as the temperature of the AOM crystal changes. While active the AOM crystal is heated by the rf power it dissipates. If the rf power to the AOM is turned off for a while in order to turn off a deflected beam, when the rf power is initially restored the first-order beam will be misaligned until the AOM crystal temperature stabilizes. The angular misalignment of the CO_2 laser AOM causes serious experimental problems, as detailed in Section 5.3.1. For visible beam AOMs, this effect is merely a nuisance. We avoid the problem by placing mechanical shutters before each set of AOMs we use. We can thus turn beams off quickly by removing the rf power to the AOM, close the mechanical shutter, and then turn the AOM rf power back on to keep the crystals warm without having them deflect any light and thus sending near-resonant light into the trapping region. Before the AOMs are to begin deflecting light again we once more turn off the rf power, open the mechanical shutters, then turn the rf power back on.

AOMs are used to create the many different frequencies required for the slower and the MOT. Figure 3.14 shows the optical setup used to create the requisite frequencies. There are two double-pass AOM arms, one for generating the MOT frequency, the other for the repumper frequency. In three places there is a $\lambda/2$ waveplate before a cube polarizing beam splitter (PBS). This setup allows the ratio of power transmitted by the PBS to the power it reflects to be varied by rotating the $\lambda/2$ waveplate. This changes the power in the two linear polarizations. For example, the $\lambda/2$ waveplate before the cube PBS in the repumper arm is adjusted to give a $3:1$ ratio of MOT beam to repumper beam power. Mechanical shutters are placed

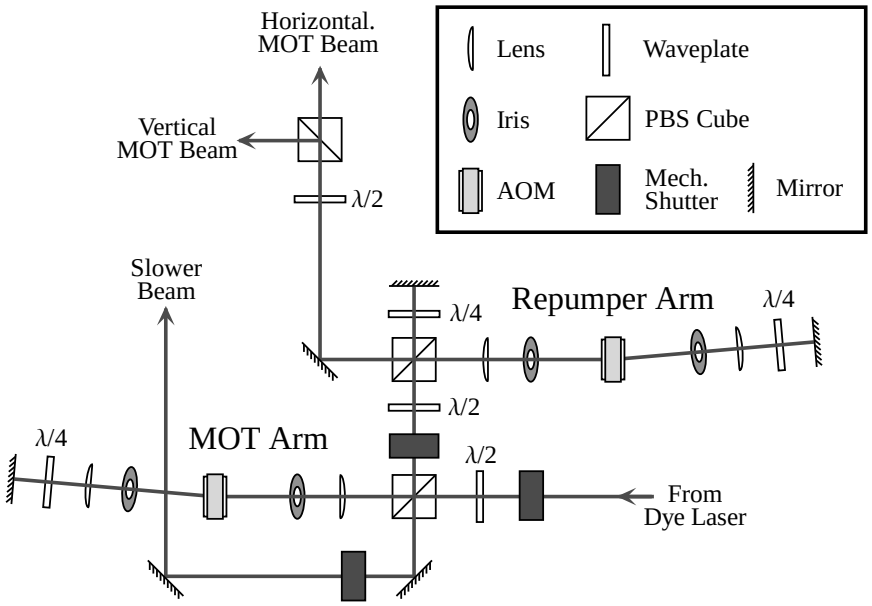

Figure 3.14: The optical setup used to create the slower and MOT beams.

in the slower beam, the MOT/repumper beams, and before the entire MOT and slower optical setup. Even when nominally off, the AOMs deflect a little bit of light; these shutters serve to block that small amount of leakage light. Without them, enough near-resonant laser light is scattered into the vacuum system to heat the atoms in the CO_2 laser trap. In addition, the shutters allow us to keep the AOM crystals warm, as explained above.

The MOT is formed from six counter-propagating laser beams, two along each orthogonal axis. Tradition calls for the use of three beams which are then retroreflected with opposite polarization to form the six beams. We use two beams, one vertical with respect to the table, the other horizontal, as will be explained below. Doing so increases the intensity in all beams, which in turn increases the number of atoms trapped in the MOT as compared to the traditional three-beam setup. The combined MOT and repumper beams are divided in two, so that a mixture of MOT and repumper beams are present in both vertical and horizontal beams. The

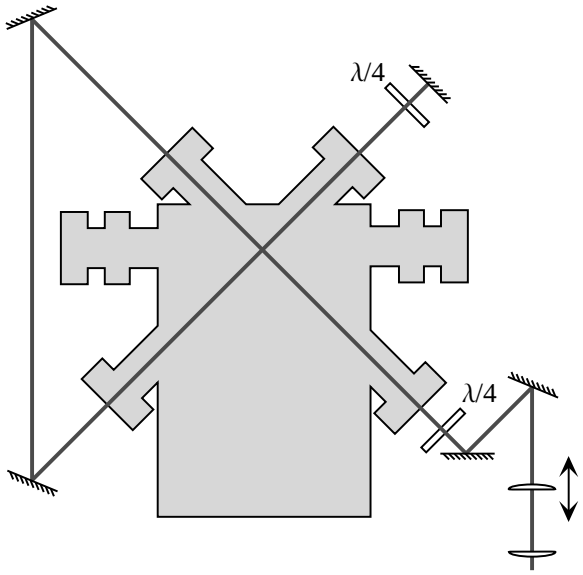

Figure 3.15: The optical setup of the MOT beams. Only the beam which is horizontal to the table is shown. The telescope's second lens can be moved to adjust the telescope's collimation.

beams pass through two lenses, which act as an expanding telescope, then through a $\lambda/4$ plate, which produces the required circularly-polarized light. The light then enters the vacuum system. The vertical beam travels through the vacuum system from top to bottom, while the horizontal beam threads through the system in an X pattern, as shown in Figure 3.15. After the beams exit the vacuum system, they pass through another $\lambda/4$ plate before being retroreflected back through the system.

Two refinements to the above system help increase the MOT's trapping efficiency. First, the horizontal beam must be deflected by several mirrors while it is circularly polarized. The standard mirrors used in the experiment are dielectric ones, which alter the ellipticity of circularly-polarized light. To minimize this effect, the mirrors which deflect the horizontal beam are front-surface silvered mirrors, which minimize the circular polarization's distortion. Second, the mirrors, vacuum viewports, and $\lambda/4$ plates do not transmit all of the incident beam's power,

resulting in retroreflected beams which have less power than their counterparts. To compensate for this effect, the vertical and horizontal beams are made to be slightly converging, giving a more constant intensity by decreasing beam size as their power decreases. One of the lenses of the expanding telescope is mounted on a translation stage so that the beam convergence can be set experimentally.

3.4.6 MOT Loading Procedure

During initial loading, the MOT beam is detuned by approximately six linewidths (6Γ) to the red of the $|F = {}^3\!/_2\rangle \rightarrow |F' = {}^5\!/_2\rangle$ transition, while the repumper beam is detuned by around 2Γ. (For ^{6}Li, $\Gamma/2\pi = 5.9\,\mathrm{MHz}$.) Both of these frequencies are set experimentally to produce the greatest number of trapped atoms. The detuning of 6Γ does not produce the coldest atoms in the MOT, though; it merely serves to trap more high-velocity atoms than if the detuning were less, as the MOT beams are blue-shifted by the velocity of such atoms. According to Doppler cooling theory (Section 3.4.4), the lowest temperature occurs when the beams are detuned by $\Gamma/2$. Therefore, after five seconds[5] of loading with the high-intensity 6Γ beams, the MOT beams' frequency is changed to $\Gamma/2$ and the repumper beams' frequency is changed to be exactly resonant. Simultaneously the intensity of both sets of beams are lowered, as less power is required when the beams are nearly resonant than when they are significantly detuned. This cooling phase produces atoms with a Doppler-limited temperature of $\sim 150\,\mu\mathrm{K}$ at a density of $10^{11}/\mathrm{cm}^3$. The cooling phase lasts for 20 ms, after which the repumper beams are turned off and the MOT beams tuned exactly to resonance and their intensity lowered further. With the repumper

[5] In general, five seconds of MOT loading is sufficient to produce the maximum number of atoms in the CO_2 laser trap, though on occasion we let the MOT load for ten seconds if the dye laser power has decreased over the course of the experiment.

beams off, the MOT beams optically pump the atoms into the two $|F = 1/2\rangle$ ground states, which are the ones we wish to confine in the CO_2 laser trap. The optical pumping phase lasts for $100\,\mu$s, after which the MOT beams are extinguished, and the shutters for the MOT/repumper beams and the slower beam are closed.

3.5 CO_2 Laser Trapping

Once the MOT has confined the atoms, they are ready to be loaded into the CO_2 laser trap. The CO_2 laser will change the ^{6}Li transition frequency through light shifts, but for moderate CO_2 laser intensities, this shift is small compared to the detuning of the MOT beams. Because of this, the CO_2 laser trap can be loaded continuously from the MOT by spatially overlapping the two. In this section I will discuss the optical setup required to route the CO_2 laser beam from the laser to the vacuum system so that it intersects the MOT. The greater the CO_2 laser's power, the more atoms it traps; to significantly boost the number of atoms trapped in the CO_2 laser beam, we retroreflect the beam so that it passes through the vacuum system twice. I will also explain the setup required to prevent the retroreflected beam from reaching the laser and causing feedback. Finally, I will explain how the CO_2 laser beam is aligned relative to the MOT, a task made much harder by the beam's invisibility and its lack of effect on the MOT.

3.5.1 Optical Setup

In order to cool atoms in the CO_2 laser trap, it is necessary to reduce the intensity of the CO_2 laser, as will be explained in Chapter 5. We control the intensity of the CO_2 laser with a CO_2 laser AOM. The CO_2 laser AOM diffracts a portion of the

incident beam into multiple orders. By varying the radio frequency (rf) power that is sent to the AOM crystal, the amount of CO_2 laser power in the first order can be changed; if we then use the first-order beam as our trapping beam, we can vary the intensity of the CO_2 laser.

The CO_2 laser AOM is much larger than the AOMs used for the 671 nm beams. It requires 50 W of rf power, which must be dissipated after it has passed through the crystal. This in turn requires that the AOM be water cooled to prevent the crystal from overheating and cracking. The CO_2 laser AOM is cooled by the closed-loop water system described in Section 3.3.

The actual AOM is a model AGM-4010BG1 from IntraAction Corporation. Its crystal is about 1.5 cm tall and 4.5 cm wide along the direction of laser propagation. The driver which produces the rf power for the crystal is a model GE-4050, also from IntraAction. The GE-4050 produces rf power at a fixed frequency of 40 MHz, and can be amplitude modulated to produce from 0-50 W of power, resulting in a Bragg diffraction angle of 38.5 mrad.

The depth of the CO_2 laser trap depends on beam intensity at the focused beam's waist. To achieve reasonable trap depths, it is desirable to focus the beam as much as possible. The 1/e electric field width w of a Gaussian laser beam focused in vacuum by a thin lens of focal length f is related to the width of the beam w_0 prior to the lens [77]:

$$w = \frac{f/z_0}{\sqrt{1 + (f/z_0)^2}} w_0, \tag{3.39}$$

where

$$z_0 \equiv \frac{\pi w_0^2}{\lambda}. \tag{3.40}$$

From this we see that, for small values of f/z_0, $w \propto f/w_0$. To decrease the beam's

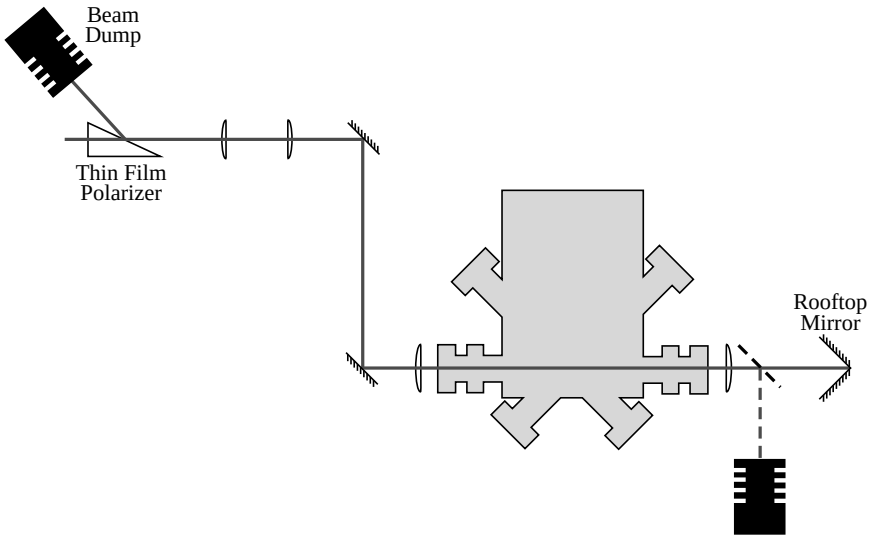

Figure 3.16: The optical setup for the CO_2 laser trap.

radius at its focus, thus increasing its intensity, one can either decrease f or increase w_0. The focusing lens's minimum focal length is limited to ∼19 cm; any smaller and the lens would have to be placed inside the vacuum system. To decrease w, then, it is necessary to use as large an w_0 as possible.

Towards that end, the 6 mm beam from the DEOS CO_2 laser is expanded by a ×10 telescope consisting of two plano-convex lenses with focal lengths of 1.2 in. and 11.25 in. The lenses are made of crystalline ZnSe and are anti-reflection coated for 10.6 μm light. The expanded beam is then focused into the vacuum system by an aspheric 19.5 cm lens, producing a spot with a $1/e^2$ intensity radius of 47 μm. An aspheric lens is used to produce the smallest spot size possible. Spherical aberration broadens the focal spot produced by a standard lens, and the effects of spherical aberration increase as the ratio of focal length to incident laser beam radius decreases. An aspheric lens is designed to eliminate spherical abberation and produce the diffraction-limited spot size.

To further increase CO_2 laser trap intensity, the beam that emerges from the

vacuum system is retroreflected and refocused into the trap region. Since the beam then retraces its original path, it must be prevented from reentering the laser and causing instabilities in the laser mode and potential damage to laser components. This is accomplished by use of a thin film polarizer, which transmits light of one polarization but diverts light of the opposite polarization. The beam exiting the vacuum system is recollimated by a second 19.5 cm aspheric lens. A rooftop mirror—two mirrors placed at right angles to each other—both reflects the beam and rotates its polarization by 90°. The mirror assembly is then located so that the two mirrors are at 45° relative to the incoming polarization. A mirror, indicated in Figure 3.16 by a dashed line, can be slid in front of the rooftop mirror to deflect the beam to a beam dump, preventing its retroreflection.

The retroreflected beam is refocused into the trap region by the second aspheric lens. It then is recollimated by the first aspheric lens and proceeds back through the optical setup until it reaches the thin film polarizer and is diverted into a beam dump.

3.5.2 Optical Alignment

Before the CO_2 laser trap can confine atoms, it must be centered in the MOT to maximize the number of trapped atoms. In addition, the retroreflected beam must be overlapped with the forward-propagating beam. These two tasks are difficult because of the invisibility of the infrared beam, which can only be located using either fluorescent plates whose fluorescence is quenched by the infrared beam's heat, or sheets of liquid crystal plastic which change color when heated. In addition, the infrared beam has no visible effect on the MOT.

Standard Alignment Procedure

To make the task of alignment easier, we overlap a visible 671 nm red beam with the CO_2 laser beam and then align the optics using the red beam. The beam sent to the locking region is deflected for this purpose. This has the advantage of allowing us to align the optics using a visible, low-power beam which, since it is resonant with the ^{6}Li transition, visibly affects the MOT.

The initial alignment step is to remove the $\times 10$ telescope and the two aspheric lenses that focus the CO_2 laser beam into the vacuum system, and to lower the mirror that blocks the rooftop mirror. The two mirrors before the vacuum system are placed using a very low-power CO_2 laser beam; the two mirrors are then used to center the beam in the two ZnSe viewports of the vacuum system. The mirror before the rooftop mirror deflects the infrared beam onto the lab wall. Once this alignment is complete, "burn marks" are made to determine the beam's actual position. An index card is placed on the wall where the infrared beam is located, then exposed to the beam's full power for no longer than it takes someone to move a beam block out of and back into the beam. The result is a small scorch mark on the card. This process is repeated much closer to the laser. The two burn marks give the beam's position.

The visible beam is then diverted from the locking region and made to overlap the path of the CO_2 laser beam by placing it so that it passes through the center of the two burn marks. This is done by placing the visible beam so that it hits the burn mark on the first card, then replacing that card with an iris, which can be opened to permit the red beam to continue on to the second burn mark. The visible beam can then be steered to pass through the iris and hit the center of the burn mark on the wall. This procedure ensures that the visible beam follows the

path of the infrared beam closely.

Before the beam is diverted, the system is set up so that a MOT is formed. The servo system which locks the laser, described in Section 3.4.5, is disengaged and the locking region beam diverted. The dye laser's frequency drift is slow enough that the MOT will persist for several minutes, and careful hand-tuning of the dye laser frequency will ensure that the MOT remains for up to an hour.

Once the visible beam is aligned using the burn marks, it is steered via the final mirror before the vacuum system until the beam hits the MOT. Since the visible beam is resonant with the trapped atoms, the beam pushes the atoms in the MOT through radiation pressure. The effect is clearly visible, as if a tiny finger were poking into the MOT and pushing the atoms out the other side. In this manner, the beam can be moved until the pushing effect, and thus the visible beam, is located in the MOT's center.

Once that is done, an iris is placed in the visible beam on the far side of the vacuum system. The first aspheric lens on the laser side of the vacuum system is placed so that the visible beam stays centered on the iris. Then another iris is placed in the beam before the aspheric lens. In placing the telescope's two lenses, the earlier iris is used to ensure proper placement of the telescope. The index of refraction for ZnSe is different for the red beam than for the infrared beam, so the visible beam after the ZnSe lenses of the telescope will not be collimated. The iris on the far side of the vacuum system is too far away from the telescope to be of much use in this situation, hence the need for a closer iris.

Finally the second aspheric lens is placed and the rooftop mirror located so as to properly retroreflect the visible beam. Prior to this, the rooftop mirror is adjusted so that its mirrors are at 90° to each other. A large HeNe laser beam is directed

onto the rooftop mirror at the point where its two mirrors meet, with half of the beam on each mirror. The retroreflected beam will spread into two distinct sections if the angle between the two mirrors is not 90°. The angle of the rooftop mirror is adjusted until the retroreflected beam is not divided. The rooftop mirror can then be placed. At that point the visible beam and the two irises are removed from the CO_2 laser path.

For final alignment of the CO_2 laser, the number of atoms trapped in the CO_2 laser trap is measured with an on-resonant probe beam and a calibrated photomultiplier tube (PMT), as explained in Section 4.1. The signal from the PMT is proportional to the number of atoms in the trap. The final position of the CO_2 laser beam is found by adjusting the beam location to maximize the PMT signal.

Alignment Using a Split Image Technique

At times, no matter how carefully the above procedure is followed, no atoms are confined in the CO_2 laser trap. Most often this is due to axial misalignment of the aspheric lens which first focuses the CO_2 laser beam into the vacuum system. The 19.5 cm aspheric lens produces a focused beam whose Rayleigh length[6] is only 0.66 mm. Thus the aspheric lens must be positioned axially with sub-millimeter accuracy.

This can be done using a split-image technique, as shown in Figure 3.17. Light from the MOT is allowed to propagate through the aspheric lens along two paths. At the image plane, the images from the two paths should overlap exactly, producing a single unified image. The image distance is chosen so that the object distance from MOT to aspheric lens is correct for the CO_2 laser beam.

[6]The Rayleigh length is defined in Section 3.1.

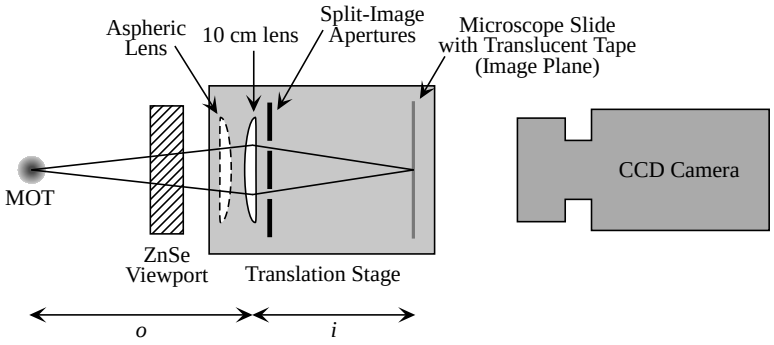

Figure 3.17: Split-image alignment technique for the first aspheric lens.

Since the MOT fluoresces at 671 nm, a 10 cm focal length plano-convex lens made of glass is used rather than the ZnSe aspheric lens. The glass lens is mounted on a translation stage along with a microscope slide, which serves as a screen, and an empty post holder for the aspheric lens. The desired object distance o for the 10 cm lens is calculated given the desired distance from the ZnSe aspheric lens to the MOT. From that object distance, the image distance i is calculated, and the microscope slide is placed a distance i from the 10 cm lens. These calculations must be made carefully, since sub-millimeter accuracy is required. The index of refraction of the quarter-inch-thick ZnSe viewport window must be taken into account, as its index of refraction will be different for the 671 nm light from the MOT than for the CO_2 laser beam. In addition, one must remember that o and i are measured from the principal points of the plano-convex lens and not either of its faces. The details of such a calculation are given in Appendix A.

Once the distances have been calculated and the microscope slide placed, a piece of translucent tape is affixed to the slide and a mask with two circular apertures is placed in front of the 10 cm lens. The tape serves to make the fluorescence visible on the microscope slide. The entire translation stage is then moved until the two separate images on the translucent tape become a single one. The light on the tape

is dim, so a CCD camera from Cohu, Inc. is used to view the fluorescence. After the images have been overlapped, the ZnSe aspheric lens may be placed in its holder and the 10 cm lens and microscope slide removed. In practice, this procedure places the aspheric lens with millimeter accuracy, close enough that final alignment may be done using the PMT alignment procedure described above.

Chapter 4

Characterizing the Optical Trap

Confining atoms in the CO_2 laser trap is only the first step. Once they are confined, we need to know how many atoms are trapped and what their density n and temperature T are. The number of trapped atoms can be determined by illuminating them with on-resonant light and measuring the resulting fluorescence. The density can be determined by performing absorption imaging on the atoms, in which near-resonant light passes through the atoms and is then imaged onto a charge-coupled device (CCD) array. The atoms absorb some of the light and scatter it away from the camera, leaving a shadow in the beam where the atoms are. The reduction in light is proportional to the number of atoms along the beam path. If the size of the trap is known, this provides a measure of the density along the path of the beam, $\tilde{n} = \int n \cdot dz$. $\tilde{n}$ is known as the column density. From the column density the number of trapped atoms and their temperature can be determined.

Use of a CCD camera system requires careful timing to ensure that all events occur in the proper order and at the proper time. For example, timing accuracies of 100 μs or better are needed to synchronize the opening of a camera shutter with the atoms' illumination by a laser beam. Because some of our experiments occur over long periods of time, the timing accuracy must be maintained for hundreds of seconds. To meet these two requirements and to provide a method of timing flexible

enough to meet all of our needs, we developed a computer-controlled timing system, as well as related equipment that can multiplex the timing system's TTL signals.

This chapter will discuss both fluorescence measurements and absorption imaging. The relationship between the absorption image on the CCD camera and the column density of the trapped atoms will be derived. Following that, I will discuss the timing system's development, including the associated computer programs and hardware. After that, the physical setup of the camera system and the characteristics of our CCD camera will be discussed. The CCD camera records a magnified image of the trapped atoms; how that magnification is measured will be explained next. I will then explain how we determine the number of atoms and their temperature from the CCD camera image using time-of-flight imaging, in which the atoms are allowed to expand freely from the trap. In addition, the steps required to include the effect of Fermi statistics on the atomic distribution will be presented. Finally, determination of the number and temperature of the trapped atoms requires that we know the oscillation frequencies of our trap. How we measure them will be the last topic of this chapter.

4.1 Fluorescence Measurement

In fluorescence measurement, an intense beam of on-resonant light is applied to trapped atoms. The atoms begin absorbing and re-emitting photons from the beam. The amount of fluorescence is proportional to the number of atoms illuminated by the beam, and is measured by a photomultiplier tube (PMT).

The scattering rate for a two-level atom is

$$\Gamma_{sc} = \frac{\Gamma}{2} \frac{I/I_{sat}}{1 + I/I_{sat} + 4(\Delta/\Gamma)^2}. \tag{4.1}$$

PMT Voltage	Gain (A/W)
500	5.16
600	26.5
700	78.5
800	202
900	477
1000	922

Table 4.1: PMT Voltages and Gain

Δ is the detuning of the beam from resonance, Γ is the transition linewidth, I is the beam intensity, and I_{sat} is the saturation intensity. For an on-resonant beam, if $I \gg I_{sat}$ then at any given time half of the atomic population is in the excited state and the photon scattering rate becomes $\Gamma_{sc} = \Gamma/2$. The power of the light scattered by N atoms in this case is $P_{sc} = N\hbar\omega_0\Gamma/2$, where $\hbar\omega_0$ is the energy of a resonant photon. The light is scattered into a 4π solid angle, so the power into the PMT depends on the ratio of its solid angle $d\Omega$ (as limited by the viewport through which the light reaches the PMT) to the full 4π solid angle.[1]

PMTs produces a current that is proportional to the light incident upon it. The proportionality constant G, given in amps/watt, depends on how large a bias voltage is applied to the PMT. The larger the bias voltage, the larger G is and the more sensitive the PMT is to small amounts of light. Table 4.1 lists representative values of G for a given bias voltage applied to our model 1894 Hamamatsu PMT. If the current from the PMT passes through a resistive load R, it creates a voltage difference across that load. The voltage can then be measured by an oscilloscope.

[1]This is not entirely true; the atoms radiate in a dipole pattern, which has an angular dependence. However, our PMT is located at the so-called "magic angle" of 55°, the angle for which the $P_2(\cos\theta)$ term of the dipole radiation pattern is zero, removing the angular dependence.

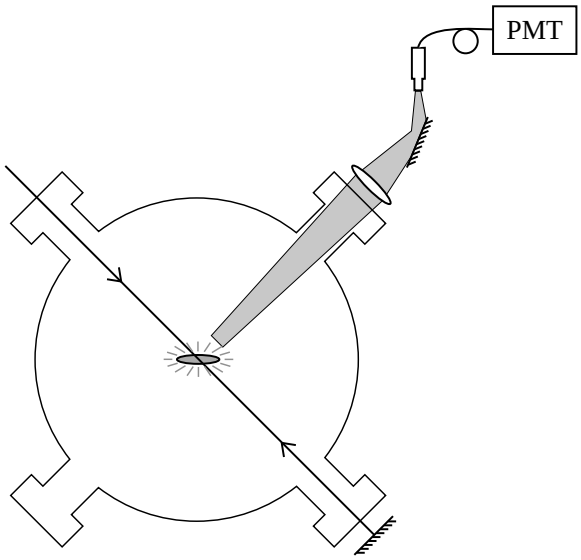

Figure 4.1: A side view of the system used to measure the fluorescence from trapped atoms. The probe beam's wavelength is 670 nm.

The measured voltage is

$$V = P_{sc}\frac{d\Omega}{4\pi}GR = N\hbar\omega_0\frac{\Gamma}{2}\frac{d\Omega}{4\pi}GR. \tag{4.2}$$

For the cycling transition in ^{6}Li, $I_{sat} = 2.55\,\mathrm{mW/cm^2}$ and $P_{sc}/N = 5.5\times10^{-12}\,\mathrm{W}$.

The physical system used to measure the fluorescence is as follows. A model 1894 Hamamatsu PMT is connected to one end of an optical fiber bundle. The other end of the bundle is positioned above a mirror which deflects fluorescent light from a viewport to the bundle. A 660-680 nm bandpass filter in the PMT housing blocks background light from sources other than the fluorescent atoms. An 8 cm achromat lens images the fluorescence onto the opening of the fiber bundle at a magnification of 1:1. The solid angle of the PMT is limited by the lens chuck which holds the achromat lens, and is $d\Omega/4\pi = 2.9\times10^{-3}$. To excite the cycling transition of ^{6}Li we use a circularly-polarized beam that is on resonance for the transition

from the $|F = 3/2\rangle$ ground state. As is the case in the MOT, atoms may decay to the lower $|F = 1/2\rangle$ ground state, requiring a repumper beam to return them to the $|F = 3/2\rangle$ state. The optical setup which generates these two beams will be discussed in Section 4.4.2.

To calibrate the gain G of the PMT, a 671 nm beam of around 200 mW of power is sent through three OD3 neutral density filters, then coupled into the fiber bundle and thence into the PMT. Prior to this, the absorption of each OD3 filter is measured by recording the power before and after the filter. The total absorption A of all three filters is then taken to be the product of their individual absorptions. Various voltages are applied to the PMT and its output both with (V_{sig}) and without (V_{bkg}) the laser beam present is measured on an oscilloscope with an input impedance R of 1 MΩ. The input power P is also recorded. The gain G in amps/watt for a given bias voltage is given by

$$G = \frac{V_{sig} - V_{bkg}}{(1 \times 10^6)\, PA}. \tag{4.3}$$

The lens, mirror, and fiber bundle are aligned by maximizing the fluorescence signal from the MOT. Since the position of the CO_2 laser trap is the same as that of the MOT, this also maximizes the signal from the CO_2 laser trap.

4.2 Absorption Imaging

When light interacts with atoms, photons are absorbed spontaneously and then re-emitted. The latter effect is the basis of fluorescence measurements; the former, of absorption imaging. If a laser beam passes through a cloud of atoms, they will cast a shadow in the beam due to photon absorption and re-emission in directions other than that of the beam propagation. The rate at which the intensity decreases

as the beam propagates is

$$\frac{dI}{dz} = -I\sigma n(x, y, z), \tag{4.4}$$

where σ is the cross section for an atom to scatter off of a photon, and is given by

$$\sigma = \frac{\sigma_0}{1 + \delta^2}. \tag{4.5}$$

$\delta \equiv (\omega - \omega_0)/(\Gamma/2)$ is the laser beam detuning in half linewidths and σ_0 is the on-resonance cross section (which, for atoms in the $|1\rangle$ and $|2\rangle$ states, is $\sigma_0 = \lambda^2/2\pi$, as will be shown in Section 4.4.4). Solving (4.4) by integrating both sides gives the intensity after the beam has passed through the atoms:

$$I = I_0 \exp\left(-\frac{\tilde{n}\sigma_0}{1 + \delta^2}\right). \tag{4.6}$$

I_0 is the incident intensity of the beam and $\tilde{n} \equiv \int n(x, y, z)\, dz$ is the column density of the sample. The light is thus reduced by a factor t, the transmission coefficient, where

$$t = e^{-\tilde{D}} = \exp\left(-\frac{\tilde{n}\sigma_0}{1 + \delta^2}\right). \tag{4.7}$$

$\tilde{D}$ is the optical density. The absorption coefficient is equal to $1 - t$.

A CCD camera measures the number of photons that reach its CCD array and from that creates an image. To measure the absorption coefficient, three images must be taken: one with no laser light, one with laser light and no atoms, and one with both laser light and atoms present. Let C_{bkg}, C_{light}, and C_{atoms} represent these three images. The image which corresponds to the fraction of photons transmitted is then

$$C_{trans} = \frac{C_{atoms} - C_{bkg}}{C_{light} - C_{bkg}} \tag{4.8}$$

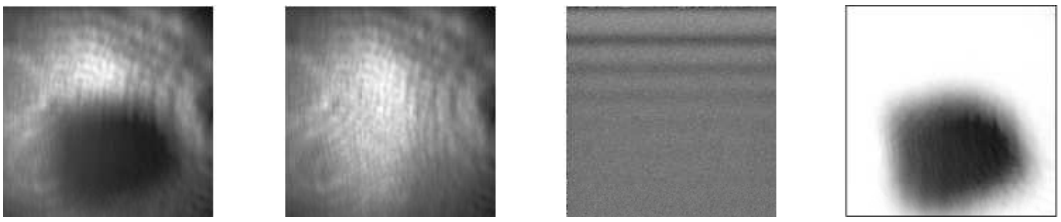

Figure 4.2: An example of the measurement of the absorption coefficient. Three images are recorded. The first is the image of the shadow cast by the atoms, the second is of the laser light, and the third is the background image with no light. From these three the fourth image, which is the fraction of photons transmitted, is calculated. In the fourth image, white areas correspond to 100% of photons transmitted and black to no photons transmitted.

and the image corresponding to the optical density $\tilde{D}$ is

$$C_{OD} = -\ln(C_{trans}). \tag{4.9}$$

The column density is directly related to the spatial profile of atoms in the CO_2 laser trap. Very cold atoms will be near the bottom of the trap potential, where it is approximately harmonic and takes the form

$$U(\mathbf{r}) = -U_0 + \frac{1}{2}M\omega_x^2 x^2 + \frac{1}{2}M\omega_y^2 y^2 + \frac{1}{2}M\omega_z^2 z^2. \tag{4.10}$$

ω_x, ω_y, and ω_z are the effective oscillation frequencies of the CO_2 laser trap. The single particle Hamiltonian in this case is $\mathcal{H}(\mathbf{r},\mathbf{p}) = p^2/2M + U(\mathbf{r})$. The (unnormalized) phase space distribution $W_0(\mathbf{r},\mathbf{p})$ of the atoms will be

$$\begin{aligned} W_0(\mathbf{r},\mathbf{p}) &= \exp\left[-\frac{\mathcal{H}(\mathbf{r},\mathbf{p})}{k_B T}\right] \\ &= \exp\left[-\frac{p^2}{2Mk_BT} - \frac{1}{2}\frac{M}{k_BT}\left(\omega_x^2 x^2 + \omega_y^2 y^2 + \omega_z^2 z^2\right)\right]. \end{aligned} \tag{4.11}$$

The spatial distribution is given by integrating W_0 over all momenta $\mathbf{p}$, resulting in

$$n(\mathbf{x}) = \frac{N_0}{\pi^{3/2} a_x a_y a_z} \exp\left[-\frac{x^2}{a_x^2} - \frac{y^2}{a_y^2} - \frac{z^2}{a_z^2}\right], \tag{4.12}$$

where a_x, b_x, and c_x are the Gaussian widths of the distribution and are given by *e.g.*

$$a_x = \sqrt{\frac{2k_B T}{M\omega_x^2}}. \tag{4.13}$$

The normalization constant has been chosen so that $\int n(\mathbf{x}) dx = N_0$, the total number of trapped atoms. The column density is[2]

$$\tilde{n}(x,y) = \int n(\mathbf{x})\, dz = \frac{N_0}{\pi a_x a_y} \exp\left[-\frac{x^2}{a_x^2} - \frac{y^2}{a_y^2}\right]. \tag{4.14}$$

From (4.14) and (4.7) we see that the image C_{OD} will be

$$C_{OD} = \frac{N_0}{\pi a_x a_y} \frac{\sigma_0}{1+\delta^2} \exp\left[-\frac{x^2}{a_x^2} - \frac{y^2}{a_y^2}\right]. \tag{4.15}$$

If the trap parameters ω_x and ω_y are known, then the number of atoms in the trap and their temperature can be determined by fitting a Gaussian to C_{OD}.

A further simplification is possible through camera binning along one axis, in which the pixel values in each column or row are added together, collapsing the two-dimensional image into a line. Binning C_{OD} along the vertical $\hat{\mathbf{y}}$ axis is equivalent to integrating (4.15) along y and dividing by the CCD camera pixel size x_p:

$$C_{1D} = \frac{N_0}{\sqrt{\pi} a_x x_p} \frac{\sigma_0}{1+\delta^2} e^{-x^2/a_x^2}. \tag{4.16}$$

[2]This assumes that the imaging axis lies along the $\hat{\mathbf{z}}$ axis of the trap, making the integration of (4.12) tractable. In our system, the camera axis is at an angle to the trap, so that the only co-linear axes are the camera and trap $\hat{\mathbf{x}}$ axes. However, we bin our pictures in the vertical direction, so that the only axis to be analyzed is the co-linear $\hat{\mathbf{x}}$ axis and so that no changes to (4.16) are required.

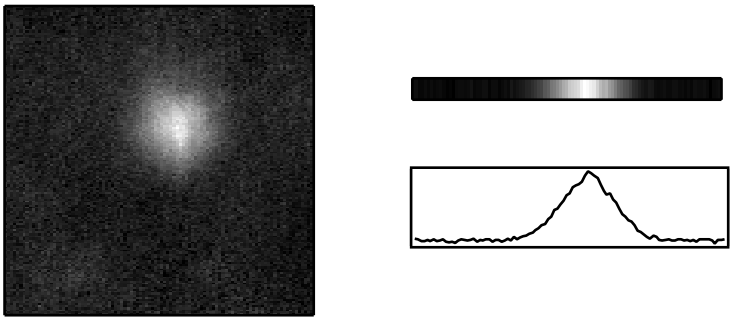

Figure 4.3: A two-dimensional image binned along its vertical axis becomes a line. The graph below the line is a plot of the line image.

Division by the pixel size is required because binning is a discrete summation, not a true integration, with a step size of x_p. No important information is lost in this operation: both the atom number and the temperature can still be determined from this one-dimensional Gaussian.

4.3 Timing System

The timing system consists of two components. The first is a computer-based timing control system that produces TTL signals at specified times. The second is a multiplexer system that allows multiple input analog signals to be routed to one device. Selection of the input signals is controlled by electronic switches, which are in turn controlled by TTL signals.

4.3.1 Computer Control

Our experiments take place over hundreds of seconds. During that time, various pieces of equipment must be controlled with an accuracy of $100\,\mu$s or less. In early experiments we used several DG535 pulse generators from Stanford Research

Systems to control timing, as they have the necessary accuracy and can have delays of 1000 s. This involved a lot of makeshift wiring, though, as each DG535 has only four TTL outputs, and those outputs can change state (from low to high or from high to low) once and only once when the DG535 is triggered. One DG535 served as the master pulse generator: the clocks of all other DG535s were synchronized to that of the master DG535, and the other DG535s were triggered by the master. In order to change states more than once in a given trigger cycle, multiple DG535 outputs were combined, either through options internal to the DG535 or by externally connecting the outputs through diode boxes that isolated the DG535 outputs from each other. Creating a working timing scheme using this system was difficult, as was altering an existing scheme.

To avoid these problems, we built a computer-controlled timing system. The system has thirty-two TTL-logic channels. The state of these channels can be varied as many times as is necessary for a given timing sequence. Creation of a timing scheme using this system does not take long, and the details of a completed scheme can be easily varied. While this system's resolution of 100 μs cannot match the 5 ps resolution of a DG535, its resolution is sufficient for all but the most demanding applications. In the one case where a smaller time resolution has been necessary, we have used a DG535 triggered by the computer timing system. The timing system can set the DG535's delays by sending GPIB commands, thus localizing all timing control at the computer.

Full details of the timing system, including an explanation of the structure of timing files, are in Appendix B. Here I will merely give an overview of the most important details.

The heart of the timing system is a Dell Precision 420 computer with 768 MB

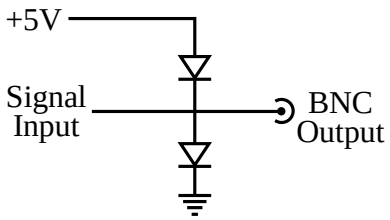

Figure 4.4: Two Schottky diodes of type 1N5711 are placed from +5 V to the BNC output signal line and from the signal line to ground. These diodes limit the ringing which occurs when the signal line changes state.

of Rambus RAM. Such a large amount of memory is necessary because the timing system software creates a large matrix of logic states for each channel at each time step. The TTL signals are created by a National Instruments PC-DIO-32HS board, which provides 32 parallel digital input/output (I/O) channels. The 32 channels are connected by a ribbon cable to a panel with 32 BNC connectors, so that the TTL signals can be routed with BNC cables. Each BNC output is attached to two Schottky diodes of type 1N5711, one from +5 V to the BNC output, the other from the BNC output to ground. They are oriented so that they begin conducting if the output line goes above +5 V or below 0 V, respectively. This limits fluctuations on the output line when it changes state.

Each timing sequence is defined by a text file that specifies the initial state of each channel and at what time steps the channel should change state. The timing file can contain variables, which in turn can be used in mathematical operations. Using these variables, one can have events occur at a time relative to prior events, rather than at an absolute time. For example, one can ensure that a probe beam will turn on 10 ms after a camera shutter is opened, regardless of when the shutter is actually opened.

The timing files are fed into a preprocessor written in the computer language Perl. The preprocessor evaluates all of the variables and mathematical operations,

MSB \ LSB	0	1
1	3	4
0	1	2

Table 4.2: Multiplexer Logic States

then produces a new file based on the original, but containing only absolute times rather than relative, variable-based ones. The new timing file is given to a LabView program that creates a channel state matrix. The matrix has one row for each channel and one column for each time step in the timing sequence. In this manner the state of the timing system at any time is defined. The LabView program can then begin the timing sequence. As part of this process the program can also send GPIB commands to laboratory equipment prior to the beginning of the timing sequence.

4.3.2 Multiplexer System

At several points in the experiment it is necessary to send multiple analog voltages to one device. For example, the number of atoms loaded in the MOT is maximized by detuning the MOT beams roughly 6Γ below resonance, but their temperature is minimized by detuning the beams by $\Gamma/2$, as explained in Section 3.4.6. The frequency of the MOT beams is set by a double-passed AOM. This frequency can be adjusted by changing the tuning voltage sent to the AOM driver. We would like to load the MOT at a detuning of 6Γ, then briefly change the tuning voltage so that the frequency changes to $\Gamma/2$, cooling the atoms to near the Doppler limit.

To do this, we use a multiplexer system. The multiplexer system has a number of electronic multiplexer chips that act as two-way and four-way switches. They take two (or four) inputs and select among them according to TTL logic. The four-way

switches are controlled by two TTL lines, the least-significant bit (LSB) and most-significant bit (MSB). Table 4.2 lists which input will be selected for a given MSB and LSB value: 0 represents 0 V and 1 represents 5 V, while the numbers inside the table are the number of the selected input. The four-way multiplexer chips used are Analog Devices ADG409BN, while the two-way multiplexers used are Analog Devices ADG436BN. Also built into the multiplexer system are 16 adjustable power supplies. These power supplies are used to provide voltages to the various AOMs in our system.

4.4 CCD Camera System

4.4.1 CCD Camera

The camera we use is a model DV434-BV from Andor Technology. Its CCD array, an EEV CCD47-10, has 1024×1024 pixels, with a pixel width of $13\,\mu$m. It is back-illuminated, and has a quantum efficiency of around 90% at 670 nm. All CCD cameras suffer from dark current, in which the CCD pixels accumulate charge due to thermal activity in their quantum wells. To minimize dark current in the camera, the DV434-BV includes a thermoelectric cooler that cools the CCD array to -40 °C during experiments.

The camera is controlled by a model CCI-010 computer card, also from Andor. The card is installed in the same computer used in the timing system. Included with the camera is the Andor-MCD software for Windows, which handles data acquisition from the CCD camera. The software also performs image processing, allowing us to record the absorption image of the probe beam in real time.

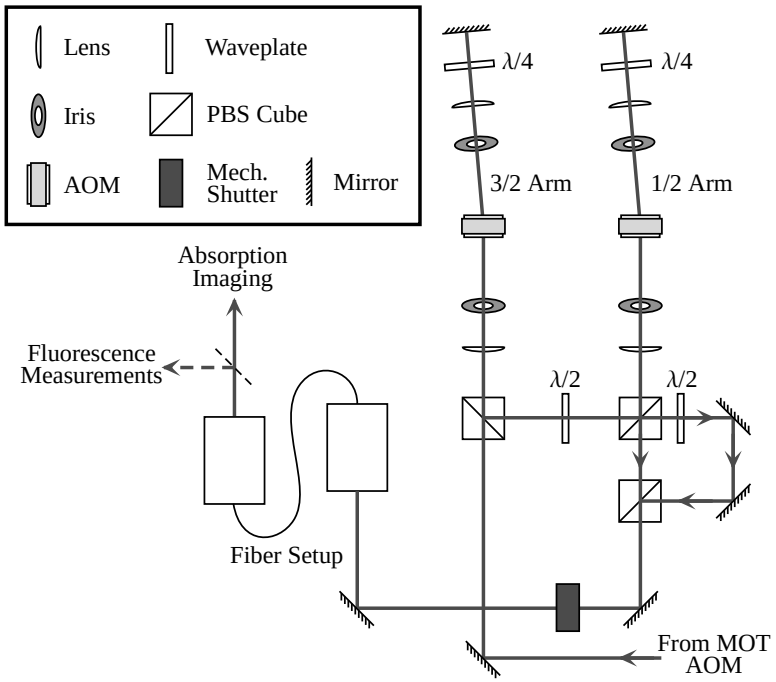

Figure 4.5: The optical setup used to create the probe beams for both fluorescence measurement and absorption imaging.

4.4.2 Optical Probe Setup

The optical probe beams for both fluorescence and absorption imaging are generated from the unshifted zero-order beam of the first MOT AOM in the MOT arm (shown in Figure 3.14). For either type of imaging, beams that are resonant with transitions from both the $|F = 1/2\rangle$ and $|F = 3/2\rangle$ ground states are required. Figure 4.5 shows the AOM setup used to generate these beams.

Imaging is easier if the camera beam's alignment does not vary during the course of an experiment. However, the direction of the dye laser beam changes as the laser mirrors are adjusted to produce the greatest amount of output power. To minimize these variations the probe beams are coupled into a short fiber. The output of the fiber gives a fixed reference point for the optical beams. Variations in input beam direction change output beam intensity but not direction. In addition, the fiber

acts as a spatial filter, ensuring that the two beams created by the two AOM arms are smooth and exactly overlapped.

After the fiber, the probe beams can be sent in either of two directions, selected by a flip-up mirror. For fluorescence measurements, the mirror after the fiber is flipped up to deflect the probe beams; for absorption imaging, the mirror is flipped down, allowing the probe beams to continue undeflected.

Fluorescence Measurement Setup

The probe beams for fluorescence measurement are sent into the chamber as shown in Figure 4.1. Two mirrors before the chamber are on translation stages, allowing the beam to be moved without altering the angle at which it enters the chamber. A mirror on the other side of the chamber retroreflects the probe beams. Doing so balances the radiation pressure force the atoms experience. Without this mirror, the atoms in the trap would be shoved by the probe beams, potentially moving far enough that their fluorescence would no longer be collected by the PMT fiber.

Absorption Imaging Setup

The atoms being imaged in absorption imaging are in the $|F = 1/2\rangle$ ground state; the $|F = 3/2\rangle$ state is empty. For this reason, the beam resonant with transitions from the $|1/2\rangle$ ground state is used as the sole imaging beam, while the beam resonant with transitions from the $|3/2\rangle$ state is diverted for use as a repumper without it being imaged onto the CCD camera. The two beams are split by a cube PBS shortly after the fiber. The cube PBS is not a perfect polarizing beam splitter, so some $|3/2\rangle$ light is not diverted and is instead imaged onto the camera. Measurements show that less than 1% of the light reaching the camera is $|3/2\rangle$ light, which can thus

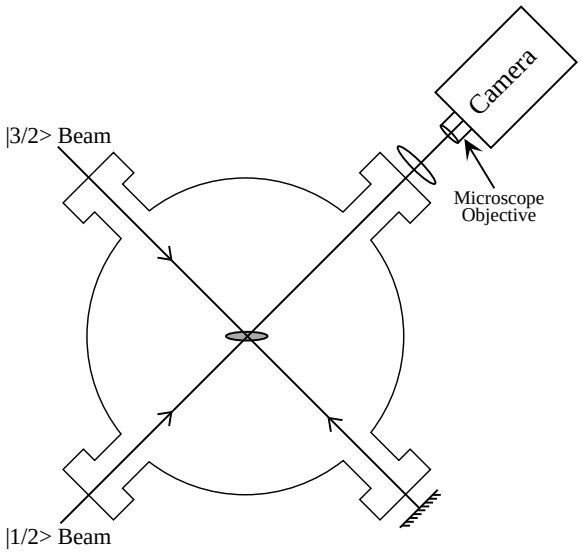

Figure 4.6: A side view of the system used in absorption imaging. The $|1/2\rangle$ beam passes through the trapped atoms, then is imaged by an achromat lens and a microscope objective onto the CCD array of the camera. The $|3/2\rangle$ beam enters through a separate set of viewports and, like the probe beams for fluorescence measurement, is retroreflected.

be considered negligible.

In absorption imaging, it is useful to detune the $|1/2\rangle$ imaging beam from resonance, so that the optical density does not become too large for very dense samples. For that reason we pass the $|1/2\rangle$ beam through two double-passed AOMs working in opposition, so that one increases the beam frequency while the other decreases it once again. By adjusting the frequency shift of one or the other of these opposition AOMs, the beam frequency can be shifted by small amounts. In addition, because this setup utilizes double-passed AOMs, variations in the beam's direction as its frequency is changed are minimized.

After the two AOMs, the $|1/2\rangle$ beam is expanded by a $\times 2$ telescope, making its intensity profile more uniform across the trap. Neutral density filters can be placed after the telescope to reduce the intensity of the $|1/2\rangle$ beam. After the telescope and

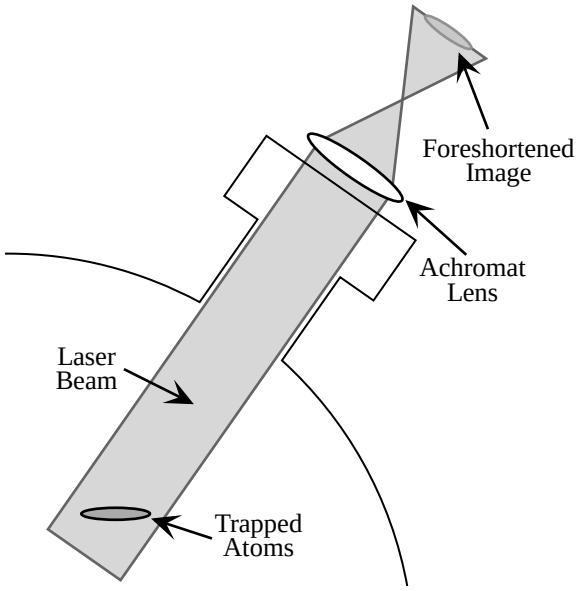

Figure 4.7: A side view of the camera beam setup. The camera beam travels through the atomic cloud at an angle of 55° with respect to the long axis of the cigar-shaped trap. This produces a foreshortened image on the CCD camera.

neutral density filters, the intensity of the camera beam is equal to $0.25\,\mathrm{W/cm^2}$, or $0.1I_{sat}$. The beam then enters the vacuum system through a viewport, illuminates the trapped atoms for $10\,\mu$s, and is imaged onto the CCD camera by an 8 cm achromat lens and a microscope objective. The camera image is then taken through the same viewport as that from which the PMT collects its light. A mirror on a detachable magnetic base, shown in Figure 4.1, can be placed after the viewport or removed as necessary. When in place it diverts light from the viewport to the PMT fiber for fluorescence measurement; when removed, light from the viewport reaches the CCD camera.

The camera beam and camera are rotated at an angle of 55° with respect to the long axis of the cigar-shaped CO_2 laser trap, producing an image which is foreshortened along the camera's vertical axis. Despite this, no changes are necessary to (4.16) if the two-dimensional image C_{OD} is binned along the foreshortened axis.

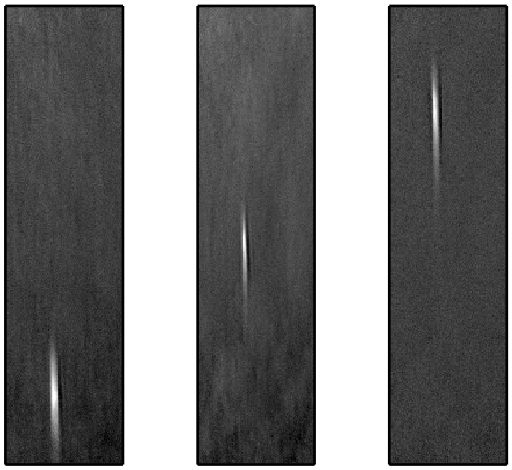

Figure 4.8: Pictures of how the CO_2 laser trap moves as its focusing lens is moved axially. This motion is used to calculate the camera magnification. In the left and right pictures, the trap lens has been displaced by an amount equal to $\pm 1.25\,\mathrm{mm}$.

The one-dimensional Gaussian distribution along the non-foreshortened axis does not change.

4.4.3 Camera Magnification

The 8 cm achromat lens that images the trap onto the camera is nearly 16.5 cm away from the trap, over twice its focal length. Because of this, the image it produces is demagnified. In turn, that demagnified image is magnified by a microscope objective in front of the CCD camera. The system's exact magnification can be determined by moving the trap a known amount and measuring the resulting motion of the trap's image. The lens which focuses the CO_2 laser beam to create the trap is mounted on a translation stage. Moving the lens axially by a distance Δ moves the location of the center of the trap by the same distance. Since the camera axis is 55° from that of the CO_2 laser trap, the trap's image will move a distance $M\Delta\cos 55°$, where

M is the imaging system's magnification. By moving the lens by several different values of Δ and taking images of the trap at each point, the magnification can be determined. Using $\Delta = \pm 1.25\,\mathrm{mm}$ we determined that the magnification of our system is $M = 3.9$.

4.4.4 Determining Atomic Number and Temperature

After an image is obtained from the CCD camera, it is processed according to (4.8) and (4.9)[3]. The image is then binned along its foreshortened axis. To find the number of atoms and their temperature, the one-dimensional distribution C_{1D} is fit to a Gaussian, and the resulting fit substituted into (4.16), giving

$$Ae^{-x^2/(wx_p)^2} = \frac{N_0}{\sqrt{\pi}a_x x_p}\frac{\sigma_0}{1+\delta^2}\,e^{-x^2/a_x^2}. \tag{4.17}$$

The width of the Gaussian fit w is measured in units of the CCD camera pixel size x_p. A comparison of the two sides of the equation show that

$$wx_p = a_x = \sqrt{\frac{2k_BT}{M\omega_x^2}} \tag{4.18}$$

and

$$\begin{aligned} A &= \frac{N_0}{\sqrt{\pi}a_x x_p}\frac{\sigma_0}{1+\delta^2} \\ &= \frac{N_0}{\sqrt{\pi}wx_p^2}\frac{\sigma_0}{1+\delta^2}, \end{aligned} \tag{4.19}$$

[3]In actuality, the Andor camera's software uses a variation on (4.8) which produces an image corresponding to the fraction of photons absorbed rather than transmitted. The only change required in (4.9) is the replacement of $-\ln(C_{trans})$ by $-\ln(1-C_{absorb})$.

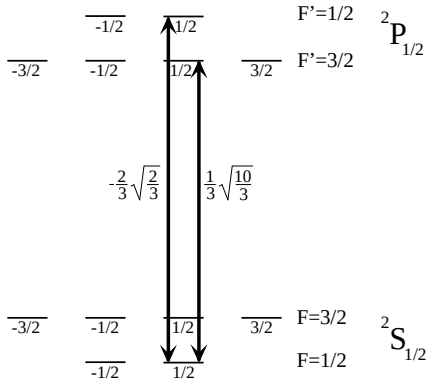

Figure 4.9: Half of the $^2S_{1/2} \rightarrow {}^2P_{1/2}$ transitions driven by the linear light of the camera beam. The small numbers under the levels are the m_F values. The $|F, m_F\rangle = |1/2, 1/2\rangle \rightarrow |3/2, 1/2\rangle$ and $|1/2, 1/2\rangle \rightarrow |1/2, 1/2\rangle$ transitions and their Clebsch-Gordan coefficients are shown.

so that

$$N_0 = \frac{A}{\sigma_0}\sqrt{\pi}\omega x_p^2(1+\delta^2). \tag{4.20}$$

All that remains is to find the resonant cross section σ_0 for the ^{6}Li atoms. Were ^{6}Li a true two-level atom, or if the camera beam were driving the cycling transition of ^{6}Li so that only two states were involved in the process, the resonant cross section would be $\sigma_0 = 3\lambda^2/2\pi$. Neither condition is true. The trapped atoms are in the $|F, m_F\rangle = |1/2, 1/2\rangle$ and $|1/2, -1/2\rangle$ states. The camera beam's linear light incoherently drives two transitions for the atoms in each state. Because the process is incoherent, the resonant cross section is modified from its two-level value by the sum of the squares of the Clebsch-Gordan (CG) coefficients for the possible transitions.

Figure 4.9 shows the two $^2S_{1/2} \rightarrow {}^2P_{1/2}$ transitions from the $|m_F = 1/2\rangle$ state that are driven by the camera beam, along with the associated CG coefficients. The two transitions from the $|m_F = -1/2\rangle$ state will be the mirror image of those from the $|m_F = 1/2\rangle$ state, and by symmetry their CG coefficients will be the same

barring possible changes in sign. Since the CG coefficients are squared in calculating σ_0, these possible minus signs can be ignored, and σ_0 will be the same for atoms in either state. The resulting value of σ_0 is

$$\sigma_0 = \frac{3\lambda^2}{2\pi} \sum_i (CG_i)^2 = \frac{\lambda^2}{\pi}. \tag{4.21}$$

Given this value of σ_0 and both (4.18) and (4.20), the trapped atoms' temperatures and number can be found:

$$T = \frac{M}{2k_B} \left(w x_p \omega_x\right)^2 \tag{4.22}$$

and

$$N_0 = A w \pi^{3/2} (1 + \delta^2) \left(\frac{x_p}{\lambda}\right)^2. \tag{4.23}$$

4.4.5 Time of Flight Measurements

It is often convenient to measure the atomic distribution after it has been released from the CO_2 laser trap, a process known as "time of flight imaging." When released, the atomic cloud expands. As will be shown, the increase in the distribution's width due to free flight serves to diminish the importance of the CO_2 laser trap size in determining the atoms' temperature.

To find the atomic spatial distribution at a time t after release assuming free expansion, it is necessary to consider the normalized one-dimensional version of the

phase space distribution from (4.11),

$$W_0(x, v_x) = \frac{N_0}{\pi a_x}\sqrt{\frac{M}{2k_BT}}\,\exp\left[-\frac{Mv_x^2}{2k_BT} - \frac{x^2}{a_x^2}\right]$$
$$= \frac{N_0}{\pi a_x v_T}\,\exp\left[-\frac{v_x^2}{v_T^2} - \frac{x^2}{a_x^2}\right], \tag{4.24}$$

where $v_T^2 = 2k_BT/M$ is the atoms' thermal velocity. After the distribution has expanded for a time t, each atom will move from its original location of x_0 to a new location given by $x = x_0 + v_x t$. The phase space distribution in terms of the initial locations of the atoms, $x_0 = x - v_x t$, will be

$$W_0(x, v_x, t) = \frac{N_0}{\pi a_x v_T}\,\exp\left[-\frac{v_x^2}{v_T^2} - \frac{(x - v_x t)^2}{a_x^2}\right]. \tag{4.25}$$

The time-of-flight spatial distribution is then

$$n(x,t) = \int W_0(x, v_x, t)\, dv_x$$
$$= \frac{N_0}{\sqrt{\pi(a_x^2 + v_T^2 t^2)}}\,\exp\left(\frac{-x^2}{a_x^2 + v_T^2 t^2}\right). \tag{4.26}$$

The number of atoms as given by (4.23) is still valid in a time-of-flight measurement. The equation for temperature becomes

$$T = \frac{Mw^2 x_p^2}{2k_b}\frac{1}{(1/\omega_r^2 + t^2)}. \tag{4.27}$$

ω_r is the radial oscillation frequency of the CO_2 laser trap. It becomes less important as t increases, since t^2 begins to dominate the $1/\omega_r^2 + t^2$ term in (4.27), thus diminishing the effect of the size of the CO_2 laser trap on the measured temperature. The length of time the trap is allowed to expand is chosen so as to limit the

optical depth of the atomic cloud, and varies from 400 μs to 1.2 ms, though images of very hot atoms are sometimes taken at 100 μs. As will be shown in Section 4.5.2, ω_r for our trap is 6600 Hz, leading to values of $1/\omega_r = 24\,\mu$s. For a 100 μs time of flight, $1/\omega_r^2$ is less than 6% of t^2; for 400 μs, the percentage drops to less than 0.4%.

4.4.6 Effect of Fermi Statistics on Temperature Measurement

As the trapped atoms are cooled to lower and lower temperatures, Fermi statistics plays an increasingly important role. In this limit, the classical Gaussian distribution assumed in (4.11) is no longer valid. Instead, the Fermi distribution must be taken into account.

Given the numbers and temperatures of the trapped atoms in our experiments, the phase space density can be found using the semiclassical Thomas-Fermi approximation [78]. In this approximation each point in phase space is given a position $\mathbf{r}$ and a wavevector $\mathbf{k}$. The density of states is then $1/(2\pi)^3$, and the total phase space density is

$$W_0(\mathbf{r},\mathbf{k}) = \frac{1}{(2\pi)^3}\frac{1}{e^{\beta(\mathcal{H}(\mathbf{r},\hbar\mathbf{k})-\mu)}+1}. \tag{4.28}$$

$\mathcal{H}(\mathbf{r},\hbar\mathbf{k})$ is the single-particle Hamiltonian, $\beta \equiv 1/k_B T$, and μ is the chemical potential. As before, we can find the density distribution by integrating W_0 over all values of momentum $\mathbf{p} = \hbar\mathbf{k}$. Given that $W_0(\mathbf{r},\mathbf{p}) = W_0(\mathbf{r},\mathbf{k})/\hbar^3$,

$$\begin{aligned} n(\mathbf{r}) &= \frac{1}{(2\pi\hbar)^3}\int d^3\mathbf{p}\, W_0(\mathbf{r},\mathbf{p}) \\ &= \frac{4\pi}{(2\pi)^6\hbar^3}\int_0^\infty dp\, \frac{p^2}{e^{\beta(p^2/2M+U(\mathbf{r})-\mu)}+1}. \end{aligned} \tag{4.29}$$

The analytical solution to integrals of this form involves both the Euler gamma function $\Gamma(x)$ and the polylogarithm function of order n, $Li_n(x)$:

$$\int_0^\infty d\epsilon \frac{\epsilon^{n-1}}{e^{\beta(\epsilon-\mu)}+1} = -(1/\beta)^n \Gamma(n) Li_n(e^{\beta\mu}). \tag{4.30}$$

Given (4.30), the density distribution becomes

$$n(\mathbf{r}) = -\frac{1}{\hbar^3}\left(\frac{Mk_bT}{2\pi}\right)^{3/2} Li_{3/2}\left(e^{\beta(\mu-U(\mathbf{r}))}\right). \tag{4.31}$$

To find the column density $\tilde{n}(x,y)$, and from it the one-dimensional spatial distribution, one must integrate (4.31). This task is made easier with use of the series expansion of the polylogarithm function about $x = 0$,

$$Li_n(x) = \sum_{k=1}^{\infty} \frac{x^k}{k^n}. \tag{4.32}$$

The column density is then

$$\begin{aligned}
\tilde{n}(x,y) &= \int dz\, n(\mathbf{r}) \\
&= -\frac{1}{\hbar^3}\left(\frac{Mk_bT}{2\pi}\right)^{3/2} \sum_{k=1}^{\infty} \int_{-\infty}^{\infty} dz\, \frac{(e^{\beta\mu})^k}{k^{3/2}} \left(e^{-\beta U(\mathbf{r})}\right)^k \\
&= -\frac{1}{\hbar^3}\left(\frac{Mk_bT}{2\pi}\right)^{3/2} \sum_{k=1}^{\infty} \frac{(e^{\beta\mu})^k}{k^{3/2}} \left(e^{-\frac{x^2}{a_x^2}-\frac{y^2}{a_y^2}}\right)^k \int_{-\infty}^{\infty} dz\, e^{-\frac{kz^2}{a_z^2}} \\
&= -\frac{1}{\hbar^3}\left(\frac{Mk_bT}{2\pi}\right)^{3/2} \sum_{k=1}^{\infty} \frac{\left(e^{\beta\mu - x^2/a_x^2 - y^2/a_y^2}\right)^k}{k^{3/2}} \frac{a_z}{k^{1/2}} \\
&= -\frac{a_z}{\hbar^3}\left(\frac{Mk_bT}{2\pi}\right)^{3/2} Li_2\left(e^{\beta\mu - x^2/a_x^2 - y^2/a_y^2}\right).
\end{aligned} \tag{4.33}$$

Similarly, the one-dimensional spatial distribution is

$$\begin{aligned} n(x) &= \int dy\, \tilde{n}(x,y) \\ &= -\frac{a_y a_z}{\hbar^3}\left(\frac{M k_b T}{2\pi}\right)^{3/2} Li_{5/2}\left(e^{\beta\mu - x^2/a_x^2}\right). \end{aligned} \tag{4.34}$$

The modification to (4.34) in time-of-flight measurements is straightforward, as time of flight from a harmonic trap is equivalent to evolution in a time-independent harmonic trap whose spatial variables are scaled appropriately [79]. For free expansion the scaling is $x \to x/\sqrt{1+\omega_r^2 t^2}$ and $n(x) \to n(x)/\sqrt{1+\omega_r^2 t^2}$.

In practice, we first determine the number of trapped atoms using a Gaussian fit to the time-of-flight data and (4.23). For the range of trapped atom temperatures in our experiments, this produces at most a 1-2% error. Once that is done, we re-fit the distribution using an equation based on (4.34),

$$C_{1D} = A\frac{Li_{5/2}\left(e^{\beta\mu - \frac{x^2}{a_x^2 + v_T^2 t^2}}\right)}{Li_{5/2}\left(e^{\beta\mu}\right)}. \tag{4.35}$$

Here A is used only as a fit parameter.

The programmatic version of (4.35) uses the series expansion of $Li_{5/2}$. Since the expansion in (4.32) is valid only for $|x| < 1$, outside that range we use an alternate series expansion,

$$Li_n(x) = \Gamma(1-n)\left[\ln\left(\frac{1}{x}\right)\right]^{n-1} + \sum_{k=0}^{\infty}\frac{\zeta(n-k)\ln^k(x)}{k!}, \tag{4.36}$$

where $\zeta(n)$ is the Riemann zeta function. For μ we use the approximation given in

Ref. [78],

$$\mu(T,N) = \begin{cases} -k_B T \ln\left[6\left(\frac{T}{T_f}\right)^3\right] & \frac{T}{T_f} \geq .556, \\ k_B T_f \left[1 - \frac{\pi^2}{3}\left(\frac{T}{T_f}\right)^2\right] & \frac{T}{T_f} < .556. \end{cases} \tag{4.37}$$

The Fermi temperature T_F is calculated using the total number of atoms N in both states, the Planck constant h, and the geometric mean of the trap frequencies $\nu = (\nu_x \nu_y \nu_z)^{1/3}$:

$$T_F = \frac{1}{k_B} h\nu (3N)^{1/3}. \tag{4.38}$$

4.5 Measuring Trap Parameters

The measurements of temperature and number depend on the trap's oscillation frequencies, requiring that we determine those frequencies ahead of time. To do so, we use two methods: we shake the trap from side to side, and we change the intensity of the CO_2 laser to excite the atoms parametrically. Both methods require the use of the CO_2 laser AOM described in Section 3.5.1.

4.5.1 Modification of the CO_2 Laser Acousto-Optic Modulator Driver

To shake the trap from side to side, the direction of the CO_2 laser beam must be changed. This can be done by varying the frequency of the rf power sent to the AOM, since the direction of the first-order beam from an AOM depends on the rf power's frequency.

Since the CO_2 laser AOM rf driver (model GE-4050 from IntraAction Corporation) has no frequency modulation capabilities, we modified it as shown in Fig-

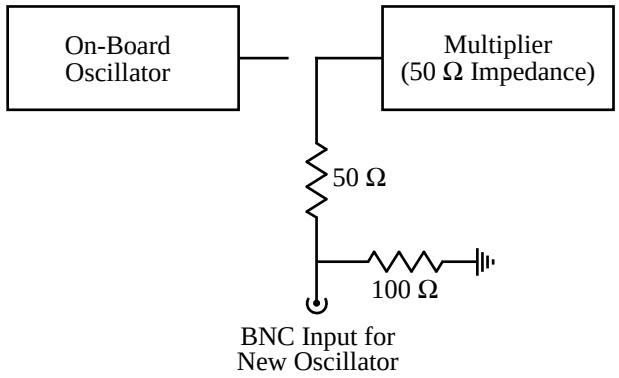

Figure 4.10: The modification made to the GE-4050 driver for the CO_2 laser AOM. The on-board oscillator was detached from the rf multiplier, and a BNC added to the front of the driver box. The appropriate rf frequency is fed to the multiplier through the BNC connection.

ure 4.10. The GE-4050 consists of an oscillator section, which produces +7 dBm of 40 MHz rf power, and a multiplier section, which uses a model SRA-1 MiniCircuits amplifier to amplify the rf signal to up to 50 W. We disconnected the oscillator section from the multiplier section and instead connected the multiplier section to a BNC on the driver's front panel. The low-power rf signal is generated by an Agilent E4420B rf signal generator, which can produce frequencies from 250 kHz to 2 GHz. That rf signal is fed to the multiplier section through the new BNC input on the driver's front panel. The multiplier section has a maximum power rating of around +7 dBm, while the E4420B is capable of producing +13 dBm of rf power. To prevent damage to the multiplier section, two resistors are added to halve the power from the E4420B.

The AOM is placed directly after the CO_2 laser's output. Diffraction efficiencies of 80-85% into the first order can be achieved, though losses due to partial absorption of the CO_2 laser beam by the crystal drop the overall efficiencies to 73-78%. The AOM causes astigmatism in the diffracted beam due to thermal lensing in the AOM crystal. To correct this astigmatism, following the AOM are two 2.0 in. focal length

cylindrical lenses oriented so that they focus in the vertical direction.

4.5.2 Shaking the Trap

To determine the trap's radial frequencies, we shake the trap from side to side. This is done by sinusoidally varying the rf frequency from the E4420B rf signal generator by ± 6 kHz. This frequency modulation (FM) of the rf power driving the AOM produces position modulation at the trap, as described in Section 3.2.2. Atoms in the trap are heated most strongly when the modulation frequency matches one of the trap's radial. Once the trap has been shaken, the strength of the heating is determined using release and recapture methods, in which the CO_2 laser power is turned off for a brief moment,[4] then turned on again. The higher the temperature of the trapped atoms, the further they will move during the period in which the CO_2 laser power is zero. If they move sufficiently far during that period, they will not be recaptured by the CO_2 laser trap when the laser power is restored. The number of atoms remaining in the trap after release and recapture is thus a measure of how high the atoms' temperature was: the fewer the atoms, the hotter their temperature.

The best results are achieved using cold atoms, since they are in the harmonic potential near the trap's bottom. Accordingly, the first step in measuring the trap frequencies by shaking the trap is to evaporatively cool the atoms, as explained in Chapter 5. Following that, FM of the AOM driving power occurs for 1 s. During that time the modulation frequency is linearly decreased by 10 Hz. This is done because, as the atoms' energy increases, the resonance frequency of the trap for those atoms decreases. Once FM is completed, the CO_2 laser is turned off for

[4]The CO_2 laser power is turned off by turning off the rf signal from the E4420B. This results in no driving power reaching the AOM, and hence no power in the first-order beam.

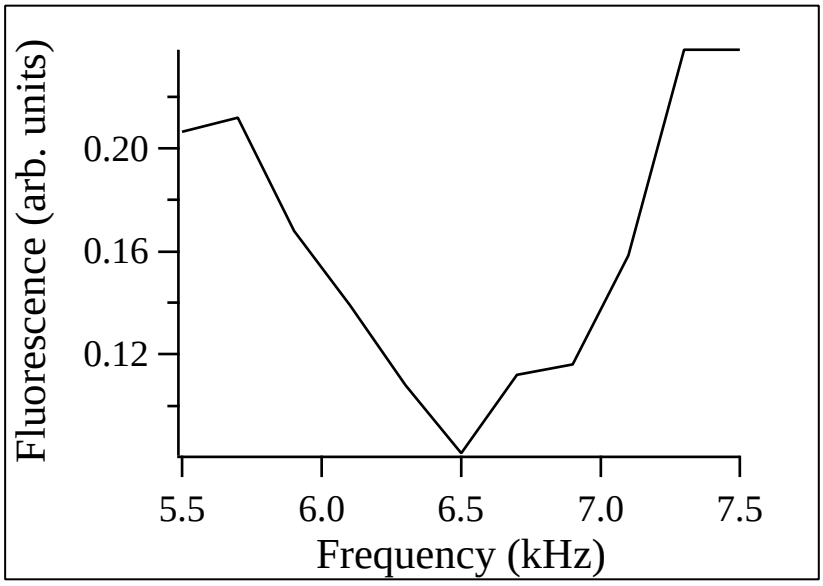

Figure 4.11: A graph of the atomic fluorescence, and thus number of atoms remaining, after the trap is shaken as a function of modulation frequency. The frequency given is the initial modulation frequency before the 10 Hz linear sweep begins.

500 μs, then turned on once more. Finally, the number of atoms remaining in the trap are measured by fluorescence measurement. This process is repeated for various FM frequencies.

Figure 4.11 shows a graph of PMT signal (and thus the number of atoms remaining in the trap) as a function of initial modulation frequency. The drop in signal at 6.5 kHz can be clearly seen. To determine the final frequency, we used frequency steps of 25 Hz around 6.5 kHz and reduced the FM sweep to 1 Hz. In addition, Mike Gehm's Monte-Carlo simulation of the modulation by showed that the measured frequency should be approximately 10% less than the actual frequency; this frequency shift was theoretically confirmed in a later paper by Jáuregui [80]. The final value of the radial resonance frequency was 6.6 kHz.

4.5.3 Parametric Resonance

Shaking the trap from side to side gives very clear and direct results, with high signal-to-noise ratios. Unfortunately, shaking the trap from side to side is not a good way of determining the axial trap frequency. Instead, we use intensity modulation to determine the axial trap frequency, as intensity fluctuations can affect all three of the trap axes. The intensity modulation will parametrically excite atoms in the trap if the frequency of the intensity noise is equal to twice that of a trap frequency, as shown in Section 3.2.1. This method of determining trap parameters is known as parametric resonance [21].

The experimental procedure for parametric resonance is the same as for shaking the trap, with three changes. One, the AOM's driving power is amplitude modulated rather than frequency modulated, so that the CO_2 laser intensity is modulated. The amplitude modulation (AM) depth is 5% of the maximum intensity, and occurs for 1 s. During that time the modulation frequency is linearly decreased. The amount by which it decreases can be from 100 Hz to 1 Hz; we begin with a wide sweep in order to find the rough location of the resonances, then narrow the sweep to better pinpoint them. Two, because the amplitude is being modulated sinusoidally, the central value of laser intensity must be lower than 100%. Otherwise, part of the AM will be truncated. We use a central CO_2 laser intensity of 85%, which changes the measured frequencies by a factor of $\sqrt{.85} = .92$. Three, instead of performing release and recapture, we cut the CO_2 laser power to ten percent of maximum. Because the trapping potential is harmonic only near the bottom of the well, we believe the resonance frequencies are most accurately determined if the loss of atoms from the well's bottom tenth is measured. Thus, the well depth is lowered to ten percent of its maximum value and held there long enough for atoms that were trapped higher

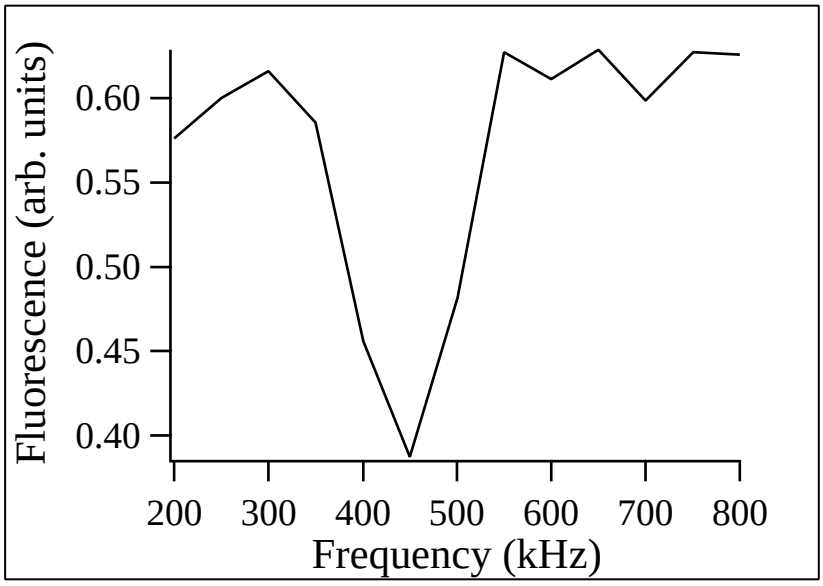

Figure 4.12: A graph of the number of atoms remaining after parametric resonance as a function of initial AM frequency.

in the well to escape the trapping region. After that the number of atoms in the well's bottom tenth is measured via fluorescence measurement.

Figure 4.12 is a graph of the number of atoms remaining in the bottom tenth of the trap as a function of initial AM frequency. The largest dip occurs at 450 Hz. Because parametric resonance, like heating due to intensity noise, occurs at $2\nu_{tr}$, the actual axial frequency as indicated by the figure is $(450/2)/.92 = 245$ Hz. However, we have reason to believe that this is inaccurate. Monte Carlo simulation by Michael Gehm has shown that the resonance frequency of a Gaussian trap as measured by parametric resonance is noticeably lower than what would be measured in a harmonic trap. The shift depends on the atomic temperature, and arises because the restoring force in a Gaussian trap decreases as the radius increases. An analytic treatment is given in Ref. [80]. Another estimate of the axial frequency can be found by measuring the beam spot size at the trap and using (3.11) to find ω_z.

Measurements of the beam's power, size, and radial frequency show that the beam $1/e^2$ intensity radius at the trap is $r_0 = 47\,\mu$m, and its trap depth is $U_0 = 690\,\mu$K. Since the beam is Gaussian, its radius and Rayleigh length are related by $z_0 = \pi r_0^2/\lambda$. Using these figures, we see that $z_0 = 660\,\mu$m and $\omega_z = 340\,$Hz.

Chapter 5

Evaporative Cooling to Degeneracy

The basic process of evaporation is familiar to anyone who has ever drunk a cup of hot liquid such as coffee. Over time, water molecules in the coffee are able to escape as steam, changing from a liquid to a gaseous state. Because these molecules have high energies, they take with them an amount of energy that is appreciably greater than the average energy of the molecules that remain behind. As the high-energy water molecules escape, the coffee's temperature decreases due to rethermalization of the remaining molecules.

The concept of evaporation can be generalized to any process in which energetic particles confined by a finite potential escape that potential. When the escape of particles is coupled with collisions among the remaining bound particles, which redistribute the particle's energy, cooling occurs. This simple concept has led to dramatic results in cold atom experiments, most notably the observation of Bose-Einstein condensation.

There are two keys to evaporation as a cooling process: the most energetic atoms must be preferentially removed, and the remaining atoms must experience elastic collisions in order to rethermalize. Removal of the most energetic atoms ensures that the departing atoms carry with them an amount of energy greater

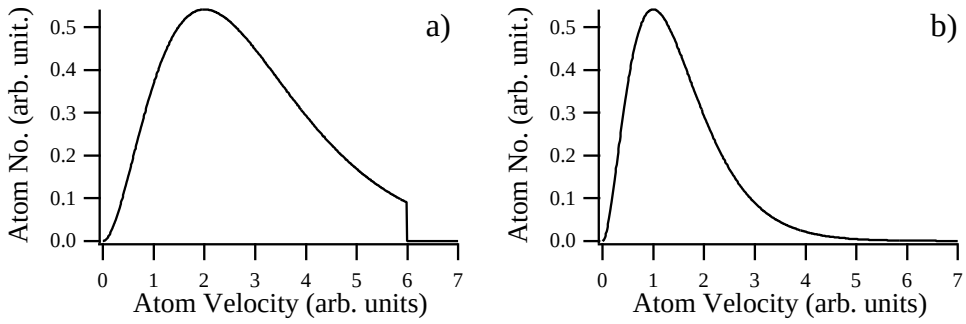

Figure 5.1: How evaporation works to cool atoms. In a) the high-energy tail of a Maxwell-Boltzmann distribution is removed, truncating the maximum allowed energy. After the remaining atoms are allowed to collide and rethermalize, a new Boltzmann distribution forms, one with a lower average energy as shown in b).

than the average. The greater the removed atoms' energy, the more effective the evaporation. Elastic collisions are necessary in order to redistribute the thermal energy of the remaining atoms. Without them, the energy distribution of the bound atoms would not change, and evaporation would merely lead to a loss of atoms without a concurrent decrease in temperature and increase in phase space density. The atoms' energy distribution is initially a Maxwell-Boltzmann one, in which the probability of particles having an energy E is proportional to $\exp(-E/k_BT)$. After atoms with an energy $E > E_t$ are removed and as the atoms rethermalize, collisions serve to produce more higher-energy atoms which can then be removed in turn. As this process continues and the temperature T decreases, fewer and fewer atoms are scattered into the high-energy tail of the Maxwell-Boltzmann distribution, since the probability of an atom having an energy greater than E_t decreases as $\exp(-E_t/k_BT)$. Eventually evaporation will stagnate, and the atomic sample will cease to cool.

Evaporation can continue if E_t is lowered, removing atoms with less and less energy. If E_t is lowered appropriately, a balance can be maintained between the two extremes of stagnant evaporation and the removal of atoms with too low of an

energy to cool the remaining atoms effectively. The usual process, then, is to follow free evaporation, in which E_t is held constant, with forced evaporation, in which E_t is lowered.

Evaporative cooling of neutral alkali atoms in magnetic traps led to the observation of Bose-Einstein condensation (BEC) in 1995 [1, 2, 3]. The evaporation threshold E_t in a magnetic trap is set using rf-driven transitions [81]. An rf field flips the spin of trapped atoms that have sufficient energy, and since magnetic traps can only trap atoms with the proper spin, the spin-flipped atoms are no longer trapped and can escape. The energy selectivity of the rf transition comes from the Zeeman shift of the trapped atoms, which varies with the atoms' potential energy. Changing the frequency of the rf field changes E_t, allowing forced evaporation to occur.

A different approach must be used for atoms trapped in an optical trap, as optical traps can confine atoms in any spin state. E_t is equal to U_0, the optical trap depth, and is therefore changed by lowering the power of the laser beam(s) forming the optical trap and hence U_0. If the trap depth is lowered adiabatically, no heating occurs.

This chapter will develop the tools, both theoretical and experimental, required for evaporative cooling in our CO_2 laser trap. The kinetic theory of evaporation will be explained. The theory models the evaporative process using a Boltzmann equation, as developed in Ref. [82] and extended by Ken O'Hara [26]. The theory requires the assumption of sufficient ergodicity, in which the phase space distribution depends only on the single-particle Hamiltonian due to the ergodic motion of the trapped atoms. The result is a Boltzmann equation that takes into account both the fermionic nature of our trapped atoms and the time-dependent trap depth $U(t)$.

While the Boltzmann equation fully describes the evaporative process, its solution requires numerical integration which can take a day or more. To provide an estimate of the number of atoms remaining after evaporation and their temperature, and also to give a better physical understanding of the evaporative process, we have developed scaling laws for the phase-space density, number, and elastic collision rate as a function of the well depth. The derivation of these scaling laws will be provided, and those scaling laws used to determine how the trap depth should be lowered over time.

In earlier chapters I discussed the various ground states of ^{6}Li, and why some were more desirable to trap and cool than others. We found a mixture of the $|1\rangle$ and $|2\rangle$ states to be ideal. In this chapter the $|1\rangle - |2\rangle$ mixture will be further explored. Its scattering length a_{12} is zero when there is no magnetic field, so in order to provide the elastic collisions necessary for rethermalization a magnetic field must be applied. How we do that will be explained.

The CO_2 laser optical setup as earlier outlined cannot be used for evaporation, as there is no way to lower the laser power. In this chapter we add an acousto-optic modulator (AOM) in the CO_2 laser beam path. The AOM allows us to vary the power of the CO_2 laser beam by varying the rf power applied to the AOM crystal. In addition, we add a movable mirror which serves to remove the retroreflected beam, as the retroreflected beam will present difficulties during evaporation.

While the AOM allows the CO_2 laser power to be varied, it does so at a cost. As the rf power to the AOM is changed, the angular direction of the beam varies, causing it to be clipped by lens mounts and the edges of the ZnSe window leading into the vacuum system. We have attempted to prevent the variation from occurring using two methods, as outlined in this chapter: imaging the beam as it emerges from

the AOM, and changing the frequency of the AOM rf power to alter the angular direction of the beam and cancel the uncontrolled angular deviation.

Finally, with all of these tools in place, we can cool ^{6}Li into the degenerate regime. Over the course of sixty seconds, the CO_2 laser power is decreased, then brought back to its maximum. The atoms are cooled to a temperature of $T/T_F = 0.48$, well into the degenerate regime.

5.1 Boltzmann Equation Approach to Evaporation

A kinetic theory model of evaporation using a Boltzmann equation and the assumption of sufficient ergodicity was developed in Ref. [82]. This treatment considered evaporation of a single-component classical gas from a fixed-depth trap. In the experiments described in this dissertation, a two-component gas is cooled in a Gaussian trap whose depth is lowered in order to maintain evaporative cooling. The atoms are cooled to the point that Fermi statistics begin to have a noticeable effect. Ken O'Hara extended the theory from Ref. [82] to take into account the Gaussian trap of varying depth, the two states of the trapped atoms, and the atoms' Fermi statistics [26]. Here I will present the basic results of his extended theory.

5.1.1 Density of States in the Optical Trap

In what follows we will need to know the density of states in the optical trap. The temperature of atoms confined in our experiments is large enough that it is useful to treat the discreet states of the optical trapping potential $U(\mathbf{r})$ as if they form a

continuum. In this case, the density of states $\mathcal{D}(\epsilon)$ will be

$$\mathcal{D}(\epsilon) = \frac{1}{(2\pi\hbar)^2}\int d^3r\, d^3p\, \delta\left(\epsilon - \frac{p^2}{2M} - U(\mathbf{r})\right) \tag{5.1}$$

$$= \frac{2\pi(2M)^{3/2}}{(2\pi\hbar)^3}\int\limits_{U\leq\epsilon} d^3r\, \sqrt{\epsilon - U(\mathbf{r})}, \tag{5.2}$$

where integration of the momentum integral has limited the spatial integral to those values of $\mathbf{r}$ for which $U(\mathbf{r}) \leq \epsilon$. $\mathcal{D}(\epsilon)d\epsilon$ is the number of states which have energies lying between ϵ and $\epsilon + d\epsilon$.

The potential for a focused Gaussian beam, as shown in (3.7), is Gaussian in the x and y directions and Lorentzian in the z direction. To simplify matters, the Lorentzian dependence along z will be approximated by a Gaussian. In this approximation, the potential of the CO_2 laser trap is

$$U(\mathbf{r},t) = U_0(t)\left[1 - \exp\left(\frac{x^2}{a^2} - \frac{y^2}{b^2} - \frac{z^2}{c^2}\right)\right], \tag{5.3}$$

where $U_0(t)$ is the time-dependent trap depth and a, b, and c are the $1/e^2$ intensity radii in the x, y, and z directions. Here I have not assumed that the beam is cylindrically symmetrical, as was assumed in (3.7). In the limit that $x \ll a$, $y \ll b$, and $z \ll c$, the potential is approximately harmonic, with frequencies of *e.g.* $\omega_x = \sqrt{2U_0(t)/(Ma^2)}$.

Given (5.3), the density of states then becomes

$$\mathcal{D}(\epsilon) = \mathcal{D}_{ho}(\epsilon)g_1(\epsilon). \tag{5.4}$$

$\mathcal{D}_{ho}(\epsilon) \equiv \epsilon^2/(2\hbar^3\omega_x\omega_y\omega_z)$ is the density of states for a harmonic oscillator and

$$g_1(\epsilon) = \frac{16}{\pi\beta^2}\sqrt{\alpha^3(1-\beta)}\int_0^1 du\, u^2\sqrt{e^{\alpha(1-u^2)}-1}, \tag{5.5}$$

where $\beta \equiv \epsilon/U_0(t)$ and $\alpha \equiv -\ln(1-\beta)$.

5.1.2 The Boltzmann Equation and the Ergodic Assumption

Evaporation of atoms from a trap with a potential $U(\mathbf{r},t)$ involves the rethermalization of an atomic gas, with atoms in the high-energy tail of the atomic energy distribution escaping from the trap. The phase space distribution of the trapped atoms $f(\mathbf{r},\mathbf{p},t)$ evolves over time as the atoms collide, rethermalize, and in some cases gain enough energy to escape. If the atoms which have an energy ϵ that is greater than the trap energy ϵ_t escape the trap without experiencing another collision, as is the case in our system, the evolution of the phase space density is described by the Boltzmann equation [83],

$$\left(\frac{\mathbf{p}}{M}\cdot\boldsymbol{\nabla}_{\boldsymbol{r}} - \boldsymbol{\nabla}_{\boldsymbol{r}}U(\mathbf{r},t)\cdot\boldsymbol{\nabla}_{\boldsymbol{p}} + \frac{\partial}{\partial t}\right) f(\mathbf{r},\mathbf{p},t) = \mathcal{I}(\mathbf{r},\mathbf{p}). \tag{5.6}$$

$\mathcal{I}(\mathbf{r},\mathbf{p})$ describes how the atoms collide. In general this term is given by

$$\begin{aligned}\mathcal{I}(\mathbf{r},\mathbf{p}_1) = &-\frac{1}{2}\sum_{\mathbf{p}_2,\mathbf{p}_3,\mathbf{p}_4} R(\mathbf{p}_1\mathbf{p}_2\rightarrow\mathbf{p}_3\mathbf{p}_4) f(\mathbf{r},\mathbf{p}_1) f(\mathbf{r},\mathbf{p}_2) \\ &+\frac{1}{2}\sum_{\mathbf{p}_2,\mathbf{p}_3,\mathbf{p}_4} R(\mathbf{p}_3\mathbf{p}_4\rightarrow\mathbf{p}_1\mathbf{p}_2) f(\mathbf{r},\mathbf{p}_3) f(\mathbf{r},\mathbf{p}_4),\end{aligned} \tag{5.7}$$

where $R(\mathbf{p}_i\mathbf{p}_j \rightarrow \mathbf{p}_k\mathbf{p}_l)$ is the rate for atoms with initial momenta $\mathbf{p}_i$ and $\mathbf{p}_j$ to scatter into states with momenta $\mathbf{p}_k$ and $\mathbf{p}_l$.

Equation (5.6) can be simplified by the assumption of "sufficient ergodicity." The basis of this assumption is that the phase space distribution $f(\mathbf{r}, \mathbf{p}, t)$ depends only on the single-particle Hamiltonian $\mathcal{H}(\mathbf{r}, \mathbf{p}, t) = \mathbf{p}^2/2M + U(\mathbf{r}, t)$, due to the motion of the trapped atoms being ergodic. In this assumption the phase space density is

$$\begin{aligned} f(\mathbf{r}, \mathbf{p}, t) &= \int d\epsilon\, \delta\left(\epsilon - \frac{p^2}{2M} - U(\mathbf{r}, t)\right) f(\epsilon, t) \\ &= \int d\epsilon, \delta\left(\epsilon - \mathcal{H}(\mathbf{r}, \mathbf{p}, t)\right) f(\epsilon, t). \end{aligned} \tag{5.8}$$

$f(\epsilon, t)$ is the occupation number for trap eigenstates with energy ϵ at a time t. The number of atoms whose energy lies between ϵ and $\epsilon + d\epsilon$ is $f(\epsilon)\mathcal{D}(\epsilon)d\epsilon$.

To simplify the Boltzmann equation in light of the condition of sufficient ergodicity, we apply $(2\pi\hbar)^{-3}\int d^3r\, d^3p\, \delta\left(\epsilon - {}^{p^2}/_{2M} - U(\mathbf{r}, t)\right)$ to both sides of (5.6). On the left-hand side of the equation, the gradient terms sum to zero [82], leaving

$$\int \frac{d^3r\, d^3p}{(2\pi\hbar)^3}\, \delta\left(\epsilon - \frac{p^2}{2M} - U(\mathbf{r}, t)\right) \frac{\partial}{\partial t} f(\mathbf{r}, \mathbf{p}, t). \tag{5.9}$$

The time derivative of f may be found using two facts. One, $f(\mathbf{r}, \mathbf{p}, t) = f(\mathcal{H}(\mathbf{r}, \mathbf{p}, t))$. Two, the only part of the Hamiltonian that is explicitly time-dependent is the trap potential $U(\mathbf{r}, t)$, since the trap potential will be decreased

during forced evaporative cooling. Using these facts,

$$\begin{aligned}\frac{\partial f(\mathcal{H})}{\partial t} &= \frac{\partial f}{\partial \mathcal{H}}\frac{\partial \mathcal{H}}{\partial t} + \frac{\partial f}{\partial t} \\ &= \frac{\partial f}{\partial \epsilon}\dot{U} + \frac{\partial f}{\partial t}.\end{aligned} \tag{5.10}$$

Applying this result to (5.9) and using the density of states from (5.1) gives

$$\begin{aligned}&\int \frac{d^3r\, d^3p}{(2\pi\hbar)^3}\,\delta\left(\epsilon - \mathcal{H}(\mathbf{r},\mathbf{p},t)\right)\left(\frac{\partial f}{\partial t} + \frac{\partial f}{\partial \epsilon}\dot{U}\right) \\ &\qquad = \mathcal{D}(\epsilon)\frac{\partial f}{\partial t} + \int \frac{d^3r\, d^3p}{(2\pi\hbar)^3}\,\delta\left(\epsilon - \mathcal{H}(\mathbf{r},\mathbf{p},t)\right)\frac{\partial f}{\partial \epsilon}\dot{U} \\ &\qquad = \mathcal{D}(\epsilon)\left(\frac{\partial f}{\partial t} + \frac{\partial f}{\partial \epsilon}\langle\dot{U}(\mathbf{r},t)\rangle_\epsilon\right).\end{aligned} \tag{5.11}$$

Here $\langle\dot{U}(\mathbf{r},t)\rangle_\epsilon$ is the ergodic average of $\dot{U}$, and is defined as

$$\mathcal{D}(\epsilon)\langle\dot{U}(\mathbf{r},t)\rangle_\epsilon \equiv \int \frac{d^3r\, d^3p}{(2\pi\hbar)^3}\,\delta\left(\epsilon - \mathcal{H}(\mathbf{r},\mathbf{p},t)\right)\dot{U}(\mathbf{r},t). \tag{5.12}$$

On the right-hand side of (5.6), the collision integral becomes [26, 84]

$$\begin{aligned}&\frac{M\sigma}{\pi^2\hbar^3}\int d\epsilon_1\, d\epsilon_2\, d\epsilon_3\,\delta(\epsilon_1+\epsilon_2-\epsilon_3-\epsilon)\mathcal{D}(\epsilon_{min}) \\ &\qquad \times\{f(\epsilon_1)f(\epsilon_2)[1-f(\epsilon_3)][1-f(\epsilon)] \\ &\qquad\quad - f(\epsilon_3)f(\epsilon)[1-f(\epsilon_1)][1-f(\epsilon_2)]\},\end{aligned} \tag{5.13}$$

where ϵ_{min} is the smallest of ϵ_1, ϵ_2, ϵ_3, and ϵ. The effect of Fermi statistics is taken into account by the various factors of $[1-f(\epsilon)]$, since as the occupation number for a given energy approaches unity the probability for a fermion to scatter into that energy state vanishes.

Combining (5.11) and (5.13) give the Boltzmann equation in the ergodic approximation,

$$\mathcal{D}(\epsilon)\left(\frac{\partial f(\epsilon,t)}{\partial t}+\frac{\partial f(\epsilon,t)}{\partial \epsilon}\langle \dot{U}(\mathbf{r},t)\rangle_{\epsilon}\right)=\frac{M\sigma}{\pi^2\hbar^3}\int d\epsilon_1\, d\epsilon_2\, d\epsilon_3\, \delta(\epsilon_1+\epsilon_2-\epsilon_3-\epsilon)\mathcal{D}(\epsilon_{min}) \times\{f(\epsilon_1)f(\epsilon_2)[1-f(\epsilon_3)][1-f(\epsilon)] - f(\epsilon_3)f(\epsilon)[1-f(\epsilon_1)][1-f(\epsilon_2)]\}. \tag{5.14}$$

A computer program written by Ken O'Hara integrates (5.14) using a fourth-order Runga-Kutta algorithm with an adaptive step-size. Using this program we can determine the expected temperature for a given set of initial conditions, though the set of initial conditions that can be considered is limited by the day or so that the integration program takes to run.

5.1.3 Scaling Laws

In order to provide physical insight and to give an estimation of the number of atoms remaining after forced evaporation and their temperature, we have developed scaling laws for the phase-space density, number, and elastic collision rate as a function of the well depth. Comparison of these laws with integration of (5.14) shows excellent agreement between the two.

Integration of (5.14) shows that free evaporative cooling stagnates at temperatures that are around $1/10$ of the well depth. If, during forced evaporation, the trap depth is lowered slowly and the elastic collision rate is high enough, the atoms' temperature will remain at approximately $k_BT/U = 1/10$. In what follows, we will therefore assume that the atoms are first evaporatively cooled to a given ratio of well

depth to temperature $\eta \equiv U/k_BT$, which they will then maintain as the trapping potential is adiabatically lowered. For $\eta \simeq 10$ we can approximate the Gaussian trapping potential as being harmonic and use the harmonic density of states.

To determine the scaling laws, we first must determine the rate of energy loss from the trap.[1] As the atoms evaporate, they will have an average energy of $U + \alpha k_BT$, where $0 \leq \alpha \leq 1$ [82]. From the s-wave Boltzmann equation, $\alpha \equiv (\eta - 5)/(\eta - 4)$ [85]. The energy loss arising from evaporation is equal to the rate at which atoms leave the trap times their average energy, $\dot{N}(U + \alpha k_BT)$. In addition, since the trap is being lowered adiabatically at a rate $\dot{U}$, the energy will change due to the changing potential energy. The average potential energy in a harmonic potential is $E/2$, so the rate of change of the potential energy will be $(\dot{U}/U)E/2$. The total rate of change in energy is then

$$\dot{E} = \dot{N}(U + \alpha k_BT) + \frac{\dot{U}}{U}\frac{E}{2}. \tag{5.15}$$

In the classical limit, $E = 3Nk_BT$. In this limit the time rate of change of the internal energy can be written as

$$\begin{aligned} \dot{E} &= \frac{\partial E}{\partial T}\dot{T} + \frac{\partial E}{\partial N}\dot{N} \\ &= 3Nk_B\dot{T} + 3k_BT\dot{N}. \end{aligned} \tag{5.16}$$

Since we are assuming that the atoms remain at a constant η, we can replace $k_B\dot{T}$

[1] Energy loss due to background gas collisions will be neglected at first, as they do not change the derivation of the scaling laws.

with $\dot{U}/\eta$. Equating (5.15) and (5.16) and substituting in for E and T then gives

$$\dot{N}\left(U+\alpha\frac{U}{\eta}\right)+\frac{3}{2}\frac{\dot{U}}{\eta}=3N\frac{\dot{U}}{\eta}+3\frac{U}{\eta}\dot{N}. \tag{5.17}$$

Solving (5.17) gives the scaling law for the number of atoms,

$$\frac{N}{N_i}=\left(\frac{U}{U_i}\right)^{\frac{1}{2}\frac{3}{\eta'-3}}, \tag{5.18}$$

where i denotes the initial conditions after free evaporation and stagnation, $N = N(t)$, $U = U(t)$, and $\eta' = \eta + \alpha = \eta + (\eta - 5)/(\eta - 4)$.

For a classical harmonic oscillator potential, the phase space density is

$$\rho = N\left(\frac{h\nu}{k_B T}\right)^3, \tag{5.19}$$

where $\nu = \nu(t) \propto \sqrt{U}$ is the geometric mean of the trap oscillation frequencies. Using (5.18) gives the scaling law for phase space density,

$$\frac{\rho}{\rho_i}=\left(\frac{U_i}{U}\right)^{\frac{3}{2}\frac{\eta'-4}{\eta'-3}}=\left(\frac{N_i}{N}\right)^{\eta'-4}. \tag{5.20}$$

For an energy-independent cross section, $\gamma = \gamma(t) \simeq n_0\bar{v}\sigma$, where $n_0 \simeq N/a^3$ is the peak spatial density, $\bar{v} = \sqrt{8k_BT/\pi M} \sim \sqrt{U/\eta}$ is the average velocity, and a^3 denotes the size of the atomic cloud. However, the cloud size stays fixed during evaporation, so that $n_0 \sim N$. Thus $\gamma \sim N\sqrt{U}$. Using (5.20) to remove the N dependence from γ gives the collision rate scaling law:

$$\frac{\gamma}{\gamma_i}=\left(\frac{U}{U_i}\right)^{\frac{1}{2}\frac{\eta'}{\eta'-3}}. \tag{5.21}$$

All of these scaling laws neglect background gas collisions. Such collisions can be treated by modifying (5.15): a loss rate of $-\Gamma_{bg}E$ is added and $\dot{N}$ is replaced with $\dot{N}_{evap} = \dot{N} + \Gamma_{bg}N$. With these changes, the scaling laws become

$$\frac{N}{N_i} = \left(\frac{U}{U_i}\right)^{\frac{1}{2}\frac{3}{\eta'-3}} e^{-\Gamma_{bg}t}, \tag{5.22}$$

$$\frac{\rho}{\rho_i} = \left(\frac{U_i}{U}\right)^{\frac{3}{2}\frac{\eta'-4}{\eta'-3}} e^{-\Gamma_{bg}t} = \left(\frac{N_i}{N}\right)^{\eta'-4} e^{-\Gamma_{bg}(\eta'-3)t}, \tag{5.23}$$

and

$$\frac{\gamma}{\gamma_i} = \left(\frac{U}{U_i}\right)^{\frac{1}{2}\frac{\eta'}{\eta'-3}} e^{-\Gamma_{bg}t}, \tag{5.24}$$

where t is the length of time for which the potential is lowered.

From the scaling laws and evaporation rate we can derive the time dependence of the trap depth, subject to the condition that the atoms remain at fixed and large η. To lowest order in $\exp(-\eta)$, and neglecting background collisions, the rate of atom loss due to evaporation is given by the s-wave Boltzmann equation as

$$\dot{N} = -2(\eta - 4)\exp(-\eta)\gamma N. \tag{5.25}$$

Using both this equation and (5.21), and differentiating (5.18) gives the time dependence of the well depth:

$$U(t) = \frac{U_i}{(1 + t/\tau)^{\beta}}, \tag{5.26}$$

where the exponent β is given by

$$\beta = \frac{2}{\eta'}(\eta' - 3) \tag{5.27}$$

and the time constant τ is given by

$$\frac{1}{\tau} = \frac{2}{3}\eta'(\eta - 4)\gamma_i e^{-\eta}. \tag{5.28}$$

For a two-state 50-50 mixture of fermions, the initial elastic collision rate is $\gamma_i = \pi N_i M \sigma \nu_i^3/(k_B T)$, where ν_i is the initial geometric mean of the trap oscillation frequencies.

5.2 The $|2\rangle - |1\rangle$ Mixture

As explained in Section 2.6, we evaporatively cool a mixture of atoms in the $|1\rangle$ and $|2\rangle$ states. These states exhibit no s-wave spin-exchange collisions. Since both states comprise the $|F = 1/2\rangle$ manifold of hyperfine states, preparation of the atomic sample in the two states is readily achieved by using pumping light resonant with transitions from the $|F = 3/2\rangle$ ground states to empty the $|F = 3/2\rangle$ level. This pumping light will excite atoms in the $|F = 3/2\rangle$ states until they decay into the $|1\rangle$ and $|2\rangle$ states and are no longer excited by the laser beam. The experimental details of this procedure are covered in Section 3.4.6.

The scattering length a_{12} for the $|1\rangle - |2\rangle$ mixture as a function of magnetic field B is shown in Figure 5.2. One remarkable feature of a_{12} is that it is zero at $B = 0$, and increases as the magnetic field strength increases. While this requires that a magnetic field be present in order for interactions, and thus evaporation,

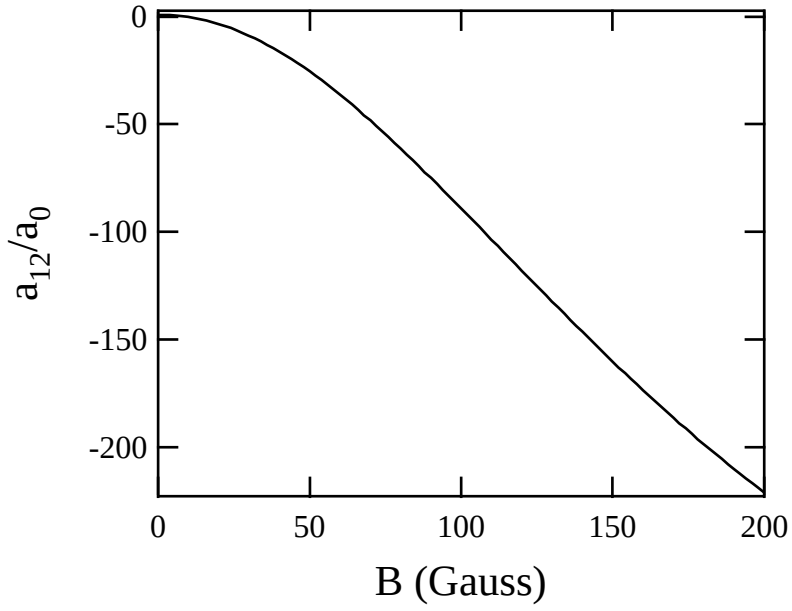

Figure 5.2: How the scattering length a_{12} for the states $|1\rangle$ and $|2\rangle$ varies with low magnetic field.

to take place, it also provides a convenient way of turning on and off interactions between the atoms. In the experiment we provide the necessary magnetic field using the same coils that provide the MOT gradient field. A mechanical relay reverses the direction of current in one of the coils, changing their configuration from anti-Helmholtz to Helmholtz. Those coils produce $\sim 130\,\mathrm{G}$ of magnetic field, resulting in a scattering length of $a_{12} \simeq -100\,\mathrm{a_0}$.

At much higher magnetic fields, near $B = 850\,\mathrm{G}$, the $|1\rangle - |2\rangle$ mixture exhibits a Feshbach resonance. In that region, the scattering length varies widely over a $\sim 200\,\mathrm{G}$ range of B. We are currently constructing coils that will allow us to produce magnetic fields of nearly $1100\,\mathrm{G}$ in the region of the CO_2 laser trap and thus explore the Feshbach resonance and resonance superfluidity.

5.3 Additions to the Optical Setup

Before evaporative cooling of the trapped atoms can occur, the CO_2 laser optical setup as detailed in Section 3.5.1 must be altered. For one thing, the CO_2 laser's intensity must be varied in order for evaporation not to stagnate over time. For another, the retroreflected CO_2 laser beam needs to be blocked before CO_2 laser intensity is lowered, as variations in the direction of the front-going beam will be mirrored in the opposite direction by the rooftop mirror, exacerbating any heating due to position fluctuations.

5.3.1 Acousto-Optic Modulator

In order to vary the CO_2 laser beam intensity, we use an acousto-optic modulator (AOM) that is designed to deflect 10.6 μm light. The AOM used was first described in Section 3.5.1; I will only describe some of its features here.

As with the AOMs used with 670 nm light, the CO_2 laser AOM scatters a certain percentage of the input light into higher-order diffracted beams. By varying the alignment of the AOM crystal with respect to the incoming beam, the efficiency with which light is scattered into the first-order beam can be maximized. Changing the power and frequency of the radio frequency (rf) power sent to the crystal can in turn alter the first-order beam produced by the AOM. If the frequency of the rf power is changed, the direction of the first-order beam will change. If the amplitude of the rf power is decreased, the power scattered into the first-order beam similarly decreases, though the relationship is not linear. It is the latter effect which we use to lower the depth of our CO_2 laser trap during forced evaporation.

The AOM crystal is made of Ge, which is opaque to visible light and has a larger absorption coefficient than ZnSe. Its absorption is highly sensitive to temperature,

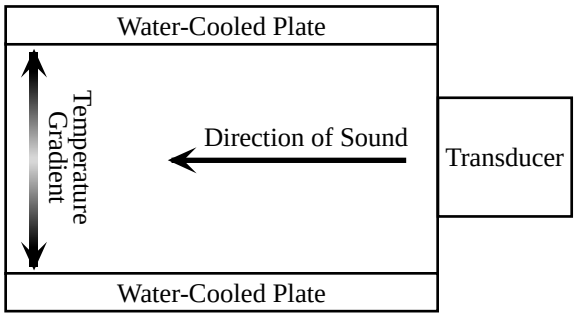

Figure 5.3: Location of the water-cooled plates which in turn cool the AOM crystal. In the figure, the laser beam propagates out of the plane of the page.

increasing as the Ge heats. The major source of heat in the crystal is the 50 W of rf power, which must be dissipated after passing through the crystal. The heat has two noticeable effects on the first-order beam: it causes beam ellipticity and changes beam direction.

As far as we have been able to determine, the ellipticity is due to thermal lensing, in which a temperature gradient across the Ge crystal focuses the beam. The AOM crystal is water-cooled by a closed water loop system that maintains a constant temperature of 15 °C. The cooling only occurs on the top and bottom faces of the crystal, since its other faces are the input and output faces for the laser beam and for the sound waves. This produces a different temperature gradient across the crystal in the vertical and horizontal directions, which leads to different rates of focusing in the two directions. The result is an elliptical first-order beam. To correct the ellipticity, two 1.969 in. focal length cylindrical lenses are placed after the AOM. The cylindrical lenses change the divergence of the first-order beam in the vertical direction, keeping the beam from becoming elliptical. As the rf power is lowered these lenses no longer work correctly, since the difference between the temperature gradients in the vertical and horizontal directions lessen as the amount of heat produced by the rf power changes. The result is a beam which becomes more

elliptical as the rf power is lowered, resulting in a decrease in the product of the trap frequencies $\nu_x\nu_y\nu_z$.

As the rf power is lowered, the direction of the first-order beam changes as well. The likely cause of this is the change in the index of refraction of Ge as the crystal temperature changes. Measurements made as the rf power is decreased show that the angle at which the first-order beam leaves the AOM changes by 2.8 mrad as the rf power is varied from the maximum to near its minimum. Since the first-order beam is expanded by a $\times 10$ telescope, this angular deviation results in a linear displacement of nearly one inch at the telescope's final lens. How we have attempted to compensate for this deviation is the subject of Section 5.4.

The amplitude voltage is controlled by an Agilent 33120A arbitrary waveform generator, the output of which is filtered by a low-pass filter with a time constant of 0.2 s. The generator allows the CO_2 laser power to be varied arbitrarily. Agilent Intuilink software transmits a requested waveform to the 33120A from the Dell Precision 420 computer, which is also used to control the timing system. The actual waveform is generated by a Perl script; Perl was chosen for its advanced file-writing capabilities. Given a waveform's mathematical shape, the Perl script writes a file, which can then be read by the Intuilink software.

The amount of power scattered into the first-order beam does not vary linearly with the driving rf power. In addition, how the deflected power and the rf power are related depends on how fast the rf power is varied due to thermal effects. Experimentation has shown that, for a linear ramp of rf power from a full 50 W to 0 W, the deflected CO_2 laser power as a function of rf power does not change once the ramp takes 10 s or longer. This time scale fits well with our experiments, as we lower the CO_2 laser power relatively slowly. Even if the trap is initially lowered at

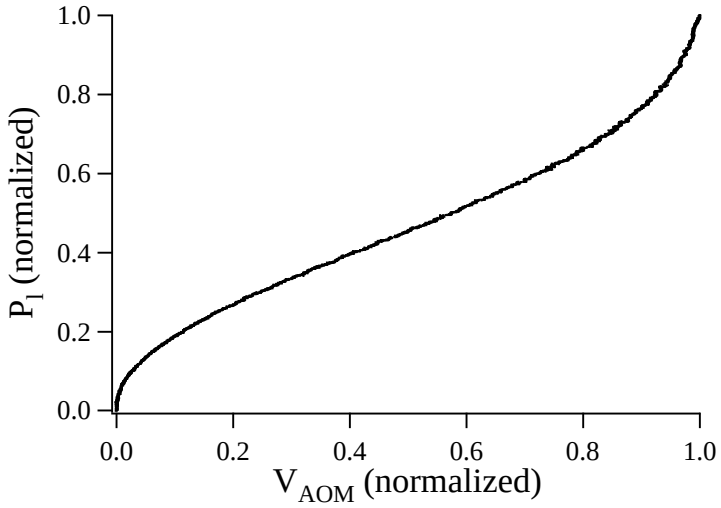

Figure 5.4: The AOM voltage as a function of CO_2 laser power, both normalized to 1. A normalized AOM voltage of 1 corresponds to an actual voltage of 4.54 V.

a fast enough rate that thermal effects become important, the rate of lowering will quickly slow, allowing the thermal effects to become negligible once more.

Since we wish to specify the CO_2 laser power, we measure $P_l(V_{AOM})$, the CO_2 laser power as a function of the amplitude voltage fed to the CO_2 laser AOM, then invert the graph to give $V_{AOM}(P_l)$, as shown in Figure 5.4. Using $V_{AOM}(P_l)$ we can determine what voltage should be fed to the AOM in order to produce a given amount of CO_2 laser power. To measure the CO_2 laser power, we use the infrared detector and setup shown in Figure 3.4. A 10 s voltage ramp is applied to the AOM over three ranges: from 100% of the maximum allowed voltage to 0, from roughly 20% to 0, and from 7% to 0. These voltage ranges roughly correspond to ramps beginning at 100%, 10%, and 1% of the maximum deflected CO_2 laser power, respectively. For the 20% ramp one of the CaF_2 attenuators is removed from before the infrared detector; for the 7% ramp both attenuators are removed. In this manner a very accurate measurement of $P_l(V_{AOM})$ can be made over several

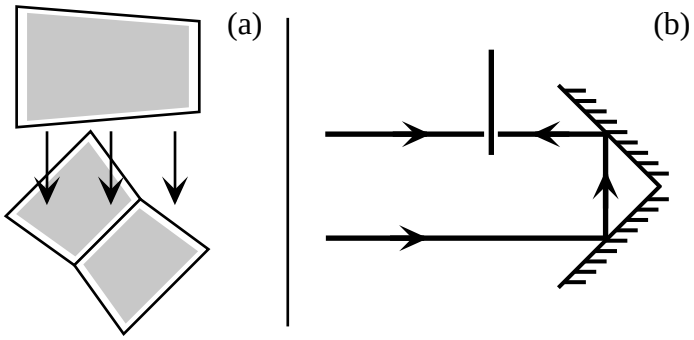

Figure 5.5: (a) A front view of the flat mirror which can be lowered to block the rooftop mirror, removing the retroreflected beam. (b) A cross-sectional view of the rooftop mirror as it is partially blocked by a lowered mirror. The two lines with arrowheads represent the edges of the expanded CO_2 laser beam. One side of the beam is blocked as it travels towards the rooftop mirror; the other side is blocked after it is flipped by the rooftop mirror.

orders of magnitude. Both the applied voltage $V_{AOM}(t)$ and the CO_2 laser power $P_l(t)$ are recorded on a Tektronix TDS644B oscilloscope. Six scans are taken for each ramp and the results averaged. Once the measurements have been made, the data is scaled from 0-1, plotted parametrically and then fitted to an nth-order polynomial, giving $V_{AOM}(P_l)$. First the 100% ramp is fitted. Once that is done, the starting values of the 20% ramp can be determined from the first fit. Then the 20% ramp can be fitted, and its fit used to determine the starting values of the 7% ramp. The resulting $V_{AOM}(P_l)$ is piecewise-continuous and accurate down to $\sim 0.0001 P_{max}$.

5.3.2 The "Chopper"

The angular deviation of the first-order beam from the AOM as the rf power is lowered makes it crucial that the retroreflected CO_2 laser beam be blocked before forced evaporation begins. Otherwise, we risk having one trap evolve into two potentially separate traps during the course of forced evaporation, dividing our

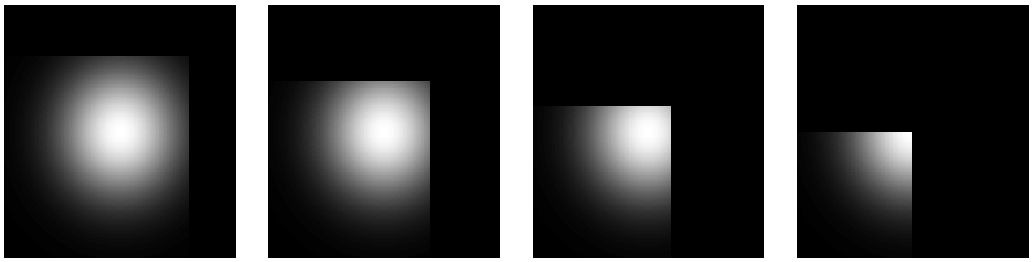

Figure 5.6: Calculated image plots of the CO_2 laser beam after being occluded by the flat mirror. In each successive plot the flat mirror has been lowered further.

sample of atoms. At the same time, removal of the retroreflected beam must not disturb the trapped atoms.

The simplest method of removing the beam is to block the rooftop mirror with a flat mirror, deflecting the CO_2 laser beam as it first exits the vacuum system and preventing it from being retroreflected. Such a mirror could be raised above the rooftop mirror for much of the experiment, then lowered when the retroreflected beam needed to be removed. Figure 5.5 shows a front view of a flat mirror that can be lowered to block the rooftop mirror. The figure also shows how the CO_2 laser beam is affected by the flat mirror. In the process of retroreflecting the CO_2 laser beam the rooftop mirror also flips the beam about an axis that is 45° from both the horizontal and vertical axes. This is equivalent to transforming the original profile such that $x \rightarrow y$ and $y \rightarrow x$. Therefore, as the flat mirror begins to occlude the rooftop mirror, the CO_2 laser beam is cut from two sides at once, as if by two mirrors at right angles to each other. One side will encounter the flat mirror as it propagates towards the rooftop mirror; the other side, when it has been flipped by the rooftop mirror. Figure 5.6 shows the profile of the retroreflected CO_2 laser beam as the flat mirror is lowered.

Fortunately, the retroreflected beam is focused into the trap region by a lens.

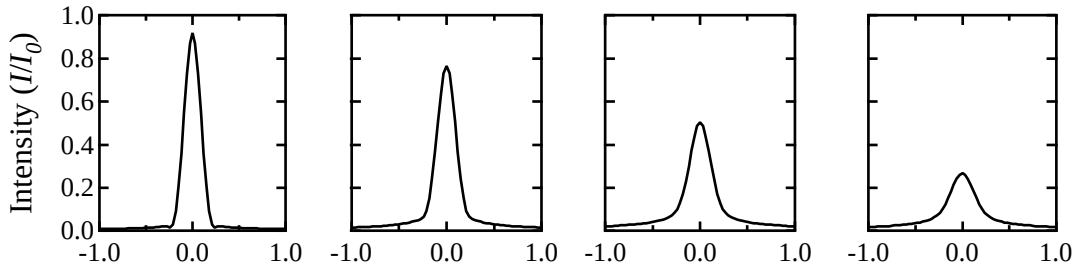

Figure 5.7: One-dimensional slices through the middle of the Fourier-transformed occluded beam. The graphs correspond to the beam profile at the trap due to the various occluded beam profiles in Figure 5.6. Intensity is given in units of the peak intensity I_0 before occlusion begins.

When a collimated beam passes through a lens, its profile at the lens focus is the Fourier transform of its profile at the lens itself. The Fourier transform of a Gaussian beam is Gaussian; the Fourier transform of a clipped Gaussian beam is nearly Gaussian, with most of the deviations occurring in the wings of the Gaussian. Figure 5.7 contains graphs of the middle of the beam at the trap region due to the various occluded profiles in Figure 5.6. The irregularities in the Fourier-transformed beam occur where there is little CO_2 laser power, and thus correspond to points where the trapping potential is low, *i.e.* near the top of the trapping potential. If the atoms are allowed to cool evaporatively prior to the mirror being lowered, then none of the atoms will be near the top of the trapping potential. From the atom's standpoint, the trap will smoothly evolve to a single-beam trap.

To lower the mirror, we constructed the "Chopper." The Chopper consists of a carriage that is situated behind the rooftop mirror and rides up and down on rails, a long arm that passes to one side of the rooftop mirror, and a flat mirror attached to the end of the long arm. The carriage is controlled by an air-filled dashpot. A dashpot is made from a piston that slides in a cylinder filled with either air or oil, and is the mechanical impedance element, analogous to a resistor in an electrical

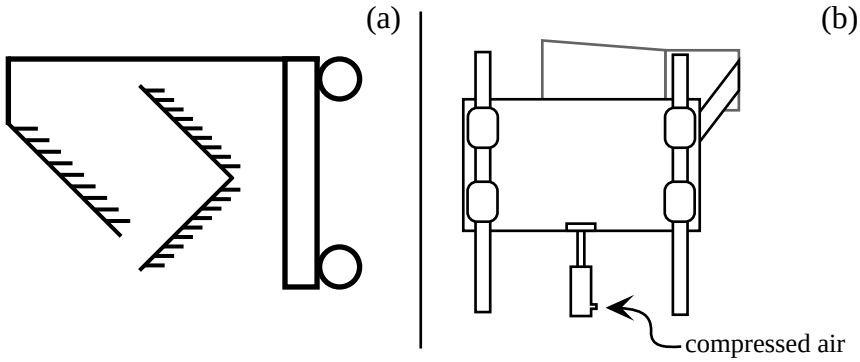

Figure 5.8: The Chopper. (a) A top view of the Chopper as it is placed around the rooftop mirror. (b) A schematic of the Chopper as viewed from behind.

circuit. When a force is applied to it, a dashpot produces a viscous damping force equal to $F_{dash} = -\mu v$, where μ is the dashpot's damping coefficient and v is the piston's velocity. As shown in Figure 5.8, the carriage and attached dashpot are aligned vertically. When the carriage is released from the top position, gravity pulls it down. It speeds up until such time as the damping force from the dashpot equals that of gravity, causing the mirror to move at a constant velocity and smoothly occlude the retroreflected CO_2 laser beam. A knob on the dashpot controls how quickly air is forced from the cylinder, thus altering μ. The knob is set so that the mirror takes about five seconds to travel from its top position to its final position in front of the rooftop mirror. To raise the carriage, the dashpot's piston is filled with compressed air from a tank. Airflow is controlled by a solenoid valve. Electronics allow this valve to be open or closed by a TTL logic signal. When compressed air flows into the dashpot, the resulting pressure raises the carriage to its upper position. When the valve is closed, removing the compressed air, the dashpot empties of its excess air and the carriage is pulled down by gravity. Although the upper motion is not as smooth as the downward, the mirror is only raised following an evaporation sequence and prior to loading the MOT and CO_2 laser trap for a new sequence. At

that time, any problems with the retroreflected beam profile can be ignored safely, as long as the flat mirror is fully raised by the time trap loading is complete and the MOT beams are shut off.

5.4 Correcting First-Order Beam Misalignment

As explained in Section 5.3.1, as the rf power fed to the CO_2 laser AOM is varied, the angle at which the first-order beam emerges from the AOM changes. As the rf power is varied from full to off, the first-order beam angle changes by 2.8 mrad. The first-order beam thus moves horizontally at the first lens of our $\times 10$ telescope, which converts this small linear motion to a large displacement of nearly an inch, causing much of the beam to be clipped by either the final lens holder in the telescope or the lens holder just before the vacuum system's ZnSe window. We have attempted to solve this problem in two ways: by imaging the beam as it emerges from the AOM and by actively compensating for the angular change by changing the frequency of rf power fed to the AOM.

5.4.1 The Imaging Approach

The main problem with the angular deviation is how the $\times 10$ telescope converts the resulting small horizontal motion into a large horizontal deviation at its output. The closer to the AOM the $\times 10$ telescope is placed, the less displacement will occur, since the displacement is proportional to how far the beam has propagated from the AOM. It would be ideal if the $\times 10$ telescope could be placed directly at the exit face of the AOM crystal.

This cannot be done, as the zeroth-order beam must be allowed to propagate

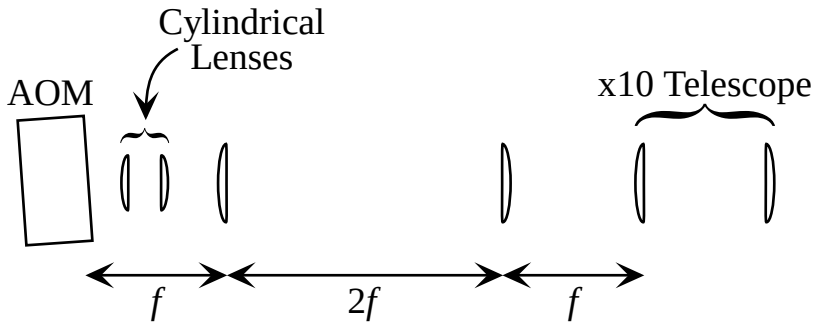

Figure 5.9: The $4f$ setup used to image the first-order beam as it emerges from the AOM and place that image on the input of the $\times 10$ telescope.

far enough that it may be safely deflected into a beam dump without disturbing the first-order beam. What can be done is place lenses in the "$4f$" configuration in order to image the first-order beam as it exits the AOM onto the input of the $\times 10$ telescope. The $4f$ configuration consists of two lenses forming a $\times 1$ refractor telescope, as shown in Figure 5.9. The lenses share a common focal length f (we used two 7.5 in. focal length lenses) and are placed a distance $2f$ apart. The $4f$ system's first lens is placed a distance f after the AOM, while the $\times 10$ telescope is placed a distance f after the $4f$ system. The first-order beam is thus imaged directly from the exit of the AOM onto the $\times 10$ telescope.

When set up, this system did indeed negate the linear displacement of the first-order beam as it emerged from the $\times 10$ telescope. No deviation at the lens before the vacuum system was observed as the AOM rf power was varied from full to off. There was another problem that made this solution unworkable: interference. The DEOS CO_2 laser employs a rectangular waveguide in its construction in order to produce the maximum amount of power in the TEM_{00} mode. At full power, this waveguide produces a small amount of "ghosting," in which a small amount of laser power is produced along the horizontal direction, as shown in (a) of Figure 5.10. When the ghosted beam passes through the AOM, the beam's wings have a slightly

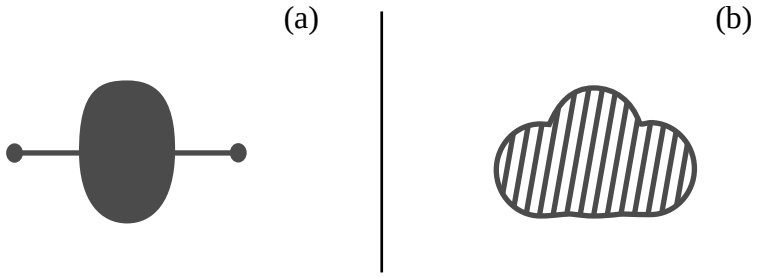

Figure 5.10: A sketch of the CO_2 laser beam (a) as it emerges from the CO_2 laser and (b) directly after the $\times 10$ telescope with the $4f$ system in place.

different angular displacement its main body. Directly after the AOM, the beam's wings and body overlap spatially, causing an interference pattern, but as the beam propagates, its wings move away from the main first-order beam. With the $4f$ system in place, the beam is sampled at the point where the interference pattern exists, causing the beam emerging from the $\times 10$ telescope to look like that shown in (b) of Figure 5.10. The interference does not disappear until the first-order beam is allowed to propagate for some distance, at which point the angular displacement once again becomes a linear one on the input to the $\times 10$ telescope.

5.4.2 AOM Frequency Correction

The second method of correcting the angular misalignment of the first-order beam is to change the frequency of the rf power fed to the AOM, changing the angle of the first-order beam by an amount equal and opposite to that caused by AOM heating. To vary the frequency of the rf power, we modified the AOM driver as explained in Section 4.5.1.

To determine what frequencies are required, we allow the CO_2 laser beam to propagate around 19 ft. to an iris. Since the angular displacement is caused mostly by the rf power heating the crystal, we can lower the CO_2 laser's power to diminish

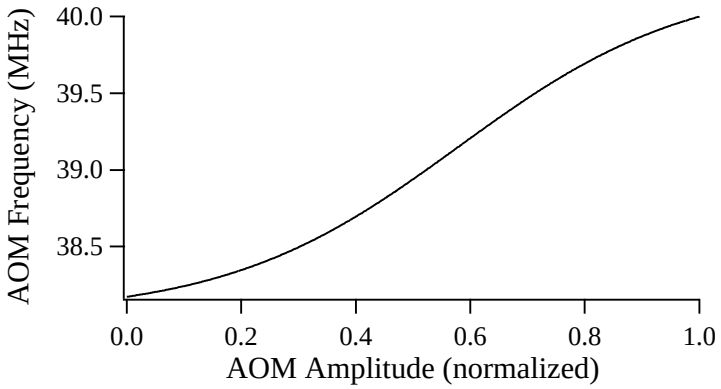

Figure 5.11: The frequency correction required to keep the CO_2 laser beam from being angularly misaligned as a function of AOM amplitude voltage.

the danger in allowing the CO_2 laser beam to propagate that distance. We lowered the amplitude voltage fed to the AOM driver, then adjusted the rf power's frequency until the beam was once again aligned on the iris. Figure 5.11 shows the required frequency correction as a function of AOM amplitude voltage. It is well approximated by a sigmoid function,

$$f(V) = f_{base} + \frac{\delta}{1 + \exp((V - V_{half})/r)}, \tag{5.29}$$

where f_{base}, δ (the amplitude of the deviation from f_{base}), V_{half} (the voltage at which the frequency deviation is equal to $\delta/2$), and r (the rate at which the deviation changes) are all fit parameters.

The drawback to this approach is that all measurements were done at steady state, and the angular deviation is due to thermal effects. When the AOM amplitude voltage is lowered continuously, the frequency correction is incorrect until the temperature of the AOM crystal has a chance to stabilize. To account for this, we approximate the thermal effect by adding a virtual electronic RC filter to the frequency correction. The software that generates the frequency correction waveform

$f(t)$ then transforms that waveform according to

$$f'(t) = \frac{e^{-t/RC}}{RC} \int_0^t f(\tau) e^{\tau/RC} d\tau + f(0) e^{-t/RC}, \tag{5.30}$$

where RC is the filter's effective time constant. Experimentation showed that a time constant of $RC = 1.3\,\mathrm{s}$ kept the beam from moving significantly as the AOM amplitude voltage was lowered.

The rf signal for the AOM is created by an Agilent E4420B rf generator, then amplified within the AOM driver. Frequency correction is accomplished by frequency modulating the E4420B using an Agilent 33250A arbitrary waveform generator. The voltage wave corresponding to the appropriate frequency correction is created by the same Perl script which creates the AOM amplitude voltage waveform. The script generates the voltage waveform, then uses that waveform in generating the frequency correction waveform. Both waveforms are sent to their respective arbitrary waveform generators by the IntuiLink software.

The frequency correction scheme does work, but it introduces noise, as the frequency stability of the E4420B decreases noticeably when frequency modulation is engaged. In initial experiments, when the FM was engaged, after ten seconds of forced evaporation 150,000 atoms remained with a temperature of $20\,\mu$K; without FM that number fell to 80,000 atoms but their temperature was $7\,\mu$K. The increased loss of atoms was due to the CO_2 laser beam misaligning once FM was turned off, making the power decrease as the beam was clipped. We are currently investigating ways of making the rf frequency stable enough during frequency modulation for frequency correction to be a viable solution.

5.5 Evaporation to Degeneracy

The CO_2 laser trap is loaded by spatially overlapping it with the MOT, causing the MOT and CO_2 laser trap to come into thermal and diffusive equilibrium with each other. This occurs over the five seconds of MOT loading (Section 3.4.6). Once that is complete, the MOT, repumper, and slower beams are turned off and the MOT atoms allowed to disperse. The two-beam CO_2 laser trap typically confines 3.5×10^6 atoms at a temperature[2] of $150\,\mu$K.

For free evaporation (*i.e.* evaporation in which trap well depth is not adiabatically lowered), the current in one of the two MOT magnets is reversed by a mechanical relay, switching the magnets from an anti-Helmholtz configuration to a Helmholtz one. To do this, the magnets are switched off for 1 ms to allow all eddy currents to die away; the relay is switched, taking 500 ms; and the magnets are turned back on. Both magnets receive 23 A of current, producing a bias field of 130 G at the CO_2 laser trap. This field yields a scattering length of $a_{12} \simeq -100a_0$.

Free evaporation is allowed to occur for six seconds. The Chopper arm is lowered some four seconds after free evaporation begins and removes the retroreflected CO_2 laser beam over the course of one second, after which free evaporation continues for another second to ensure that evaporation has stagnated. At the conclusion of free evaporation, 1.3×10^6 atoms remain at a temperature of $50\,\mu$K. The corresponding phase space density is equal to $\rho_i = 8\times10^{-3}$. A longer free evaporation phase does not appreciably decrease either the number of atoms or their temperature, indicating that evaporation has stagnated. Our trap depth is approximately $690\,\mu$K, indicating that stagnation has occurred at $\sim 1/14$ of the trap depth.

[2]All temperatures in this chapter are measured by time-of-flight absorption imaging unless otherwise noted.

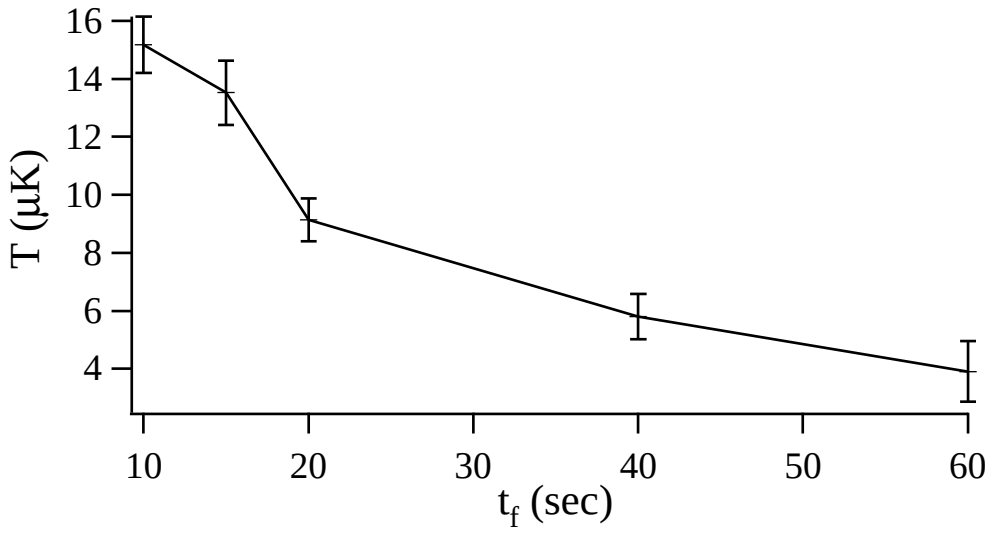

Figure 5.12: The average temperature of the trapped atoms after t_f seconds of forced evaporation

Following free evaporation, the trap's depth is adiabatically lowered according to (5.26). Assuming $\eta = 10$ gives[3] $\beta = 1.45$ and $1/\tau = 1.97\times10^{-3}\gamma_i$. For a 50-50 two-state mixture of fermions, $\gamma_i = \pi N_i M\sigma\nu_i^3/(k_B T)$. For a scattering length of $a_{12} \simeq -100a_0$, $\sigma = 8\pi a_{12}^2 = 0.7\times10^{-11}\,\mathrm{cm}^2$. The initial geometric mean of our trap frequencies is $\nu_i = (\nu_x\nu_y\nu_z)^{1/3} = 2.4\,\mathrm{kHz}$. Using $N_i = 1.3\times10^6$ and $T_i = 50\,\mu\mathrm{K}$ yields $\gamma_i = 4.4\times10^2\,\mathrm{s}^{-1}$ and $\tau = 0.89\,\mathrm{s}$. We do not lower with that time constant, however. For one thing, as the rf power to the AOM is lowered, the beam becomes more elliptical, reducing $\nu_x\nu_y\nu_z$ by a factor of two greater than that expected on the basis of lowered laser power alone. For another, the frequency correction scheme given in Section 5.4.2 introduces an unacceptable amount of noise, leading us to allow the CO_2 laser beam to misalign as the AOM rf power is lowered. We align the beam to minimize the clipping which occurs, but the remaining clipping further

[3]We take $\eta = 10$ and not 14 in order to have a conservative estimate of how quickly to lower the trap. Integration of the Boltzmann equation showed that η should remain at 10 or greater, and we did not want to trust that our high value of $\eta = 14$ would remain true throughout evaporation.

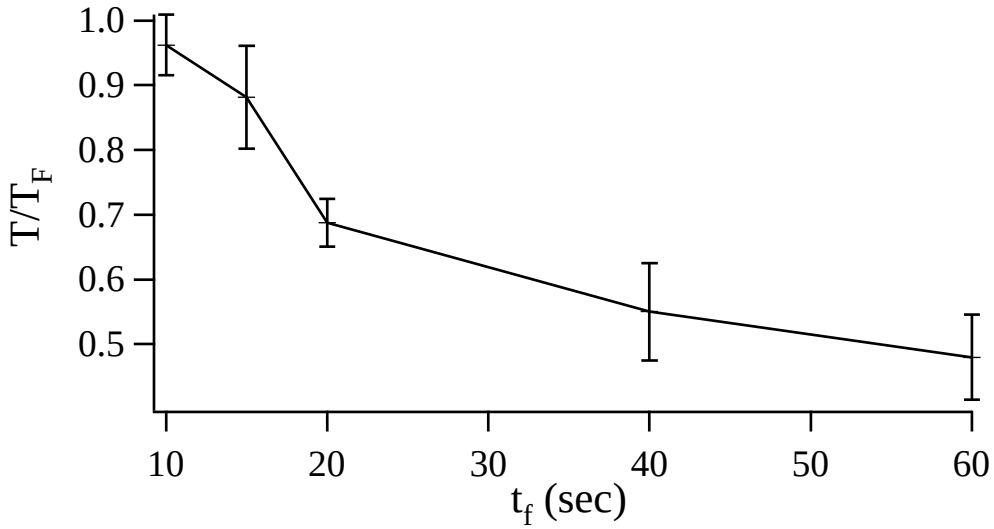

Figure 5.13: The average ratio of the atoms' temperature to the Fermi temperature after t_f seconds of forced evaporation.

distorts the beam. To compensate for beam distortion, we increase τ to 3 seconds.

We lower the trap for a time t_f ranging from a few to sixty seconds. During that time, the temperature decreases, as shown in Figure 5.12. The number also decreases, but overall the phase space density increases, as indicated by the decreasing ratio of T/T_F, shown in Figure 5.13. After the trap has been lowered, CO_2 laser power is increased to its maximum value. Since both depth and trap frequencies changes as the laser power changes, returning to the maximum value after evaporation provides a fixed point of comparison for all values of t_f. Power is increased exponentially over a period of five seconds. We can measure how well evaporation has worked by calculating the evaporation efficiency $\chi = ln(\rho_f/\rho_i)/ln(N_i/N_f)$ [81].

After free evaporation but prior to forced evaporation, $N = 1.3{\times}10^6$, $T = 50\,\mu$K, $T_F = 18.1\,\mu$K, and the phase space density for each state is $\rho \simeq (T_F/T)^3/6 \simeq 0.008$ [78]. After ten seconds of forced evaporation, the well depth should be $U/U_i = 0.12$. $N = 8 \times 10^5$ atoms at a temperature of $T \simeq 15.4\,\mu$K remain. The Fermi

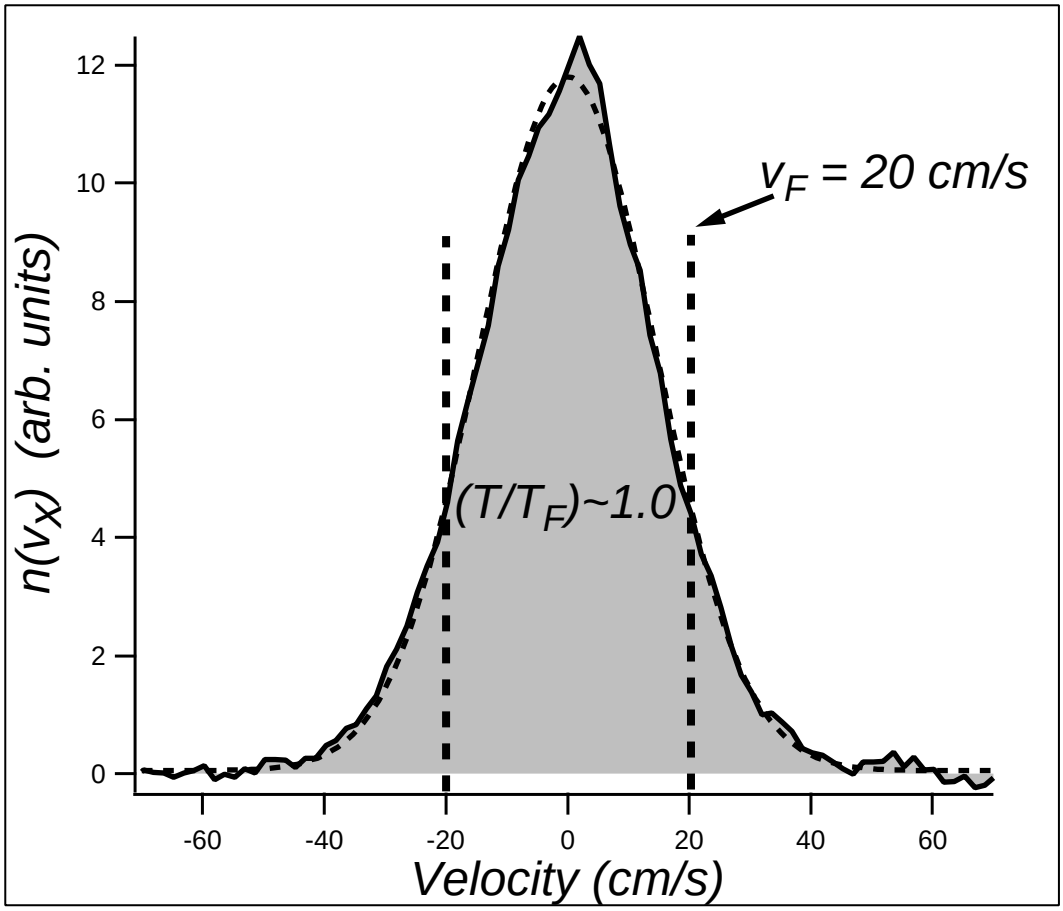

Figure 5.14: The velocity distribution of the trapped atoms after ten seconds of forced evaporation.

temperature, which is given by (4.38), is $T_F = 15.4\,\mu$K, resulting in $T/T_F = 1$ and $\rho = 0.17$. Efficiency at this point is $\chi = 6.3$. According to the scaling laws, the number of atoms remaining should be 8.7×10^5 and the phase space density should be 0.13. The number of atoms given by the scaling laws is within 10% of our measured number of atoms. The measured phase space density is greater than that calculated using the scaling laws. This is most likely due to beam clipping reducing the well depth below $U/U_i = .12$.

Figure 5.14 shows the velocity distributions for $t_f = 10\,$s. The dashed lines

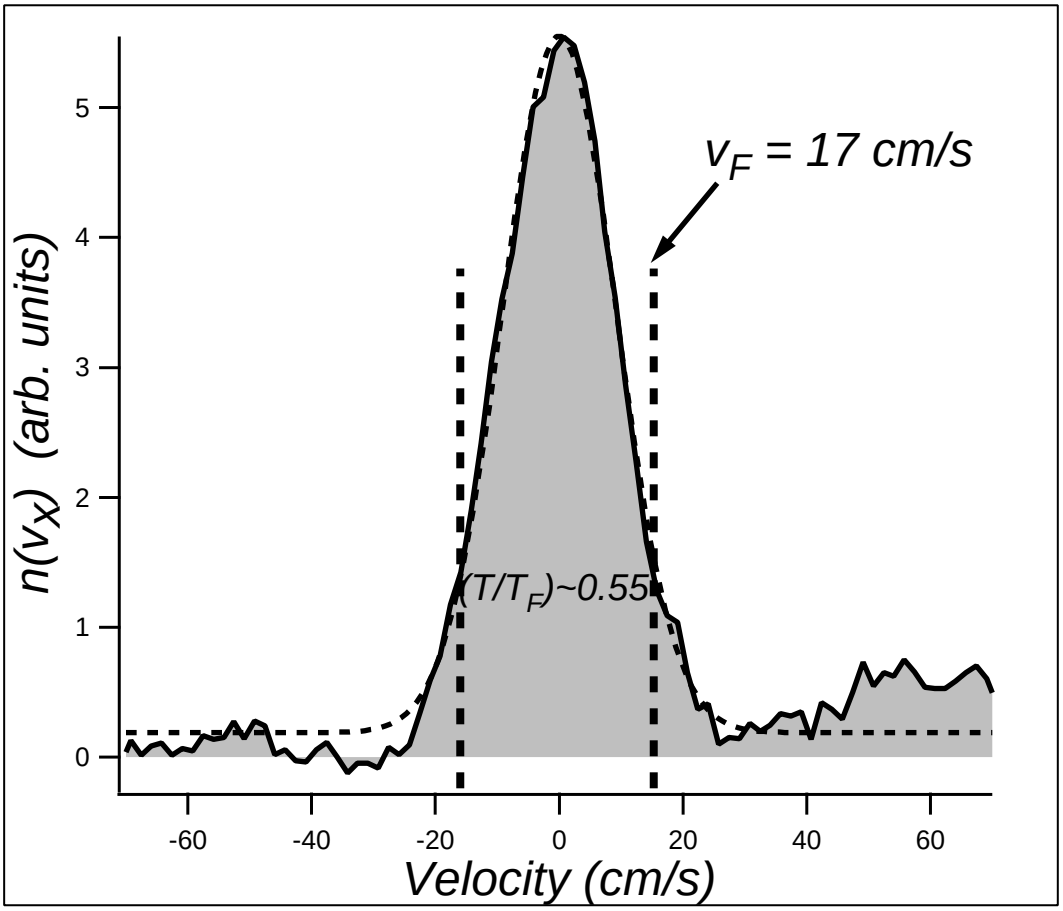

Figure 5.15: The velocity distribution of the trapped atoms after forty seconds of forced evaporation.

indicate the Fermi velocity, given by $\sqrt{2k_BT_F/M}$.

Degeneracy occurs at $\sim t_f = 40\,\mathrm{s}$, at which point $N = 3\times10^5$, $T \simeq 5.8\,\mu\mathrm{K}$, and $T/T_F = 0.55$, giving $\rho \simeq 1$. Figure 5.15 shows the velocity distribution for this amount of forced evaporation. Significantly more of the atoms lie within the Fermi velocity than after ten seconds of forced evaporation. The efficiency has dropped to $\chi = 3.41$, indicating that cooling has not kept pace with atom loss.[4] The scaling laws predict that the number of remaining atoms should be 6.2×10^5. The increased

[4]It should be noted that an efficiency of 3.41 is comparable to the best achieved in magnetic traps [81].

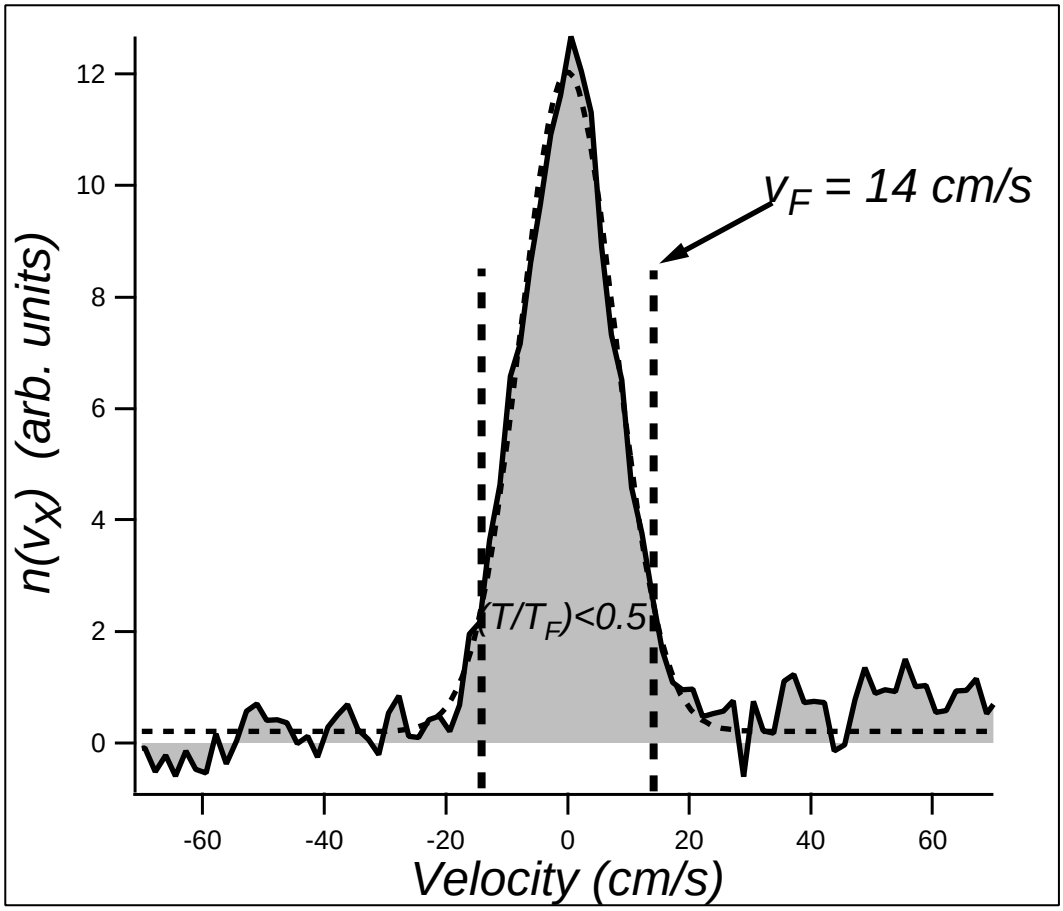

Figure 5.16: The velocity distribution of the trapped atoms after sixty seconds of forced evaporation.

loss of atoms is caused by increased CO_2 laser beam clipping as CO_2 laser power is lowered.

At $t_f = 60\,\mathrm{s}$, $N = 1\times10^5$, $T \simeq 4\,\mu\mathrm{K}$, and $T/T_F = 0.5$. The atomic velocity distribution is shown in Figure 5.16. For $t_f > 60\,\mathrm{s}$, the phase space density *decreases*: clipping increases to the point that atoms are lost without a concurrent decrease in temperature.

5.6 Summary

This chapter has developed the necessary experimental and theoretical tools to cool trapped fermions to the degenerate regime in an optical trap. The kinetic theory of evaporation was developed, using an s-wave Boltzmann equation which accounts for both the fermionic nature of the trapped atoms and the time dependency of the trap depth. In addition, scaling laws were developed in order to give better physical insight and a method of quickly determining the approximate number of atoms remaining after evaporation and their temperature. These scaling laws also defined how the trap should be lowered over time.

To the CO_2 laser optical setup an AOM and the Chopper were added. The AOM allows CO_2 laser power to be varied as a function of time, providing the required lowering of trap depth in order to prevent evaporative cooling from stagnating. The AOM causes beam ellipticity and an angular deviation, both of which vary as AOM rf power is lowered. The ellipticity cannot be corrected except at full power, while the angular deviation can, to a certain extent, be compensated for. Two methods of compensation were given, one involving imaging the emerging first-order beam onto the $\times 10$ telescope, the other involving altering the frequency of the rf power to actively correct angular deviation. Neither approach has proved completely effective, though alterations to the frequency variation approach may make it a feasible solution in the near future. Due to the angular deviation of the first-order AOM beam, the retroreflected beam must be removed before forced evaporation begins. That is accomplished by the Chopper, a pneumatically-controlled mirror which, when lowered, deflects the beam emerging from the vacuum system into a beam dump and thus removing the retroreflected beam.

With those changes in place, we began evaporation of ^{6}Li. Using a 50-50 mixture

of the $|1\rangle$ and $|2\rangle$ ground state of ^{6}Li, we have produced a degenerate gas of fermions, the first created by all-optical means. Degeneracy was achieved after forty seconds of evaporation. After sixty seconds, temperatures of $T/T_F = 0.48$ were achieved. Further evaporative cooling was prevented by misalignment of the first-order beam. When the frequency compensation method is perfected, even lower temperatures and greater phase-space densities should be achieved.

Chapter 6

Density of a Two-Component Interacting Fermi Gas at Zero Temperature

Having evaporatively cooled fermions to the quantum degenerate regime using an optical trap, the question becomes: what next? A number of very exciting experiments are possible, including the study of superfluidity and how the gas's collective oscillations damp as a function of the scattering length. These experiments hinge on our ability to achieve a broad range of scattering lengths.

Such a range can be achieved with the help of a Feshbach resonance, as mentioned in Chapter 2. The $|1\rangle - |2\rangle$ mixture used in our experiments is predicted to exhibit a Feshbach resonance at a magnetic field of 850 G. In the region of the Feshbach resonance, the scattering length varies from large and positive to large and negative. Towards this end, new magnets are being constructed and added to our vacuum system; these magnets should be able to achieve fields in excess of 1000 G.

Once the magnets are in place, one of the first things to explore is how the scattering length a changes as a function of magnetic field. The change can be observed by monitoring the density distribution of the trapped gas. Changes in the scattering length alter the interaction strength between fermions of different spin, and can even make the interactions attractive or repulsive. In turn, the gas's

density distribution will change in response to the changing interaction. The density changes are most notable by comparing the density when a is large and negative (and thus attractive) and when a is large and positive.

To prepare for such future experiments, this section will develop the theory necessary to show how the density at zero temperature changes as a function of a. A force-balance approach will be used in the mean field approximation, where the forces due to the trap, the Fermi pressure of the atoms, and the mean-field interaction of one state on another sum to zero. The zero-temperature limit is used because it is most applicable to fermions that are cooled well into the quantum degenerate regime, and because the theory is more tractable in this limit.

6.1 Force Balance

The density distribution for an ideal fermionic gas has been calculated using a semi-classical Thomas-Fermi approximation [78]. For non-ideal, interacting fermionic gases, the density distribution has been found by taking the Hamiltonian of the gas [55] and using it to calculate the expectation of the number operator $\langle a^\dagger_{\mathbf{k},\alpha} a_{\mathbf{k},\alpha}\rangle$ for all states of momentum $\mathbf{k}$ and both hyperfine states α [15]. Doing so requires a Bogoliubov transformation of the Hamiltonian, replacing the usual fermion creation and annihilation operators $a_{\mathbf{k},\alpha}$ and $a^\dagger_{\mathbf{k},\alpha}$ with ones for quasiparticles, $b_{\mathbf{k},\alpha}$ and $b^\dagger_{\mathbf{k},\alpha}$. The gas's stability can also be found by computing its free-energy density and using that to compute the sound velocities in the gas.

However, the density distribution can also be found by considering the forces on the fermions. In equilibrium, all of these forces must sum to zero, constraining the density of the two hyperfine fermionic states. To find the sound velocities of the gas, and thus its mechanical stability, small perturbations in the density can be

considered and their speed of propagation readily found. The rest of this chapter will be devoted to finding the fermion density distribution as a function of a using this force balance approach. Initially, the density distribution for a single-state fermionic gas will be considered; once that is done, the results will be expanded for a two-state gas by using a mean-field approximation of the states' interaction. Following that, the sound velocity in the gas will be derived and used to set limits on mechanical stability. Finally, the two-state gas results will be explored using experimentally-feasible details.

6.1.1 Homogeneous ^{6}Li Gas

For a gas comprised of a single state of ^{6}Li, there will be two forces in equilibrium: the force due to the gas's pressure, and the force due to the trap. The local pressure for the single-state ^{6}Li gas is given by the derivative of the gas's average energy with respect to the local volume,

$$P = -\frac{\partial \langle E \rangle}{\partial V}. \tag{6.1}$$

At zero temperature, the atom's average energy can be found by integrating the single-particle energy $\hbar^2 k^2/2M$ up to the Fermi wave number k_F:

$$\begin{aligned} \langle E \rangle &= \frac{V}{(2\pi)^3} \int_0^{k_F} 4\pi k^2 \frac{\hbar^2 k^2}{2M}\, dk \\ &= \frac{V}{(2\pi)^3} \frac{4\pi\hbar^2}{2M} \frac{k_F^5}{5}. \end{aligned} \tag{6.2}$$

The dependence of k_F on the local volume V can be seen by considering the number of atoms N in the local volume, which is given by the volume of the Fermi

sphere in momentum space,

$$N = \frac{V}{(2\pi)^3}\frac{4}{3}\pi k_F^3. \tag{6.3}$$

Solving (6.3) for k_F and substituting that value into (6.2),

$$\langle E\rangle = \frac{3}{5}\frac{\hbar^2}{2M}\left(6\pi^2\right)^{2/3}\frac{N^{5/3}}{V^{2/3}}. \tag{6.4}$$

The single-state gas pressure is then

$$\begin{aligned} P = -\frac{\partial\langle E\rangle}{\partial V} &= \frac{\left(6\pi^2\right)^{2/3}}{5}\frac{\hbar^2}{M}\left(\frac{N}{V}\right)^{5/3} \\ &= \frac{\left(6\pi^2\right)^{2/3}}{5}\frac{\hbar^2}{M}n^{5/3}, \end{aligned} \tag{6.5}$$

where $n = N/V$ is the gas's local density.

The pressure gives rise to a force per volume,

$$\begin{aligned} \mathbf{f}_P = -\boldsymbol{\nabla}P &= -\frac{\partial P}{\partial n}\boldsymbol{\nabla}n \\ &= -\frac{\left(6\pi^2\right)^{2/3}}{3}\frac{\hbar^2}{M}n^{2/3}\boldsymbol{\nabla}n. \end{aligned} \tag{6.6}$$

The pressure force's direction is along the reverse gradient of the density, as expected. At equilibrium, the pressure force will balance the trap force per volume,

$$\mathbf{f}_T = nF_T = -n\boldsymbol{\nabla}U_T, \tag{6.7}$$

where U_T is the trap potential. The force balance equation is then

$$-\frac{(6\pi^2)^{2/3}}{3}\frac{\hbar^2}{M}n^{2/3}\boldsymbol{\nabla}n - n\boldsymbol{\nabla}U_T = 0. \tag{6.8}$$

Dividing (6.8) by $-n$ and noting that $n^{-1/3}\boldsymbol{\nabla}n = {}^3\!/_2\boldsymbol{\nabla}n^{2/3}$,

$$\frac{(6\pi^2)^{2/3}}{2}\frac{\hbar^2}{M}\boldsymbol{\nabla}n^{2/3} + \boldsymbol{\nabla}U_T = 0. \tag{6.9}$$

This equation indicates that the quantity

$$\frac{(6\pi^2)^{2/3}}{2}\frac{\hbar^2}{M}n^{2/3} + U_T, \tag{6.10}$$

which is the local chemical potential, must be a constant, so that its gradient is zero. The value of this constant can be found by noting that, at the trap center, $U_T = 0$. If we denote the local density at the trap center as $n_i = n(0)$, then we arrive at an equation for the trapped gas density,

$$\frac{(6\pi^2)^{2/3}}{2}\frac{\hbar^2}{M}n^{2/3} + U_T = \frac{(6\pi^2)^{2/3}}{2}\frac{\hbar^2}{M}n_i^{2/3}. \tag{6.11}$$

If the above equation is correct, the central density n_i should be equal to the Fermi density n_F, and the spatial distribution should be that of a Fermi gas. This can be verified by solving (6.11) for n, then integrating it over all space to find N,

the total number of atoms. Solving (6.11) for n gives

$$\begin{aligned} n &= \left(n_i^{2/3} - \frac{2M}{(6\pi^2)^{2/3}\hbar^2}U_T\right)^{3/2} \Theta\left[n_i^{2/3} - \frac{2M}{(6\pi^2)^{2/3}\hbar^2}U_T\right]^{3/2} \\ &= \left(n_i^{2/3}\right)^{3/2}\left(1 - \frac{2M}{(6\pi^2)^{2/3}\hbar^2 n_i^{2/3}}U_T\right)^{3/2} \Theta\left[n_i^{2/3} - \frac{2M}{(6\pi^2)^{2/3}\hbar^2 n_i^{2/3}}U_T\right]^{3/2} \\ &= n_i\left(1 - \frac{U_T}{\epsilon_{F0}}\right)^{3/2} \Theta\left[1 - \frac{U_T}{\epsilon_{F0}}\right]^{3/2}, \end{aligned} \tag{6.12}$$

where the constant ϵ_{F0} has been used to simplify notation. The Heaviside step function Θ is necessary to ensure that n is positive.

The trap potential in the harmonic limit is

$$U_T(x,y,z) = \frac{1}{2}M\left(\omega_x^2 x^2 + \omega_y^2 y^2 + \omega_z^2 z^2\right), \tag{6.13}$$

where the ω terms are the trap oscillation frequencies. We can simplify the trap potential by working in a scaled coordinate system where $x' = \omega_x x$, $y' = \omega_y y$, and $z' = \omega_z z$. In this coordinate system the trap potential is merely

$$U_T(r') = \frac{1}{2}Mr'^2, \tag{6.14}$$

where $r'^2 = x'^2 + y'^2 + z'^2$. The integral of (6.12) over all space is thus

$$\begin{aligned} N &= \int d^3\,\mathbf{r}\; n \\ &= \frac{4\pi n_i}{\omega_x\omega_y\omega_z}\int dr'\; r'^2\left(1 - \frac{M}{2\epsilon_{F0}}r'^2\right)^{3/2}\Theta\left[1 - \frac{M}{2\epsilon_{F0}}r'^2\right]^{3/2} \end{aligned} \tag{6.15}$$

The integral can be solved by making the substitution $\sin\theta = \sqrt{M/2\epsilon_{F0}}\; r'$ and

integrating from 0 to $\pi/2$:

$$\begin{aligned}
&\int dr'\ r'^2 \left(1 - \frac{M}{2\epsilon_{F0}} r'^2\right)^{3/2} \Theta\left[1 - \frac{M}{2\epsilon_{F0}} r'^2\right]^{3/2} \\
&\quad = \left(\frac{2\epsilon_{F0}}{M}\right)^{3/2} \int_0^{\pi/2} d\theta\ \cos\theta\ \sin^2\theta \cos^3\theta \\
&\quad = \left(\frac{2\epsilon_{F0}}{M}\right)^{3/2} \frac{\pi}{32} \\
&\quad = \frac{n_i 6\pi^2\hbar^3}{M^3} \frac{\pi}{32}.
\end{aligned} \tag{6.16}$$

Substituting (6.16) into (6.15) and defining $\sigma_x = \sqrt{\hbar/M\omega_x}$ gives

$$N = \frac{3\pi^4}{4} (\sigma_x \sigma_y \sigma_z)^2 n_i^2, \tag{6.17}$$

or

$$n_i = \frac{1}{\pi^2} \sqrt{\frac{4}{3}} \frac{\sqrt{N}}{\sigma_x \sigma_y \sigma_z}. \tag{6.18}$$

The right-hand side of this equation is indeed equal to the Fermi density n_F, and the spatial distribution is that of an ideal trapped Fermi gas [78].

6.1.2 Two-State ^{6}Li Gas

While (6.11) is valid for one state, it must be modified if two spin states of ^{6}Li are present. Two such spin states will interact with each other through two-body collisions; those collisions can be represented in a mean-field approximation at zero temperature by a local potential with strength $U_c = 4\pi\hbar^2 a n'/M$, where a is the scattering length and n' is the density of the other spin state [86].

The local potential serves to couple the densities of the two spin states n_1 and n_2. A derivation similar to the above, but with U_T replaced by $U_T + U_c$, results in

the conserved quantity

$$\frac{(6\pi^2)^{2/3}}{2}\frac{\hbar^2}{M}n_1^{2/3} + \frac{4\pi\hbar^2 a}{M}n_2 + U_T, \tag{6.19}$$

analogous to (6.10). An identical quantity exists for an exchange of n_1 and n_2 in (6.19). The conserved quantity's value can again be found by considering its value at the trap center, where $U_T = 0$. The result is two coupled equations for the densities of the two spin states,

$$\begin{aligned}
\frac{(6\pi^2)^{2/3}}{2}\frac{\hbar^2}{M}n_1^{2/3} + \frac{4\pi\hbar^2 a}{M}n_2 + U_T &= \frac{(6\pi^2)^{2/3}}{2}\frac{\hbar^2}{M}n_{1i}^{2/3} + \frac{4\pi\hbar^2 a}{M}n_{2i} \\
\frac{(6\pi^2)^{2/3}}{2}\frac{\hbar^2}{M}n_2^{2/3} + \frac{4\pi\hbar^2 a}{M}n_1 + U_T &= \frac{(6\pi^2)^{2/3}}{2}\frac{\hbar^2}{M}n_{2i}^{2/3} + \frac{4\pi\hbar^2 a}{M}n_{1i},
\end{aligned} \tag{6.20}$$

where n_{1i} and n_{2i} are the spin densities at the trap center.

6.2 Stability of the Gas

Not all solutions of (6.20) are physically valid. Some of them may correspond to mechanically-unstable states of the gas. For a system with attractive interactions ($a < 0$), at large densities the gas will become a fluid or solid, while for a system with repulsive interactions ($a > 0$), at large densities the two spin states will phase separate [15].

Mechanical instability occurs when the velocity of the two normal sound modes in the gas become complex. If the sound velocity is complex, then the small gas displacements which occur during a sound wave grow, causing instability. The instability criterion can thus be found by calculating the sound velocity inside the gas.

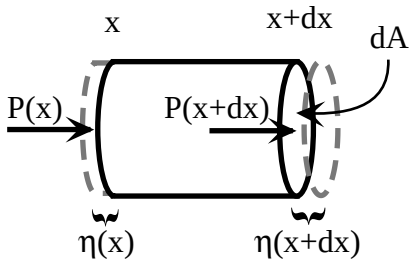

Figure 6.1: The displacement of a small cylindrical region of gas by a sound wave. One end of the cylinder is located at x; the other, at $x + dx$. dA is the surface area of the infinitesimally-small cylinder. η is the amount of displacement caused by the pressure P. Both η and P vary as a function of x.

Consider the one-dimensional displacement of an infinitesimally-small cylinder of gas of length dx, as shown in Figure 6.1. $\eta(x)$ is a measure of the displacement of one of the cylinder ends due to the pressure $P(x)$. The surface area of the cylinder ends is dA.

The pressure on both ends of the cylinder will give rise to a force,

$$\begin{aligned} F &= P(x)\,dA - P(x+dx)\,dA = dA\,(P(x) - P(x+dx)) \\ &= -dx\,dA\frac{\partial P}{\partial x}. \end{aligned} \tag{6.21}$$

The force will cause an acceleration in the gas equal to $\partial^2\eta/\partial t^2$. If the gas has a mass density of $\rho = nM$, where n is the gas density and M the mass of ^{6}Li, then $F = Ma$ is equivalent to

$$\begin{aligned} dx\,dA\,\rho\frac{\partial^2\eta}{\partial t^2} &= -dx\,dA\frac{\partial P}{\partial x} \\ &= -dx\,dA\frac{\partial P}{\partial \rho}\frac{\partial \rho}{\partial x}. \end{aligned} \tag{6.22}$$

The cylinder's mass density is the number of atoms in the cylinder, N, times their mass and divided by the cylinder's volume. That volume is equal to dA times

its length,

$$\begin{aligned}(x + dx + \eta(x + dx)) - (x + \eta(x)) &= dx + (\eta(x + dx) - \eta(x)) \\ &= dx + dx\frac{\partial \eta}{\partial x}. \end{aligned} \tag{6.23}$$

The cylinder's mass density is then

$$\begin{aligned}\rho = \frac{NM}{dA\, dx\left(1 + \frac{\partial \eta}{\partial x}\right)} &= \frac{\rho_0}{1 + \frac{\partial \eta}{\partial x}} \\ &\simeq \rho_0 \left(1 - \frac{\partial \eta}{\partial x}\right), \end{aligned} \tag{6.24}$$

where $\rho_0 = NM/(dA\, dx)$ is the unperturbed mass density.

Substituting this value of ρ into (6.22) gives, to lowest order in η,

$$\rho_0 \ddot{\eta} = \frac{\partial P}{\partial \rho}\rho_0 \frac{\partial^2 \eta}{\partial x^2}. \tag{6.25}$$

How the pressure changes with respect to mass density is related to the sound velocity v_s by

$$v_s^2 = \frac{\partial P}{\partial \rho}. \tag{6.26}$$

Therefore, (6.25) can be rewritten as

$$\ddot{\eta} = v_s^2 \eta'', \tag{6.27}$$

which allows plane-wave solutions for η,

$$\eta = Ae^{i(kx - \omega t)}, \tag{6.28}$$

where A is the amplitude of the plane wave, k is its wave number, and $\omega = v_s k$. The plane-wave solution confirms the stability criterion: if v_s is complex, then η will have a real component which will grow in time, causing small displacements to increase in magnitude.

To find v_s for a two-component gas of ^{6}Li, consider the force on the gas per volume[1],

$$\begin{aligned} \mathbf{f} &= -\boldsymbol{\nabla} P - n\boldsymbol{\nabla} U \\ &= -\frac{\partial P}{\partial n}\boldsymbol{\nabla} n - n\boldsymbol{\nabla} U, \end{aligned} \tag{6.29}$$

where U is the total potential acting on the gas. From the previous section we know that the single-state gas pressure is given by (6.5) and that the potential U will be the sum of the trap potential and the mean-field potential arising from the other state,

$$U_{1,2} = U_T + U_c = U_T + \frac{4\pi\hbar^2 a}{M} n_{2,1}. \tag{6.30}$$

The force along the direction of sound propagation will be equal to the mass times the acceleration, as before:

$$M n_{1,2} \frac{\partial^2 \eta_{1,2}}{\partial t^2} = -\frac{(6\pi^2)^{2/3}}{3}\frac{\hbar^2}{M} n_{1,2}^{2/3}\frac{\partial n_{1,2}}{\partial x} - n_{1,2}\left(\frac{\partial U_T}{\partial x} + \frac{4\pi\hbar^2 a}{M}\frac{\partial n_{2,1}}{\partial x}\right). \tag{6.31}$$

Just as the mass density ρ is given by (6.24), the number density $n_{1,2}$ is given by

$$n_{1,2} = n_{(1,2)0}\left(1 - \frac{\partial \eta_{1,2}}{\partial x}\right), \tag{6.32}$$

[1]In what follows, the subscripts 1 and 2 denote the two different states, and the combinations $1,2$ and $2,1$ denote that the given equation has the same form for the appropriate combination of states.

where $n_{(1,2)0}$ is the unperturbed number density of the gas. The partial derivative of $n_{1,2}$ with respect to x is

$$\frac{\partial n_{1,2}}{\partial x} \simeq \frac{\partial n_{(1,2)0}}{\partial x} - n_{(1,2)0}\frac{\partial^2 \eta_{1,2}}{\partial x^2}, \tag{6.33}$$

where the term

$$\frac{\partial n_{(1,2)0}}{\partial x}\frac{\partial \eta_{1,2}}{\partial x} \tag{6.34}$$

has been neglected because $n_{(1,2)0}$ varies much more slowly than $\eta_{1,2}$ with respect to x. Using this derivative, (6.31) can be written as

$$\begin{aligned} M n_{(1,2)0}\ddot{\eta}_{1,2} = {} & \frac{(6\pi^2)^{2/3}}{3}\frac{\hbar^2}{M} n_{(1,2)0}^{2/3}\left(n_{(1,2)0}\frac{\partial^2 \eta_{1,2}}{\partial x^2} - \frac{\partial n_{(1,2)0}}{\partial x}\right) \\ & - n_{(1,2)0}\frac{\partial U_T}{\partial x} + \frac{4\pi\hbar^2 a}{M} n_{(1,2)0}\left(n_{(2,1)0}\frac{\partial^2 \eta_{2,1}}{\partial x^2} - \frac{\partial n_{(2,1)0}}{\partial x}\right). \end{aligned} \tag{6.35}$$

(6.35) can be simplified further by dividing it by $n_{(1,2)0}$ and noting that it contains the terms

$$\begin{aligned} & \frac{(6\pi^2)^{2/3}}{3}\frac{\hbar^2}{M} n_{(1,2)0}^{2/3}\frac{\partial n_{(1,2)0}}{\partial x} + \frac{4\pi\hbar^2 a}{M}\frac{\partial n_{(2,1)0}}{\partial x} + \frac{\partial U_T}{\partial x} \\ & \qquad = \frac{(6\pi^2)^{2/3}}{2}\frac{\hbar^2}{M}\frac{\partial n_{(1,2)0}^{2/3}}{\partial x} + \frac{4\pi\hbar^2 a}{M}\frac{\partial n_{(2,1)0}}{\partial x} + \frac{\partial U_T}{\partial x} \\ & \qquad = \frac{\partial}{\partial x}\left(\frac{(6\pi^2)^{2/3}}{2}\frac{\hbar^2}{M} n_{(1,2)0}^{2/3} + \frac{4\pi\hbar^2 a}{M} n_{(2,1)0} + U_T\right). \end{aligned} \tag{6.36}$$

The term in parentheses is the conserved quantity from (6.19). Since we have assumed a one-dimensional distribution, $\partial/\partial x$ is a one-dimensional gradient, and

thus (6.36) is zero[2]. (6.35) is then

$$\ddot{\eta}_{1,2} = \frac{\left(6\pi^2\right)^{2/3}}{3}\frac{\hbar^2}{M^2}n_{(1,2)0}^{2/3}\frac{\partial^2\eta_{1,2}}{\partial x^2} + \frac{4\pi\hbar^2 a}{M^2}n_{(2,1)0}\frac{\partial^2\eta_{2,1}}{\partial x^2}. \tag{6.37}$$

Substituting in the plane-wave solutions for η, which are

$$\eta_{1,2} = A_{1,2}e^{i(kx-\omega t)}, \tag{6.38}$$

and simplifying gives the following matrix equation for A_1 and A_2:

$$\begin{pmatrix} \frac{\left(6\pi^2\right)^{2/3}}{3}\frac{\hbar^2}{M^2}n_{10}^{2/3} - v_s^2 & \frac{4\pi\hbar^2 a}{M^2}n_{20} \\ \frac{4\pi\hbar^2 a}{M^2}n_{10} & \frac{\left(6\pi^2\right)^{2/3}}{3}\frac{\hbar^2}{M^2}n_{20}^{2/3} - v_s^2 \end{pmatrix}\begin{pmatrix} A_1 \\ A_2 \end{pmatrix} = 0. \tag{6.39}$$

Two constants will be used to simplify further notation,

$$\alpha \equiv \frac{\left(6\pi^2\right)^{2/3}}{3}\frac{\hbar^2}{M^2} \qquad\qquad \beta \equiv \frac{4\pi\hbar^2 a}{M^2}. \tag{6.40}$$

(6.39) will be true when

$$\begin{vmatrix} \alpha n_{10}^{2/3} - v_s^2 & \beta n_{20} \\ \beta n_{10} & \alpha n_{20}^{2/3} - v_s^2 \end{vmatrix} = 0. \tag{6.41}$$

Solving this determinant for v_s gives the rather long algebraic expression

$$v_s^{\pm} = \left(\frac{\alpha}{2}\left(n_{10}^{2/3} + n_{20}^{2/3}\right) \pm \frac{1}{2}\sqrt{\alpha^2\left(n_{10}^{2/3} - n_{20}^{2/3}\right)^2 + 4\beta^2 n_{10}n_{20}}\right)^{\frac{1}{2}}. \tag{6.42}$$

[2]Physically, this is the equilibrium condition. The force due to sound waves can thus be viewed as perturbations about this condition.

For both sound modes $v_s^{\pm}$ to be real, we need

$$\frac{\alpha}{2}\left(n_{10}^{2/3}+n_{20}^{2/3}\right) > \frac{1}{2}\sqrt{\alpha^2\left(n_{10}^{2/3}-n_{20}^{2/3}\right)^2+4\beta^2 n_{10}n_{20}}, \tag{6.43}$$

which simplifies to

$$\begin{aligned}(n_{10}n_{20}) &< \left(\frac{\alpha}{\beta}\right)^6 \\ &< \left(\frac{\pi}{48|a|^3}\right)^2.\end{aligned} \tag{6.44}$$

This stability limit is the same for both positive and negative a.

For a gas with an equal number of atoms in both states, the stability limit will always be satisfied as a consequence of unitarity. For zero-temperature fermions, $n = k_F^3/6\pi^2$ [78]. If $n_{10} = n_{20} = n$, then the stability condition may be rewritten as

$$\left(\frac{k_F^3}{6\pi^2}\right)^2 < \left(\frac{\pi}{48|a|^3}\right)^2 \tag{6.45}$$

or

$$k_F|a| < \frac{\pi}{2}. \tag{6.46}$$

a is related to the s-wave scattering cross section σ by $\sigma = 4\pi a^2$ at zero temperature, and the maximum scattering amplitude is given by the unitarity limit, $\sigma \leq 4\pi/k_F^2$. Rewriting the unitarity limit in terms of a and rearranging gives

$$k_F|a| \leq 1, \tag{6.47}$$

which is a tighter constraint than the stability limit.

6.3 Density Calculation

The coupled equations in (6.20) can be readily solved under the assumption that the gas contains an equal number of atoms in state 1 and 2, and that $n_1 = n_2$ (and, therefore, $n_{1i} = n_{2i}$). In practice we load near-equal populations of atoms in the two states, making the first assumption a reasonable one. Given the two equations' symmetry, the second assumption is likewise reasonable: if $\int n_1\, d^3x = \int n_2\, d^3x = N$, then $n_1 = n_2$ is an obvious solution to the coupled equations.

These two assumptions lead to a single equation,

$$\frac{\left(6\pi^2\right)^{2/3}}{2}\frac{\hbar^2}{M}n^{2/3} + \frac{4\pi\hbar^2 a}{M}n + U_T = \frac{\left(6\pi^2\right)^{2/3}}{2}\frac{\hbar^2}{M}n_i^{2/3} + \frac{4\pi\hbar^2 a}{M}n_i. \tag{6.48}$$

To make this equation more tractable, I introduce the new dimensionless variables $\gamma = (n/n_c)^{1/3}$ and $\gamma_i = (n_i/n_c)^{1/3}$, where n_c is a characteristic density scale to be determined later[3]. Substituting these variables into (6.48) and rearranging gives

$$\gamma^2 + \frac{8\pi a}{\left(6\pi^2\right)^{2/3}}n_c^{1/3} + \frac{2M}{\hbar^2\left(6\pi^2 n_c\right)^{2/3}}U_T = \gamma_i^2 + \frac{8\pi a}{\left(6\pi^2\right)^{2/3}}n_c^{1/3}\gamma_i^3, \tag{6.49}$$

which is cubic in γ. To further aid analysis, two variables are defined:

$$A \equiv \frac{8\pi a}{\left(6\pi^2\right)^{2/3}}n_c^{1/3} \tag{6.50}$$

and

$$B \equiv -\frac{2M}{\hbar^2\left(6\pi^2 n_c\right)^{2/3}}U_T + \gamma_i^2 + A\gamma_i^3. \tag{6.51}$$

[3]Experimentally we know that, given $\sim 100,000$ atoms, $n_c = 10^{13}$/cc is a good order-of-magnitude estimate for the density.

The cubic equation for the density in terms of these two variables is

$$A\gamma^3 + \gamma^2 - B = 0. \tag{6.52}$$

The trap potential in the harmonic limit is

$$U_T(x, y, z) = U_0 \left(\frac{x^2}{b^2} + \frac{y^2}{b^2} + \frac{z^2}{z_0^2} \right), \tag{6.53}$$

where U_0 is the trap depth, b is the $1/e^2$ intensity radius and z_0 the Rayleigh length of the CO_2 laser beam at the trap center. We can simplify the trap potential by working in a scaled coordinate system where $x' = x/b$, $y' = y/b$, and $z' = z/z_0$. In this coordinate system the trap potential is merely

$$U_T(r') = U_0 r'^2, \tag{6.54}$$

where $r'^2 = x'^2 + y'^2 + z'^2$. In light of this, (6.51) becomes

$$B(r') \equiv -\frac{2M}{\hbar^2 \left(6\pi^2 n_c\right)^{2/3}} U_0 r'^2 + \gamma_i^2 + A\gamma_i^3. \tag{6.55}$$

The type of solutions to a cubic equation can be determined by examining the equation's discriminant. For (6.52), the discriminant is

$$j = \frac{B(r)^2}{A^2} - \frac{4B(r)}{27A^4}. \tag{6.56}$$

When $j < 0$, (6.52) has one real solution and two imaginary ones. When $j = 0$, the cubic equation has two real solutions. When $j > 0$, the cubic equation has three real solutions. For our equation, $j < 0$ for small values of r'. The value of r' for

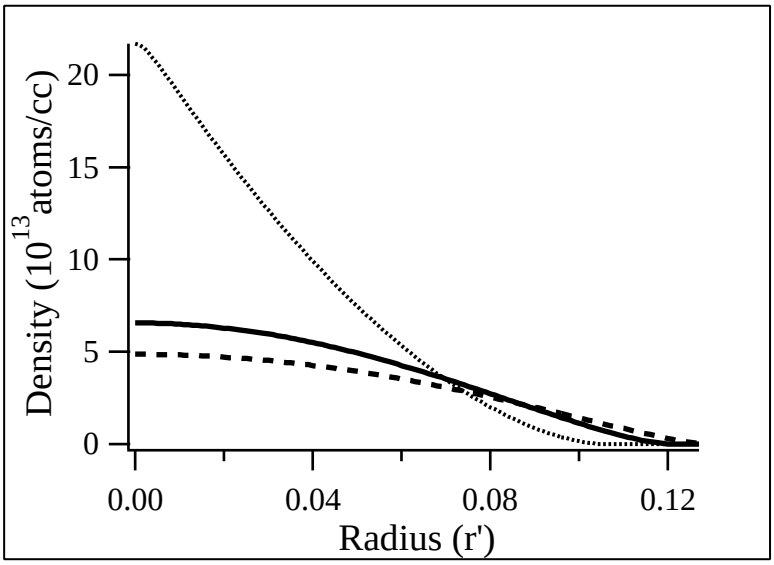

Figure 6.2: The radial density distribution of 100,000 trapped fermions per state. The solid line is for $a = 0$, the dashed line for $a = 1250\,a_0$, and the dotted line for $a = -1250\,a_0$.

which j becomes zero is the point at which the physical density distribution ends. Thus there is only one physical solution to (6.52), which can be found numerically with relative ease.

Given the constraints that $j < 0$ and that $(n_1 n_2) < (\pi/48|a|^3)^2$, the zero-temperature density distribution γ^3 can be found for a wide range of scattering lengths by choosing a value of γ_i so as to give an appropriate number of trapped atoms. The number of atoms in a single state is given by

$$N = \int_{j<0} 4\pi n_c r^2 \gamma^3 \, dr, \tag{6.57}$$

where γ is a function of r, the scattering length a, and the density at the center of the trap γ_i. In practice, trial values of γ_i are chosen and N is calculated; γ_i is then adjusted until N is equal to the required number of atoms.

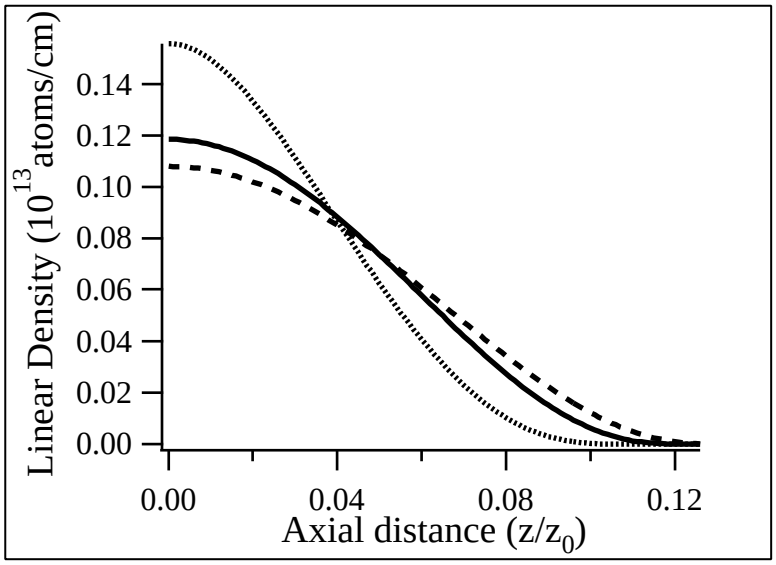

Figure 6.3: The axial density distribution of 100,000 trapped fermions per state. As in Figure 6.2, the solid line is for $a = 0$, the dashed line for $a = 1250\,a_0$, and the dotted line for $a = -1250\,a_0$.

Figure 6.2 is a plot of the radial density of 100,000 atoms per state for three scattering lengths: 0, $1250\,a_0$, and $-1250\,a_0$. As expected, the distribution for $a = 1250\,a_0$ is wider than the others, and the one for $a = -1250\,a_0$ is sharply peaked near the center.

In the context of our experiment, we will be taking absorption images with our CCD camera, then binning the resulting pictures to leave only the axial distribution, as explained in Section 4.2. The axial density distribution is given by

$$n(z) = \int_{j<0} 2\pi\rho\gamma^3\, d\rho. \tag{6.58}$$

Figure 6.3 is a graph of the same three density distributions as in Figure 6.2 integrated according to (6.58). Unsurprisingly, the integration along two axes tends to lessen the differences among the three density distributions. The three are still quite

different, especially the $a = -1250\,a_0$ distribution, and should be distinguishable experimentally. Since the sign of the scattering length will change as the magnetic field is tuned through a Feshbach resonance, the density change can be used to characterize the scattering length behavior at that resonance.

6.4 Summary

This chapter has presented a theory for calculating the zero-temperature density distribution of a two-state fermionic gas by balancing the forces on that gas. The mechanical stability of the gas was also found by considering density perturbations and then finding how fast those perturbations propagated.

For the purposes of numerically calculating the density distribution, the simplifying assumption that the two hyperfine states would contain equal populations was made, and that this would lead to equal density distributions for the states. Following those assumptions, both the full density distributions and the one-dimensional axial density distributions were calculated for a range of scattering lengths a. The density distributions were found to vary noticeably if a is varied from large and positive to large and negative.

Chapter 7

Conclusion

This dissertation has described the first production of a degenerate Fermi gas by all-optical means and the characterization of that gas. It builds on our group's prior work developing ultrastable optical traps, which in turn overcame the (previously unexplained) heating rates which limited optical trap lifetimes. While the prior work involved a custom-built CO_2 laser, my dissertation experiments involved a commercially-available laser. Use of a commercial laser has simplified the experimental setup required to optically trap and cool atoms for long periods of time, and in doing so made such an experimental setup more accessible to researchers.

Using this commercial laser, Mike Gehm and I have trapped and evaporatively cooled a ^{6}Li gas to the quantum degenerate regime. We were the fourth group to reach fermionic degeneracy (following [30], [31], and [32]), and the first to do so using an optical trap. The importance of optical traps is such that all groups exploring fermionic degeneracy are now employing optical traps as their final-stage trap rather than magnetic ones [87].

The work presented in this dissertation will hopefully lay the foundation for studies of a number of exciting physical processes in Fermi gases, from collective oscillations to high-temperature Fermi superfluidity. In preparation for those studies, this dissertation also presented the theory of an interacting zero-temperature

Fermi gas's density distribution and how that distribution changes as a function of the s-wave scattering length.

7.1 Chapter Summary

Chapter 1 began by placing my dissertation work in the context of our group's experiments. The work I did was to a large extent in tandem with that done by Mike Gehm; his dissertation serves as a companion to this one. The chapter continued by motivating the trapping of neutral ^{6}Li in order to study fermionic quantum degeneracy and potentially fermionic superfluidity. Dilute and degenerate alkali gases are of general interest to both experimentalists and theorists. "Degeneracy" means that the wave functions of the gas's atoms overlap, causing the gas to exhibit macroscopic quantum behavior. "Dilute" means that the interparticle interactions are weak, making the theoretical treatment of such systems more tractable than in other quantum degenerate systems such as superconducting electrons in metals or superfluid liquid helium. The chapter also gave a historical overview of cooling and trapping techniques that have been applied to dilute alkali gases.

At cold temperatures, fermions will not interact with other fermions in the same quantum state, though such interactions are necessary to cool a fermionic gas and to observe superfluidity. Accordingly, Chapter 2 explored how a two-state mixture of ^{6}Li atoms interacts at cold temperatures. At the low temperatures employed in our experiment, atoms scatter elastically through an s-wave interaction. The interaction can be parameterized by a single number, the s-wave scattering length a_s. The two states of ^{6}Li we work with, $|1\rangle - |2\rangle$, exhibit a widely-tunable s-wave scattering length: interactions in the $|1\rangle - |2\rangle$ system can be varied from strongly attractive to strongly repulsive. This tunability arises in part from a Feshbach

resonance which occurs at an experimentally-accessible magnetic field.

There are other reasons to favor the two lowest states of ^{6}Li. Atoms in those states do not exhibit spin-exchange s-wave collisions, which would serve to knock atoms out of the trap. In the absence of a magnetic field, a_s for these two states is zero, allowing us to turn interactions on or off by applying or removing a magnetic field. The $|1\rangle$ and $|2\rangle$ states cannot be confined in a magnetic trap, as they are strong-field-seeking states; they can only be confined in an optical trap.

Chapter 2 also discussed the possibility of observing Fermi superfluidity in ^{6}Li, either through the formation of Cooper pairs as in traditional BCS theory or through the strongly-interacting regime of resonance superfluidity. According to theoretical predictions, the critical temperature for superfluidity in ^{6}Li can be as high as half the Fermi temperature, one of the highest ratios of critical temperature to Fermi temperature ever seen in a Fermi superfluid.

Following that, Chapter 3 discussed the physics of optical traps, since only optical traps will confine a $|1\rangle - |2\rangle$ mixture of ^{6}Li. Optical traps had historically suffered from unexplained heating rates. Our work showed that most of this heating arose from noise in lasers used to form optical traps. We developed a model of noise-induced heating which indicated that, unless the intensity and pointing noise of a laser were minimized, optical trap lifetimes would be severely limited. Accordingly, we found and purchased a commercial CO_2 laser which had noise characteristics sufficient for our needs. The noise spectra of the commercial CO_2 laser indicated that our trap lifetime would be limited by the background gas pressure in our vacuum system and not by noise in the laser.

Chapter 3 also gave an overview of the trapping apparatus used in our experiments. The ultrahigh vacuum system, the ^{6}Li oven, the slower, and the magneto-

optical trap (MOT) were discussed. The vacuum system achieves pressures of less than 10^{-11} Torr. After the MOT is loaded, its beams are brought closer to resonance and lowered in intensity, resulting in atoms with a temperature of $\sim 150\,\mu$K at a density of $10^{11}/\text{cm}^3$. The optical hardware necessary to create the CO_2 laser trap is discussed in this chapter, including the alignment techniques for overlapping the focused CO_2 laser beam with the MOT.

Chapter 4 describes how we determine the number of atoms in the trap and their density. Two methods of imaging are used: fluorescence imaging and absorption imaging. In fluorescence imaging, the trapped atoms are illuminated with on-resonant light and the scattered light is measured with a photomultiplier tube (PMT). The light is proportional to the number of atoms in the trap. Fluorescence imaging cannot determine the density of the trapped atoms; for that, we use absorption imaging. A near-resonant beam is passed through the atoms, which scatter the light and leave a shadow in the beam. The beam and shadow are subsequently imaged onto a CCD camera. From the CCD image we determine both the number and the density of the atoms by fitting the measured atomic distribution to a semiclassical Thomas-Fermi model.

To control the camera, PMT, and other equipment in the experiment with submillisecond timing over many tens of seconds, we developed a computer-controlled timing system and multiplexer. The timing system uses custom-designed software and commercial hardware to produce TTL signals and control hardware. The multiplexer allows us to switch among different analog values based on TTL signals. Together, the multiplexer and timing system control our experiment. Using all of this equipment, we were able to measure the radial and axial frequencies of our CO_2 laser trap by shaking the trap from side to side and by modulating the laser

intensity in such a way as to parametrically excite the trapped atoms. Our trap has a radial frequency of 6.6 kHz and an axial one of 340 Hz.

With that, all of the pieces are in place to cool ^{6}Li to degeneracy. Chapter 5 describes the process of evaporation, and includes a Boltzmann equation model of evaporation first described in Ref. [82] and further extended by Ken O'Hara. Using this model we are able to predict how many atoms will remain and at what temperature following evaporation. The model shows that evaporation occurs rapidly, then stagnates when the temperature of the atoms reaches about $1/10$ that of the trap depth. In order for evaporation to continue, the trap depth must be lowered by reducing the CO_2 laser beam intensity. The correct time dependence of the trap depth was determined using scaling laws which give the phase-space density, number, and elastic collision rate as a function of the trap depth.

The time-dependent trap depth poses a problem, as the CO_2 laser beam intensity is controlled by an acousto-optical modulator (AOM). The AOM changes both the alignment and the ellipticity of the CO_2 laser beam as its rf power is varied. We attempted to correct the misalignment with a "$4f$" lens arrangement, which served to distort the beam shape, and by varying the frequency of rf power fed to the AOM, which introduced noise that heated the trapped atoms. Though we were unable to correct the beam's misalignment and changing ellipticity, we were still able to reach the quantum degenerate regime. After forty seconds of forced evaporative cooling, we produced a quantum degenerate gas of 3×10^5 ^{6}Li atoms at a temperature of $T = 5.8\,\mu$K, which, in units of the Fermi temperature, is $T/T_F = 0.55$. After sixty seconds, 10^5 atoms remain at a temperature of $T \simeq 4\,\mu$K and $T/T_F = 0.48$. Beyond sixty seconds, the phase space density of the atoms *decreases*, because clipping increases to the point that the the rate of decrease in trap power exceeds the

rate required for evaporative cooling, causing some atom loss without a concurrent decrease in temperature.

In Chapter 6, the density of a zero-temperature fermionic gas as a function of s-wave scattering length a_s was explored. The density was calculated using a force balance approach in the mean field approximation. In addition, the criterion for the gas's mechanical stability was found. Both the full density distributions and the one-dimensional axial density distributions were calculated for a range of a_s. The density distributions were found to vary noticeably as a_s was varied from large and positive to large and negative.

7.2 Improvements to the Experiment

The two most immediate improvements to the experimental apparatus are decreasing the misalignment of the CO_2 laser beam as the AOM rf power is lowered and the installation of higher-field magnets. Since the work described in this dissertation was performed, new magnets capable of providing 1100 G for ten seconds have been constructed and installed. These magnets provide a number of benefits. At very high fields, a_s for the $|1\rangle - |2\rangle$ mixture approaches the triplet scattering length of $-2240a_0$. Given such a large interaction, evaporation should take place much faster. Whereas it used to take forty seconds to reach the degenerate regime, with sufficiently strong fields degeneracy should be attainable in a matter of seconds, minimizing trap loss due to noise and other forms of heating. Such strong magnets also provide the chance of exploring the Feshbach resonance, which is predicted to occur at around 850 G. As of yet, no definitive measurement of this Feshbach resonance has been made.

The most pressing experimental problem is the changes in the CO_2 laser beam

as the AOM rf power is lowered. The beam misalignment and changes in ellipticity ultimately limit how much cooling can occur, as the beam becomes increasingly more clipped as the rf power is lowered. We believe that both of these effects are due to temperature gradients in the AOM crystal. Decreasing the temperature of the cooling water sent to the AOM does not alleviate this problem, since the center of the crystal remains at a higher temperature than the walls while rf power is being fed to it.

Since the heat cannot be removed quickly enough to prevent a temperature gradient, and since external solutions have failed, one possible solution would be to keep the rf power constant. This could be achieved by feeding in two frequencies of rf power: the standard 40 MHz and some lower frequency such as 30 MHz. The two frequencies would produce two separate first-order beams. The beam due to the 40 MHz frequency would be used as before. The beam due to the 30 MHz frequency would be blocked. As the 40 MHz frequency component of the rf power was decreased, the 30 MHz frequency component would be increased so as to maintain a constant amount of rf power. In this manner, the heating of the crystal should remain constant and the 40 MHz beam would have a constant direction and ellipticity.

7.3 Future Outlook

Optical traps are in and of themselves useful tools, and our use of a commercial CO_2 laser in their creation has helped make optical traps generally accessible. Optical traps have been used to make optical lattices. One-dimensional optical lattices can be made by retroreflecting the laser beam through the trapping region while maintaining its polarization; two- and three-dimensional lattices can be formed

from additional retroreflected beams along the other orthogonal axes. Such optical lattices can be used in quantum computation [88] and in the study of tunnelling resonances [89]. Optical lattices are also promising for studies of high-T_c superconductors. Fermi gases trapped in an optical lattice are like atoms at the lattice sites of a crystal, and are described by a Hubbard Hamiltonian, one of the theoretical models of high-T_c superconductors [90].

Ultracold Fermi gases are of interest for their collisional properties. Precision measurements of the electric dipole moment (EDM) of atoms [91] as well as atomic clock measurements [92, 93] are limited by collisions between atoms, since those collisions cause systematic shifts in frequency and limit the atoms' coherence lifetime. An ultracold Fermi gas in a single superposition state is collisionless, and thus should exhibit long coherence times.

Collective oscillations of a degenerate Fermi gas is a promising field of study. The behavior of a two-component Fermi gas when it is allowed to oscillate depends on the interaction strength between the two components. A $|1\rangle - |2\rangle$ ^{6}Li mixture has widely-tunable interactions, allowing observations similar to those made in BECs [40,41,42].

The area of greatest promise is superfluidity. While the formation of Cooper pairs may occur at experimentally-inaccessible temperatures [60], recent work has shown that exploration of resonance superfluidity may be within our experimental reach [16, 63, 17, 94]. In resonance superfluidity, a Feshbach resonance is exploited to increase the scattering length dramatically. The resulting superfluid would be neither a BCS superfluid nor BEC, as BCS superfluids have weakly-bound Cooper pairs, while BECs are composed of bosons which in turn are composed of very tightly bound fermions. Instead, it would lie somewhere between the two regimes. This crossover regime has yet to be explored, and may involve surprising physical

effects [62].

Appendix A

Split-Image Calculation

The ZnSe lens which focuses the CO_2 laser beam into the MOT must be axially placed with sub-millimeter accuracy. This is done using a split-image technique, as explained in Chapter 3. In the split-image technique, the ZnSe lens, a glass lens, and a screen are mounted on a translation stage. The location of the screen relative to the two lenses is chosen so that, if the translation stage is moved until the MOT is imaged by the glass lens onto the screen, the ZnSe lens is properly located. This involves calculating the object and image distances of the glass lens used in the procedure, and the calculation must take into account a number of factors if sufficient accuracy is to be achieved. For one, the thin lens approximation cannot be used; the image and object distances must be measured from the principal points of the lens. (Figure A.1 shows the focal points and principal points of a plano-convex lens, and the distances that will be used in the following explanation. This information was taken from the 1999 Melles Griot catalog.) For another, there is a .25 in. thick ZnSe window between the lenses and the magneto-optical trap; its effect on the optical path length must be included in the calculation.

The location of the glass lens is not crucial. Its distance from the ZnSe lens will be used in calculating the location of the screen. Once the ZnSe and glass lenses have been placed on the translation stage, the procedure for determining the

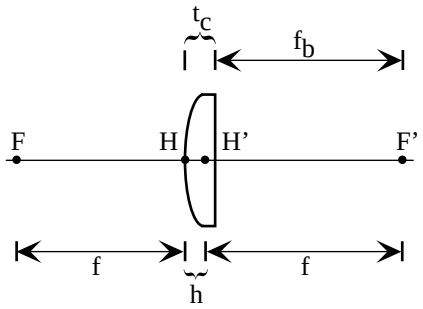

Figure A.1: The focal lengths and principal points of a plano-convex lens. H and H' are the principal points; F and F' are the two focal points of the lens. f is the effective focal length of the lens, as measured from the principal points. f_b is the back focal length, as measured from the flat lens surface. (Note that the front focal length, measured from the curved surface to F, is the same as the effective focal length f, and so is not shown.) t_c is the thickness of the lens. The hiatus h is the distance between the two principal points.

screen's location is as follows. First, the physical distance from the ZnSe lens to the MOT must be calculated. Then, given that distance and the separation of the ZnSe and glass lenses, the optical distance from the MOT to the glass lens is calculated. From this the image distance is calculated, and at that distance is placed the screen on which the MOT's image is projected. Once that is done, the ZnSe lens can be removed and the split-image technique performed.

We wish to place the ZnSe lens such that it and the MOT are separated by an optical path length equal to the ZnSe lens's back focal length f_b. The physical distance corresponding to this optical distance will be lessened by the effect of the .25 in. thick ZnSe window between the lens and the MOT. The physical distance d_m will be

$$d_m = f_b - (n_{10.6} - 1)\, t, \tag{A.1}$$

where $n_{10.6}$ is the index of refraction of ZnSe for 10.6 μm light and t is the thickness of the ZnSe window.

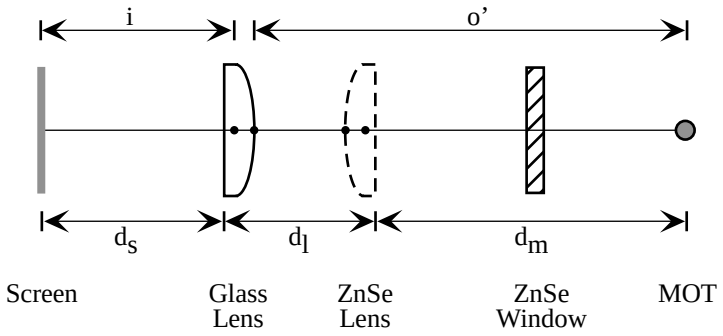

Figure A.2: The distances involved in the split-image setup. d_m is the physical distance from the flat edge of the ZnSe lens to the MOT, d_l is the distance between the flat edges of the two lenses, and d_s is the distance from the flat edge of the glass lens to the screen. o' is the physical distance corresponding to the object distance o from glass lens to MOT; i is the image distance from glass lens to screen.

The physical distance o' from the MOT to the glass lens's first principal point will be

$$o' = d_m + d_l - t_c, \tag{A.2}$$

where d_l is the separation between the two lens's flat edges and t_c is the thickness of the glass lens. This physical distance will correspond to an optical (object) distance of

$$o = o' + (n_{671} - 1)\, t, \tag{A.3}$$

where n_{671} is the ZnSe window's index of refraction for 671 nm light.

The object and image distances are related by the usual formula,

$$\frac{1}{o} + \frac{1}{i} = \frac{1}{f}, \tag{A.4}$$

where f is the effective focal length of the glass lens. The physical distance at which

	ZnSe	**Glass**
t_c	0.1796"	0.1665"
h	0.1049"	0.05635"
f_b	7.425"	3.8268"
f	7.5"	3.9370"
n_{671}	2.507	1.517
$n_{10.6}$	2.4028	-

Table A.1: Lens Characteristics

to set the screen, d_s, is then

$$d_s = i - (t_c - h)\,, \tag{A.5}$$

where h is the hiatus of the glass lens.

Table A.1 gives the characteristics of both the ZnSe lens which focuses the CO_2 laser beam into the trapping region and the glass lens used for split-image detection. The back focal length f_b is calculated using a formula which is correct for a plano-convex lens:

$$f_b = f - \frac{t_c}{n}, \tag{A.6}$$

where n is the index of refraction at whatever wavelength is appropriate: $10.6\,\mu$m for the ZnSe lens; 670 nm for the glass lens.

Substituting the appropriate values from above into equation (A.1), we find the physical distance d_m from the ZnSe lens to the MOT to be $d_m = 7.074$". In our split-image experiment, the glass and ZnSe lenses are separated by a distance $d_l = 1.075$". The physical distance from the MOT to the glass lens is then $o' = 7.9825$", and the optical distance is $o = 8.3592$". The image formed by the glass lens will occur at

$$i = \frac{of}{o - f} = 7.4420". \tag{A.7}$$

The screen is then placed a distance $d_s = 7.2483$" from the glass lens. In practice, the screen is placed by machining a square brass rod of the appropriate length, then using that rod as the ruler by placing it between the glass lens and the screen.

Appendix B

The Computer-Controlled Timing System

The computer-controlled timing system was developed in order to provide control of a number of events in sequence via TTL logic, and to do so without depending on the system of Stanford Research Systems (SRS) DG535 pulse generators that was used in the past.

In the original scheme, several DG535s were employed and their internal clocks synchronized to one another. Each DG535 has four outputs; however, these four outputs cannot be arbitrarily controlled. After a DG535 is triggered, each of its outputs can only change state once, either moving from low (0 V) to high (+5 V) logic or from high to low. Multiple DG535 outputs must be combined in order to change states multiple times; this was accomplished either through options internal to the DG535 or by connecting cables together through diode boxes which isolated the DG535 outputs from each other. In addition, to maintain synchronization there had to be one master DG535 from which all other pulse generators were triggered.

Creating a working timing scheme using this system was painful at best and nearly impossible at worst. *Changing* a working timing system without starting from scratch could take several days to accomplish.

In the current scheme, a computer independently controls thirty-two TTL-logic

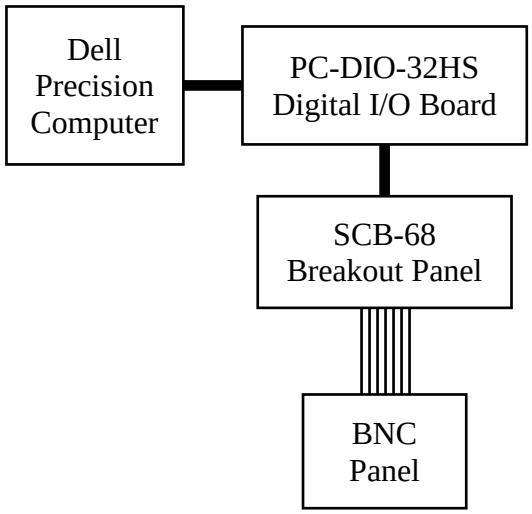

Figure B.1: A block diagram of the physical components of the timing system.

outputs. The state of each of those outputs, or channels, can be changed arbitrarily. One disadvantage to this scheme is that the computer's timing accuracy is limited to about 100 μs. The benefit of increased flexibility far outweighs this disadvantage, and this accuracy can be maintained over hundreds of seconds. In the few cases which require greater timing accuracy we use a single DG535 which is triggered by the computer-controlled timing system.

B.1 Physical Components

The timing system is controlled by a Dell Precision 420 computer with 768 MB of Rambus RAM. The amount of RAM is important, since the timing system software creates a large matrix of logic states for each channel at each time step.

The actual signals are generated by a National Instruments PC-DIO-32HS board, which provides 32 parallel digital input/output (I/O) channels. The board is attached to a SCB-68 breakout box via a shielded cable. The SCB-68 makes each of those 32 I/O channels accessible via terminal blocks, and also provides both a

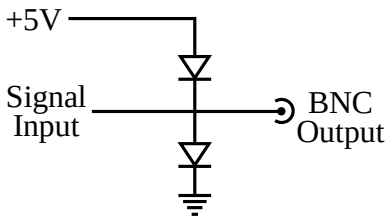

Figure B.2: Two Schottky diodes are placed from +5 V to the BNC output signal line and from the signal line to ground. These diodes limit the ringing which occurs when the signal line changes state.

ground terminal and a +5 V terminal.

Attached to the SCB-68 breakout box is a standard fifty-pin ribbon cable connector. The pin layout of the connector is as follows: pins 1 through 32 are attached to I/O channels 1 through 32, pins 45 and 46 are attached to the +5 V terminal, and pins 49 and 50 are attached to the ground terminal. A ribbon cable then carries the trigger signals from the SCB-68 to a panel with thirty-two BNC outputs placed near the experiment, one for each I/O channel.

Each of the BNCs is attached to two Schottky diodes of type 1N5711. These diminish the amount of ringing and overshoot that occur on the digital channels. Schottky diodes are fast-reacting diodes often used for cleaning up digital signals. One diode goes from the signal connection to the +5 V line; the other, from the signal line to ground. In theory they keep the signal from going much above +5 V or below 0 V; in practice there is still a lot of ringing on the 100-ns time scale.

B.2 The Basic Timing File

The software part of the timing system is rather complex, as it involves a Perl script for preparsing timing files[1], LabView code to run the I/O board, and LabView modules written in C to create the channel state matrix that is sent to the I/O board. The LabView code invokes the Perl script, which reads in a timing file and writes a processed version of the file; the LabView code then reads in the processed version and its C modules translate that processed file into a channel state matrix. The LabView code also provides a user interface for loading timing files and running timing sequences.

The timing file is a text file which defines which channels are to be used, what names are given to each channel, and when the channels should change state. Their layout is as follows:

---

[1]Perl was originally designed to process text files and create new ones from them, making it a good language choice for this application. A number of books teaching Perl are available; I recommend *Programming Perl* (known affectionately as "the camel book"), from O'Reilly & Associates, Inc.

[optional GPIB lines]

[total time] [delta t] [number of channels]

[Channel 1 name]

[initial state] [switching time 1] [switching time 2] ...

[Channel 2 name]

[initial state] [switching time 1] [switching time 2] ...

⋮

[Total time] is how long this particular timing sequence will run in seconds. [delta t] is the time step for the timing sequence in seconds. This time step defines the time unit for the switching times. [number of channels] is how many channels are in the file.

Each channel is defined by two lines in the timing file. The first is the name of the channel. The timing system displays this name in its user interface to aid adjustment of individual channels. The second line defines the initial state of the channel—either 0 for low (i.e. 0 V) or 1 for high (i.e. +5 V)—and a list of times when the channel should change state. The times are given as integers in units of delta t.

The timing file can optionally begin with one or more GPIB command lines. GPIB is a data bus used to control lab equipment. The LabView program which reads in the timing files can send GPIB commands to equipment before the timing sequence begins. A GPIB command line is defined as:

GPIB: [GPIB address]: [GPIB string]

Each GPIB device has a numbered address, from 1 to 15, and will accept different command strings depending on its function. The LabView program sends the commands in the GPIB string section to the device whose GPIB address matches the one given in the GPIB command line.

A simple timing file looks like:

```
GPIB: 6: TM1;TL2.5
6.03 .0001 32

MOT Amplitude LSB
0 50000 50040 50041 50190 60041 60141

MOT Amplitude MSB
0 50040 50190 60041 60141
⋮
```

This example timing file runs for 6.03 seconds, has 32 channels, and a time step of a tenth of a millisecond. The first channel controls the least-significant bit (LSB) of the AOM amplitude which runs the MOT. It begins at 0 V, switches to +5 V after 5 seconds, switches low 4 ms later, switches high 100 μs after that, and so on. Before the timing sequence begins, the string TM1;TL2.5 is sent to the GPIB device at address 6.

There is one subtlety to making a timing file: there must be exactly sixteen or thirty-two channels defined, even if not all of the channels are used. Otherwise,

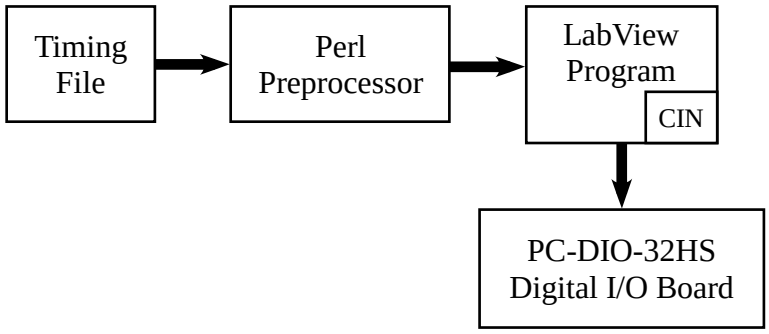

Figure B.3: A block diagram of the software components of the timing system. The timing file is fed to each program in turn, as indicated by arrows. CIN stands for Code Interface Node; the LabView modules which are written in C are CINs.

LabView will throw an unrelated error and not run the timing system. This appears to be a bug in LabView.

B.3 The Perl Preprocessor

Many of our experiments involve varying the length of time for which atoms are held in the CO_2 laser trap. Changing a timing file in this event becomes difficult, as the timing of so many events depends on the timing of other events. For example, if one increases the length of time that atoms are held in the CO_2 laser trap, the time when the CCD camera probe beam is unshuttered and illuminating the camera must be adjusted. Likewise, the CCD camera shutter must be open at a different time. If a timing file as defined above is used, many numbers must be individually changed to alter just one duration.

The Perl preprocessor addresses this deficiency. Before a timing file is parsed by the LabView program, it is passed through a Perl script called parse-timing.pl. Using this preprocessor it is possible to define variables, include files which define other variables, and perform arithmetic functions using these variables. This allows

flexibility in defining a timing file. Instead of defining the exact time when a probe beam turns on, one can instead use variables to insure that the probe beam turns on *e.g.* 10 ms after the camera shutter opens, regardless of when exactly that happens. This approach allows the duration of any event to be adjusted simply by changing one or two variables.

The addition of the preprocessor requires a change to the structure of the timing files.

[Definition line]
[Definition line]
⋮

GPIB: [GPIB address]: [GPIB string]
[total time] [delta t] [number of channels]
⋮

The definition lines consist of variable definitions, comments, or Perl code. Any number of definition lines, including zero, is allowed. There must be no blank lines between definition lines, though whitespace is allowed on a line. The block of definition lines is followed by one or more blank lines and then the original timing file structure.

Of the three items listed above (variable definitions, comments, and Perl code), only variables may appear in the actual timing section of the timing file. Mathematical operations using variables are allowed inside the timing section, but the variable must be the first element of the expression, and there can be no whitespace in the mathematical expression. For instance,

```
0 1000 $probe_time+1000
```

is a perfectly valid line in the timing file, but

```
0 1000 1000 + $probe_time
```

is not, because the variable does not come first in the expression `1000 + $probe_time` and there is whitespace in the expression.

Variables begin with a `$`, and can consist of letters, numbers, underscores, or dashes. Variables are defined when they are assigned a value: `$variable = 100;`. Note that a variable definition line ends with a semicolon. The usual math functions are allowed; `$probe_time = 10*$on_time+30;` is a valid variable definition, for example. As this example also shows, variables can be used in the definition of other variables. The only restriction is that any variables to the right of the equals sign must have been defined earlier.

Comments are introduced by the # character, and continue from that point to the end of the line. It is hoped that users of the timing system will use comments to make their timing files more readable by humans rather than merely to add snide remarks. Comments can be on a line by themselves, or can be placed at the end of a variable definition or line of Perl code.

Perl code is marked by a `@`. The at symbol is not part of the code; it merely signals the Perl script that what follows the `@` should be treated as actual Perl code. Using the `@` symbol, Perl code can be embedded in the timing file, which is otherwise not treated as Perl code. This ability is mainly used to include another

file filled with variable definitions by using Perl's require command. For instance, @require "Decay.inc" would include the contents of the file Decay.inc in the current timing file. Any file included in this manner must contain only variable definitions and comments, and the file should be included in the Definition Line section of the timing file.

The preprocessor replaces all instances of variables with the associated numbers, and performs all mathematical operations listed in the timing file. Once it has done all of this, it creates a new file which follows the timing file structure defined in Section B.2.

B.4 LabView and C Code

Once the preprocessor is finished, the file it created is read in by a LabView program. The LabView program then creates a large matrix of bit states, one bit for each channel which is to be controlled. That matrix is passed to the PC-DIO-32HS, which then changes the channel states at the appropriate times.

The first iteration of the timing system was written entirely in LabView. The LabView program both parsed the timing file created by the Perl preprocessor and created the associated channel state matrix. This version of the timing system was unacceptably slow, and would take several days to create a matrix from a given timing file. Fortunately, LabView provides Code Interface Nodes, or CINs, which allow code written in another language to be called from LabView. This code is often much faster than code written in LabView, since LabView uses a graphical interface and emphasizes user comfort over raw speed. Using a CIN, the LabView program calls a routine written in C, which in turn creates the channel state matrix. The C code is orders of magnitude faster than the similar LabView code, and can

create a matrix in a few seconds at most. All operations on the channel state matrix are done using CINs and C code rather than LabView code.

Once this matrix has been created, the LabView program allows the user to run the timing sequence once or loop the sequence until stopped by the user. In addition, an individual channel can be set high or low for the duration of the sequence, preventing it from changing state. The names of the channels as defined in the timing file are displayed to make selecting the correct channel an easier task.

B.5 Example of Creating a Timing File

To conclude this appendix, I will demonstrate the creation of a timing file for evaporation in the full CO_2 laser well, from the initial determination of what events need to happen when, to the final form of the timing file.

B.5.1 Sequence of Events

The sequence of events for full well evaporation is as follows. First, the CO_2 laser trap is loaded from the MOT for five seconds. Next, the frequencies and intensities of the MOT and repumper beams are adjusted to produce a cooling phase for 20 ms, as explained in Section 3.4.6. Then the repumper beams are extinguished, allowing the MOT beams to optically pump all of the atoms into the two lowest ground states. This optical pumping phase lasts for 100 μs, after which the MOT beams are extinguished.

Following this, the MOT magnets are turned off, one magnet's polarity is reversed, and then both magnets are re-energized to provide the magnetic field necessary for evaporation to occur. During evaporation, the backgoing beam chopper

(Section 5.3.2) is lowered. After a variable amount of evaporation time, the magnets are turned off and their polarity restored to the original state.

Following this, two camera images are taken. The first is an image of the atoms' shadow; the second, a reference image containing only the laser light with no atoms. From these the actual absorption image is calculated (Section 4.2). Because the camera cannot take another image while it is transferring data from the previous image to the computer, the two images are taken two seconds apart. Finally, the system is returned to its original state in preparation for the next evaporation sequence.

B.5.2 Mapping Events to Variables

After the proper sequence of events has been determined, the next step in creating a timing file is to map each event to a variable in the timing file. Doing so allows the actual timing of events to be modified easily.

When creating these variables, it is useful to define each event's variable in terms of when the event prior to it begins and how long the prior event lasts. For example, I will define the "begin the optical pumping phase" variable in terms of when the cooling phase begins and how long the cooling phase is to last. The standard time step we use for all of our timing files is $100\,\mu$s, so all variables will be defined in units of $100\,\mu$s.

Although there is a separate timing file for each different experiment, all of the timing files share several things in common. The length of time of the MOT loading phase is always five seconds; the cooling phase, 20 ms; the optical pumping phase, $100\,\mu$s. Mechanical shutters have an opening and closing time which must be taken into account. To keep from having to repeat this information over and over, we

created a separate file containing variables for this common information. That file, Timing Include.txt, is then included in all timing files.

This file has three variables which control the length of time of the loading, cooling, and optical pumping phase:

```
$mot_loading_time = 50000;
$mot_cooling_time = 200;
$mot_optical_pumping_time = 1;
```

(Remember that the variables are in units of 100 μs each, so that a variable setting of 200 is equivalent to 20 ms.) It has two variables which account for the time it takes for our mechanical shutters to open and close:

```
$shutter_lead = 80;
$shutter_lag = 150;
```

The first variable accounts for how long shutters take to open: 8 ms. The second accounts for how long they take to close: 15 ms. There are four variables for the camera:

```
$camera_lead = 200;
$camera_lag = 200;
$camera_probe_time = 10;
$wait_before_taking_ref = 20000;
```

The first two are equivalent to the two shutter variables above, but are specifically for the camera shutter. The third variable is how long a camera exposure is. Note that camera exposure time is not equal to the probe beam's duration. The fourth is how long to wait between taking the shadow image and the reference image. Three variables have to do with the MOT magnets:

```
$magnet_turnoff = 10;
$magnet_turnon = 20;
$flip_mags_delay = 4800;
```

The first two are how long the magnets take to turn on and off, while the second is how long the relay which reverses the polarity of the MOT magnets takes to change

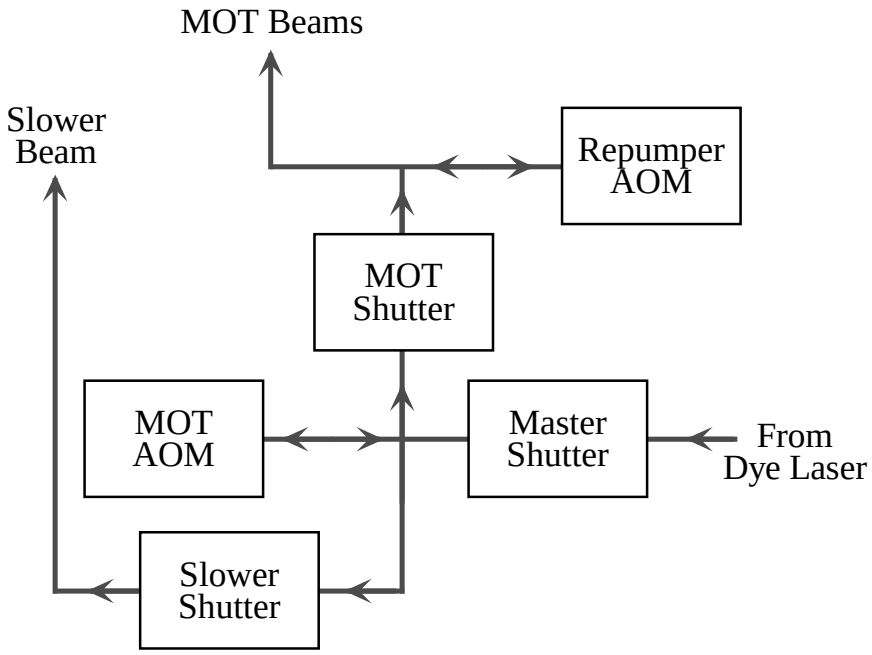

Figure B.4: A block diagram of the optical setup which produces the MOT, repumper, and slower beams. The actual AOMs, mirrors, shutters, and lenses involved in the optical setup are shown in Figure 3.14.

state. Finally, there are two variables which have to do with full-well evaporation:

```
$fw_evap_time = 60000;
$backbeam = 0;
```

The former is how long to evaporate in the full CO_2 laser well, and the latter is when, after the MOT magnets are turned off, the chopper should be lowered. It is set to zero because the chopper mechanism is driven by an air dashpot, and takes several seconds to move even after the timing system sends the signal to lower the chopper.

Given the contents of Timing Include.txt, we can now create the variables for our timing file. The timing file will begin with the MOT loading phase's settings. Figure B.4 shows a block diagram of the optical setup which produces the MOT, repumper, and slower beams. The timing system controls both of the AOMs and all

three of the shutters shown in the diagram. The first events will involve the AOMs in Figure 3.14, since they will be the MOT cooling phase, optical pumping phase, and shut-off:

```
$mot_cooling = $mot_loading_time;
$mot_opt_pump = $mot_cooling + $mot_cooling_time;
$mot_off = $mot_opt_pump + $mot_optical_pumping_time;
```

All three of these events are referenced to when the prior event begins (which is at time 0 for the loading phase) and how long the prior event should last.

As soon as the MOT beams are off, the magnets are turned off, their polarity switched, and then turned back on. They remain on during for the entire full-well evaporation period, then turn off and their polarity is restored.

```
$magnets_off = $mot_off;
$flipper_on = $magnets_off + $magnet_turnoff;
$reversed_magnets_on = $flipper_on + $flip_mags_delay;
$reversed_magnets_off = $reversed_magnets_on + $fw_evap_time;
$flipper_off = $reversed_magnets_off + $magnet_turnoff;
```

The two $flipper variables refer to the relay which reverses the MOT magnets' polarity. Care is taken to ensure that the relay does not switch while current is flowing through the MOT magnets.

Following that, two camera images are taken. This involves opening the camera shutter, turning on a probe beam to illuminate the camera (and atoms, if any), then closing the camera shutter. Figure B.5 shows a block diagram of the probe beam's optical setup. The timing system will control the probe shutter and AOMs in the $^3/_2$ and $^1/_2$ AOM arms; the two imaging AOMs will be controlled by the pulse generator.

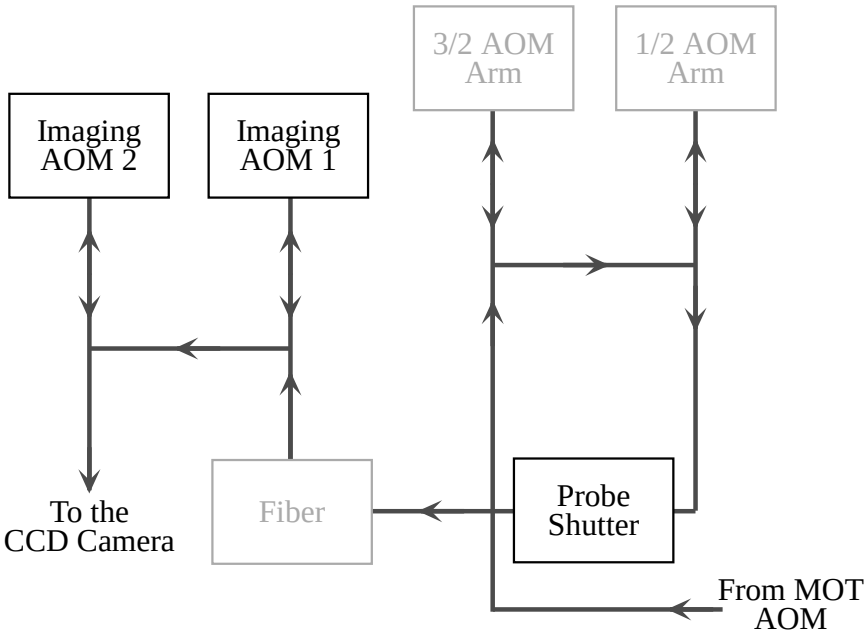

Figure B.5: A block diagram of the probe beam's optical setup. The actual AOMs, mirrors, and lenses involved in the probe beam's optical setup are shown in Figure 4.5.

```
$pulse_gen_trigger = $reversed_magnets_off+$magnet_turnoff+$wait_before_probing;
$lpw1 = 0;
$lpw2 = $lpw1+1E-5;
$lpd = "1E-5";
$probe_shutter_open = $pulse_gen_trigger-$shutter_lead;
$probe_shutter_close = $pulse_gen_trigger+100;
```

The probe beam AOMs are controlled by a Stanford DG535 pulse generator, since accuracies of 10 μs are needed. The probe beam is blinded by two AOMs, which may have different rise and fall times. To set how long the probe beam is on accurately, the first AOM is turned on at `$lpw1` seconds after `$pulse_gen_trigger`, then the second one is turned on at `$lpw2`, allowing the second AOM to control the duration of the probe beam. `$lpd` is the duration of the probe beam, also given in seconds. `$lpw1`, `$lpw2`, and `$lpd` are given in fractions of seconds (such as `1E-5` for 10 μs) rather than in integer multiples of 100 μs because they are sent via GPIB to the DG535, which

uses seconds as its base unit. Finally, the two $probe_shutter variables control when the shutter shown in Figure B.5 is opened and closed.

Concurrent with the probe beam being turned on, the camera shutter must be opened. The shutter will be opened before the pulse generator is triggered, and closed after the exposure time (which is set in Timing Include.txt).

```
$camera_shutter_open = $pulse_gen_trigger - $camera_lead;
$camera_shutter_close = $camera_shutter_open+$camera_lead+$camera_probe_time;
```

After the first image has been taken, the CO_2 laser is turned off to allow any remaining atoms to escape and a second picture is taken.

```
$co2_off = $camera_shutter_close+$wait_before_taking_ref-1000;
$co2_on = $camera_shutter_close+$wait_before_taking_ref+100;
```

The CO_2 laser is turned off briefly just before the reference image is taken. Following that, the camera shutter is again opened and the probe beam is turned on.

```
$pulse_gen_trigger2 = $camera_shutter_close + $wait_before_taking_ref;
$probe_shutter_open2 = $pulse_gen_trigger2-$shutter_lead;
$probe_shutter_close2 = $pulse_gen_trigger2+100;
$camera_shutter_open2 = $pulse_gen_trigger2 - $camera_lead;
$camera_shutter_close2 = $camera_shutter_open2+$camera_lead+$camera_probe_time;
```

After the second image is taken, the MOT magnets can be turned back on, as can the MOT beams. These should be the final events in the timing file, so the end time will be referenced to it.

```
$magnets_on = $camera_shutter_close2 + $camera_lag + 1000;
$end_time = $magnets_on + 9;
$mot_on = $end_time - 1;
```

The extra 900 μs in $end_time is to ensure that it is indeed the final event in the timing file.

Even though we've reached the last event, a few things haven't been taken into account. The slower shutter should be closed when the MOT beams are turned off, and re-opened when the MOT magnets turn back on at the end of the timing

sequence:

```
$slower_shutter_close = $mot_off - $shutter_lead;
$slower_shutter_open = $magnets_on;
```

Similarly, the MOT shutter should close when the MOT beams are turned off and reopen at the end of the sequence (though without $shutter_lead being taken into account, as we don't want the MOT shutter clipping the MOT beams while they're still on):

```
$mot_shutter_close = $mot_off;
$mot_shutter_open = $magnets_on;
```

The master shutter is a little more complex. It must be open any time the MOT beams or probe beam are on. It will close when the MOT shutter closes, reopen when the probe shutter does, close when the probe shutter re-closes, and open when the probe shutter re-opens.

```
$master_shutter_close = $mot_shutter_close;
$master_shutter_open = $probe_shutter_open;
$master_shutter_close2 = $probe_shutter_close;
$master_shutter_open2 = $probe_shutter_open2;
```

The direction of the beams emerging from the AOMs depends on their temperature, as explained in Section 3.4.5. Because of this, we keep the AOMs' rf power on as much as possible, so that the crystal remains warm and the intensity through the double-passed AOMs remains near its maximum. We keep the MOT AOMs warm by turning them on shortly after the MOT shutter closes and again shortly after the probe shutter has closed:

```
$restart_mot_aos = $mot_shutter_close + $shutter_lag;
$restart_mot_aos2 = $probe_shutter_close + $shutter_lag;
```

Finally, the chopper must be lowered during full-well evaporation, then re-raised at the very end of the timing sequence.

Channel	Chan. Name	Channel	Chan. Name
1	MOT Amplitude LSB	17	Hummer MSB
2	MOT Amplitude MSB	18	PMT Gate
3	MOT Frequency LSB	19	None
4	MOT Frequency MSB	20	CO2 Controller
5	Repumper Freq. LSB	21	MOT Magnet Flipper Logic
6	Repumper Freq. MSB	22	Master Shutter
7	None	23	None
8	None	24	Camera Shutter
9	None	25	Pulse Generator Trigger
10	Probe Shutter	26	Camera AOs Warming Trig.
11	Slower Shutter	27	None
12	MOT Shutter	28	None
13	Probe On/Off	29	None
14	Repumper On/Off	30	Backgoing Beam Chopper
15	None	31	None
16	Hummer LSB	32	None

Table B.1: Timing System Channel Assignments

```
$chop_beam = $reversed_magnets_on + $backbeam;
$unchop_beam = $end_time - 1;
```

B.5.3 Mapping Event Variables to Channels

Once all of the events have been assigned variables, those variables can be assigned to physical channels. Table B.1 lists the channel assignments for this timing file. The "LSB" and "MSB" designations are for the least significant bit and most significant bit of a multiplexer four-way switch, as explained in Section 4.3.2.

The first channels are the ones dealing with the MOT and repumper AOMs. Those AOMs can be in one of four states: loading phase, cooling phase, optical pumping phase, or off. Table B.2 gives the four states in terms of the MSB and LSB of the appropriate multiplexer four-way switch. The table is valid for both the frequency and amplitude settings.

		LSB 0	LSB 1
MSB	1	Opt. Pumping	Off
	0	Loading	Cooling

Table B.2: MOT/Repumper AOM States

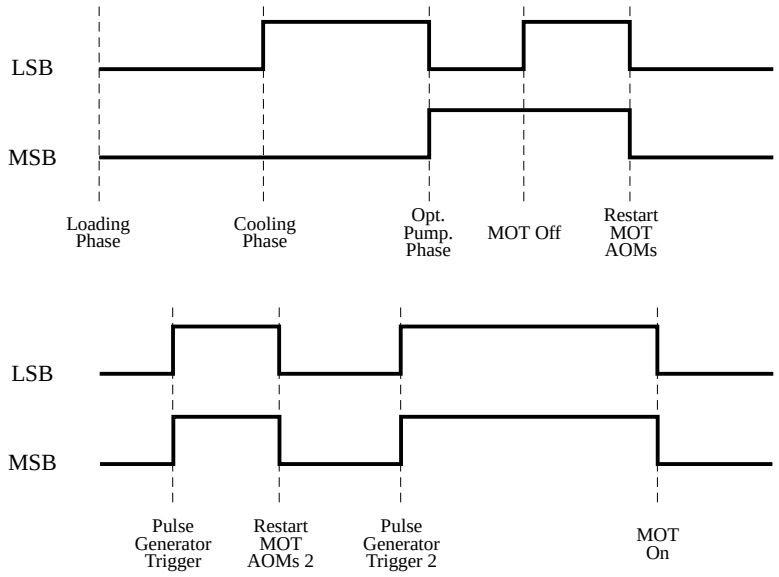

Figure B.6: Timing diagram for the MOT AOM LSB and MSB channels. The LSB diagram is valid for channels 1 and 3 of Table B.1, the amplitude and frequency LSB; the MSB diagram is valid for channels 2 and 4. The diagram is not to scale.

Figure B.6 gives the timing diagram for the MOT frequency and amplitude LSB and MSB channels, based in part on the settings given in Table B.2. The diagram shows when the LSB and MSB channels change state, referenced to specific events in the timing sequence. Based on that diagram, and using the variables from Section B.5.2, the first four channels in the timing file are

MOT Amplitude LSB
0 $mot_cooling $mot_opt_pump $mot_off $restart_mot_aos $pulse_gen_trigger $restart_mot_aos2 $pulse_gen_trigger2 $mot_on

MOT Amplitude MSB
0 $mot_opt_pump $restart_mot_aos $pulse_gen_trigger $restart_mot_aos2 $pulse_gen_trigger2 $mot_on

MOT Frequency LSB
0 $mot_cooling $mot_opt_pump $mot_off $restart_mot_aos $pulse_gen_trigger $restart_mot_aos2 $pulse_gen_trigger2 $mot_on

MOT Frequency MSB
0 $mot_opt_pump $restart_mot_aos $pulse_gen_trigger $restart_mot_aos2 $pulse_gen_trigger2 $mot_on

The repumper AOM frequency LSB and MSB channels are similar to those for the MOT AOM frequency, except that the repumper AOM can be left off during the MOT AOM rewarming phases and the probe beam phases.

Repumper Frequency LSB
0 $mot_cooling $mot_opt_pump $mot_off $mot_on

Repumper Frequency MSB
0 $mot_opt_pump $mot_on

Channels 7, 8, and 9 are not used in this timing file, though for historical reasons they will be set high.

```
Channel 7
1

Channel 8
1

Channel 9
1
```

The three shutter channels switch states at times set by their eponymous variables. The probe shutter is initially closed, so its channel's initial state is 0; the other two shutters are initially open, so their channels' initial state is 1. The probe shutter is opened and closed twice, once for each time the probe beam is turned on.

```
Probe Shutter
0 $probe_shutter_open $probe_shutter_close $probe_shutter_open2 $probe_shutter_close2

Slower Shutter
1 $slower_shutter_close $slower_shutter_open

MOT Shutter 1
$mot_shutter_close $mot_shutter_open
```

The Probe On/Off channel controls whether or not the probe beam AOMs (in the $3/2$ and $1/2$ arms of Figure B.5) are on. To keep the AOMs warm throughout the experiment, the probe AOMs are left on until just before the probe shutter is opened, turned back on when the pulse generator fires, left on until the probe shutter opens a second time, and then turned back on when the pulse generator fires a second time.

```
Probe On/Off
1 $probe_shutter_open $pulse_gen_trigger $probe_shutter_open2 $pulse_gen_trigger2
```

Similarly, the Repumper On/Off channel controls whether or not the MOT's repumper AOMs are on. As mentioned above, the repumper AOMs need only be on when the MOT itself is on. Channel 15 is not used in this timing file.

```
Repumper On/Off
1 $mot_off $mot_on

Channel 15
0
```

The Hummer LSB and MSB channels control the state of the "Hummer," which produces the MOT magnets' current. The Hummer can be in one of four states. In this timing file, two states will be used: on (corresponding to MSB high and LSB low) and off (corresponding to both channels low). The LSB channel will begin low and stay low. The MSB channel will begin high, switching states when the magnets are to be turned on or off.

```
Hummer LSB
0

Hummer MSB
1 $magnets_off $reversed_magnets_on $reversed_magnets_off $magnets_on
```

The PMT gate channel controls when the photomultiplier tube is active. In this timing file, the PMT is not used. The CO2 Controller channel controls whether the CO_2 laser AOM is on or off; when the channel is high, the AOM is on and light from the CO_2 laser reaches the trapping region. The MOT Magnet Flipper Logic controls the relay which reverses the MOT magnets' polarity.

```
PMT Gate
0

Channel 19
0

CO2 Controller
1 $co2_off $co2_on

MOT Magnet Flipper Logic
1 $flipper_on $flipper_off
```

The polarity of the Master Shutter is opposite that of other shutters: when its

channel is low, the shutter is open. The Camera Shutter has the same polarity as the other shutters.

Master Shutter
0 $master_shutter_close $master_shutter_open $master_shutter_close2 $master_shutter_open2

Channel 23
0

Camera Shutter Trigger
0 $camera_shutter_open $camera_shutter_close $camera_shutter_open2 $camera_shutter_close2

The pulse generator is triggered by the rising edge of the Pulse Generator Trigger channel. Because the pulse generator merely needs a rising edge, the channel can return to its original state one time step after it changes state.

Pulse Generator Trigger
0 $pulse_gen_trigger $pulse_gen_trigger+1 $pulse_gen_trigger2 $pulse_gen_trigger2+1

Like the probe beam AOMs in the 3/2 and 1/2 arm, the imaging AOMs must be kept warm. While those AOMs are normally controlled by the pulse generator, the signal lines from the pulse generator are combined with the output from the Camera AOs Warming Trigger line in a logical AND. The Camera AOs Warming Trigger is on when the probe shutter is closed, and off when it is open. The lag of the probe shutter must be taken into account when turning the channel back on.

Camera AOs Warming Trigger
1 $probe_shutter_open $probe_shutter_close+$shutter_lag $probe_shutter_open2 $mot_on

The only channel remaining to be defined is the Backgoing Beam Chopper.

```
Channel 27
0

Channel 28
0

Channel 29
0

Backgoing Beam Chopper
0 $chop_beam $unchop_beam

Channel 31
0

Channel 32
0
```

The timing file will also require the GPIB commands for the pulse generator and the line which defines how long the timing sequence will take, the time step size, and the number of channels. The pulse generator's GPIB address is 6; for an explanation of the commands being sent to the DG535, please see the SRS DG535 manual.

```
GPIB: 6: TM1;TL2.5
GPIB: 6: DT2,1,$lpw1;DT3,2,$lpd+.001;DT5,2,$lpw2;DT6,5,$lpd;
$end_time*.0001 .0001 32
```

The timing file is now complete. The variables' definitions begin the timing file, followed by the GPIB commands and the line defining how long the timing sequence takes, and concluding with the channel definitions listed above. If, in the course of running the experiment which corresponds to this timing file, one of the times contained in the variables needs to be changed, the timing file must be edited and then re-loaded into the LabView program once the current timing sequence has ended.

Appendix C

Fermionic Density Calculation

The following Mathematica notebook will reproduce the calculations used to produce the density distributions from Chapter 6.

Definitions

$$\textbf{phyconsts} = \{\ \textbf{mass} \to 10^{-23},\ \textbf{hbar} \to 1.055 * 10^{-27},\ \textbf{n0} \to 10^{13},\ \textbf{U0} \to (690 * 1.381 * 10^{-22}),\ \textbf{bohr} \to 0.529 * 10^{-8}\ \};$$

Calculate the Fermi density given a number of atoms. fermiGamma0 gives the $\gamma 0$ value which corresponds to the given Fermi density for the appropriate # of atoms.

$$\textbf{FermiN}[\textbf{N\_}] := 1/\pi^2\ \textbf{Sqrt}[4/3]\ \textbf{Sqrt}[\textbf{N}\ (2\pi)^3\ 6600 * 6600 * 340]/(\textbf{hbar}/\textbf{mass})^{3/2}\ /.\ \textbf{phyconsts}$$

$$\textbf{FermiN}[100000]$$

$$\textbf{fermiGamma0}[\textbf{N\_}] := (\textbf{FermiN}[\textbf{N}]/\textbf{n0})^{1/3}\ /.\ \textbf{phyconsts}$$

$$\textbf{fermiGamma0}[100000]$$

U(r) is the potential, and constX the "constants" in front of the γ terms.

$$\textbf{U}[\textbf{r\_}] := \textbf{U0} * \textbf{r}^2$$

$$\textbf{constA}[\textbf{a\_}] := -\left(8\pi \textbf{a}(\textbf{n0})^{1/3}/(6\pi^2)^{2/3}\right)$$

$$\textbf{constB}[\textbf{r\_}] := 2\ \textbf{mass}\ \textbf{U}[\textbf{r}]/(\textbf{hbar}^2\ (6\pi^2\ \textbf{n0})^{2/3})$$

$$\textbf{constC}[\textbf{a\_}, \textbf{r\_}, \gamma\textbf{0\_}] := \textbf{-constB}[\textbf{r}] + \gamma\textbf{0}^2 - \textbf{constA}[\textbf{a}]\ \gamma\textbf{0}^3$$

```
oldeqn = γ^2 - constA[a] γ^3 - constC[a, r, γ0] == 0
```

This cubic eqn has a discriminant. When that discriminant is < 0, there is one real and two imaginary roots. When the discriminant is 0, there are two real roots. When > 0, there are three real roots. The proper solution to the above equation has one real sol'n, and so exists only so long as the discriminant is < 0. Note: DO NOT HAND-SIMPLIFY the following equation. For some reason, if you e.g. cancel some of the constCs, Mathematica only returns two roots, both imaginary. Who knows?

```
discrimLimit[a_, γ0_] := r /. Solve[
    constC[bohr * a, r, γ0]^2 -
    4 constC[bohr * a, r, γ0]/(27 constA[bohr * a]^2) ==
    0 //. phyconsts, r][[4]]
```

The Density Functions

Even though the density function for a = 0 doesn't need the parameter "a" passed to it, I leave it in so that it has the same calling pattern as the density function for a != 0. The same for its limit.

```
NoADensity[a_, r_, γ0_] :=
    Sqrt[γ0^2 - (2 mass/(hbar^2 (6π^2 n0)^(2/3)))U0 r^2]^3 /. phyconsts

NoADensityLimit[a_, γ0_] :=
    Sqrt[γ0^2 hbar^2 (6π^2 n0)^(2/3)/(2 mass U0)] /. phyconsts
```

And now, the density function for a != 0. NSolve returns an array of possible roots; we select the proper one.

```
OldDensity[ayy_, arr_, gee_] :=
    Module[{partnum = Evaluate[If[ayy < 0, 2, 3]]},
    γ^3 /. Part[NSolve[
    oldeqn //. Flatten[{phyconsts, a → (bohr*ayy),
    r → arr, γ0 → gee}], γ],
    partnum]]
```

A function which returns the proper density, regardless of whether a = 0 or a < 0.

```
DensityFn[a_, r_, γ0_] := If[a == 0,
    If[r < NoADensityLimit[a, γ0], NoADensity[a, r, γ0], 0],
    If[r < discrimLimit[a, γ0], OldDensity[a, r, γ0], 0]]
```

Calculate the number of atoms in a density distribution.

```
CalcNumber[a_, γ0_] := Module[{F, LIM},
    If [a == 0, F = NoADensity; LIM = NoADensityLimit,
    F = OldDensity; LIM = discrimLimit];
    NIntegrate[4π n0 r^2 F[a, r, γ0] /. phyconsts,
    {r, 0, LIM[a, γ0]}] * (2 U0 / (mass * (2π 6600)^2))
    *Sqrt[2 U0 / (mass *(2π 340)^2)] /. phyconsts]

Plot[OldDensity[-.001, r, 1.870458],
    {r, 0, discrimLimit[-.001, 1.870458]}]
```

Comparing the Various Density Distributions

I'll need to calculate what central densities are required for various scattering lengths given the condition that we have 100,000 atoms in each state.

```
fermiGamma0[100000]

CalcNumber[1250, 1.69334]

CalcNumber[1000, 1.72041]

CalcNumber[500, 1.78489]

CalcNumber[300, 1.81589]

CalcNumber[100, 1.85100]

CalcNumber[0, 1.87046]

CalcNumber[-100, 1.89144]

CalcNumber[-300, 1.93907]

CalcNumber[-500, 1.99693]

CalcNumber[-1000, 2.2431]

CalcNumber[-1250, 2.7889]
```

Note that I can't go to a much higher scattering length than -1200 a0. If I do, I can't pick a central density large enough to give me 100,000 atoms. For a < 0, as I turn up the central density the # of atoms rises, then falls, never reaching 100,000. For a > 0, as I turn up the central density the numerical solution never converges. Why? you ask. Because I'm moving into the unstable region, where there are too many atoms for a given scattering length.

Now I'll collate all of these numbers into an array containing elements that are equal to {scattering length, central density}. This array can then be mapped to a function in order to plot the densities for all of these pairs at once.

```
LenGammaArray = {{1250, 1.69334}, {1000, 1.72041},
      {500, 1.78489}, {300, 1.81589}, {100, 1.85100},
      {0.00001, 1.87046}, {-100, 1.89144},
      {-300, 1.93907}, {-500, 1.99693},
      {-1000, 2.2431}, {-1250, 2.7889}};

Plot[Evaluate[Map[DensityFn[#[[1]], r, #[[2]]] &,
      LenGammaArray]], {r, 0, discrimLimit[1250, 1.69334]}]

Plot[{DensityFn[0, r, 1.87046], DensityFn[-100, r, 1.89144],
      DensityFn[-500, r, 1.99693], DensityFn[-1000, r, 2.2431],
      DensityFn[-1250, r, 2.7889]},
      {r, 0, NoADensityLimit[0, 1.87046]}]

Plot[{DensityFn[100, r, 1.9], DensityFn[300, r, 1.9],
      DensityFn[500, r, 1.9], DensityFn[1000, r, 1.9],
      DensityFn[1250, r, 1.9], DensityFn[0, r, 1.9],
      DensityFn[-100, r, 1.9], DensityFn[-500, r, 1.9],
      DensityFn[-1000, r, 1.9]}, {r, 0, discrimLimit[1250, 1.9]}]
```

Axial Distribution

Let's find what the density distribution along the axis of the trap will be by taking the density distribution and integrating through rho. (Note that the trap has cylindrical symmetry.)

```
neweqn = oldeqn /. r^2 → ρ^2 + z^2

cylindLimit[a_, z_, γ0_] := ρ /. Solve[
```

```
constC[bohr*a, Sqrt[ρ^2 + z^2], γ0]^2
- 4 constC[bohr*a, Sqrt[ρ^2 + z^2],
γ0]/(27 constA[bohr*a]^2) == 0 //. phyconsts, ρ][[4]]

cylindDensity[a_, z_, γ0_] := If[
    z < discrimLimit[a, γ0], NIntegrate[
    2πρ OldDensity[a, Sqrt[ρ^2 + z^2],
    γ0], {ρ, 0, cylindLimit[a, z, γ0]}], 0]

cylindDensity[-.001, 0, 1.9]

Plot[cylindDensity[-.001, z, 1.9],
    {z, 0, discrimLimit[-.001, 1.9]}]

Plot[Evaluate[Map[cylindDensity[#[[1]], z, #[[2]]] &,
    LenGammaArray]], {z, 0, discrimLimit[1250, 1.69334]}]

Plot[{cylindDensity[-.0001, z, 1.87046],
    cylindDensity[-100, z, 1.89144],
    cylindDensity[-500, z, 1.99693],
    cylindDensity[-1000, z, 2.2431],
    cylindDensity[-1250, z, 2.7889]},
    {z, 0, NoADensityLimit[0, 1.87046]}]

Plot[{cylindDensity[-.0001, z, 1.9], cylindDensity[-100, z, 1.9],
    cylindDensity[-500, z, 1.9], cylindDensity[-1000, z, 1.9]},
    {z, 0, NoADensityLimit[0, 1.9]}]
```

Let's make sure the cylindrical density integrates to the appropriate # of atoms.

```
NIntegrate[2 n0 cylindDensity[-1000, z, 2.2431] /. phyconsts,
    {z, 0, cylindLimit[-1000, 0, 2.2431]}]*
    (2 U0/(mass*(2π 6600)^2))*
    Sqrt[2 U0/(mass*(2π 340)^2)] /. phyconsts
```

Bibliography

[1] M. H. Anderson, J. R. Ensher, M. R. Matthews, C. E. Wieman, and E. A. Cornell. Observation of Bose-Einstein condensation in a dilute atomic vapor. *Science*, 269(0):198, July 1995. 1, 127

[2] C. C. Bradley, C. A. Sackett, J. J. Tollett, and R. G. Hulet. Evidence of Bose-Einstein condensation in an atomic gas with attractive interactions. *Phys. Rev. Lett.*, 75(9):1687, August 1995. *ibid.*, 79(6):1170, August 1997. 1, 127

[3] K. B. Davis, M.-O. Mewes, M. R. Andrews, N. J. van Druten, D. S. Durfee, D. M. Kurn, and W. Ketterle. Bose-Einstein condensation in a gas of sodium atoms. *Phys. Rev. Lett.*, 75(22):3969, November 1995. 1, 127

[4] A. Einstein. *Sitzungsber. Kgl. Preuss. Akad. Wiss.*, 1:3, 1925. 1

[5] S. Inouye, M. R. Andrews, J. Stenger, H.-J. Miesner, D. M. Stamper-Kurn, and W. Ketterle. Observation of Feshbach resonances in a Bose-Einstein condensate. *Nature*, 392(0):151, March 1998. 1

[6] J. L. Roberts, N. R. Claussen, James P. Burke, Jr., Chris H. Greene, E. A. Cornell, and C. E. Wieman. Resonant magnetic field control of elastic scattering of cold ^{85}Rb. *Phys. Rev. Lett.*, 81(23):5109, December 1998. 1

[7] Ph. Courteille, R. S. Freeland, D. J. Heinzen, F. A. van Abeleen, and B. J. Verhaar. Observation of a Feshbach resonance in cold atom scattering. *Phys. Rev. Lett.*, 81(1):69, July 1998. 1

[8] M.-O. Mewes, M. R. Andrews, D. M. Kurn, D. S. Durfee, C. G. Townsend, and W. Ketterle. Output coupler for Bose-Einstein condensed atoms. *Phys. Rev. Lett.*, 78(4):582, January 1997. 1

[9] E. W. Hagley, L. Deng, M. Kozuma, J. Wen, K. Helmerson, S. L. Rolston, and W. D. Phillips. A well-collimated quasi-continuous atom laser. *Science*, 283:1706, March 1999. 1

[10] I. Bloch, T. W. Hänsch, and T. Esslinger. Atom laser with a cw output coupler. *Phys. Rev. Lett.*, 82(15):3008, April 1999. 1

[11] E. R. Dobbs. *Helium Three*. Oxford University Press, 2000. 2

[12] G. M. Bruun and C. W. Clark. Hydrodynamic excitations of trapped Fermi gases. *Phys. Rev. Lett.*, 83(26):5415, December 1999. 2

[13] L. Vichi and S. Stringari. Collective oscillations of an interacting trapped Fermi gas. *Phys. Rev. A*, 60(6):4734, December 1999. 2

[14] H. T. C. Stoof, M. Houbiers, C. A. Sackett, and R. G. Hulet. Superfluidity of spin-polarized ^{6}Li. *Phys. Rev. Lett.*, 76(1):10, January 1996. 2, 15

[15] M. Houbiers, R. Ferwerda, H. T. C. Stoof, W. I. McAlexander, C. A. Sackett, and R. G. Hulet. Superfluid state of atomic ^{6}Li in a magnetic trap. *Phys. Rev. A*, 56(6):4864, December 1997. 2, 38, 162, 168

[16] M. Holland, S. J. J. M. F. Kokkelmans, M. L. Chiofalo, and R. Walser. Resonance superfluidity in a quantum degenerate Fermi gas. *Phys. Rev. Lett.*, 87(12):120406, September 2001. 2, 40, 188

[17] E. Timmermans, K. Furuya, P. W. Milonni, and A. K. Kerman. Prospect of creating a composite Fermi-Bose superfluid. *Phys. Lett. A*, 285(3-4):228, July 2001. 2, 188

[18] R. Combescot. Trapped ^{6}Li: A high T_c superfluid? *Phys. Rev. Lett.*, 83(19):3766, November 1999. 2

[19] H. J. Lee, C. S. Adams, N. Davidson, B. Young, M. Weitz, M. Kasevich, and Steven Chu. Dipole trapping, cooling in traps, and long coherence times. *At. Phys.*, 14(323):258, 1995. 3, 17, 54

[20] C. S. Adams, H. Lee, N. Davidson, M. Kasevich, and S. Chu. Evaporative cooling in a crossed dipole trap. *Phys. Rev. Lett.*, 74(18):3577, May 1995. 3, 54

[21] T. Takekoshi and R. J. Knize. CO_2 laser trap for cesium atoms. *Opt. Lett.*, 21(1):77, January 1996. 3, 52, 122

[22] M. D. Barrett, J. A. Sauer, and M. S. Chapman. All-optical formation of an atomic Bose-Einstein condensate. *Phys. Rev. Lett.*, 87(1):010404, July 2001. 3, 4, 16

[23] M. Houbiers and H. T. C. Stoof. Cooper-pair formation in trapped atomic Fermi gases. *Phys. Rev. A*, 59(2):1556, February 1999. 3

[24] K. M. O'Hara, S. R. Granade, M. E. Gehm, T. A. Savard, S. Bali, C. Freed, and J. E. Thomas. Ultrastable CO_2 laser trapping of lithium fermions. *Phys. Rev. Lett.*, 82(21):4204, May 1999. 3, 17, 46

[25] S. R. Granade, M. E. Gehm, K. M. O'Hara, and J. E. Thomas. All-optical production of a degenerate Fermi gas. *Phys. Rev. Lett.*, 88(12):120405, March 2002. 3, 16, 18

[26] K. M. O'Hara. *Optical Trapping and Evaporative Cooling of Fermionic Atoms*. PhD thesis, Duke University, 2000. 3, 30, 31, 33, 50, 59, 71, 74, 75, 127, 129, 133

[27] E. W. Hagley, L. Deng, W. D. Phillips, K. Burnett, and C. W. Clark. The atom laser. *Optics & Photonics News*, May 2001:22, May 2001. 6

[28] E. A. Cornell, J. R. Ensher, and C. E. Wieman. Experiments in dilute atomic Bose-Einstein condensation. In M. Inguscio, S. Stringari, and C. E. Wieman, editors, *Bose-Einstein Condensation in Atomic Gases: Proceedings of the International School of Physics "Enrico Fermi"*, page 15. Italian Physical Society, 1999. 7

[29] N. R. Newbury and C. Wieman. Resource letter TNA-1: Trapping of neutral atoms. *Am. J. Phys*, 64(1):18, January 1996. 8

[30] B. DeMarco and D. S. Jin. Onset of Fermi degeneracy in a trapped atomic gas. *Science*, 285(5434):1703, September 1999. 14, 19, 181

[31] A. G. Truscott, K. E. Strecker, W. I. McAlexander, G. Partridge, and R. G. Hulet. Observation of Fermi pressure in a gas of trapped atoms. *Science*, 291(5513):2570, March 2001. 14, 19, 181

[32] F. Schreck, L. Kaykovich, K. L. Corwin, G. Ferrari, T. Bourdel, J. Cubizolles, and C. Salomon. Quasipure Bose-Einstein condensate immersed in a Fermi sea. *Phys. Rev. Lett.*, 87(8):080403, August 2001. 14, 19, 181

[33] Z. Hadzibabic, C. A. Stan, K. Dieckmann, S. Gupta, M. W. Zwierlein, A. Görlitz, and W. Ketterle. Two-species mixture of quantum degenerate Bose and Fermi gases. *Phys. Rev. Lett.*, 88(16):160401, 2002. 14, 19

[34] J. L. Bohn. Cooper pairing in ultracold ^{40}K using Feshbach resonances. *Phys. Rev. A*, 61(5):053409, May 2000. 15

[35] A. Ashkin. Acceleration and trapping of particles by radiation pressure. *Phys. Rev. Lett.*, 24(4):156, January 1970. 15

[36] H. J. Lee, C. S. Adams, M. Kasevich, and S. Chu. Raman cooling of atoms in an optical dipole trap. *Phys. Rev. Lett.*, 76(15):2658, April 1996. 17

[37] C. S. Adams and E. Riis. Laser cooling and trapping of neutral atoms. *Prog. Quant. Electr.*, 21(1):1, 1997. 17, 54

[38] T. A. Savard, K. M. O'Hara, and J. E. Thomas. Laser-noise-induced heating in far-off resonance optical traps. *Phys. Rev. A*, 56(2):R1095, August 1997. 17, 55, 56, 57

[39] M. E. Gehm, K. M. O'Hara, T. A. Savard, and J. E. Thomas. Dynamics of noise-induced heating in atom traps. *Phys. Rev. A*, 58(5):3914, November 1998. 17

[40] D. M. Stamper-Kurn, M. R. Andrews, A. P. Chikkatur, S. Inouye, H.-J. Miesner, J. Stenger, and W. Ketterle. Optical confinement of a Bose-Einstein consensate. *Phys. Rev. Lett.*, 80(10):2027, 1998. 20, 188

[41] D. S. Hall, M. R. Matthews, J. R. Ensher, C. E. Wieman, and E. A. Cornell. Dynamics of component separation in a binary mixture of Bose-Einstein condensates. *Phys. Rev. Lett.*, 81(8):1539, August 1998. 20, 188

[42] P. Maddaloni, M. Modugno, C. Fort, F. Minardi, and M. Inguscio. Collective oscillations of two colliding Bose-Einstein condensates. *Phys. Rev. Lett.*, 85(12):2413, September 2000. 20, 188

[43] S. D. Gensemer and D. S. Jin. Transition from collisionless to hydrodynamic behavior in an ultracold Fermi gas. *Phys. Rev. Lett.*, 87(17):173201, October 2001. 20

[44] B. DeMarco and D. S. Jin. Spin excitations in a Fermi gas of atoms. *Phys. Rev. Lett.*, 88(4):040405, January 2002. 20

[45] C. J. Joachain. *Quantum Collision Theory.* North-Holland Publishing Company, 1983. 28, 29

[46] E. Fermi. Sul moto dei neutroni lenti. *Ricerca Scient.*, VII:13, 1936. 29

[47] R. Côté, A. Dalgarno, and M. J. Jamieson. Elastic scattering of two ^{7}Li atoms. *Phys. Rev. A*, 50(1):399, July 1994. 31

[48] B. Barakat, R. Bacis, F. Carrot, S. Churassy, P. Crozet, F. Martin, and J. Verges. Extensive analysis of the $X\,^1\Sigma_g^+$ ground state of $^7Li_2$ by laser-induced fluorescence fourier transform spectrometry. *Chemical Physics*, 102:215, 1986. 31

[49] D. D. Konowalow and M. L. Olson. The electronic structure and spectra of the $X\,^1\Sigma_g^+$ and $A\,^1\Sigma_u^+$ states of Li_2. *J. Chem. Phys.*, 71(1):450, July 1979. 31

[50] I. Schmidt-Mink, W. Müller, and W. Meyer. Ground- and excited-state properties of Li_2 and Li_2^+ from *ab initio* calculations with effective core polarization potentials. *Chemical Physics*, 92:263, 1985. 31

[51] Z.-C. Yan, J. F. Babb, A. Dalgarno, and G. W. F. Drake. Variational calculations of dispersion coefficients for interacctions among H, He, and Li atoms. *Phys. Rev. A*, 54(4):2824, October 1996. 31

[52] E. R. I. Abraham, W. I. McAlexander, J. M. Gerton, R. G. Hulet, R. Côté, and A. Dalgarno. Triplet s-wave resonance in ^{6}Li collisions and scattering lengths of ^{6}Li and ^{7}Li. *Phys. Rev. A*, 55(5):R3299, May 1997. 31

[53] W. T. Zemke and W. C. Stwalley. Analysis of long-range dispersion and exchange interactions of two lithium atoms. *J. Phys. Chem.*, 97(10):2053, 1993. 31

[54] D. D. Konowalow, R. M. Regan, and M. E. Rosenkrantz. The "most likely" potential energy curve for the lowest $^3\Sigma_u^+$ state of Li_2. *J. Chem. Phys.*, 81(10):4534, November 1984. 31

[55] H. T. C. Stoof, J. M. V. A. Koelman, and B. J. Verhaar. Spin-exchange and dipole relaxation rates in atomic hydrogen: Rigorous and simplified calculations. *Phys. Rev. B*, 38(7):4688, September 1988. 32, 162

[56] M. Houbiers, H. T. C. Stoof, W. I. McAlexander, and R. G. Hulet. Elastic and inelastic collisions of Li-6 atoms in magnetic and optical traps. *Phys. Rev. A*, 57(3):R1497, March 1998. 33, 42, 43

[57] A. J. Moerdijk, B. J. Verhaar, and A. Axelsson. Resonances in ultracold collisions of ^{6}Li, ^{7}Li, and ^{23}Na. *Phys. Rev. A*, 51(6):4852, June 1995. 35

[58] J. M. Blatt. *Theory of Superconductivity.* Academic Press, New York, 1964. 36

[59] J. Bardeen, L. N. Cooper, and J. R. Schrieffer. Theory of superconductivity. *Phys. Rev.*, 108(5):1175, December 1957. 37

[60] A.J. Leggett. Cooper pairing in spin-polarized Fermi systems. *Journal de Physique Colloque*, 41(C-7):19, 1980. 38, 39, 40, 188

[61] M. A. Baranov, Yu. Kagan, and M. Yu. Kagan. On the possibility of a superfluid transition in a Fermi gas of neutral particles at ultralow temperatures. *JETP Lett.*, 64(4):301, August 1996. 39

[62] M. Randeria. Crossover from BCS theory to Bose-Einstein condensation. In A. Griffin, D. W. Snoke, and S. Stringari, editors, *Bose-Einstein Condensation*, pages 355–392. Cambridge Univ. Press, 1995. 40, 189

[63] S. J. J. M. F. Kokkelmans, J. N. Milstein, M.L. Chiofalo, R. Walser, and M. J. Holland. Resonance superfluidity: Renormalization of resonance scattering theory. *Phys. Rev. A*, 65(5):053617, 2002. 40, 188

[64] K. M. O'Hara, M. E. Gehm, S. R. Granade, S. Bali, and J. E. Thomas. Stable, strongly attractive, two-state mixture of lithium fermions in an optical trap. *Phys. Rev. Lett.*, 85(10):2092, September 2000. 46

[65] A. Ashkin. Trapping of atoms by resonance radiation pressure. *Phys. Rev. Lett.*, 40(12):729, March 1978. 46

[66] R. Loudon. *The Quantum Theory of Light*. Oxford University Press, New York, second edition, 1983. 50

[67] S. Friebel, C. D'Andrea, J. Walz, M. Weitz, and T. W. Hänsch. CO_2-laser optical lattice with cold rubidium atoms. *Phys. Rev. A.*, 57(1):R20, January 1998. 52

[68] M. Weidemüller, H. Engler, M. Nill, T. Weber, and R. Grimm. Lithium and cesium in a quasi-electrostatic CO_2-laser trap. *Laser Spectroscopy. 14th International Conference. ICOLS99*, page 336, 1999. 52

[69] T. Takekoshi, J. R. Yeh, and R. J. Knize. Quasi-electrostatic trap for neutral atoms. *Opt. Comm.*, 114(5):421, February 1995. 52

[70] L. Windholz. Precise stark-effect investigations of the lithium D_1 and D_2 lines. *Phys. Rev. A*, 46(9):5812, November 1992. 52

[71] C. A. Baird. Design and characterization of a multi-coil zeeman slower. Master's thesis, Duke University, 1996. 67, 74

[72] T. A. Savard. *Raman Induced Resonance Imaging of Trapped Atoms*. PhD thesis, Duke University, 1998. 68

[73] V. I. Balykin, V. S. Letokhov, and V. I. Mishin. Observation of free Na atom cooling in a resonant laser field at scanning frequency. *JETP Lett*, 29(10):614, May 1979. 73

[74] P. D. Lett, W. D. Phillips, S. L. Rolston, C. E. Tanner, R. N. Watts, and C. I. Westbrook. Optical molasses. *J. Opt. Soc. Am. B*, 6(11):2084, November 1989. 74

[75] M. L. Marable. *Adaptive Resonance Imaging and All-Optical Interferometry.* PhD thesis, Duke University, 1995. 75, 76

[76] J. R. Gardner. *Ultra-High Resolution Atom Imaging in a Light-Shift Gradient.* PhD thesis, Duke University, 1995. 77

[77] A. Yariv. *Optical Electronics.* Holt, Rinehart and Winston, New York, fourth edition, 1991. 84

[78] D. A. Butts and D. S. Rokhsar. Trapped Fermi gases. *Phys. Rev. A*, 55(6):4346, June 1997. 115, 118, 155, 162, 167, 174

[79] G. M. Bruun and C. W. Clark. Ideal gases in time-dependent traps. *Phys. Rev. A*, 61(6):061601(R), May 2000. 117

[80] R. Jáuregui. Nonperturbative and perturbative treatments of parametric heating in atom traps. *Phys. Rev. A*, 64(5):053408, November 2001. 121, 123

[81] W. Ketterle and N. J. van Druten. Evaporative cooling of atoms. *Adv. At. Mol. Opt. Phys.*, 37:181, 1996. 127, 155, 157

[82] O. J. Luiten, M. W. Reynolds, and J. T. M. Walraven. Kinetic theory of the evaporative cooling of a trapped gas. *Phys. Rev. A*, 53(1):381, January 1996. 127, 129, 132, 135, 185

[83] K. Huang. *Statistical Mechanics.* Wiley, New York, 1987. 131

[84] E. G. Harris. *A Pedestrian Approach to Quantum Field Theory.* John Wiley & Sons, Inc., 1972. 133

[85] K. M. O'Hara, M. E. Gehm, S. R. Granade, and J. E. Thomas. Scaling laws for evaporative cooling in time-dependent optical traps. *Phys. Rev. A*, 64(5):051403(R), November 2001. 135

[86] H. T. C. Stoof, M. Bijlsma, and M. Houbiers. Theory of interacting quantum gases. *NIST J. Res*, 101(4):443, 1996. 167

[87] T. Loftus, C. A. Regal, C. Ticknor, J. L. Bohn, and D. S. Jin. Resonant control of elastic collisions in an optically trapped Fermi gas of atoms. *Phys. Rev. Lett.*, 88(17):173201, April 2002. 181

[88] D. DeMille. Quantum computation with trapped polar molecules. *Phys. Rev. Lett.*, 88(6):067901, February 2002. 188

[89] B. K. Teo, J. R. Guest, and G. Raithel. Tunneling resonances and coherence in an optical lattice. *Phys. Rev. Lett.*, 88(17):173001, April 2002. 188

[90] E. Dagotto. Correlated electrons in high-temperature superconductors. *Rev. Mod. Phys.*, 66(3):763, July 1994. 188

[91] M. V. Romalis and E. N. Fortson. Zeeman frequency shifts in an optical dipole trap used to search for an electric-dipole moment. *Phys. Rev. A*, 59(59):4547, June 1999. 188

[92] S. J. J. M. F. Kokkelmans, B. J. Verhaar, K. Gibble, and D. J. Heinzen. Predictions for laser-cooled Rb clocks. *Phys. Rev. A*, 56(6):4389, December 1997. 188

[93] P. J. Leo, P. S. Julienne, F. H. Mies, and C. J. Williams. Collisional frequency shifts in ^{133}Cs fountain clocks. *Phys. Rev. Lett.*, 86(17):3743, April 2001. 188

[94] Y. Ohashi and A. Griffin. The BCS-BEC crossover in a gas of Fermi atoms with a Feshbach resonance. See cond-mat/0201262, 2002. 188

Biography

Stephen Granade was born on August 29, 1972 in Arkadelphia, Arkansas. In 1990 he was graduated from Arkadelphia High School and chose to attend Ouachita Baptist University. An inability to settle on one field of study resulted in him being graduated *Summa Cum Laude* in 1995 with degrees in physics and theatre arts. He married Misty Clark on May 28, 1995; the following fall he enrolled in the graduate physics program at Duke University. In 1996 he joined Professor John E. Thomas's lab, working on the trapping and cooling of fermionic lithium to the quantum degenerate regime. He was awarded the Fritz London Fellowship for this work in 2001. He received his A.M. from Duke in 1998 and his Ph.D. in 2002, both in Physics.

Publications

K. M. O'Hara, S. L. Hemmer, S. R. Granade, M. E. Gehm, J. E. Thomas, V. Venturi, E. Tiesinga, and C. J. Williams. "Measurement of the Zero Crossing in a Feshbach Resonance of Fermionic ^{6}Li," accepted by *Physical Review A*, (2002).

S. R. Granade, M. E. Gehm, K. M. O'Hara, and J. E. Thomas. "All-Optical Production of a Degenerate Fermi Gas," *Physical Review Letters* **88**, 120405 (2002). Highlighted in *Physics Today*, *Photonics Spectra*, *Photonics News*, and *AIP News Briefs*.

K. M. O'Hara, M. E. Gehm, S. R. Granade and J. E. Thomas, "Scaling Laws for Evaporative Cooling in Time-Dependent Optical Traps," *Physical Review A* **64**, 051403(R) (2001).

K. M. O'Hara, S. R. Granade, M. E. Gehm and J. E. Thomas, "Loading Dynamics of CO_2 Laser Traps," *Physical Review A* **63**, 043403 (2001).

K. M. O'Hara, M. E. Gehm, S. R. Granade, S. Bali and J. E. Thomas, "Stable, Strongly Attractive, Two-State Mixture of Lithium Fermions in an Optical Trap" *Physical Review Letters* **85**, 2092 (2000).

T. A. Savard, S. R. Granade, K. M. O'Hara, M. E. Gehm and J. E. Thomas, "Raman-Induced Magnetic Resonance Imaging of Atoms in a Magneto-Optical Trap," *Physical Review A* **60**, 4788 (1999).

S. Bali, K. M. O'Hara, M. E. Gehm, S. R. Granade and J. E. Thomas, "Quantum-diffractive background gas collisions in atom-trap heating and loss," *Physical Review A* **60**, R29 (1999).

K. M. O'Hara, S. R. Granade, M. E. Gehm, T. A. Savard, S. Bali, C. Freed and J. E. Thomas, "Ultrastable CO_2 laser trapping of lithium fermions," *Physical Review Letters* **82**, 4204 (1999). Highlighted in *Physical Review Focus*, on the web page of *Science* magazine, in *Physics World* and *Physics Today*, and in *Scientific American*.

S. R. Granade and T. W. Drueding, "Variation in Material Removal in Gaussian Removal Processes," *Optical Engineering* **35**, 3267 (1996).

Presentations

S. R. Granade, M. E. Gehm, K. M. O'Hara, and J. E. Thomas. "Preparation of a Degenerate, Two-Component Fermi Gas by Evaporation in a Single Beam Optical Trap," *OSA Technical Digest Series*, QELS2002 (2002).

M. E. Gehm, S. R. Granade, K. M. O'Hara, and J. E. Thomas. "All-Optical Production of a Degenerate Fermi Gas," *Bulletin of the American Physical Society*, DAMOP2002 (2002).

J. E. Thomas, K. M. O'Hara, S. R. Granade, M. E. Gehm and M.-S. Chang, "Optical Trapping of a Two-Component Fermi Gas," submitted to *Proceedings of the International Conference on Laser Science*, (2001).

K. M. O'Hara, M. E. Gehm, S. R. Granade, M.-S. Chang, and J. E. Thomas, "Coherence in an Optically-Trapped Fermi Gas," submitted to *Proceedings of the Eighth Rochester Conference on Coherence and Quantum Optics*, (2001).

M. E. Gehm, S. R. Granade, M.-S. Chang, K. M. O'Hara and J. E. Thomas, "Optically-Trapped Fermi Gas," *OSA Technical Digest Series*, QELS2001 (2001).

K. M. O'Hara, S. R. Granade, M. E. Gehm, M.-S. Chang and J. E. Thomas, "Modeling the Evaporative Cooling of Fermionic Atoms in an Optical Trap," *OSA Technical Digest Series*, QELS2001 (2001).

K. M. O'Hara, M. E. Gehm, S. R. Granade, S. Bali and J. E. Thomas, "Evaporative Cooling of Lithium Fermions in an Ultrastable Optical Trap," *Bulletin of the American Physical Society*, DAMOP2000 (2000).

S. R. Granade, K. M. O'Hara, M. E. Gehm, S. Bali and J. E. Thomas, "Spatial Loading Dynamics of CO_2 Laser Traps," *Bulletin of the American Physical Society*, DAMOP2000 (2000).

K. M. O'Hara, S. R. Granade, M. E. Gehm, S. Bali and J. E. Thomas, "Evaporative Cooling of Lithium Fermions in a Stable Optical Trap," *Bulletin of the American Physical Society*, SES99 (1999).

K. M. O'Hara, S. R. Granade, M. E. Gehm, T. A. Savard, S. Bali and J. E. Thomas, "Ultrastable CO_2 Laser Trapping of Lithium Fermions," *Bulletin of the American Physical Society*, CENTENNIAL (1999).

T. A. Savard, S. R. Granade, K. M. O'Hara, M. E. Gehm and J. E. Thomas, "Raman-Induced Magnetic Resonance Imaging of Trapped Atoms in a MOT," *Bulletin of the American Physical Society*, DAMOP1998 (1998).